First principles studies of adsorption, diffusion and reactivity of nanoclusters on surfaces

A Thesis
Submitted For the Degree of
DOCTOR OF PHILOSOPHY
in the Faculty of Science

by

Nisha Mammen

CHEMISTRY AND PHYSICS OF MATERIALS UNIT
JAWAHARLAL NEHRU CENTRE FOR ADVANCED SCIENTIFIC RESEARCH
Bangalore – 560 064

JANUARY 2016

To my Parents and Nithya

DECLARATION

I hereby declare that the matter embodied in the thesis entitled "**First principles studies of adsorption, diffusion and reactivity of nanoclusters on surfaces**" is the result of investigations carried out by me at the Chemistry and Physics of Materials Unit, Jawaharlal Nehru Centre for Advanced Scientific Research, Bangalore, India under the supervision of Prof. Shobhana Narasimhan and that it has not been submitted elsewhere for the award of any degree or diploma.

In keeping with the general practice in reporting scientific observations, due acknowledgement has been made whenever the work described is based on the findings of other investigators.

_____

Nisha Mammen

CERTIFICATE

I hereby certify that the matter embodied in this thesis entitled "**First principles studies of adsorption, diffusion and reactivity of nanoclusters on surfaces**" has been carried out by Ms. Nisha Mammen at the Chemistry and Physics of Materials Unit, Jawaharlal Nehru Centre for Advanced Scientific Research, Bangalore, India under my supervision and that it has not been submitted elsewhere for the award of any degree or diploma.

Prof. Shobhana Narasimhan
(Research Supervisor)

Acknowledgements

On completing my thesis, the person I would like to thank first and the most is my Ph.D. advisor, Prof. Shobhana Narasimhan. I have really enjoyed every moment working with her, on every project that I have handled. She has introduced me to interesting problems, and in most cases, when we got stuck or when work became boring, she always found ways to bring 'new twists' to the problems to make the work interesting. I thank her for being patient with me, for encouraging me and believing in me. We have had interesting and long conversations not only on scientific matters but also on art, books, love and even fairy tales. She has given me oppotunities to explore myself and improve not only my scientific temperament but also my personal life. She has given me chances to travel to many countries for conferences and also to visit renowned scientific institutions. She has baked cakes and pastries for us and many wonderful meals. I have learnt a lot from her, and there is still so much more I have to learn from her.

Next, I would like to thank my collaborators, Prof. Stefano de Gironcoli, Dr. Prasenjit Ghosh, Prof. Ram Seshadri, Dr. Leonardo Spanu, Prof. Stefan Vajda, Dr. Eric Tyo, Sukanya Ghosh and Rajdeep Banerjee. I especially thank Simone Piccinin for helpful discussions and suggestions.

I thank my course instructors for the scientific courses in JNCASR: Prof. U. Waghmare, Prof. S. Pati, Prof. N. S. Vidhyadhiraja, Prof. Balasubramanian, Prof. Sundaresan, Prof. Eswaramoorthy, Prof. Maji, Prof. Narayan, Prof. Chandrabhas Narayan, Prof. Shivaprasad, Prof. Kulkarni, Prof. Ranganathan, Prof. Subi George and Prof. Govindraju. I also thank all the TSU and CPMU faculty. I would also like to acknowledge the educative and helpful lectures by Prof. S. Baroni, Prof. S. de Gironcoli, Prof. R. Gebauer, Prof. S. Scandolo and Prof. M. Weinert.

I thank all my past and present labmates - Prasenjit, Jaita, Mighfar, Madhura, Brandon, Debosruti, Kanchan, Sananda, Vasudevan, Lakshmi, Bulumoni, Debarati, Debdipto, Sukanya, Rajdeep, Rajiv, Devina, Somesh, Saikat and Sourav for the lively lab atmosphere. We have had several fun activities and interactive group discussions in our group.

I thank my seniors, Mighfar and Madhura for answering my doubts and helping me understand the basics in our work. I thank Madhura, Kanchan and Sananda for all the discussions we have had regarding each other's work and for their ideas on my work. I thank Debdipto, Sukanya and Vasudevan for helping me with my thesis proofreading and in making the list of abbreviations.

I thank my Integrated Ph.D. classmates, Ritu, Vini, Urmi, Nitesh, Piyush, Abhay, Bivas and Soumik for making the first two years in JNCASR so much fun in spite of the busy course schedule.

I also acknowledge the funding from the Indo-Italian DST-MAE grant, ICMS-SISSA grant, IUPAP Women in Physics grant, TUE-CMS, GRC, Psi-k, Indo-French CEFIPRA grant and JNCASR for supporting me. I would like to acknowledge computational facilities from TUE-CMS (Amit, Ershad, Bharti, Vijay, Anand), CINECA, and CURIE.

I thank everyone in the Academic Section, especially Dr. Princy and Sukanya Ma'am. I thank Mr. Jayachandra, Mr. Gururaj, Ms. Jayamangala, Mr. Ramakrishna and Ms. Kalavati and all others in the Administrative Section for helping me with all the administrative procedures. I thank Dr. Archana and the Dhanvantri staff, the library staff, the complab staff and all the hostel staff including the cleaning and mess aunties.

I thank my teachers in school and Govt. Women's College in Thiruvananthapuram. I especially remember Dr. Sunita Rani, Ms. Esther Prema, Dr. Dinesh and Dr. Thomas at this time. I also thank my friends in Kerala: Saranya, Achu and Nitha.

During my Ph.D. tenure, I have also had the opportunity to join a dance class and learn Mohiniattam from Ms. Swapna Raju. She has been really patient with me and forgiving, for all the times I have missed classes due to work. I also thank my music teachers Ms. Seetha Krishnan, Ms. Amrutha Venkatesh and Ms. Vidya. Music and dance have made me the person I am today, and without these life would be just be dull and boring.

I made several good friends after coming to JNCASR, and thank each one of them for making my stay here so memorable. I thank Kanchan, Sananda, Sharmila, Arun, Sunil, Lakhumi, Vibhu anna, Chakri, Darth-Sid, Hema, Milli, Aditi, Pande and many more. I thank Shashank for being there for me always.

Finally, I thank my sister, Nithya for always bringing a smile to my face, and my loving parents for always supporting and believing in me. I dedicate this thesis to them.

Synopsis

In Chapter 1, we give a brief introduction to the problems studied in the thesis. Catalysts are materials that increase the rate of a chemical reaction by providing an alternative pathway with a lower activation barrier. Because of their huge industrial and biological significance, any advances in producing new or improved catalysts can represent significant progress, both intellectually and commercially. With the advent of nanoscience, there has arisen the possibility of using nanoparticles as catalysts. Such nanocatalysts are of great interest, both because they are frequently more reactive than conventional catalysts, and because one then requires smaller amounts of the catalyst material; we note that many commercially important catalysts are precious metals.

In this thesis, we explore three different themes, all of which are vital for the effective performance of nanocatalysts. Nanoclusters are generally placed on an (oxide) support when used in applications. Since larger sized nanoparticles are thermodynamically more stable, there is a tendency for smaller nanoparticles to diffuse on the support and then coalesce to form larger sized particles. This process is known as sintering and we study it in Section A. It is well known that the shape and charge state of nanoparticles have a huge impact on their catalytic activity. It is desirable to find an easy and practical way of tuning the particle morphology and charge. This problem is tackled in Section B. Finally, the performance of catalysts that are metal nanoparticles is frequently degraded by oxidation. It is generally believed that smaller particles get oxidized more easily. We would like to verify if this is true, and if so what is the smallest size metallic cluster that would be stable against oxidation for a given set of reaction conditions. These questions are addressed in Section C.

In Chapter 2, we discuss the main computational techniques and theoretical formalisms used in this thesis: density functional theory (DFT), the nudged elastic band method, constrained minimization, simulated annealing and *ab initio* atomistic thermodynamics.

In Chapter 3, we study the adsorption and the diffusion mechanisms of Pt_n clusters (n = 1–4) on the defect free MgO(100) surface, and the adsorption of these clusters at oxygen vacancy sites or F-centers on the surface. We find that these clusters tend to bind

more strongly at the F-center sites than on the defect free surface. We look at the possible growth processes for the growth of Pt_n clusters on the defect free surface and at F-center sites. We compare all the results that we obtain for Pt with those obtained for Pd clusters on the MgO(100) by earlier authors. We find that the diffusion barriers are higher for the Pt_n clusters than for the Pd_n clusters on MgO(100), which suggests that Pt clusters are less likely to sinter than Pd clusters.

In Chapter 4, we propose and demonstrate that substrate doping can be used as a simple technique to tune the morphology of supported Au clusters. Using the model system of Au_{20}/Aldoped MgO, we show that substrate doping can stabilize a two dimensional planar (P) geometry instead of the otherwise stable three dimensional tetrahedral (T) geometry. We explain this as arising from a charge transfer from the doped substrate to the Au cluster; the greater the doping, the greater the charge transfer. This idea of substrate doping to switch the morphology of Au clusters from 3D to 2D has been subsequently verified experimentally for the growth of Au clusters on Mo-doped CaO. We go on to confirm these experimental findings by repeating our calculations for Au_{20}/Mo-doped CaO; here too we find that substrate doping can trigger a change in morphology. We also find that substrate doping has a significant effect on the adsorption site and the geometry of small clusters of Au_n/Al-doped MgO; n = 1–3.

In Chapter 5, we show that substrate doping not only affects the morphology of the supported Au clusters, but also increases the reactivity of these clusters. To study the reactivity of an Au cluster, we have chosen a simple model reaction, viz., the dissociation of an O_2 molecule. We find that the barrier for dissociation is more than halved on the Au(P)/2.78% Al-doped MgO as compared to the barrier on Au(T)/MgO. We also find that the barriers for O_2 dissociation decrease monotonically as we increase the substrate doping. We find that the *d*-band model which was introduced to explain trends in the reactivity of transition metals and noble metals cannot explain our observed results. However, we find that if one includes the behavior of not just the *d*-states but also the *sp*-states of Au, we are able to explain this observed increase in the reactivity of Au clusters due to substrate doping. We introduce a new descriptor for reactivity that incorporates the effects of the *s*-, *p*- and *d*-bands.

In Chapter 6, we further investigate the role of *s* and *p* electrons in determining Au reactivity when the coordination number or charge is changed. The *d*-band model assumes that the *sp*-bands are static and play no role in the reactivity of transition metals. We check if this is true when we change the coordination of Au atoms by changing structure or by going from a face site to an edge site to an apex site on an Au_{20}(T) cluster and also when we change the charge state of an Au cluster. In all situations considered we find that the *sp*-states shift significantly and interestingly shift more than the *d*-states. Our results suggest that the changes in the *s*- and *p*-states are important to explain changes in reactivity.

In Chapter 7, we study gas phase Cu_nO_x clusters. To study the size-dependence of oxidation/reduction, we consider three different sizes, $n = 4$, 12 and 20. By combining density functional theory with *ab initio* atomistic thermodynamics, we obtain pressure-temperature phase diagrams for the clusters and the bulk. We find that the phase diagrams obtained for the clusters are very different from the phase diagram of bulk Cu and its oxides. We study these clusters in two different environmental conditions and determine the temperature and pressure at which these nanoclusters oxidize/reduce.

In Chapter 8, we study Cu_nO_x clusters supported on hydroxylated amorphous alumina. We see that the geometries of the Cu_nO_x clusters change significantly upon deposition on the support. We find that the tendency of the cluster to oxidize increases or decreases in the presence of the support depending on the size of the cluster. For the supported clusters, we see a clear sizedependent trend, the smaller the cluster, the more easily it oxidizes. We use a novel method of comparing our theoretical predictions for the size-dependent transitions of supported Cu clusters with experimental XANES results, and find excellent agreement between the two.

In Chapter 9, the main conclusions in each chapter are summarized and an outlook for possible directions for the future is discussed.

List of Publications

Included in thesis

1. "Tuning the Morphology of Gold Clusters by Substrate Doping", Nisha Mammen, Shobhana Narasimhan and Stefano de Gironcoli, *J. Am. Chem. Soc.* **133** (9), 2801 (2011).

2. "Substrate doping: A strategy for enhancing reactivity on gold nanocatalysts by tuning *sp* bands", Nisha Mammen, Stefano de Gironcoli and Shobhana Narasimhan, *J. Chem. Phys.* **143**, 144307 (2015).

3. "Trends in the Electronic Structure of Extended Gold Compounds: Implications for Use of Gold in Heterogeneous Catalysis", Mao-Sheng Miao, Joshua A. Kurzman, Nisha Mammen, Shobhana Narasimhan and Ram Seshadri, *Inorg. Chem.* **51** (14), 7569 (2012).

4. "Diffusion and Sintering of small Pt clusters on MgO(100) surfaces", N. Mammen and S. Narasimhan (in preparation).

5. "The unsuspected role of *s* and *p* electrons in the reactivity of Au nanoparticles", S. Ghosh, R. Banerjee, N. Mammen and S. Narasimhan (in preparation).

6. "Size-dependent Phase Transitions of Sub-nanometer Cu Clusters: Correlating *Ab initio* predictions and XANES measurements of Oxidation and Reduction", N. Mammen, L. Spanu, E. Tyo, B. Yang, A. Halder, S. Seifert, M. Pellin, S. Vajda, S. Narasimhan (preprint available).

7. "Tuning the morphology of Au clusters by substrate doping: *ab initio* results supporting experiments on Au clusters deposited on Mo-doped CaO", N. Mammen and S. Narasimhan (in preparation).

8. "Effect of Substrate doping on the adsorption geometries of small Au clusters", N. Mammen and S. Narasimhan (in preparation).

9. "Size-dependent oxidation and reduction of gas phase Cu clusters", N. Mammen, L. Spanu and S. Narasimhan (in preparation).

Not included in thesis

- "Elastic displacements and step interactions on metallic surfaces: Grazing-incidence x-ray diffraction and *ab initio* study of Au(332)", G. Prévot, Y. Girard, V. Repain, S. Rousset, A. Coati, Y. Garreau, Jaita Paul, Nisha Mammen and Shobhana Narasimhan, *Phys. Rev. B* **81**, 075415 (2010).

- "Effect of substrate anion doping on the work function of the substrate: implications for catalysis", S. Ghosh, N. Mammen and S. Narasimhan (preprint available).

- "Surface alloys of non-magnetic and magnetic metals on W(110)", N. Mammen, and S. Narasimhan (in preparation).

List of Symbols and Abbreviations

E^{ZPE}	Zero point energy
E_{xc}^{GGA}	Exchange correlation energy within the GGA
$E^{barr}(q_I)$	Charge barrier function when using COMB interatomic potential
$E^{corr}(R_{IJ}, \theta_{IJK})$	Angular correction term when using COMB interatomic potential
$E^{polar}(R_{IJ})$	Polarizability of the system when using COMB interatomic potential
$E^{vdW}(R_{IJ})$	van der Waals energy when using COMB interatomic potential
E_0	Ground state energy of the system
E_F	Fermi energy
$E_I^{self}(q_I)$	Self-energy of atom I when using COMB interatomic potential
E_T	Potential energy of the system when using COMB interatomic potential
E_b	Binding energy
$E_s(\mathbf{R})$	Born-Oppenheimer potential energy surface
E_H	Hartree energy
E_{IJ}^{Coul}	Coulombic interaction between atoms I and J when using COMB interatomic potential
$E_{IJ}^{short}(R_{IJ})$	Pair interaction between atoms I and J when using COMB interatomic potential
E_{xc}	Exchange-correlation energy
F	Helmholtz free energy
G	Gibbs free energy
H_e	Electronic Hamiltonian
I_{h}	Icosahedral symmetry
M_I	Nuclear mass of I^{th} ion

O_{h}	Octahedral symmetry
T	Temperature
U	Potential energy in classical MD
V_{KS}^{σ}	Kohn-Sham potential
V_d	Coupling matrix element for interaction between molecular level and metal d-band
V_{ext}	External potential
V_{sp}	Coupling matrix element for interaction between molecular level and metal sp-band
W_d	d bandwidth
W_{sp}	sp bandwidth
Z_I	Atomic number of I^{th} ion
$\Psi(\mathbf{R}, \mathbf{r})$	Wavefunction of the total system
$\boldsymbol{\mathcal{R}^i}$	Position of the i^{th} image in NEB
$\chi_s(\mathbf{R})$	Nuclear wavefunctions
ϵ_a	Molecular Antibonding state
ϵ_b	Molecular Bonding state
$\hat{H}$	Hamiltonian for a many body interacting system
$\hbar$	Planck's constant
$\mathbf{b}_1, \mathbf{b}_2$ and $\mathbf{b}_3$	Primitive reciprocal lattice vectors
μ	Chemical potential
σ	Spin of the electrons
$\mathbf{G}$	Reciprocal lattice vector
$\mathbf{R}_I$	Nuclear position of I^{th} ion
$\mathbf{a}$	Acceleration
$\mathbf{k}$	Wavevector
$\mathbf{r}_i$	Electronic position of i^{th} electron
$\{\psi_s(\mathbf{R}, \mathbf{r})\}$	Complete set of electronic eigenstates
e	Electronic charge
$g(r)$	Pair correlation functions
k	Spring constant when using NEB

k_B	Boltzmann's constant
$m(\mathbf{r})$	magnetic density of the system
m_e	Electronic mass
$n(\mathbf{r})$	Electronic charge density
$n_0(\mathbf{r})$	Ground state charge density
$p(X)$	Partial pressure of chemical species X
v_α	α-component of the velocity of the particles in the system
N_β	Number of divisions in reciprocal space along β direction
1D	One-dimensional
2D	Two-dimensional
3D	Three-dimensional
AIATD	*Ab initio* atomisic thermodynamics
BCC	Body centered cubic
BEP	Brønsted-Evans-Polanyi
BFGS	Broyden-Fletcher-Goldfarb-Shanno algorithm
BZ	Brillouin zone
COMB	Charge Optimized Many-Body potential
D	Diamond lattice
DFT	Density Functional Theory
DOS	Density of states
ECN	Effective coordination number
FCC	Face centered cubic
GGA	Generalized gradient approximation
HC	Honeycomb sheet
HOMO	Highest occupied molecular orbital
K-S	Kohn-Sham
LUMO	Lowest unoccupied molecular orbital
MD	Molecular dynamics
MEP	Minimum energy path
NEB	Nudged elastic band
PAW	Projector augmented wave

PBE	Perdew, Burke and Ernzerhof
PES	Potential energy surface
P	Au_{20} planar isomer
QEq	Electronegativity equalization
RHS	Right-hand-side
SC	Simple cubic
Sq	Square sheet
TS	Triangular sheet
T	Au_{20} tetrahedral isomer
UHV	Ultra-high vacuum
XANES	X-ray absorption near edge spectroscopy

List of Figures

List of Tables

Contents

0

Chapter 1

Introduction

1.1 Nanomaterials as Catalysts

Catalysts are vital to our existence. Without them, most products that we use like medicines, polymers, perfumes, fabrics, lubricants, etc. would not be available to us. Catalysts are materials that make a chemical reaction more favorable to proceed by providing an alternative pathway with a lower activation barrier. Any advances in producing new or improved catalysts represent significant progress, both intellectually and economically. A few of the desired properties in an improved catalyst are a longer lifetime, being cheaper, and/or being more effective (by lowering the activation barriers further) than existing catalysts. When making any improvement in these catalysts, one should also keep in mind environmental demands, and always try to replace a polluting chemical reaction with an environmentally friendly alternative.

If one wishes to gain the best possible understanding, and rationally design better catalysts, computational studies play as important a role as experiments do. The field of computational catalysis really took off only in the 1990s,[1] mainly due to the advent of more powerful computers, which could be used to carry out calculations based on improved computational methods like density functional theory[2] and quantum mechanics/molecular mechanics.[3] Nowadays, it is possible to describe catalytic reactions at surfaces in great

detail, and with enough accuracy to favorably compare results from computational approaches to catalysis, with experiments. Experiments on catalysis can be very complex, and computational studies can help to break down this complexity, so that one can study separately the effect of several individual parameters on the reactivity and the performance of a catalyst. Computational studies focus on the mechanistic understanding of catalytic processes, and can provide suggestions as to which parameter(s) can be tuned, and how, for enhancing the desired property of the catalyst.

Using the vast data from computational calculations, one can also put forth models that can explain trends in the reactivity of several catalysts; one such example is the *d*-band model suggested by Hammer and Nørskov.[4,5] This model suggests that one can predict the reactivity of a transition metal just by looking at its *d*-band density of states, extracting a single parameter called the *d*-band center, which is the weighted average of the *d*-band density of states. This parameter can be used to screen for possible catalysts with increased activity and improved selectivity.[6]

With the advent of nanoscience, it is now possible to use nanoparticles as catalysts. Several elements and materials like aluminium, iron, titanium dioxide, silica and clay have been used as catalysts in the form of ultrafine particles for many years, however the explanation for the tremendous increase in reactivity when the catalyst size was reduced, was not fully understood. Initially, it was thought that the increase in reactivity arises due to the increase in the proportion of surface species that are catalytically active and also due to the increase in the number of surface defects. With the development of nanoscience, and the accompanying better understanding of phenomena at the nanoscale, we are now aware that in addition to the increase in surface area and heterogeneity of atomic structure, catalytic nanoparticles also exhibit quantum size effects in their electronic structure. As the dimensionality reduces on going from the bulk extended systems to two dimensional sheets, to one dimensional wires and to zero dimensional clusters, we also see a decrease in the coordination number of the atoms in the system. This is another important reason for the dramatic increase in the reactivity of materials upon going from the bulk to nanosystems. Another advantage of using nanoparticles as catalysts is that the reduction

in size allows us to use less quantity of the catalyst material, and considering especially that many important catalysts used today are precious metals, this can be a significant factor. Catalytic nanoclusters and their properties form the theme of this thesis.

Nanoclusters are frequently placed on an oxide support when used in applications. These supports can improve properties like distribution, stability and also the reactivity of these nanoclusters. The support can improve the reactivity of clusters in three ways: (1) by modifying the charge state of the cluster,[7–11] (2) by modifying the shape of the cluster,[10,11] and also (3) by the appearance of new catalytically active sites at the cluster-support interface.[7,8] The systems that we have looked at in this thesis include (a) Pt clusters on MgO, (b) Au clusters on MgO (and CaO), and (c) Cu clusters on hydroxylated amorphous Al_2O_3. Pt and Cu are already good catalysts in their extended forms, but in Au (which is inert in extended forms) we see a particularly dramatic increase in the reactivity when we go from the extended forms to the nano size. All three elements have been shown to be very good catalysts for several reactions. For example, Pt is an important catalyst in catalytic converters used in automobile exhausts, it is also a good catalyst for the decomposition of hydrogen peroxide into water and oxygen,[12] and the oxidative dehydrogenation of propane.[13] Nanoparticles of Au have been found to show a high catalytic activity towards the oxidation of CO,[14] the oxidation of ethanol,[15] and the oxidation of glucose,[16] among many other reactions. Cu is used as a catalyst in, for example, the low-temperature water-gas shift reaction,[17] the synthesis of methanol from aldehyde[18] and the oxidative steam reforming of methanol to produce hydrogen.[19]

In all the investigations described in this thesis, the main computational method we have used is density functional theory (DFT).[2,20] Using DFT, we calculate the total energy of the system, which is used to determine the stability of different phases, and calculate quantities like the formation energy and the adsorption energy. To estimate the minimum energy pathway of a reaction, we have used two techniques: the nudged elastic band method,[21,22] and constrained minimization. To generate initial guesses for the geometries of Cu clusters (both freestanding and on amorphous hydroxylated alumina), we have employed the method of simulated annealing[23] using classical potentials, these initial

geometries were then refined further using quantum mechanical density functional theory calculations. In one of the sections of this thesis, we have also used the method of *ab initio* atomistic thermodynamics,[24,25] which combines DFT and thermodynamics, and allows us to extend our zero temperature calculation results to relevant temperatures and pressures. All computational techniques and theoretical formalisms are described in Chapter 2 of this thesis.

1.2 Controlling the Reactivity of Nanocatalysts

We have explored three important themes in this thesis, all of which are of great importance in determining the performance of a nanocatalyst. First we consider the cluster size: nanoclusters that are placed on an oxide support tend to diffuse on the support, and then coalesce to form larger sized particles. This is driven by thermodynamics, since the bulk is always lower in energy than clusters, and, in general, larger sized clusters are always lower in energy than smaller clusters. This process is called sintering, and we study this in Section A of this thesis. If (as generally happens) the reactivity is reduced at larger sizes, then sintering reduces the catalytic performance, and hence is undesirable. Next, it is known that the reactivity of a nanocluster is highly sensitive to its shape and charge state, and it is desirable to find an easy and practical way to control these properties. We address this issue in Section B of this thesis. Finally, in addition to the shape and charge of a cluster, the oxidation state of the atoms in the cluster is also crucial in determining the reactivity of the cluster. It is well known that for several reactions the performance of a metal nanocatalyst is degraded by oxidation, and it is also believed that usually, smaller clusters have a higher tendency to oxidize. Therefore, it is important to know what is the optimum size of the catalyst one should use for a given set of reaction conditions that would be stable against oxidation. However, we should point out that, on the other hand, there are also certain reactions where some degree of oxidation is considered desirable for optimal catalytic performance. These questions are addressed in Section C of this thesis.

1.2.1 A: Diffusion and Sintering of Nanoclusters on a Support

Sintering is a process in which two smaller clusters combine to form a larger cluster on the support. This is one of the ways that can lead to the degradation of catalytic nanoclusters. We would like all clusters on the support to be of a desired monodisperse size that it is optimal for catalytic activity, and therefore do not wish for the clusters to coalesce or sinter to form larger size particles. In order to study sintering, one needs to identify diffusion mechanisms, nucleation energetics and the role of defects such as surface O vacancies (F-centers) in the growth processes of nanoclusters on substrates.

In Chapter 3, we study the adsorption and diffusion mechanisms of small Pt_n clusters (n = 1–4) on the defect-free MgO(100) surface. We also look at the adsorption of Pt_n clusters on the MgO(100) surface with oxygen vacancy sites called F-centers. Finally, we look at the possible processes for the growth of Pt_n clusters on the defect-free surface and at the F-center sites. We also compare all the results that we obtain for Pt, with corresponding results obtained by earlier authors for Pd clusters on MgO(100)[26,27] and for Ag and Au clusters on MgO(100).[28]

1.2.2 B: Controlling the Morphology, Charge State and Reactivity of Nanoclusters

In this section, we try to find ways to improve the reactivity of Au clusters, as well as gain a better understanding of the underlying processes, and come up with a new descriptor for reactivity. It is known that changing the size,[29] the shape[30,31] or the charge state[32] of an Au cluster can affect its reactivity significantly. We propose an alternative method, which is simple and yet lends itself easily to applications, to control the shape and the charge state of an Au cluster.

As a model system, we first choose to study the Au_{20} cluster; this is a robust and highly stable cluster with a high catalytic activity towards CO oxidation.[33,34] It has two stable isomers: one with a three-dimensional tetrahedral geometry (T) and another with a two-dimensional planar geometry (P). It is known both experimentally and theoretically that Au_{20} prefers the tetrahedral geometry in the gas phase as well as when supported on

oxide supports like MgO. However, due to the reduced coordination, and a higher number of perimeter Au – substrate interface sites, one may speculate that the (P) cluster may be a better catalyst.[31] Previous authors have suggested methods to flip the order of stability of the Au_{20} isomers, so as to favor the planar cluster: (i) by placing the Au_{20} cluster on an ultrathin film of MgO supported on Mo,[10,11,31,35] and (ii) by placing the system of Au_{20} over the metal supported MgO thin film in a high electric field of the order of 1 V/nm.[36] These methods, though successful, may not be easily transferable to large-scale applications. We therefore propose, in this thesis, a third method to stabilize the planar geometry, viz., doping the substrate with an electron donor impurity. We demonstrate the success of this method on the system of Au_{20} on Al-doped MgO.[37] Our idea of cluster morphology tuned by substrate doping has subsequently been experimentally verified for the growth of Au clusters on Mo-doped CaO,[38] where the authors found that the Au clusters prefer a 3D growth on pristine CaO, while forming planar one-atomic-layer thick clusters on Mo-doped CaO. Motivated by these experimental results, we have gone on to carry out calculations on Au_{20} clusters supported on CaO. We again find, in agreement with the experiments, that the Au_{20} clusters prefer the 3D (T) geometry on pristine CaO, but prefer to wet the surface to form the (P) cluster on Mo-doped CaO. Finally, in this chapter, we also investigate the effect of substrate doping on small Au_n clusters; $n = 1$–3.

The truly interesting question of course, is whether these changes in cluster morphology also affect catalytic performance. Therefore, in Chapter 5, we investigate how substrate doping affects the reactivity of the supported Au clusters. To do this, we have chosen as a simple model reaction, the dissociation of an O_2 molecule adsorbed on the Au cluster. We find that due to substrate doping, the dissociation barrier is more than halved, which corresponds to an increase in the reaction rates at room temperature of five orders of magnitude. We also find that the barrier for O_2 dissociation decreases monotonically as we increase the doping concentration in the substrate.

To explain the observed trend in reactivity, we look into the *d*-band model, which was proposed by Hammer and Norskov,[4,5] to explain the trends in reactivity of transition metals. This model assumes that the *sp*-bands are static and the reactivity of metals

can be predicted by just one parameter, the *d*-band center. Briefly summarized, the *d*-band model states that the higher in energy the *d*-band center is, the better is the catalyst. However, on analyzing our results on the shift in the *d*-band center as a function of doping, we see that the *d*-band center moves in the direction opposite to what is expected, if it were to explain the observed trend in reactivity. We also find that in addition to the *d*-states, the *s*- and *p*-states of Au are greatly affected by substrate doping, and are far from static. We make use of these results to propose a new descriptor to explain the reactivity of Au clusters deposited on a doped substrate.

In Chapter 6, we investigate the role of *s* and *p* electrons in Au reactivity. The *d*-band model has previously been used to explain why bulk Au is the most noble of all metals[39] and also explain the origin of the catalytic activity in nano Au.[30] The *d*-band model assumes that the *sp*-bands are static and play no role in the reactivity of transition metals. However, we have seen that this is not true in the case of Au supported on doped substrates. In this chapter we check whether the *sp*-states are static or mobile when we change the coordination of Au atoms by reducing dimensionality (going from extended systems to surfaces to nanoclusters) or by going from a face site to an edge site to an apex site on an Au_{20}(T) cluster. We also look at what happens to the *s*- and *p*-states when Au clusters are negatively charged. In all situations considered, we find that the *sp*-states shift significantly, and interestingly, shift more than the *d*-states. From these results, we conclude that the *s*- and *p*-states may play a vital role in Au catalysis.

1.2.3 C: Controlling the Oxidation State of Atoms in a Nanocluster

In this section, we study the oxidation and reduction of gas phase and supported Cu clusters as a function of temperature and pressure. For certain reactions like the steam reforming reaction, the Cu based catalyst is required to be in an oxide state,[40] while for other reactions like the synthesis of methanol, the catalyst is required to be in the elemental state.[18] So it is clear that depending on the reaction, the oxidation of the catalyst can either promote or degrade the activity of the catalyst. The tendency of nanoclusters towards oxidation is size-dependent, and so it is important to know what size of the cluster is

best to use for a given set of reaction conditions. To determine this, we need to know at what temperature and pressure nanoparticles oxidize, and the size-dependence of this phenomenon. In Chapters 7 and 8, we study gas phase and supported Cu_nO_x clusters respectively. In both cases, we study three different sizes, n = 4, 12 and 20, and their phase transitions in two different environmental conditions: (a) in the presence of O_2, and (b) in the presence of H_2 and H_2O.

In addition to generating the phase diagrams for the clusters in the gas phase and when supported on hydroxylated amorphous alumina, we also compare our results on the supported clusters with experimental results on the same systems in the two different environments. We propose a novel technique by which one can compare theory and X-ray absorption near edge spectroscopy (XANES) experiments on nanoclusters based on XANES spectra of known compounds. On carrying out such a comparison, we obtain extremely satisfying agreement between theory and experiment.

The main conclusions from each chapter, and a brief outlook for future prospects, are summarized in Chapter 9 of this thesis.

Chapter 2

Computational Techniques and Theoretical Formalism

2.1 Density Functional Theory

Density Functional Theory (DFT) is one of the most successful quantum mechanical approaches to compute the electronic structure of matter. It is very accurate and it can be applied to a wide range of materials, from atoms, molecules and nanosystems to solids and surfaces. One of the highlights of this theory is that it is completely *ab initio*, i.e., it takes only the atomic numbers and the atomic masses of the atoms in the material as inputs for the computation, and uses no empirical data from experiments. Using this theory, the ground state properties of a many-body system can be determined by using functionals. Functionals are functions of another function: in this case the energy of the system is written in terms of the spatially dependent electron density. The use of functionals of the electron density hence explains the name "Density Functional Theory". In this section, we give a brief overview of some of the relevant formalism.

2.1.1 The Many-Body Problem

The Hamiltonian for a many-body interacting system of nuclei and electrons is given by:[41]

$$\hat{H} = -\sum_{I} \frac{\hbar^2}{2M_I}\nabla_I^2 - \frac{\hbar^2}{2m_e}\sum_{i}\nabla_i^2 + \frac{1}{2}\sum_{I\neq J}\frac{Z_I Z_J e^2}{|\mathbf{R}_I - \mathbf{R}_J|} - \sum_{i,I}\frac{Z_I e^2}{|\mathbf{r}_i - \mathbf{R}_I|} + \frac{1}{2}\sum_{i\neq j}\frac{e^2}{|\mathbf{r}_i - \mathbf{r}_j|}, \tag{2.1}$$

where the nuclear positions, nuclear masses and the atomic numbers of the atoms in the system are given by $\mathbf{R}_I$, M_I and Z_I respectively, and the indices I, J run over all the nuclei in the system; while the electronic positions, electronic mass and charge are given by $\mathbf{r}_i$, m_e and e respectively, with indices i, j that run over all the electrons in the system, and $\hbar$ is Planck's constant. The first two terms on the right-hand side (RHS) of the equation are respectively, the nuclear and electronic kinetic energy contributions to the Hamiltonian. The subsequent terms take into account the Coulombic interactions between pairs of nuclei, between pairs consisting of a nucleus and an electron, and between pairs of electrons, respectively.

2.1.2 Born-Oppenheimer Adiabatic Approximation

As the electrons are much lighter in mass than the nuclei, they tend to move much faster as compared to the sluggish motion of nuclei. The time scales related to the electronic motion are much smaller than the time scales related to nuclear motion, due to which it is assumed that the nuclei are effectively motionless over electronic time scales and when the nuclei move, they only see a smeared out potential from the speedy electrons. The Born-Oppenheimer approximation[42] thus makes it possible to treat the electrons in the system using a time-independent Schrödinger equation for electrons in a stationary external (nuclear) potential.

Applying this approximation to Eq. (2.1), the first term on the RHS becomes very small and can be treated as a perturbation. The wavefunctions and energies of the electrons can be described in such a way that they have only a parametric dependence on the nuclear postions $\mathbf{R}$. The wavefunction of the total system, $\Psi(\mathbf{R}, \mathbf{r})$ can be written as:

$$\Psi(\mathbf{R},\mathbf{r}) = \sum_s \chi_s(\mathbf{R})\psi_s(\mathbf{R},\mathbf{r}) \tag{2.2}$$

where $\{\psi_s(\mathbf{R},\mathbf{r})\}$ is a complete set of electronic eigenstates for each $\mathbf{R}$, and $\chi_s(\mathbf{R})$ are the nuclear wavefunctions.[43] Note that the position vectors $\mathbf{r}$ and $\mathbf{R}$ denote the set of all position vectors $\{\mathbf{r}_i\}$ and $\{\mathbf{R}_I\}$ of the electrons and the nuclei respectively. Now, the many-body equation in Eq. (2.1) can be re-written as a set of two coupled differential equations.[43]

$$\left[-\frac{\hbar^2}{2m_e}\sum_i \nabla_i^2 + \frac{1}{2}\sum_{I\neq J}\frac{Z_I Z_J e^2}{|\mathbf{R}_I-\mathbf{R}_J|} - \sum_{i,I}\frac{Z_I e^2}{|\mathbf{r}_i-\mathbf{R}_I|} + \frac{1}{2}\sum_{i\neq j}\frac{e^2}{|\mathbf{r}_i-\mathbf{r}_j|}\right]\psi_s(\mathbf{R},\mathbf{r}) = E_s(\mathbf{R})\psi_s(\mathbf{R},\mathbf{r}), \tag{2.3}$$

$$\left[-\sum_I \frac{\hbar^2}{2M_I}\nabla_I^2 + E_s(\mathbf{R})\right]\chi_s(\mathbf{R}) = \varepsilon\chi_s(\mathbf{R}). \tag{2.4}$$

$E_s(\mathbf{R})$ is the solution of Eq. (2.3), and is the smeared out potential seen by the nuclei due to the speedy electrons. $E_s(\mathbf{R})$ is called the Born-Oppenheimer potential energy surface, and when it is known, Eq. (2.4) becomes easily solvable. The solution to Eq. (2.3), however, is not straightforward within the quantum mechanical framework and requires further approximations to deal with the Coulomb two-body terms and the exchange and correlation interactions.

2.1.3 Density Functional Theory

Density Functional theory was a landmark development in the field of computational science that enabled electronic structure theory to be applied to real problems, and led to the Nobel Prize in Chemistry being awarded to Walter Kohn in 1998. It describes a complete reformulation of the Schrödinger equation, one in which the many-body N-electron wavefunction is replaced by the electronic density as the basic variable. This, of course, makes the calculation much simpler as it implies that the electronic density (which depends only on position, which is a three-variable quantity) can give us all the information contained in the wavefunction (which is a $3N$-variable quantity).

The electronic density, $n(\mathbf{r})$, is determined from the many-electron wavefunction using the electronic density operator, $\hat{n}(\mathbf{r})$, as given below:[41]

$$n(\mathbf{r}) = \frac{\langle \psi \left| \hat{n}(\mathbf{r}) \right| \psi \rangle}{\langle \psi | \psi \rangle}; \hat{n}(\mathbf{r}) = \sum_{i=1}^{N} \delta(\mathbf{r} - \mathbf{r}_i). \tag{2.5}$$

DFT further simplifies the problem by replacing the many-body interacting electron system with a single-electron non-interacting system and including a term that incorporates all the many-body effects in the system through a term that describes the exchange and correlation between the electrons.

2.1.3.1 Hohenberg-Kohn Theorems

The basic framework of DFT is based on two theorems introduced by Hohenberg and Kohn.[2] The theorems are as stated below.

Theorem I: For any system of interacting particles in an external potential $V_{ext}(\mathbf{r})$, the potential $V_{ext}(\mathbf{r})$ is determined uniquely, up to an additive constant, by the ground state particle density $n_0(\mathbf{r})$.[41]

This theorem suggests that the external potential in a system can be uniquely determined from its ground state electronic density. Using this external potential, the Schrödinger equation can be solved to determine the many-body wavefunction; and from the wavefunction, the observable electronic density can be determined. This allows a self-consistent procedure to be utilized to determine the true ground state density and the true ground state wavefunction of the system.

Theorem II: A universal functional for the energy $E[n]$ in terms of $n(\mathbf{r})$ can be defined, valid for any external potential $V_{ext}(\mathbf{r})$. For any particular $V_{ext}(\mathbf{r})$, the exact ground state energy of the system is the global minimum value of this functional, and the density $n(\mathbf{r})$ that minimizes the functional is the exact ground state density $n_0(\mathbf{r})$.[41]

The ground state expectation value of any observable can be written as a functional of $n_0(\mathbf{r})$ of the system; energy being the most important observable that is calculated. This

second theorem suggests that the energy that corresponds to the true ground state electronic density will always be lower than the energy corresponding to any other density.

The electronic Hamiltonian, H_e, of the system is given by:[41]

$$H_e = -\frac{\hbar^2}{2m_e}\sum_i \nabla_i^2 + \frac{1}{2}\sum_{i\neq j}\frac{e^2}{|\mathbf{r}_i - \mathbf{r}_j|} + \sum_i V_{ext}(\mathbf{r}_i); \tag{2.6}$$

the ground state energy of the system, E_0, written as functionals of $n_0(\mathbf{r})$, is given by:

$$E_0[n_0] \equiv \langle \Psi_0[n_0] \mid H_e \mid \Psi_0[n_0]\rangle = T_e[n_0] + E_{e-e}[n_0] + \int V_{ext}(\mathbf{r})n_0(\mathbf{r})d\mathbf{r}, \tag{2.7}$$

where $T_e[n_0]$ and $E_{e-e}[n_0]$ are respectively, the kinetic energy and the energy due to interactions between the electrons in the system. The total energy in the ground state is rewritten as:

$$E_0[n_0] = F[n_0] + \int V_{ext}(\mathbf{r})n_0(\mathbf{r})d\mathbf{r}, \tag{2.8}$$

where $F[n_0]$ is a universal functional of the density that is the same for all electronic systems. It is system-independent and depends only on the electronic density of the system. The second term on the RHS of Eq. 2.8 is also a functional of the density, and it is system-dependent as it contains the information regarding the electron-nuclei interactions in the system, and/or any other external potential.

DFT in principle is exact, but problems arise because the true functional form of $F[n_0]$ is unknown. It is due to this inadequacy in our knowledge that approximations need to be used, making DFT approximate in its application. To deal with the functional $F[n_0]$, an *ansatz* was proposed by Kohn and Sham[20]; this representation made it possible for the widespread and successful application of DFT to real problems.

2.1.3.2 Kohn-Sham Representation

The Kohn-Sham (K-S) representation[20] allows for the mapping of a N-electron interacting problem onto a problem comprised of N non-interacting single-electrons, with the same

electronic density. These N electrons are assumed to occupy a set of orbital states called the Kohn-Sham states, such that each state can contain two electrons, following Pauli's exclusion principle. These fictitious states, $\psi_s(\mathbf{r})$, are related to the true ground state electronic density by:

$$n_0(\mathbf{r}) = 2\sum_{s=1}^{N/2} |\psi_s(\mathbf{r})|^2, \tag{2.9}$$

where s is an index that runs over all the occupied Kohn-Sham states,[41] and the factor of 2 arises from spins.

The approximation used for the universal functional $F[n]$ can be summarized in this equation:

$$F[n] = T_0[n] + E_H[n] + E_{xc}[n]. \tag{2.10}$$

Each term in the above equation is described below:

1. Here, $T_0[n]$ is the kinetic energy of the fictitious non-interacting electrons. This comprises a majority of the kinetic energy of the many-electron system and is calculated using the equation:[44]

$$T_0[n] = -2\frac{\hbar^2}{2m_e}\sum_{s=1}^{N/2}\int \psi_s^*(\mathbf{r})\nabla^2\psi_s(\mathbf{r})d\mathbf{r}. \tag{2.11}$$

2. $E_H[n]$ is the Hartree term that separates out the electron-electron Coulombic interaction from any residual energy contribution due to the exchange asymmetry and correlations. The Hartree energy, E_H, is given by,[44]

$$E_H[n] = \frac{e^2}{2}\int \frac{n(\mathbf{r})n(\mathbf{r}')}{|\mathbf{r}-\mathbf{r}'|}d\mathbf{r}d\mathbf{r}'. \tag{2.12}$$

3. $E_{xc}[n]$ is the exchange-correlation energy that accounts for the kinetic energy difference between the many-electron interacting system and the N single-electrons

non-interacting system; and also the residual energy contributions due to the exchange asymmetry and correlations. It is given by the equation:

$$E_{xc}[n] = F[n] - (T_0[n] + E_H[n])\,. \tag{2.13}$$

The functional forms of $T_0[n]$ and $E_H[n]$ are known, and they can be easily calculated. The functional forms for the rest of the energy contributions, however, are not known, and are heaped into the third term, $E_{xc}[n]$. There are different working approximations for this term with varying levels of accuracy and varying computational costs: some of them are described in the next section.

On applying the Kohn-Sham representation of the universal function $F[n]$, Eq. (2.8) can be written as:

$$E_0[n_0] = T_0[n_0] + E_H[n_0] + E_{xc}[n_0] + \int V_{ext}(\mathbf{r}) n_0(\mathbf{r}) d\mathbf{r}, \tag{2.14}$$

$$= T_0[n_0] + \int V_{KS}(\mathbf{r}) n_0(\mathbf{r}) d\mathbf{r}, \tag{2.15}$$

where V_{KS} is assumed to be the effective potential experienced by the fictitious non-interacting electrons.

Alternatively, the Kohn-Sham equations can be written as:[44]

$$\left\{ -\frac{\hbar^2}{2m_e}\nabla^2 + V_{\mathrm{KS}}(\mathbf{r}) \right\} \psi_s(\mathbf{r}) = E_\alpha \psi_s(\mathbf{r}), \tag{2.16}$$

and

$$V_{\mathrm{KS}}(\mathbf{r}) = V_H(\mathbf{r}) + V_{xc}(\mathbf{r}) + V_{ext}(\mathbf{r}). \tag{2.17}$$

The three equations, Eqs. (2.9), (2.16) and (2.17) can be used self-consistently to determine the true ground state electronic density and wavefunction of a system; a flowchart describing this procedure is shown in Fig. 2.1. If one could start with a good guess for the electronic density, n^{inp}, the K-S potential could be calculated from Eq. (2.17); using the K-S potential, Eq. (2.16) could be solved to determine the K-S states, $\psi_s(\mathbf{r})$; and to complete the loop, the electronic density, n^{out} can be extracted as an observable of the K-S

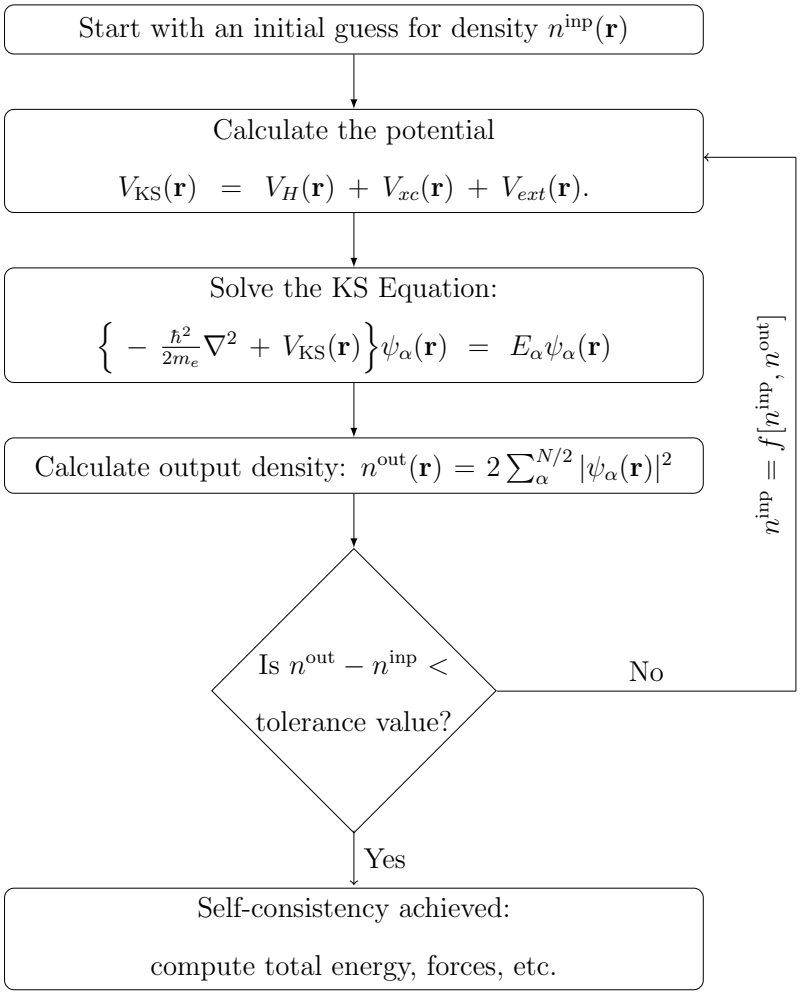

Figure 2.1: *Flow chart representing the self-consistency loop used to iteratively solve the Kohn-Sham equations*

states. The output density obtained can be combined with the input density using a mixing scheme to give us a new input density for the next iteration of the self-consistent loop. This procedure is continued until the difference between the input and output densities is lower than a pre-defined tolerance value. Various mixing schemes exist that help speed up convergence, the most common one being the modified Broyden's mixing method.[45,46]

On achieving convergence in the self-consistent loop, the electronic ground state energy can be calculated. To this energy, the Coulomb interaction energy between the nuclei which was dropped earlier is added, to give the total ground state energy.[41]

2.1.3.3 Exchange-Correlation Functionals

The exchange-correlation functional is the term in the K-S equations that accounts for all the many-body effects in the system. In addition to the Coulombic interactions between the electrons, there are interactions that arise due to the spin of the electrons, called the exchange interactions. The correlation energy on the other hand, is defined as the difference in energy between the exact energy and the sum of the kinetic, Hartree and exchange energies of the system. The functional form of the exchange-correlation interaction is not known, and approximations are used to treat these terms. In this thesis, we have used two forms of the generalized gradient approximation (GGA): one developed by Perdew, Burke and Ernzerhof (PBE)[47,48] and another suggested by Perdew and Wang (PW91).[49]

Generalized Gradient Approximations

The electronic density in a real system may be inhomogeneous in its distribution. To take this into account, it is necessary to consider the electronic density and also the gradient for the electronic density. To do this, a variety of ways were proposed[47–49] and these are collectively known as the Generalized Gradient Approximations (GGA). The exchange correlation functional has the form:[44]

$$E_{xc}^{\mathrm{GGA}}[n] = \int d\mathbf{r}\ n(\mathbf{r})\epsilon_{xc}([n], |\nabla n(\mathbf{r})|), \tag{2.18}$$

where $\epsilon_{xc}([n], |\nabla n(\mathbf{r})|)$ is the exchange-correlation energy per electron, that depends on the local density $n(\mathbf{r})$ as well as the gradient of the density $|\nabla n(\mathbf{r})|$.

The GGA is often known to underbind, which can result in lattice constants that are too large. Some properties, such as magnetic moments, are usually estimated well using the GGA.

2.1.4 Plane Wave Basis Set

Wavefunctions or Kohn-Sham states are continuous functions and are difficult to handle in a computer. To deal with this, the K-S states are usually expanded in terms of a basis set, so that their information is stored as a number of coefficients in the computer.

One can choose the appropriate basis function for a calculation from a variety of basis functions like plane waves,[50,51] Gaussian functions, Muffin Tin Orbitals[52] and localized atomic orbitals[53]. In this thesis, we have used plane wave basis sets, as implemented in the Quantum ESPRESSO[50] and VASP packages.[54–57]

The greater the number of basis functions used, the better will be the accuracy; but the more you use, the slower will be the calculation. The time taken to solve the Kohn-Sham equations in a computational calculation is (for exact matrix diagonalization) roughly proportional to the cube of the number of basis functions considered, though various techniques can be used to reduce the time taken.

Bloch's theorem states that the wavefunction of an electron placed in a periodic potential can be written as the product of a plane wave and a periodic function.[58] This suggests that, when working with extended periodic systems, one can use a set of mutually orthonormal plane waves to expand the wavefunction. The K-S states can be expanded in terms of plane waves:[44]

$$\psi_{s,\mathbf{k}}(\mathbf{r}) = \sum_{\mathbf{G}} c_{s,\mathbf{k}+\mathbf{G}} e^{i(\mathbf{k}+\mathbf{G})\cdot\mathbf{r}} \tag{2.19}$$

where $\mathbf{G}$ is a reciprocal lattice vector, and $\mathbf{k}$ is a wavevector in the first Brillouin zone. Any observable of the wavefunction can be calculated by summing over the occupied Bloch states at a given $\mathbf{k}$ point and then integrating over all k-points within the Brillouin zone.

The number of plane waves used can be easily increased until the energy converges; however, this will increase the matrix size and thus the computational time. To achieve a balance between accuracy and computational cost, one truncates this expansion with a kinetic energy cutoff: keeping all plane waves $e^{i(\mathbf{k}+\mathbf{G})\cdot r}$, such that $(\hbar^2/2m_e)|\mathbf{k}+\mathbf{G}|^2 \leq E_{cut}$.[41]

If the described wavefunction of the electron oscillates very rapidly or is very highly peaked in a region of space, a large number of plane waves will be required to accurately represent it. The high computational expense due to this can be reduced by using pseudopotentials, which are described in the next section.

2.1.5 Pseudopotential Approximation

An electron in an atom experiences forces due to the nucleus and also due to other electrons in the atom. The difficulty in determining these forces and interactions is another problem that electronic structure calculations need to overcome.

Core electrons in an atom are tightly bound to the nucleus, and their wavefunctions are highly peaked in the region close to the nucleus, also called the core region. A large number of plane waves would be required to accurately describe such core electron wavefunctions, leading to a high plane wave cutoff. The valence electron wavefunctions on the other hand, due to the orthogonality rules, display oscillations in the core region. This again requires a large number of plane waves to describe. These two requirements together lead to huge computational costs and such calculations become almost impossible when using a plane wave basis set.

The widely used pseudopotential approximation[59,60] suggests that one could do a calculation by freezing the core electrons with the nucleus, and considering only the valence electrons in the atom. Further, it replaces the core region of the atom with a hypothetical potential that treats accurately enough, the interaction between the valence electrons and the 'ionic core', yet converges faster with respect to the size of the plane wave basis. This drastic approximation is seemingly justified, as chemical bonding and most material properties depend only on the valence electrons in the atom.

While constructing a pseudowavefunction for an atom, a core radius cutoff is decided, such that the pseudo wavefunction matches exactly with the true wavefunction beyond this radius; but inside this core radius, the pseudo wavefunction is designed to be nodeless and free of oscillations. This helps to get rid of high Fourier components and makes the calculation computationally cheaper.[61] The Kohn Sham equation is then inverted in this reference configuration to obtain the pseudopotential.

A good pseudopotential should obey certain conditions.[61] (1) The pseudo wavefunction and its first and second derivatives should match smoothly at the core radius cutoff. (2) The pseudopotential generated for an atom should be transferable to treat different chemical environments. (3) It was believed earlier that a good pseudowavefunction is

one which would conserve the electronic charge; such pseudopotentials are called norm-conserving pseudopotentials.[62]

The use of norm-conserving pseudopotentials ensures that the scattering properties of the atom are properly described. These pseudopotentials are also usually highly transferable.[62] This approximation helps reduce the computational cost appreciably, but the constraint of norm-conservation still puts quite a load on the computation in certain cases where one may still require a large plane wave cutoff.

2.1.5.1 Ultrasoft pseudopotentials

Another leap forward in the field of electronic structure calculations was represented by the introducion of ultrasoft pseudopotentials, suggested by D. Vanderbilt.[63] This approximation relaxes the constraint of norm-conservation, thereby reducing the computational cost even further. The electronic charge that is left out in this pseudo wavefunction is accounted for by adding an 'augmentation' charge in the core region of the pseudo wavefunction. To deal with this, in addition to the plane wave energy cutoff, a charge density cutoff is introduced which should typically be 8 to 12 times the value of the plane wave cutoff used for wavefunctions. This however adds minimally to the computational cost.

2.1.5.2 Projector Augmented Wave potentials

The projector augmented wave (PAW) method[64,65] is an approach that has developed from a combination of ideas from pseudopotential[62] and linear augmented-plane-wave methods.[66] It is an all-electron method that works with the full all-electron wavefunction and determines the all-electron potential from the full charge densities. To deal with the oscillations in the wavefunction near the nucleus, all integrals are evaluated as a combination of integrals of smooth functions extending throughout space and treating the localized contributions by radial integration over muffin-tin spheres, as in the augmented plane wave approach.[41]

Using the orthogonalized plane wave formulation, one defines a smooth part of a valence wavefunction $\tilde{\psi}(\mathbf{r})$, and then generates the all-electron wavefunction by a simple linear

transformation, $\psi(\mathbf{r}) = \mathcal{T}\tilde{\psi}(\mathbf{r})$. The transformation is assumed to be unity except within a sphere centered at the nucleus, $\mathcal{T} = 1 + \mathcal{T}_0$. The smooth wavefunction is expanded in terms of partial waves m within the sphere:[41]

$$|\tilde{\psi}\rangle = \sum_m c_m |\tilde{\psi}_m\rangle; \tag{2.20}$$

and the corresponding all-electron wavefunction is written as,

$$|\psi\rangle = \mathcal{T}|\tilde{\psi}\rangle = \sum_m c_m |\psi_m\rangle; \tag{2.21}$$

$$= |\tilde{\psi}\rangle + \sum_m c_m \left\{ |\psi_m\rangle - |\tilde{\psi}_m\rangle \right\}. \tag{2.22}$$

If the transformation is linear in nature, the coefficients in the expansion must be given by a projection in each sphere,

$$c_m = \langle \tilde{p}_m | \tilde{\psi} \rangle, \tag{2.23}$$

for a set of projection operators $\tilde{p}$. If the projection operators are related to the partial waves by the biorthogonality condition, $\langle \tilde{p}_m | \tilde{\psi}_{m'} \rangle = \delta_{mm'}$, then the one-center expansion of the smooth function $\tilde{\psi}$ equals $\tilde{\psi}$ itself. There are many possible choices for the projectors just as for pseudopotentials, the difference being that the transformation $\mathcal{T}$ in the PAW method still involves the full all-electron wavefunction,[41]

$$\mathcal{T} = 1 + \sum_m \left\{ |\psi_m\rangle - |\tilde{\psi}_m\rangle \right\} \langle \tilde{p}_m |. \tag{2.24}$$

Furthermore, these expressions can be applied equally well to describe core and valence states to derive all-electron results. This method is more computationally efficient than earlier methods, is exact when converged, and has no problems in transferability.

2.1.6 k-point sampling

Any observable of the wavefunction is calculated by summing over all the occupied states at a given k-point and then integrating over all k-points (wavevectors) in the first Brillouin zone (BZ). Instead of integrating over the infinite number of k-points in the BZ, one has to, in practice, sum over a finite number of discrete k-points. Monkhorst and Pack suggested a method to generate a uniform set of points according to the symmetry of the system, using the formula:[67]

$$\mathbf{k}_{n_1,n_2,n_3} = \sum_{\beta=1}^{3} \frac{2n_\beta - N_\beta - 1}{2N_\beta}\mathbf{b}_\beta \qquad (n_\beta = 1, 2, 3, ..., N_\beta), \tag{2.25}$$

where N_β is the number of divisions in reciprocal space along the βth direction (β = 1, 2, 3) and $\mathbf{b}_1, \mathbf{b}_2$ and $\mathbf{b}_3$ are the primitive reciprocal lattice vectors.

Quantum ESPRESSO uses a similar equation, but allows the possibility to generate a uniform grid of k-points with an offset. The allowed values for the offset parameter, sk_β are 0, in which case there is no offset, and 1, in which case the grid is displaced by half a grid step in the corresponding direction. The formula used is:[50]

$$\mathbf{k}_{n_1,n_2,n_3} = \sum_{\beta=1}^{3} \frac{2(n_\beta - 1) + sk_\beta}{2N_\beta}\mathbf{b}_\beta \qquad (n_\beta = 1, 2, 3, ..., N_\beta), \tag{2.26}$$

The higher the number of k-points considered in the Brillouin zone, the better will be the accuracy of the calculation; but the more you use, the slower is the calculation. The computational time for the calculation scales linearly with the number of k-points. Symmetries of the system are usually used to reduce the BZ to the irreducible BZ, so that only k-points in the irreducible BZ need to be considered for the calculation.[68]

For isolated systems or very large supercells, it is sufficient to sample the k-space only at the Brillouin zone origin $\mathbf{k} = (0, 0, 0)$, also known as the Γ point. For artificially periodic supercells, it is sufficient to choose only one division along the aperiodic directions.[68]

2.1.7 Smearing

Recall that any observable of the wavefunction is calculated by summing over all the occupied states at a given k-point and then integrating over all k-points in the first Brillouin zone (BZ). In the case of metals, at $T = 0$, this corresponds to a summation over all k-points within the Fermi surface. Due to the sharp discontinuity in k-space on going from occupied states to the unoccupied states, this situation calls for a large number of k-points in order to reproduce the Fermi surface accurately.[68]

Even if one uses a large number of k-points, which is not an ideal situation as it would require huge computational time, the band crossings above and below the Fermi level may still lead to convergence problems when calculating the self-consistent field loop.[68]

One way to deal with this is to replace the sharp, discontinuous step function (at temperature $T = 0$) at E_F with a smoother function, which could be an approximation to the step function, and allow for partial occupancies at E_F. In effect, the occupancies are smeared out, or broadened near the Fermi level. Using this method ensures faster convergence with respect to the number of k-points, but not necessarily to the right answer. The larger the smearing, the better is the convergence with respect to k-points, but the lower is the accuracy.[68]

There are several successful techniques used for this purpose of smearing out the sharp Fermi function. Gaussian smearing[69] is one, where the levels are broadened by Gaussian functions; however, the errors introduced can be large. Methfessel and Paxton suggested another technique where the step function is expanded in terms of Hermite functions, which are actually products of Hermite polynomials and Gaussian functions.[70] This technique has a problem with negative occupation values which can cause problems in visualizing densities of states. To treat the problems related to negative occupancies, a new technique was introduced by Marzari and Vanderbilt.[71] Here the delta function is approximated using a Gaussian function multiplied by a first order polynomial.

2.1.8 Force Calculations: Hellmann-Feynman theorem

The ability to compute the forces on the atoms in a system, quickly and accurately, is important for many reasons, e.g., in order to determine the optimized geometry of the system. The forces acting on the atoms can be calculated as the first derivative of the total energy of the system with respect to the atomic positions. This procedure, however, would be very tedious considering the large number of self-consistent calculations that would need to be carried out for a number of different atomic configurations. Hellmann and Feynman proved the existence of a simpler method to calculate forces in a system: their theorem suggests that the derivative of the total enegy is related to the expectation value of the derivative of the Hamiltonian:[72]

$$F_I = -\frac{\partial \langle E(\mathbf{R}_I) \rangle}{\partial \mathbf{R}_I} = -\left\langle \frac{\partial H}{\partial \mathbf{R}_I} \right\rangle = -\int \frac{\partial V_{\mathbf{R}_I}(\mathbf{r})}{\partial \mathbf{R}_I} n_{\mathbf{R}_I}(\mathbf{r}) d\mathbf{r}, \tag{2.27}$$

where $n_{\mathbf{R}_I}(\mathbf{r})$ is the ground state electronic density for a given set of nuclear co-ordinates $\{\mathbf{R}_I\}$.

2.1.9 Spin-Polarized Density Functional Theory

When studying systems with magnetic and spintronic properties, it is necessary to consider also the spin of the electrons. The methodology used in spin-polarized DFT is the same as in conventional DFT, the only difference being that here, the total electronic density is split into the spin up and spin down electronic densities; and the coupled Kohn-Sham equations are solved for each of them. The spin-polarized electronic densities are given by:

$$n^{\sigma}(\mathbf{r}) = 2 \sum_{s=1}^{N^{\sigma}} \psi_s^{\sigma *}(\mathbf{r}) \psi_s^{\sigma}(\mathbf{r}), \tag{2.28}$$

where $\sigma = \{\uparrow, \downarrow\}$, is the spin of the electron, and N^{σ} is the number of orbitals of spin σ. The sum of the spin up and spin down electronic densities is the total electronic density

in the system: $n(\mathbf{r}) = n^{\uparrow}(\mathbf{r}) + n^{\downarrow}(\mathbf{r})$; and the difference in the spin up and spin down electronic densities is the magnetic density of the sytem: $m(\mathbf{r}) = n^{\uparrow}(\mathbf{r}) - n^{\downarrow}(\mathbf{r})$.

In the most simple form of the spin-polarized DFT, only collinear magnetism is studied with no spin-orbit interactions.

For each spin, the Kohn-Sham equations given by:

$$\left\{ -\frac{\hbar^2}{2m_e}\nabla^2 + V_{\mathrm{KS}}^{\sigma}(\mathbf{r}) \right\} \psi_s^{\sigma}(\mathbf{r}) = \epsilon_s^{\sigma}\psi_s^{\sigma}(\mathbf{r}), \tag{2.29}$$

are solved. V_{KS}^{σ}, the Kohn-Sham potential, is given by:

$$V_{\mathrm{KS}}^{\sigma}(\mathbf{r}) = V_{ext}(\mathbf{r}) + V_H(\mathbf{r}) + V_{xc}^{\sigma}(\mathbf{r}). \tag{2.30}$$

Note that the spin dependence arises only from the exchange-correlation potential. The exchange-correlation potential is defined as:

$$V_{xc}^{\sigma}(\mathbf{r}) = \frac{\delta E_{xc}[n(\mathbf{r}), m(\mathbf{r})]}{\delta n^{\sigma}(\mathbf{r})}. \tag{2.31}$$

All these equations are solved in similar fashion to the non-spin-polarized K-S equations.

2.1.10 Modeling Aperiodic Systems

The use of a plane wave basis set to describe wavefunctions makes it necessary to use periodic boundary conditions in these calculations. This is not a problem when studying extended solids, but when studying aperiodic systems like surfaces, sheets, wires, or clusters, a region of vacuum space is introduced in the unit cell along all aperiodic directions; this must be sufficiently wide so that atoms do not have spurious interactions with their periodic images in neighboring cells.

2.2 Calculating Minimum Energy Paths

Knowing the minimum energy path (MEP) for a reaction can be very useful in understanding the mechanism of the reaction, and calculating the energy barriers along the

path which could be used to calculate reaction rates. In this thesis, we have used two approaches to determine MEPs: the Nudged Elastic Band (NEB) method[21] and the constrained minimization method.[73] The former method can only be used when both the initial and final states of the reaction are known. The latter technique does not require the knowledge of the final state, but is used only when the reaction is known to proceed along a simple reaction coordinate such as stretching of a bond length or bending of a bond angle to break or form a bond.

2.2.1 Nudged Elastic Band Calculations

The Nudged Elastic Band (NEB)[21] is a method to determine the minumum energy pathway between two stable states. The initial and final states are both local minima on the potential energy surface (PES), and the minimum energy pathway is one in which every point on the path is at an energy minimum, in all directions perpendicular to the path.

A string of images is created between the known initial and final states by a linear interpolation, the energies of these images are then minimized. These images are constrained by spring forces along the band, $\mathbf{F}^i_{S\|}$, to ensure equal spacing along the reaction path; and potential forces perpendicular to the band, $\mathbf{F}^i_{\perp}$:[21]

$$\mathbf{F}^i_{\mathrm{NEB}} = \mathbf{F}^i_{\perp} + \mathbf{F}^i_{S\|}, \tag{2.32}$$

The tangent along the path, $\hat{\tau}$, is defined at each step by the unit vector from each image to the higher energy neighboring image. The forces $\mathbf{F}^i_{\perp}$ and $\mathbf{F}^i_{S\|}$ are defined by:[21]

$$\mathbf{F}^i_{\perp} = -\nabla(\boldsymbol{\mathcal{R}}^i) + \nabla(\boldsymbol{\mathcal{R}}^i) \cdot \hat{\tau^i}\hat{\tau^i}, \tag{2.33}$$

$$\mathbf{F}^i_{S\|} = k(|\boldsymbol{\mathcal{R}}^{i+1} - \boldsymbol{\mathcal{R}}^i - |\boldsymbol{\mathcal{R}}^i - \boldsymbol{\mathcal{R}}^{i-1}|)\hat{\tau^i}, \tag{2.34}$$

where $\boldsymbol{\mathcal{R}}^{\boldsymbol{i}}$ is the position of the ith image and k is the spring constant. To avoid confusion, note that we have now changed notation with respect to earlier sections in this chapter, i now indexes images rather than electrons.

As the energies of the images change, the path also develops, and once the images are all converged to their minimum energy, they represent snapshots along the true minimum energy path.

In most cases, a linear initial path may be sufficient, but in cases where the reaction may involve a rotational motion, or when an intermediate state may be known before the calculation, an initial path can be constructed with images through the intermediate image.

The climbing image NEB method[22] can be used to push the image with the highest energy, up to the transition state configuration or the saddle point in the reaction. The calculation is designed such that the highest energy image does not feel the spring forces along the band, but the force on this image along the tangent to the band is inverted. The image thereby tries to maximize its energy along the band, and at the same time tries to minimize its energy in all other directions. This process ensures that the converged image will be the exact saddle point.

The difference in energy between the saddle point and the initial state determines the energy barrier for the reaction, which is the exponential term in the Arrhenius rate equation.

2.2.2 Constrained Minimization Calculations

The constrained minimization technique is the process of optimizing the structure of a system, in the presence of certain constraints.[73] It can be used as a method to explore the PES as a function of specific internal coordinates. If a reaction follows its path through a simple reaction coordinate that can be constrained, this method can be used to determine the MEP and find the transition state. To solve a constrained optimization problem, the standard approach is to use Lagrangian multipliers:

$$L(x, \lambda) = E(x) - \lambda' h(x), \tag{2.35}$$

where $E(x)$ is the function being minimized, $h(x) = 0$ is the constraint forced on the optimization, λ is the Lagrange multiplier and L is the Lagrangian function. This defines

a set of non-linear equations that are then solved iteratively. In Quantum ESPRESSO these non-linear constraint equations are solved using the SHAKE algorithm[74].

2.3 Molecular Dynamics

Due to large computational costs, DFT methods are usually restricted to studying relatively small system sizes, typically a few hundred atoms. Alternatively, classical level simulation methods can be used to describe materials using empirical understanding of the interactions that take into account bonding effects of valence electrons, without explicitly considering the electrons themselves. This method has the ability to study large systems with high computational speed.

In this thesis, classical molecular dynamics (MD) simulations will be used to generate the initial geometries for the systems studied in Chapter 7. Here we give a basic introduction to the method of molecular dynamics.

Molecular dynamics is a method to simulate the dynamics of N interacting particles in a system with certain initial conditions and boundary conditions.[75] In classical MD, quantum effects (for example, motion of electrons) are not considered; the inaccuracies that arise from this neglect are corrected by the parametrization of the force field used to treat the interactions between the particles. In principle, all properties that are explained by classical mechanics and statistical mechanics can be computed in a MD simulation.

Molecular dynamics simulations are very similar to real experiments in many respects. A sample of N particles is first prepared, and the dynamics of the particles are solved by integrating the Newton's equations of motion until the average properties of the system no longer change with time. The system is well equilibrated before the actual measurement is performed.[76]

All measurable quantities in a MD simulation are expressed as a function of the positions and momenta of the particles in the system. For example, the definition of temperature T in a classical many-body system makes use of the equipartition of energy over all degrees of freedom; the average kinetic energy per degree of freedom is given by:

$$\left\langle \frac{1}{2} M v_\alpha^2 \right\rangle = \frac{1}{2} k_B T; \tag{2.36}$$

where k_B is Boltzmann's constant, M is the mass of the particles, and v_α is the α-component of the velocity of the particles in the system: $\alpha = x, y, z$. This equation is used as an operational definition of temperature in a simulation. The total kinetic energy of the system is first measured and then divided by the number of degrees of freedom N_f. The instantaneous temperature of the system fluctuates as the total kinetic energy of the system changes with time:[76]

$$T(t) = \sum_{I=1}^{N} \frac{M_I \mathbf{v}_I^2(t)}{k_B N_f}; \tag{2.37}$$

where $\mathbf{v}_I^2 = v_{x,I}^2 + v_{y,I}^2 + v_{z,I}^2$. The relative fluctuations in the measured temperature are of the order of $1/\sqrt{N_f}$; to get an accurate estimate of the temperature, it is important to average over many fluctuations, i.e., over a long time interval.

2.3.1 Initialization

To set the initial conditions for a molecular dynamics simulation, initial positions and velocities are assigned to all particles in the system. The values for the velocities are either selected randomly for each component v_α, or they are picked from a Maxwell-Boltzmann velocity distribution. Here, α denotes the three Cartesian directions. Subsequently, these velocities are shifted, such that the total momentum is zero, and the resulting velocities are scaled to match the mean kinetic energy E_{kin} to the desired temperature T. In thermal equilibrium, we know that the following condition holds:[76]

$$\left\langle v_{\alpha,I}^2 \right\rangle = k_B T / M_I. \tag{2.38}$$

This relation is used to define the instantaneous temperature at time t, $T(t)$:[76]

$$k_B T(t) = \sum_{I=1}^{N} \frac{M_I v_{\alpha,I}^2(t)}{N_f}. \tag{2.39}$$

The instantaneous temperature $T(t)$ is adjusted to match the desired temperature T, by scaling all velocities with a factor $(T/T(t))^{1/2}$.[76]

2.3.2 Forces Calculated from Interatomic Interaction Potentials

The calculation of the force acting on every particle is the most time-consuming part of almost all molecular dynamics simulations. The forces between particles are given by interatomic potentials or force fields. Interatomic potentials are mathematical functions that are used to calculate the potential energy of a system of atoms with a given set of positions in space. The potential energy function calculated in an MD simulation, given by:

$$U(\mathbf{R}) = U_{bonding}(\mathbf{R}) + U_{non-bonding}(\mathbf{R}) + U_{special}(\mathbf{R}), \tag{2.40}$$

is dependent only on the positions of the atom. The first term on the RHS takes into account the interactions within a molecule like bond stretching, angle bending, dihedral-angle rotation, and improper dihedral angle distortion. The dihedral angle constrains the rotation around a bond, whereas the improper dihedral angle maintains the chirality or hybridization type for certain atoms. A change in the bond length or an angle from the ideal value leads to an increase in potential energy given by:

$$\begin{aligned} U_{bonding}(\mathbf{R}) = & \sum_{bonds} \frac{1}{2} K_b (b - b_0)^2 + \sum_{\substack{bond \\ angles}} \frac{1}{2} K_\theta (\theta - \theta_0)^2 + \sum_{\substack{dihedral \\ angles}} K_\phi [1 + \cos(n\phi - \phi_0)] \\ & + \sum_{\substack{improper \\ dihedral \\ angles}} \frac{1}{2} K_\xi (\xi - \xi_0)^2, \end{aligned} \tag{2.41}$$

where b, θ, ϕ and ξ are the bond lengths, bond angles, dihedral angles and improper dihedral angles respectively. The corresponding symbols with subscript 0 are the equilibrium values for the different terms in the system and are parameters in the force field.

The dihedral-angle term has a trignometric form for its potential function, where n is the multiplicity, the number of minima as the bond is rotated through 360^o. The other three interactions have a harmonic potential functional form and the force constants for each interaction are denoted by the labels K.

Non-bonding interactions include (a) the interactions described by the Lennard-Jones potential[77] and (b) the Coulombic interactions between charges on atoms. The former interaction takes into account Pauli repulsion at short ranges due to electron-electron overlap and attraction at long ranges due to London dispersion[78] or van der Waals interactions. The potential from non-bonding interactions is given by:

$$U_{non-bonding}(\mathbf{R}) = \sum_{\substack{atom\\pairs}} \left(\frac{A}{r^{12}} - \frac{B}{r^6} \right) + \sum_{\substack{atom\\pairs}} \frac{q_I q_J}{4\pi\varepsilon_0\varepsilon_1 r}. \tag{2.42}$$

Here, r is the distance between two atoms i and j for which the non-bonding energy is calculated. $4\pi\varepsilon_0$ is a constant, and ε_1 is the relative dielectric permittivity of the material. The force-field parameters include A and B, which are Lennard-Jones constants, and q_I and q_I, which are the charges on atoms I and J respectively.

The third term on the RHS of Eq. (2.40) is optional and represents an external potential that is applied to the system.

The Buckingham potential[79] is a simplification of the Lennard-Jones potential, proposed by Richard Buckingham, which describes the Pauli repulsion energy and the van der Waals energy for a two-atom interaction as:

$$\Phi_{ij}(R) = A\exp(-BR) - \frac{C}{R^6}, \tag{2.43}$$

where A, B and C are constants. The two terms on the RHS of the above equation describe the repulsion and the attractive interaction, respectively.

Buckingham-Matsui interatomic potentials:

One of the interatomic potentials used in this thesis is a type of Buckingham potential that was suggested by Matsui.[80] It describes successfully liquids and amorphous alumina in the bulk.[81] The interaction potential between any pair of atoms, I and J, as a function

of interatomic distance R_{IJ}, is given by:[81]

$$V(R_{IJ}) = \frac{q_I q_J}{R_{IJ}} + D(B_I + B_J)\exp\left(\frac{A_I + A_J - R_{IJ}}{B_I + B_J}\right) - \frac{C_I C_J}{R_{IJ}^6}, \tag{2.44}$$

where the three terms on the RHS describe the Coulombic, repulsive, and van der Waals interactions respectively; A, B, and C are parameters, and $D = 4.184$ kJÅ^{-1}mol^{-1} is the standard force constant.

We have used this potential to generate the structure of hydroxylated amorphous alumina in Chapter 8.

Charge-Optimized Many-Body potentials:

The Charge-Optimized Many-Body (COMB) potential[82,83] was developed to help bridge the gap between quantum mechanical effects and the non-reactive interatomic potentials. It is capable of describing processes of bond formation, bond breaking, or processes where the charge state of an atom varies. It calculates the equilibrium charge on each atom by the electronegativity equalization (QEq) method. The force field parameters used in this potential are optimized against DFT and/or quantum chemical calculations. This potential makes MD simulation slower than the traditional non-reactive force fields generally used for metallic, ionic and covalent materials.

The potential energy of the system is given by:

$$\begin{aligned} E_T = \sum_I \Bigg[& E_I^{self}(q_I) + \sum_{J>I} \Big[E_{IJ}^{short}(R_{IJ}, q_I, q_J) + E_{IJ}^{Coul}(R_{IJ}, q_I, q_J) \Big] + \\ & E^{polar}(R_{IJ}, q_I) + E^{vdW}(R_{IJ}) + E^{barr}(q_I) + E^{corr}(R_{IJ}, \theta_{IJK}) \Bigg], \end{aligned} \tag{2.45}$$

where $E_I^{self}(q_I)$ is the self-energy of atom I, $E_{IJ}^{short}(R_{IJ}, q_I, q_J)$ is the pair interaction between atoms I and J, E_{IJ}^{Coul} is the Coulombic interaction, $E^{polar}(R_{IJ})$ describes the polarizability of the system, $E^{vdW}(R_{IJ})$ is the van der Waals energy, $E^{barr}(q_I)$ is a charge barrier function, and $E^{corr}(R_{IJ}, \theta_{IJK})$ is an angular correction term.

This potential is used in Section C of this thesis to generate the initial geometries for copper oxide clusters.

2.3.3 Integrating the Equations of Motion

Once all the forces between the particles are computed, we can generate the trajectories of these particles by numerically solving the Newton's equations of motion for each particle in the system:

$$M\frac{d^2\mathbf{R}}{dt^2} = -\nabla U(\mathbf{R}), \tag{2.46}$$

where M is the mass of the particle, U is the potential energy, and the force on the particle, $\mathbf{F} = -\nabla U(\mathbf{R})$.

There are several numerical algorithms available for integrating the equations of motion. Here we describe the Verlet algorithm which is one of the simplest algorithms. To derive it, one starts with the Taylor series expansion of the positions of the particles in the system around time t:

$$\mathbf{R}(t+\Delta t) = \mathbf{R}(t) + \mathbf{v}(t)\Delta t + \frac{1}{2}\mathbf{a}(t)\Delta t^2 + ... \ ;$$

where $\mathbf{R}$ is the position, $\mathbf{v}$ is the velocity (the first derivative with respect to time), and $\mathbf{a}$ is the acceleration (the second derivative with respect to time).

By summing the equations for $\mathbf{R}(t+\Delta t)$ and $\mathbf{R}(t-\Delta t)$, we get:

$$\mathbf{R}(t+\Delta t) + \mathbf{R}(t-\Delta t) = 2\mathbf{R}(t) + \mathbf{a}(t)\Delta t^2. \tag{2.47}$$

The error in the estimate for the new position is of the order of Δt^4, where Δt is the time step we choose in our molecular dynamics scheme. Note that the Verlet algorithm does not use velocity to compute the new positions; however, it can be derived from the knowledge of the trajectory, using:

$$\mathbf{v}(t) = \frac{\mathbf{R}(t+\Delta t) - \mathbf{R}(t-\Delta t)}{2\Delta t} + \mathcal{O}(\Delta t^2). \tag{2.48}$$

This expression of the velocity is only accurate to the order Δt^2; the velocity computed

is used to estimate the kinetic energy and thereby the instantaneous temperature.

2.3.4 Simulated Annealing

Annealing is a method used in metallurgy where metals are heated to high temperatures and slowly cooled to reach a low energy state with high material strength. Simulated Annealing is an analogous computational method for optimization.[23] It is a probabilistic technique that can help to determine the global minimum of a system in a large search space. Starting from a random search at high temperature, the temperature is reduced slowly with the hope of reaching the global minimum. The high temperature helps surmount energy barriers in a search for conformations with lower energy than the conformation one starts with. In the MD simulated annealing calculations done in Section C, we have used the Berendsen thermostat[84] algorithm to rescale the velocities of the particles, to control the simulation temperature.

2.4 Atomistic Thermodynanmics

DFT is often described as a zero-temperature, zero-pressure technique. This misconception arises, when thinking that DFT calculates "only" the total energy of the system. *Ab initio* atomisic thermodynamics[24,25] (AIATD) is a method that tries to draw the bridge between DFT and thermodynamics: it employs the information obtained from DFT about the first-principles potential energy surface to calculate the Gibbs free energy of the system. With this quantity, using the standard thermodynamics methodology, one can extract most macroscopic system properties. This method extends the predictive power of the first-principles technique to a more relevant temperature and pressure range; it is also useful when studying large systems that may be divided into subsystems that are mutually in equilibrium with each other. Each system is treated separately and the relations between them can be determined from their corresponding thermodynamic potentials.

Thermal quantities like free energies can be very important and useful when one is interested in studying the relative stability of several phases at a given temperature and pressure. The second law of thermodynamics states that for a closed system with energy

E, volume V, and number of particles N, the entropy S of the system is at its maximum value when it is in equilibrium. From this formulation, one can derive that if a system is in contact with a heat bath, such that its temperature T, volume V, and number of particles N are fixed, then the Helmholtz free energy $F \equiv E - TS$ is at a minimum when the system is at its most stable state. Analogously, for a system at constant pressure p, and temperature T, with number of particles N, the Gibbs free energy $G \equiv F + PV$ would be at its lowest when the system is in its most stable state. To know which of two phases (denoted by ν and ω) is stable at a given temperature and pressure, one should simply compare the Gibbs free energies G_ν and G_ω of these phases.[76]

In this thesis, the AIATD method is used in Chapters 7 and 8 to study the relative stability of different oxide phases of Cu clusters in the gas phase and supported on hydroxylated amorphous alumina, in different environmental conditions. Since the equations derived for calculating the Gibbs free energy for a system are dependent on the system and environmental conditions, we are not discussing them here but have described them in detail in Chapters 7 and 8.

2.5 Codes Used

Density Functional Theory as implemented in Quantum ESPRESSO[50] was used for studying materials described in Chapters 3–6. Classical molecular dynamics as implemented in LAMMPS[85] was used for obtaining initial guesses for geometries of systems studied in Chapters 7 and 8. These initial geometries were then improved upon making use of DFT as implemented in the VASP package.[54–57]

The figures of system structures and charge density/charge transfer plots in this thesis, were obtained using the software packages XCrySDen[86] and VESTA.[87] All two-dimensional plots in the thesis were plotted using the Xmgrace software, and three-dimensional plots were obtained using gnuplot.

Section A

Modified from Calvin and Hobbes

Chapter 3

Diffusion and Growth of Pt Clusters on MgO(100) surface

In this chapter, we consider small clusters of Pt, up to tetramers, adsorbed on the MgO(100) surface. We investigate the role of surface F-centers in the growth of Pt clusters. We also study the diffusion mechanisms and the growth processes of these small clusters on the MgO(100) surface. The motivation for this study is to understand processes like sintering, and also to compare how the growth processes of Pt clusters on the surface of MgO(100) would be different from those of clusters of other metals like Pd, Au and Ag.

3.1 Introduction

Nano-sized metallic clusters have been found to have improved and more interesting properties than their bulk counterparts. These properties make them attractive for technological applications such as in catalysis, magnetic devices[88] and photonic devices.[89] For many of these applications, the clusters are supported over oxide surfaces, and hence a great deal of effort is now devoted to studying the properties of these small metal clusters on oxide surfaces. Some of the key issues that are of interest are finding ways of forming and stabilizing islands of a desired size, identifying diffusion mechanisms of the metal atoms, nucleation dynamics and also the role of surface defects.

Experimental techniques to softly land and deposit monodispersed clusters on surfaces

have been developed, so as to prevent fragmentation of the clusters upon deposition.[90] However, the stability of the metal clusters on the surface still remains an important issue. Small metal clusters (with sizes typically less than 4 nm) supported on oxides are known to be highly unstable relative to large metal nanoparticles, they therefore tend to coalesce or sinter to form fewer and larger clusters, especially at high temperatures.[91] This is one possible mechanism for the deactivation of nanocatalysts supported on oxides. Sintering may occur by individual metal atoms breaking off from a cluster, diffusing over the surface and joining another cluster, or it may occur by entire clusters diffusing across the oxide surface and merging with other clusters when they come into contact with them. The details of the elementary steps and intermediate structures involved in such processes are poorly understood, and atomistic models to explain the kinetics of sintering are also lacking. As the size of a cluster is really crucial in determining most of the properties of the cluster, depending on the application and property sought for, it is essential to find ways to stabilize a desired cluster size, and slow down processes like sintering. In this chapter, we address this issue by studying the mechanisms and the barriers involved in the diffusion of small metal clusters, and the growth processes of these clusters on an oxide surface.

One of the metal-oxide systems that has been well studied both experimentally and theoretically is Pd on MgO(100).[26,27,92,93] Experiments on this system have shown that the size of the Pd islands grown by metal atom deposition is remarkably insensitive to the surface temperature, indicating that the nucleation kinetics involved in the growth of these islands are governed by point defects with a high trapping energy.[94] This study underlines the important role that surface defects play in the growth process. The most common defects on MgO surfaces are neutral oxygen vacancies, or F-centers, where an oxygen atom has been removed from the surface.[95] Other defects observed are divacancies due to the removal of a Mg and an O atom and also charged vacancies due to the removal of an O ion.

A widely held notion of the growth process of transition metal clusters on MgO is as follows. The metal atoms land on the surface of the flat MgO and diffuse over the

surface by hopping from one site to another. When these atoms come across a point defect, however, they get trapped due to the strong binding at the defect site. A second diffusing adatom which comes close to the adatom/defect complex also gets trapped here, and thus by the addition of other diffusing adatoms, the cluster builds up at this defect site. We shall call this growth process the 'single-step' growth process. However, on analyzing experimental measurements on Pd on MgO(100), and applying this model to extract various energy parameters such as diffusion activation energy, Pd/defect trapping energy, and dimer binding energy, one finds that different experiments lead to different sets of parameters.[92,94] This suggests that some of the assumptions made in this model may not be valid. Earlier first-principles calculations on transition and noble metal cluster nucleation on MgO(100) have shown that the tendency for the O vacancies to nucleate metal islands is strongly element dependent,[96] which suggests that this mechanism may not hold for the growth of all clusters. Another set of theoretical first-principles calculations for the nucleation of Pd dimers at defect sites of the MgO(100) surface shows that the binding energy of the second metal atom to an adatom/F-center complex is very weak, only 0.39 eV, which is only slightly higher than the dimer binding energy on the defect-free terrace, which is 0.35 eV.[97] This tells us that the F-centers may not necessarily promote the formation of dimers significantly. On applying the model to the data from experiments on Pd/MgO, in order to explain the measured island size distribution, the extracted value for the dimer binding energy on the defect site is 1.2 eV.[94] Thus, one can see that there is a significant disagreement between the theoretical calculations and the parameters obtained from experiments by fitting the standard growth model to the experimental results.

In the single-step growth process, the cluster grows in size by the addition of monomers. However, we should also consider that the cluster can grow in size by the addition of larger clusters. We shall call this process the 'multi-step' growth process. In this chapter, we calculate the energetics involved in the growth process of clusters and attempt to determine whether it is more favorable for these clusters to grow by the single-step or the multi-step growth process.

The role of F-centers in the Pd-island growth process, the mechanisms, barriers and

the rate of diffusion of Pd small clusters (n = 1–4) on the surface of MgO(100) have been studied extensively by first-principles studies.[26,27,93] The structure and diffusion of small Ag and Au clusters on the defect-free MgO(100) surface have also be studied previously.[28] The barriers for the diffusion of these clusters on the surface were calculated using the nudged elastic band method, and the clusters were found to move around the surface in interesting ways. In this chapter, we investigate how these results are altered when we have instead Pt clusters adsorbed on the surface of MgO(100).

The Pd atom has an electronic configuration of [Kr] $5s^0\ 4d^{10}$, while Pt has an electronic configuration of [Xe] $4f^{14}\ 5d^9\ 6s^1$. They are both group-10 elements in the periodic table, with Pt positioned below Pd. Ag and Au are group-11 elements in the periodic table, with Au positioned below Ag. Au is positioned to the right of Pt, and Ag is diagonally above to the right of Pt. The cohesive energies of the bulk metals decrease in the order Pt > Pd > Au > Ag, with values of 5.84 eV/atom, 3.89 eV/atom, 3.81 eV/atom and 2.95 eV/atom respectively.[58] In this chapter, we will see how the change in the nature of the metal atoms forming the cluster affects the adsorption geometries, the binding energies, the barriers and mechanisms for the diffusion and growth of small clusters on the MgO(100) surface.

3.2 Methods

We have employed spin-polarized density functional theory (DFT), as implemented in the Quantum ESPRESSO package,[50] to study gas phase and MgO-supported Pt_n clusters; n = 1–4. We have used a plane wave basis set, with cut-offs of 30 Ry and 240 Ry for wave functions and charge densities, respectively. Exchange-correlation interactions were treated using the PBE form of the Generalized Gradient Approximation.[47] Ultrasoft pseudopotentials were used to treat the interactions between the ionic core and the valence electrons.[63] Scalar relativistic pseudopotentials were used for the Pt atoms. Convergence was hastened by smearing the occupations using Gaussian smearing[69] with a broadening width of 0.027 eV.

The calculations for Pt_n clusters supported on the MgO(100) surface were carried out using a 4×4 surface unit cell with four MgO layers, the bottom two layers of MgO were

fixed and all other atoms were allowed to relax. A vacuum of thickness ∼14 Å in the surface-normal direction was used for these calculations. k-point sampling for the cells with the gas phase clusters was done only at the zone center, while for the cells with the clusters supported on MgO it was done using a $2 \times 2 \times 1$ k-point grid. The barriers for the diffusion of clusters on the MgO(100) surface were calculated using the Nudged Elastic Band (NEB) method.[22]

When determining cluster geometries, several initial geometries were considered for each n, so as to span the space of possible geometries to the extent possible, and thus give us a fair chance of obtaining the ground state structure. These structures were then optimized by making use of Hellmann-Feynman forces[72] and the BFGS algorithm.[98–101]

3.3 Results

3.3.1 Bulk Pt

To validate our calculations, we first consider bulk Pt. The equilibrium lattice constant obtained is 4.00 Å, which is in good agreement with the experimental value of 3.92 Å.[58] We also calculate the cohesive energy to be 5.43 eV/atom, which is in reasonable agreement with the experimental result of 5.84 eV/atom. The small errors observed in the lattice constant and cohesive energy are typical of the GGA.[58]

3.3.2 Pt clusters in Gas Phase

Before studying the adsorption of Pt_n clusters on the MgO(100) surface, we first consider the clusters in the gas phase. The binding energy of a cluster in the gas phase is calculated by the equation: $E_b^{gas} = \frac{1}{n}[E(Pt_n) - nE(Pt)]$ where $E(Pt_n)$ and $E(Pt)$ are the total energies obtained from DFT of the Pt_n cluster and a single Pt atom in the gas phase, respectively.

The Pt_2 dimer has a binding energy of 1.76 eV/atom, with a magnetic moment of 2 μ_B. The Pt-Pt bond length in the dimer is found to be 2.36 Å.

For the trimer, we consider two possible geometries: a triangular geometry and a linear

geometry. In the triangular geometry, Pt_3 forms an equilateral triangle of side 2.51 Å; it has a binding energy of 2.36 eV/atom and a magnetic moment of 2 μ_B. In the linear Pt_3 cluster, the two nearest-neighbor Pt-Pt bond distances are 2.38 Å each; it has a binding energy of 2.18 eV/atom and a magnetic moment of 4 μ_B.

For the tetramer Pt_4, we consider three geometries: a tetrahedron, a rhombus and a square. The binding energies of the Pt_4 clusters in these three geometries are 2.65 eV/atom, 2.59 eV/atom and 2.58 eV/atom, respectively, with magnetic moments of 2 μ_B, 4 μ_B and 2 μ_B, respectively.

All the results obtained by us for the Pt gas phase clusters are in good agreement with previous DFT results.[102–107]

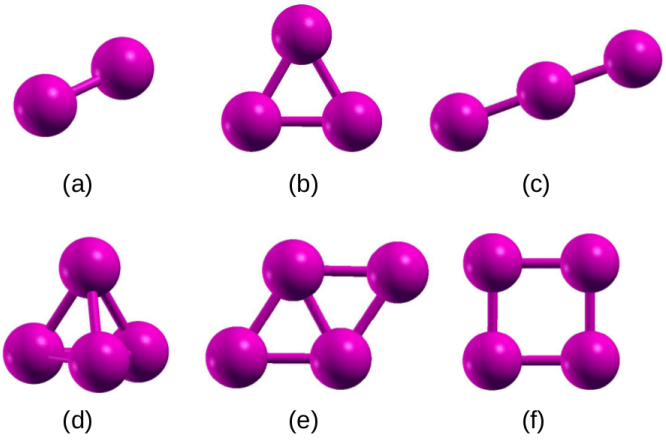

Figure 3.1: *The optimized geometries obtained for (a) Pt_2, (b) triangular Pt_3, (c) linear Pt_3, (d) tetrahedral Pt_4, (e) rhombus Pt_4 and (f) square Pt_4. For the Pt_3 cluster, the triangular cluster is lower in energy than the linear cluster by 0.54 eV, and for the Pt_4 cluster, the tetrahedral cluster is lower in energy by 0.24 eV and 0.29 eV with respect to the square and rhombus clusters, respectively.*

3.3.3 Pt clusters on MgO(100)

In this section we study the adsorption and diffusion of Pt_n clusters, n = 1–4, on the defect-free surface of MgO(100). We define the binding energy E_b of Pt_n on MgO(100) as the energy required to separate the system of Pt_n/MgO into n Pt atoms and MgO: $E_b = -\frac{1}{n}[E_{Pt_n/MgO} - E_{MgO} - nE_{Pt}]$. Note that this is the sum of the binding energy of the metal cluster and the adsorption energy of the cluster to the surface. Here $E_{Pt_n/MgO}$ and E_{MgO} are the total energies from DFT for the systems Pt_n/MgO and the MgO surface.

respectively. We calculate the activation barriers for the diffusion of these clusters on the MgO surface using the NEB method.

We also study the adsorption of these clusters at O vacancy sites (also called F-center sites) on the MgO(100) surface. The binding energy E_b^v of a cluster to the MgO surface with a surface F-center is defined as: $E_b^v = -\frac{1}{n}[E_{\mathrm{Pt}_n/\mathrm{MgO},F} - E_{\mathrm{MgO},F} - nE_{\mathrm{Pt}}]$, where $E_{\mathrm{Pt}_n/\mathrm{MgO},F}$ and $E_{\mathrm{MgO},F}$ are the total energies from DFT for the systems consisting of Pt_n adsorbed on the MgO surface slab with an O-vacancy, and for a MgO surface slab with an O-vacancy, respectively. From the data obtained from all these calculations, we then attempt to analyze and understand the energetics involved in the growth process of the clusters at these sites.

3.3.3.1 Monomer

Adsorption of Pt monomer on the defect-free MgO(100) surface

For the deposition of a Pt adatom on the defect-free MgO(100) surface, we have two possible stable adsorption sites, one in which the Pt atom is directly above the surface O atom [see Fig. 3.2(a)], and another in which the Pt atom is directly above the hollow site on the surface [see Fig. 3.2(b)]. We find that the Pt atom does not prefer to be at a bridge site above the Mg-O bond; when placed at this site, the Pt atom moves or relaxes to the position above the surface O atom. Of the two stable geometries, we find that the Pt atom energetically prefers the site above the surface O atom with a binding energy of 2.32 eV/atom, and this geometry is found to be non-magnetic. Using the method of Bader analysis[108,109] we find that when adsorbed at this site, the Pt atom becomes negatively charged by gaining 0.44 e, due to electron transfer from the substrate to the atom. The binding energy for the less stable geometry where Pt is above the hollow site is 1.48 eV/atom, and the magnetic moment is found to be 2 μ_{B}. Our results for the preferred geometry and the binding energy for the monomer on the MgO(100) surface are in good agreement with a previous DFT result.[96] However, there is also another study where the authors have found the monomer binding energy to the MgO surface to be 1.50 eV.[110]

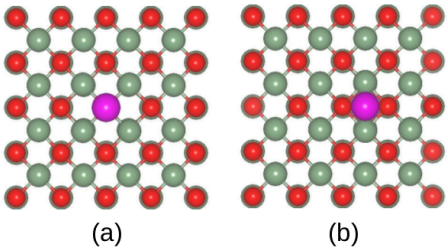

Figure 3.2: *Top views of the optimized adsorption geometries obtained for the adsorption of a single Pt atom on the defect-free MgO(100) surface: in (a) Pt is directly above a surface O atom, and in (b) Pt is above the hollow site on the surface. The adsorption geometry in (a) is lower in energy by 0.84 eV with respect to the geometry in (b). The grey, red and magenta spheres represent Mg, O and Pt atoms.*

Diffusion: Hopping of the monomers

We consider the diffusion of a Pt monomer over the surface of MgO(100) by means of a hopping process between two oxygen sites. The saddle point in this process is the geometry in which the Pt atom is above the hollow site and the activation barrier is calculated to be 0.88 eV. In Fig. 3.3, we show the energy profile for the diffusion process, as obtained from the nudged elastic band technique; the geometries of the initial state, the transition state and the final state are shown as insets in the figure.

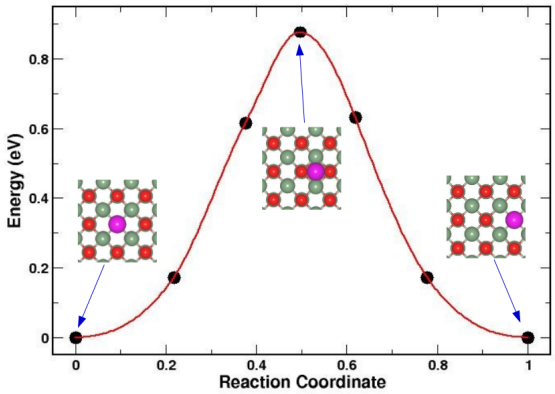

Figure 3.3: *The energy profile, as obtained from a NEB calculation, of the monomer diffusion process over the flat MgO(100) surface. The energy of the system is plotted as a function of the reaction coordinate. The Pt monomer binds to the O site with a binding energy of 2.32 eV/atom, and diffuses via a hopping mechanism from one O site to another with a barrier of 0.88 eV. The images in the insets are top views of the initial state, the transition state and the final state in the diffusion process; the grey, red and magenta spheres represent Mg, O and Pt atoms respectively.*

Adsorption of Pt monomer on MgO(100) with O vacancies

In Fig. 3.4, we show the adsorption geometry of the monomer adsorbed over a site where

the surface O atom is absent. For ease of visualization, the O-vacancy site is highlighted by a yellow sphere in the figure. The Pt atom binds very strongly to this site with a binding energy of 6.09 eV/atom. The binding energy calculated by us is in very good agreement with previous DFT results.[96] We find that when the Pt atom is adsorbed over the O-vacancy site, it gains a charge of -2.03 e; this large charge transfer from the substrate to the Pt atom explains the high binding energy of the monomer to the O-vacancy site as compared to the binding of the monomer to the defect-free surface.

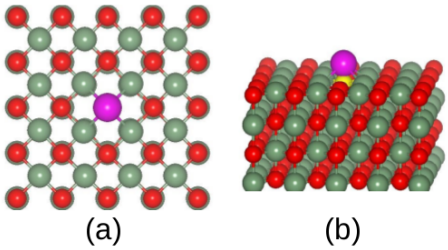

Figure 3.4: *(a) Top and (b) side views of the optimized adsorption geometry obtained for the adsorption of a single Pt atom on an O-vacancy site on the MgO(100) surface. The grey, red and magenta spheres represent Mg, O and Pt atoms. For ease of visualization, the site of the O-vacancy is highlighted by placing a yellow sphere there.*

3.3.3.2 Dimer

Adsorption of Pt dimer on the defect-free MgO(100) surface

To study the adsorption of Pt_2 on the surface of MgO(100), we consider three possible geometries; the top and side views of these geometries are shown in Fig. 3.5. They are labeled D1, D2 and D3 in the order of increasing energy or decreasing stability. In the D1 and D3 geometries, the Pt_2 dimer is adsorbed vertically, above the surface O atom or the surface hollow site respectively, while in the D2 geometry, the Pt_2 dimer is adsorbed horizontally on the surface, binding to two surface O atoms. The binding energies of the three geometries D1, D2 and D3 are 2.78 eV/atom, 2.74 eV/atom and 2.45 eV/atom, respectively. The first two geometries D1 and D2 are magnetic in nature, with magnetic moments of 2 μ_B each, whereas the D3 geometry is found to be non-magnetic. In the lowest energy geometry D1, the Pt dimer gains a charge of -0.38 e, due to charge transfer from the substrate to the Pt dimer. Our result for the preferred geometry for the Pt dimer is in agreement with a previous DFT result, however the authors of this previous study

find the binding energy of the dimer to the support to be 1.78 eV/atom; it is possible that the authors of this earlier investigation performed non-spin-polarized calculations, which would explain the discrepancy between their value and ours.[96] We note that in another study, though the authors report that Pt dimers prefer the lateral D2 geometry, they also say that the two geometries D1 and D2 are close in energy.[110] In yet another earlier work, the authors define the binding energy of the dimer on the surface as the energy required to break the dimer into two monomers adsorbed on the surface, and report this to be 0.72 eV.[96] From our calculations, we find this value to be 0.92 eV.

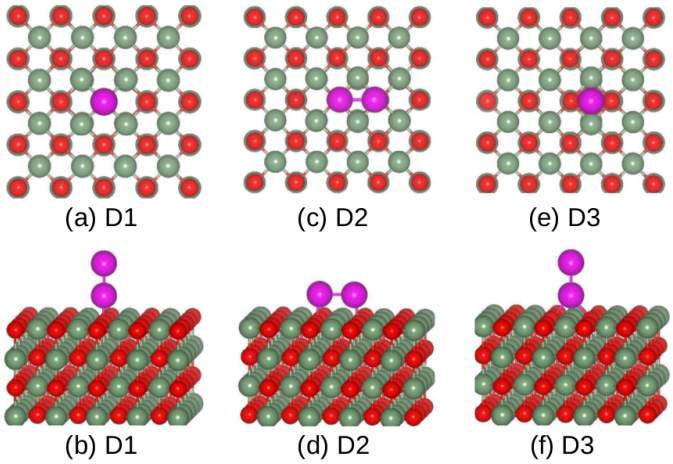

Figure 3.5: *The optimized adsorption geometries obtained for the adsorption of Pt_2 on the defect-free surface of MgO(100). (a) and (b) are the top and side views, respectively, of the D1 adsorption geometry, where Pt_2 is adsorbed vertically above a surface O atom; (c) ad (d) are the top and side views, respectively of, the D2 adsorption geometry, where Pt_2 is adsorbed horizontally bonding to two surface O atoms; and (e) and (f) are the top and side views, respectively, of the D3 geometry, where Pt_2 is adsorbed vertically above the hollow site on MgO(100). The grey, red and magenta spheres represent Mg, O and Pt atoms.*

Diffusion: Cartwheeling mechanism in the dimers

We find that there are two possible mechanisms for the diffusion of Pt dimers on the flat MgO(100) surface. One is a hopping mechanism in which the Pt dimer remains vertically upright and hops from one O site (D1 geometry) to another, passing through the saddle point where the Pt dimer is above the hollow site on the surface (D3 geometry). This diffusion pathway has an activation energy of 0.66 eV. The other pathway involves a cartwheeling mechanism in which the Pt dimer begins in an upright geometry at the O site (D1 geometry), lies flat to form the D2 geometry, and again stands upright at the

adjacent O site (D1 geometry). This pathway has a lower activation barrier of 0.42 eV, the energy profile for this pathway is shown in Fig. 3.6. The insets in the figure show the top views of the initial state in the D1 geometry, the intermediate state in the D2 geometry and the final state again in the D1 geometry.

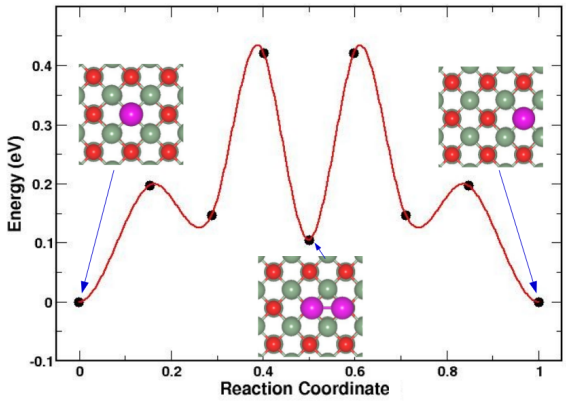

Figure 3.6: *The energy profile of the dimer diffusion over the flat MgO(100) surface, as obtained from a NEB calculation. The Pt dimer binds vertically at the O site with a binding energy of 2.78 eV/atom, and diffuses via a cartwheeling mechanism from one O site to another with a barrier of 0.42 eV. The images in the insets are top views of the initial state, the intermediate state in the D2 geometry and the final state in the diffusion process; the grey, red and magenta spheres represent Mg, O and Pt atoms respectively.*

Adsorption of Pt dimer on MgO(100) with O vacancies

In Fig. 3.7, we show two possible stable geometries for the adsorption of Pt_2 over an O-vacancy site on the MgO surface. The top and side views of the energetically preferred geometry are shown in Figs. 3.7(a) and (b), where we see that the dimer is lying horizontal on the surface directly above the O-vacancy site. This geometry has a high binding energy of 4.44 eV/atom, and the dimer gains a charge of -2.20 e due to electron transfer from the substrate to the dimer. Another stable geometry is about 1 eV higher in energy; its top and side views are shown in Figs. 3.7(c) and (d). In this geometry, the Pt dimer is vertically upright and is directly above the O-vacancy site. In both geometries, the dimer loses its magnetic moment. In an earlier work, the authors define the binding energy of the dimer at a F-center on the surface as the energy required to break the dimer into two monomers, one at the F-center and the other on the defect-free surface; they report that this process is not favorable and find a negative binding energy of -0.14 eV.[96] From our calculations, however, we find that this energy is positive and is 0.46 eV. It is possible

that the authors of this earlier study carried out non-spin-polarized calculations, if so, this may be the reason for the discrepancy between their results and ours.

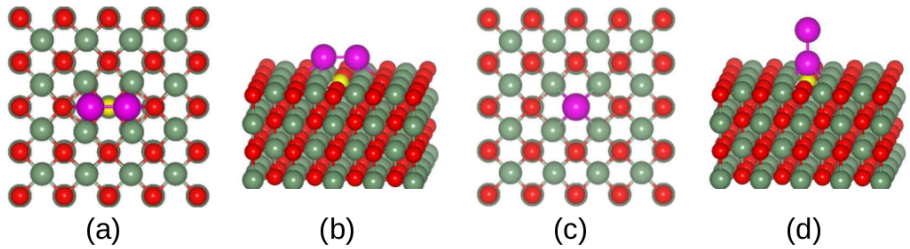

Figure 3.7: *Pt dimer on a F-center: (a) and (c) are the top views of two optimized adsorption geometries obtained for the adsorption of a Pt dimer on an O-vacancy site on the MgO(100) surface, (b) and (d) are the corresponding side views. The geometry shown in (a) and (b) is lower in energy than that shown in (c) and (d) by 1 eV. The grey, red and magenta spheres represent Mg, O and Pt atoms. For ease of visualization, the site of the O-vacancy is highlighted by a yellow sphere.*

3.3.3.3 Trimer

Adsorption of Pt trimer on the defect free MgO(100) surface

In Fig. 3.8, we show the top and side views of different adsorption geometries considered for Pt_3/MgO. They are labeled Tr1, Tr2, Tr3, Tr4, Tr5 and Tr6 in the order of decreasing stability or increasing energy. In the geometries Tr1, Tr2, Tr4, Tr5 and Tr6, the Pt_3 cluster remains in a triangular geometry, each with a different kind of binding to the surface, while in the Tr3 geometry, the Pt_3 cluster is linear in shape. In the lowest energy geometry, Tr1, the Pt trimer gains a charge of -0.67 e due to charge transfer from the substrate to the trimer.

Our results for the adsorption energies and the magnetic moments calculated for each stable geometry of Pt_3/MgO considered are listed in Table 3.1. In geometries Tr1, Tr2, Tr5 and Tr6, the Pt_3 cluster stands vertically upright forming a triangle with two Pt atoms binding to the surface; in these geometries, the two Pt atoms are bonded to two, two, three and four surface O atoms, respectively. The difference between the Tr1 and Tr2 geometries is that in Tr1, the Pt atoms bind to nearest neighbor O atoms on the surface, whereas in Tr2, the Pt atoms are bind to next-nearest-neighbor O atoms on the surface. In Tr3, the Pt_3 cluster assumes a linear geometry on the surface, with each Pt

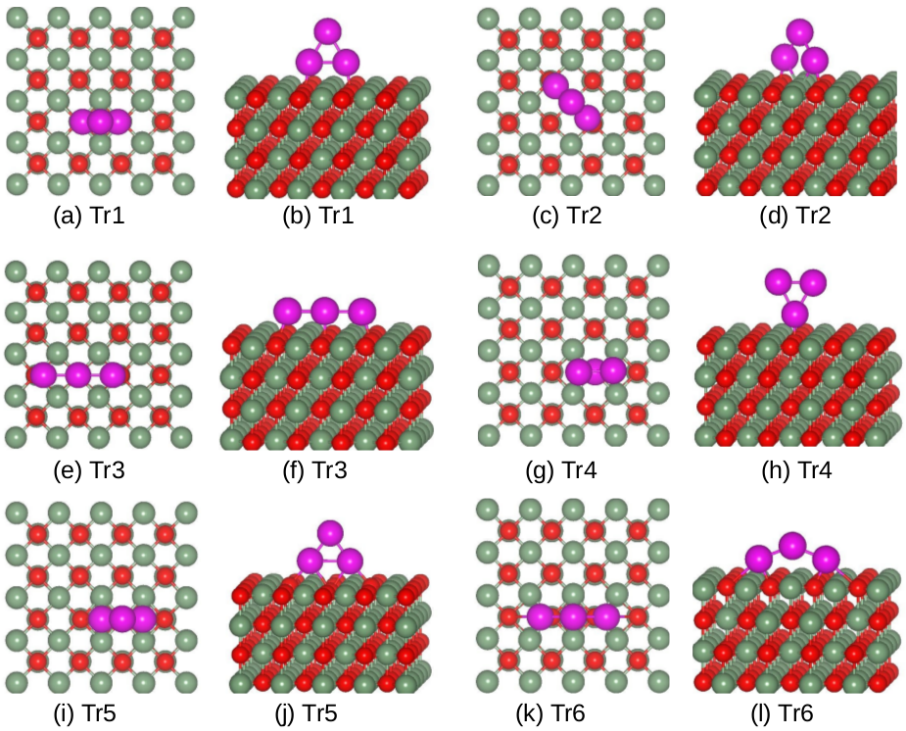

Figure 3.8: *The optimized adsorption geometries obtained for the adsorption of Pt_3 on the surface of MgO(100). (a), (c), (e), (g), (i), (k) are top views respectively; and (b), (d), (f), (h), (j) and (l) are side views respectively of Tr1, Tr2, Tr3, Tr4, Tr5 and Tr6 adsorption geometries. They are arranged in the order of increasing energy with Tr1 geometry being the geometry with the lowest energy. The grey, red and magenta spheres represent Mg, O and Pt atoms.*

atom forming a bond with a surface O atom, while in Tr4, the Pt_3 cluster binds to the surface of MgO(100) only through one Pt atom that is bonded to a surface O atom.

Diffusion: Skating mechanism in the trimers

The Pt trimer diffuses over the surface of MgO via a skating mechanism: the Pt_3 cluster starts from a Tr1 geometry, skates to a Tr2 geometry and again moves to form the Tr1 geometry at the adjacent site. The energy profile for the diffusion pathway is shown in Fig. 3.9. The insets in the figure show snapshots of the points in the diffusion pathway that correspond to the Tr1 and the Tr2 geometries. The activation energy for this pathway is calculated to be 0.60 eV. Another pathway that is possible for this trimer, but that has a higher activation barrier, is a sliding mechanism that involves the sliding of the Pt_3 from the geometry in Tr1 $\rightarrow$ Tr5 $\rightarrow$ Tr1. The Tr5 geometry is the saddle point geometry in this pathway, and the activation barrier is found to be >1.01 eV.

Pt_3/MgO	E_b (eV/atom)	Mag. Mom. (μ_B)
Tr1	3.34	0.00
Tr2	3.19	2.00
Tr3	3.03	0.00
Tr4	3.01	0.00
Tr5	2.99	2.00
Tr6	2.81	2.00

Table 3.1: *Binding energies and magnetic moments of the Pt trimer when supported on the MgO(100) surface in o different adsorption geometries. The binding energies are calculated by the equation:* $E_b = -\frac{1}{n}[E_{Pt_n/MgO} - E_{MgO} - nE_{Pt}]$.

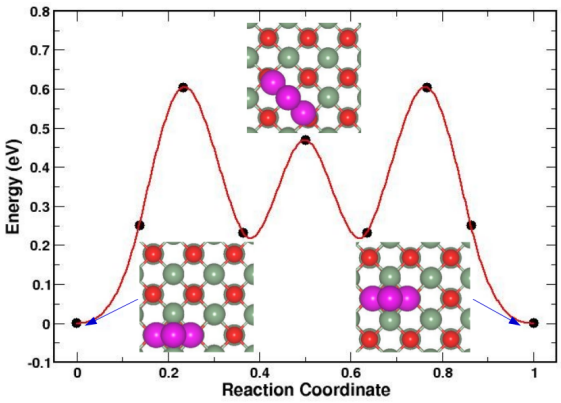

Figure 3.9: *The energy profile of the trimer diffusion over the flat MgO(100) surface, as obtained from NEB calculations. The Pt trimer stands up on the MgO surface forming a triangle and bonding to two nearest neighbor O atoms (Tr1 geometry) with a binding energy of 3.35 eV, and diffuses via a walking mechanism with a barrier of 0.60 eV. The images in the insets are top views of the initial state (in Tr1 geometry), the intermediate state (in Tr2 geometry) and the final state (in Tr1 geometry) in the diffusion process; the grey, red and magenta spheres represent Mg, O and Pt atoms respectively.*

Adsorption of Pt trimer on MgO(100) with O vacancies

Figs. 3.10(a) and (c) show the top views, and Figs. 3.10(b) and (d) show the side views, respectively, of the two geometries considered for the adsorption of Pt_3 at an O-vacancy site on MgO(100). In the geometry shown in (a) and (b), one of the Pt atoms in the trimer sits directly above the vacancy site (which, for visual ease, is highlighted in the figures by a yellow sphere), this geometry has a high binding energy of 4.21 eV/atom. The cluster gains a charge of -2.32 e due to electron transfer from the substrate to the cluster. The other geometry in (c) and (d) is only 0.07 eV higher in energy: it is positioned such that the center Pt atom of the triangle, that is not bonded to the surface, is directly above the O-vacancy site, and the other two Pt atoms bind to the neighboring four surface Mg

atoms.

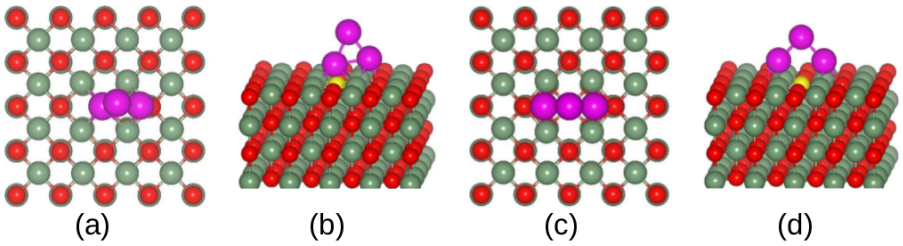

Figure 3.10: *Pt trimer at an F-center on MgO: (a) and (c) are the top views of two optimized adsorption geometries obtained for the adsorption of a Pt trimer at an O-vacancy site on the MgO(100) surface, (b) and (d) are the corresponding side views. The geometry shown in (a) and (b) is lower in energy than that shown in (c) and (d) by only 0.07 eV. The grey, red and magenta spheres represent Mg, O and Pt atoms. For ease of visualization, the site of the O-vacancy is highlighted by a yellow sphere.*

3.3.3.4 Tetramer

Adsorption of Pt tetramer on the defect-free MgO(100) surface

We have found several stable geometries for the adsorption of Pt_4 on the flat pristine surface of MgO(100), as shown in Fig. 3.11. They are labeled Tt1, Tt2, Tt3, Tt4 and Tt5 in the order of decreasing stability. In the most stable geometry, the Pt tetramer forms a distorted tetrahedron with three of the Pt atoms binding to three nearby surface O atoms. This geometry has a strong binding energy of 3.54 eV/atom, and the tetramer gains a negative charge of -0.91 e due to electron transfer from the substrate to the tetramer.

In the Tt2 geometry, the tetrahedron is more stretched out than it is in the Tt1 geometry. Three Pt atoms in the cluster bind to three next-nearest-neighbor surface O atoms making a triangle, and the fourth Pt atom stays above the triangle [see Figs. 3.11(c) and (d)]. In the Tt3 geometry, only two Pt atoms bind to the surface (similar to the D2 geometry), with the other two Pt atoms forming a line perpendicular to the first two Pt atoms [see Figs. 3.11(e) and (f)]. The Tt4 geometry is similar to Tt3, but in this case, the two Pt atoms binding to the surface bind to two third nearest neighbor O atoms, with the other two Pt atoms remaining above and forming a line perpendicular to the first two Pt atoms [see Figs. 3.11(g) and (h)]. Finally in Tt5, we have a square geometry for the Pt_4 cluster, with all four Pt atoms binding to four surface O atoms [see Figs. 3.11(i) and (j)].

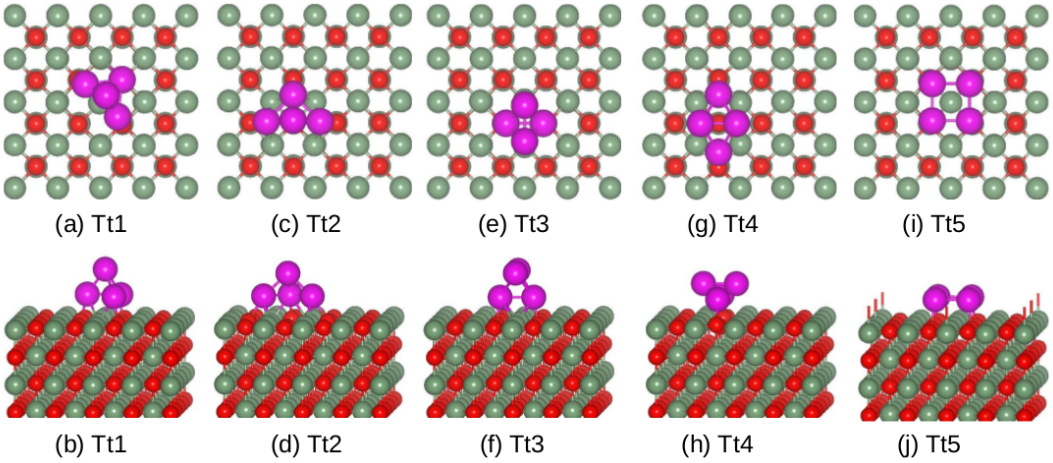

Figure 3.11: *The optimized adsorption geometries obtained for the adsorption of Pt_4 on the surface of MgO(100). (a), (c), (e), (g), (i) are top views respectively; and (b), (d), (f), (h) and (j) are side views respectively of the Tt1, Tt2, Tt3, Tt4 and Tt5 adsorption geometries. They are arranged in the order of increasing energy with Tt1 geometry being the geometry with the lowest energy. The grey, red and magenta spheres represent Mg, O and Pt atoms.*

The binding energies and the magnetic moments of each of these geometries are listed in Table 3.2.

Pt_4/MgO	E_b (eV/atom)	Mag. Mom. (μ_B)
Tt1	3.54	2.00
Tt2	3.44	2.00
Tt3	3.35	2.00
Tt4	3.28	2.00
Tt5	3.01	2.00

Table 3.2: *Binding energies and magnetic moments of the Pt tetramer when supported on MgO(100) in different adsorption geometries. The binding energies are calculated by the equation:* $E_b = -\frac{1}{n}[E_{Pt_n/MgO} - E_{MgO} - nE_{Pt}]$.

Diffusion: Rolling mechanism in the tetramers

Pt_4 clusters diffuse on the surface of the flat MgO(100) via a rolling mechanism: Tt1 $\rightarrow$ Tt3 $\rightarrow$ Tt1 with an activation barrier of 0.81 eV. The energy profile for this pathway is shown in Fig. 3.12. The insets in the figure show top views of the initial state, corresponding to the Tt1 geometry, the saddle point, which is in the Tt3 geometry, and the final state, which is again in the Tt1 geometry.

Adsorption of Pt tetramer on MgO(100) with O vacancies

Fig. 3.13 shows the top and side views of the optimized adsorption geometry obtained for

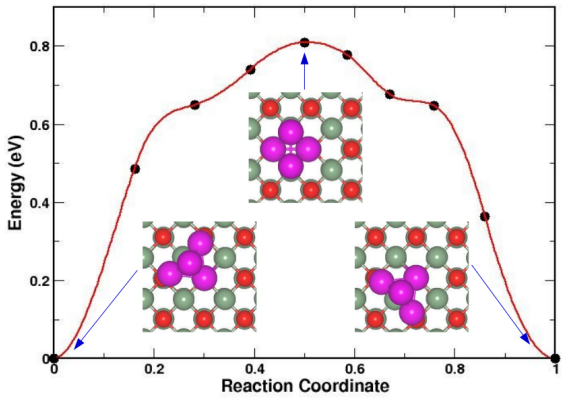

Figure 3.12: *The energy profile of the tetramer diffusion over the flat MgO(100) surface, as obtained from NEB calculations. The Pt tetramer adsorbs in the Tt1 geometry with a binding energy of 3.54 eV, and diffuses via a rolling mechanism with a barrier of 0.81 eV. The images in the insets are top views of the initial, transition and final states in the diffusion process; the grey, red and magenta spheres represent Mg, O and Pt atoms respectively.*

Pt_4 adsorbed on the MgO(100) surface with an O-vacancy. The binding energy of this cluster in this geometry is 4.24 eV/atom. We find that in the presence of the O-vacancy, the tetramer gains a negative charge of -2.45 e due to charge transfer from the substrate to the tetramer. Similar to what we find for the other sizes of the cluster, this charge transfer is again much higher than the charge transfer from the defect-free MgO substrate to the tetramer adsorbed on the surface.

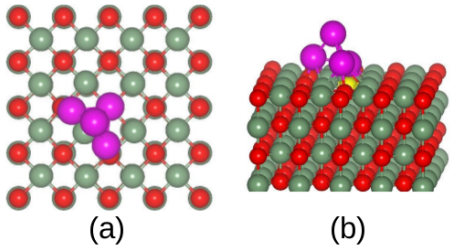

Figure 3.13: *(a) Top and (b) side views of the optimized adsorption geometry obtained for the adsorption of a Pt tetramer at an O-vacancy site on the MgO(100) surface. The grey, red and magenta spheres represent Mg, O and Pt atoms. For ease of visualization, the site of the O-vacancy is highlighted by a yellow sphere.*

3.3.4 Comparing Our Results for Pt clusters with Earlier Results for Pd, Au and Ag clusters

Above, we have studied the adsorption and diffusion of Pt clusters on the surface of MgO(100), and have also examined how the binding of the cluster to the surface is affected by the presence of surface O-vacancies. Now, it would be interesting to understand how much these results are affected by the nature of the metal of which the cluster is formed.

We compare our results for the Pt clusters with three earlier investigations on small clusters of other metals: Pd, Ag and Au. Xu *et al.* have studied the adsorption and diffusion of Pd_n clusters (n = 1–4) on the defect-free surface of MgO(100), and also the adsorption of these clusters on the MgO(100) surface with O-vacancies.[26,27] Similar studies have also been done by Barcaro and Fortunelli, where the authors have studied the adsorption and diffusion of Au_n and Ag_n clusters (n = 1–4) on the defect-free surface of MgO(100).[28] However, this study does not extend to considering the adsorption of these clusters on the MgO(100) surface with O-vacancies.

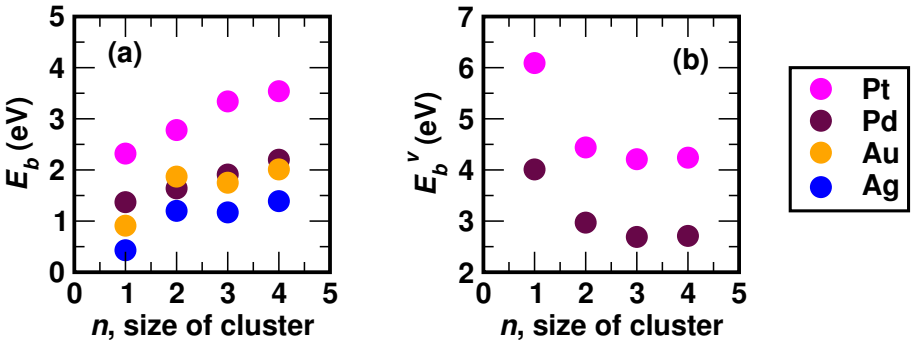

Figure 3.14: *Comparing the binding energies, E_b and E_b^v for the adsorption of different clusters on (a) the defect-free MgO(100) surface and (b) the MgO(100) surface with a surface O-vacancy. In (a), we show how E_b, calculated using the equation: $E_b = -\frac{1}{n}[E_{Pt_n/MgO} - E_{MgO} - nE_{Pt}]$ changes as a function of n, the size of the cluster, for Pt (our results), Pd[26,27], Au[28] and Ag[28]. In (b), we show how E_b^v, calculated using the equation: $E_b^v = -\frac{1}{n}[E_{Pt_n/MgO,F} - E_{MgO,F} - nE_{Pt}]$ changes as a function of n for Pt (our results) and Pd[26,27].*

In Fig. 3.14, we show how our results for the binding energies of the Pt_n clusters (shown by magenta symbols) on the MgO(100) surface differ from those of Pd, Au and Ag clusters on the same surface. In Fig. 3.14(a), we plot the values for E_b, the binding energy on the defect-free surface, and in Fig. 3.14(b), we plot the values of E_b^v, the binding energy on the surface with an O-vacancy, both as a function of n, the number of atoms

in the cluster. For all the sizes considered, and both in the presence and absence of the defect, we find that that the binding energy is highest in the case of Pt clusters.

For the adsorption of the monomers on the defect-free surface, we see that all four single atoms – Pt, Pd, Au and Ag – prefer to be on top of an oxygen site on the defect-free MgO(100) surface.[26–28] The binding energy of the monomer to the surface decreases in the order Pt > Pd > Au > Ag. For the monomer adsorption at an O-vacancy site, comparing our results for Pt to previous results for Pd, we see that the binding energy of the monomer in both cases is greatly increased as compared to the binding energy of the monomer to the defect-free surface, and the binding is also found to be higher for the Pt monomer than for the Pd monomer.[26,27] Note that the binding energy of the Pt monomer at the F-center site is especially very high (∼6.09 eV); this suggests that the monomers will definitely be trapped at these F-center sites.

For the adsorption of the dimers on the defect-free surface, we see that Pt, Au and Ag prefer an upright geometry perpendicular to the surface on top of an oxygen site on the surface (see the D1 geometry in Fig. 3.5),[28] while the Pd dimer prefers to wet the surface and lie horizontally, binding to two surface O atoms (see the D2 geometry in Fig. 3.5).[26,27] The binding energy of the dimer to the surface decreases in the order Pt > Au > Pd > Ag. On comparing the adsorption of the Pt and Pd dimers at the O-vacancy site, we again find that the binding is higher in the case of Pt than for Pd. Pt dimers prefer the geometry shown in Figs. 3.7(a) and (b), where the dimer lies flat on the surface, with the center of the Pt-Pt bond directly above the O-vacancy site. The Pd dimer on the other hand was found to prefer a geometry similar to the D2 geometry, with the O-vacancy site beneath one of the Pd atoms.[26,27]

The lowest-energy adsorption geometry obtained by us for Pt_3 on MgO is the same as that found previously for Pd_3 and Ag_3 on MgO [see Tr1 geometry in Figs. 3.8(a) and (b)]. In this geometry, the trimer forms an upright triangle with two of the atoms binding to nearest neighbor O atoms on the surface.[26–28] The Au_3 cluster, however, is found to prefer the Tr2 geometry shown in Figs. 3.8(c) and (d), where the trimer forms an upright triangle with two of the atoms binding to second neighbor O atoms on the surface.[28] As

can be seen in Fig. 3.14(a), the binding energy of the trimer on the surface decreases in the order Pt > Pd > Au > Ag. For the Pd trimer, the authors of the earlier study also found another stable geometry with the three Pd atoms forming a horizontal triangle on the surface of MgO, with a binding energy of 1.75 eV;[27] however this geometry does not seem to be stable in the case of Pt_3, Au_3 or Ag_3. The adsorption geometry that we find for Pt_3 on MgO with an O-vacancy is similar to the geometry found for Pd_3 on MgO with an O-vacancy. The binding energy for Pd_3 is 2.69 eV/atom,[27] which is again much lower than the binding energy of 4.21 eV for Pt_3 on MgO with an O-vacancy.

For the adsorption of the tetramer, again we find that the binding energy of the cluster to the defect-free surface decreases in the order Pt > Pd > Au > Ag. The Pt and Pd tetramers are found to prefer the Tt1 geometry shown in Figs. 3.11(a) and (b),[26,27] while the Au and Ag tetramers are found to prefer a rhombus geometry with only two metal atoms interacting with the surface.[28] For the adsorption of the tetramer on the surface with O-vacancy, previous authors have found the same lowest-energy adsorption geometry for Pd_4 as for Pt_4, the binding energy is again lower for the Pd_4 cluster than for the Pt_4 cluster.

When comparing the binding energies of the clusters of Pt and Pd on the MgO surface in the absence and presence of O-vacancies, we see that in the presence of the O-vacancies, the binding energy of the cluster increases significantly. This suggests that it may be safe to assume that once a cluster is adsorbed at an O-vacancy site, it is strongly bound and hence can no longer diffuse over the surface and move to other sites.

We find that in all cases, the binding energy of the Pt clusters is much higher than that of other clusters, this already suggests that the diffusion barriers may be higher for Pt clusters than for clusters of the other metals considered here, and also that processes like sintering may be slower for Pt than for other clusters. We also find that similar to the case of Pt, clusters of Au and Ag also prefer geometries that do not wet the surface of the oxide. The Pd clusters, dimer and trimer however are found to have stable geometries in which the cluster wets the surface of the oxide and lies flat on the surface.

The comparison of the diffusion mechanisms and the barriers ΔE calculated for Pt

clusters on the MgO(100) surface, and those calculated by previous authors for Pd, Au and Ag clusters are listed in Table. 3.3.

	Diffusion Mechanism	Diffusion Barrier, ΔE (eV)			
		Pt	Pd (Refs. 26,27)	Au (Ref. 28)	Ag (Ref. 28)
M	Hopping	0.88	0.34	0.22	0.10
M_2	Cartwheeling (or leapfrog)	0.42	-	>0.87	0.22
	Partial Dissociation	-	0.43	-	-
	Hopping	0.66	-	0.62	0.25
M_3	Skating (or walking)	0.60	0.48	0.19	0.12
	Flipping	-	0.50	-	-
	Sliding	1.01	0.93	-	-
M_4	Rolling	0.81	0.41	0.42	0.55
	Walking	-	-	0.60	0.21

Table 3.3: *Comparing the diffusion mechanisms and barriers ΔE calculated for Pt and those known previously for Pd clusters[26,27], Au clusters and Ag clusters[28] adsorbed on the MgO(100) surface.*

If we compare the lowest diffusion barriers obtained for the different elements and for all cluster sizes considered, we see that for all the sizes except the dimer, the Pt clusters have the highest diffusion barriers as compared to Pd, Au and Ag. In the case of the dimer, we see that the Au dimer has the highest diffusion barrier (0.62 eV) compared to Pt, Pd and Ag.

The mechanism of diffusion via hopping for the monomers seems to be the same for all the elements, the diffusion barrier for this mechanism decreases in the order Pt > Pd > Au > Ag.

For the dimers, we see that Pt_2 and Ag_2 diffuse via a cartwheeling mechanism, while Pd_2 diffuses via a mechanism that involves the partial dissociation of the dimer, and Au_2 diffuses using a hopping mechanism similar to that of the monomer.

For the trimers, we see that the clusters of all the elements have the lowest diffusion barrier for the same mechanism: viz., the skating (or walking) mechanism. Here again we see that the diffusion barrier for this mechanism decreases in the order Pt > Pd > Au > Ag.

For the tetramers, we see that Pt_4, Pd_4 and Au_4 diffuse over the MgO surface via the rolling mechanism, while the Ag_4 cluster diffuses over the MgO surface via a walking

mechanism that is similar to the skating mechanism of the trimer.

3.3.5 Growth of Clusters on the MgO(100) surface

To study the growth of clusters on the defect-free MgO(100) surface and on the MgO(100) surface with O-vacancy sites, we first define two quantities, viz., the sintering energy and the trapping energy. We define the sintering energy, E_{sinter} as the energy gained when two clusters on the defect-free MgO(100) surface combine to form a larger cluster on the defect-free surface. It is given by the equation: $E_{sinter} = -E_{\mathrm{M}_n/\mathrm{MgO}} + E_{\mathrm{M}_{n-x}/\mathrm{MgO}} + E_{\mathrm{M}_x/\mathrm{MgO}}$; where M = Pt, Pd, Au or Ag, and all the terms on the right-hand-side of the equation are the total energies (from DFT) of the corresponding systems. Similarly, we define the trapping energy as the energy gained when a cluster adsorbed at an F-center on the surface traps a diffusing cluster and forms a larger cluster at the F-center. It is calculated using the equation: $E_{trap} = -E_{\mathrm{M}_n/\mathrm{MgO\text{-}F}} + E_{\mathrm{M}_{n-x}/\mathrm{MgO}} + E_{\mathrm{M}_x/\mathrm{MgO\text{-}F}}$. Using these energies and the diffusion barriers of the clusters on the MgO(100) surface, we will now attempt to generate possible pathways for the growth of these clusters on the MgO(100) surface. This should be helpful in giving us an idea about the sintering and growth processes of these clusters on the surface. From these energy pathways, we can also try to understand whether these clusters would energetically prefer to grow by the single-step growth process or the multi-step growth process.

Growth of a dimer on the defect-free MgO surface

In Fig. 3.15, we show the energetics involved in the formation of a dimer of (a) Pt, (b) Pd, (c) Au and (d) Ag on the surface of MgO(100). We assume that the growth starts from an initial state consisting of two monomers on the surface. One of the monomers diffuses on the surface by overcoming the diffusion barrier and combines with the other monomer to form a dimer on the surface. For all four elements, we see that the dimer formation is favorable, as the energy of the system is lowered after the formation of the dimer. The diffusion barrier for the monomer decreases in the order Pt > Pd > Au > Ag; the binding energy of the monomer on the surface decreases in the same order. Since the barrier for the monomer diffusion is highest in the case of Pt, we can say that this initial step in the

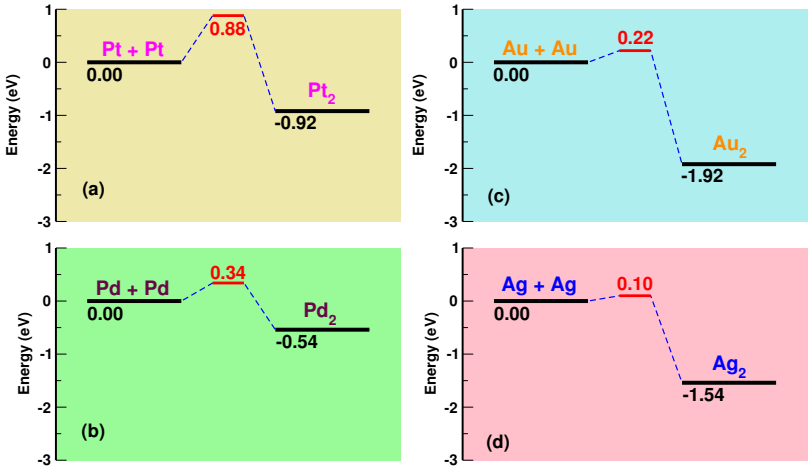

Figure 3.15: *Energetics for the growth of dimers on the defect-free MgO(100) surface for (a) Pt, (b) Pd, (c) Au and (d) Ag. In all cases, we start with two monomers on the surface. A monomer overcomes the diffusion barrier, diffuses over the surface and finally combines with the other monomer to form a dimer on the surface. We find that the monomer diffusion barrier is highest in the case of Pt. We also find that the energy gained by the system due to the formation of a dimer from two monomers on the surface is highest in the case of Au. Note that while the numbers in black are absolute values of the total energy of the system (with the energy of the initial state set equal to 0), the numbers in red are values of the barrier height for the forward reaction for that individual step. Values for Pd, Au and Ag are extracted from Refs. 26–28.*

growth process of these clusters is less likely to occur (in a given time interval) in the case of Pt than in the case of other clusters. If we compare the energy gained by the system due to the formation of a dimer from two monomers on the surface, we see that this energy gain is highest in the case of Au. This suggests that the tendency to form dimers will be highest in the case of Au monomers as compared to monomers of the other elements.

Growth of a trimer on the defect-free MgO surface

In Fig. 3.16, we show the energetics involved in the growth of a trimer or M_3 cluster on the surface of MgO(100), starting from three monomers on the surface. The growth pathways are shown for (a) Pt_3, (b) Pd_3, (c) Au_3 and (d) Ag_3. The formation of the trimer occurs in two consecutive steps: (i) M + M + M $\rightarrow$ M_2 + M, and (ii) M_2 + M $\rightarrow$ M_3. In the first of these steps, a monomer diffuses and coalesces with another monomer to form a dimer. The second step can occur along two paths: (A) either a monomer can diffuse and coalesce with a stationary dimer, or (B) a dimer can diffuse and coalesce with a stationary monomer. For Pt, the minimum energy pathway (i.e., the path with the lowest barriers) corresponds to path (B), while for Pd, Ag and Au, it corresponds to path (A). In the

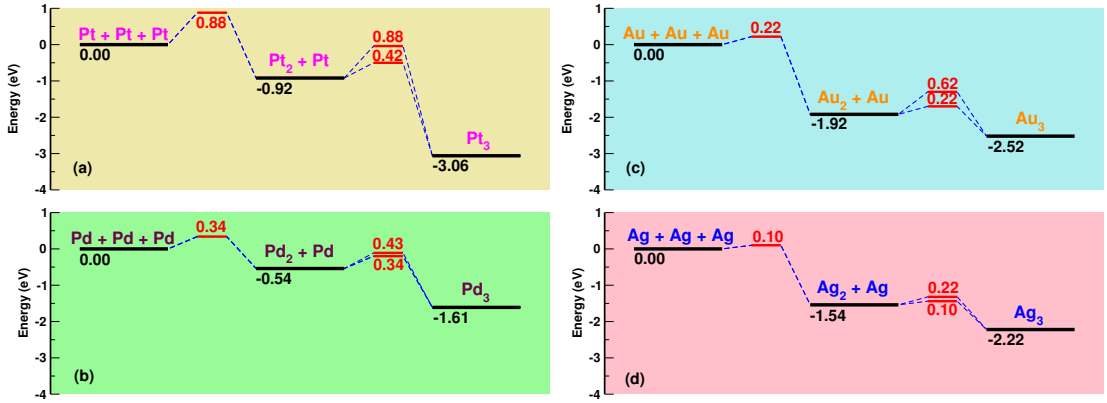

Figure 3.16: *The growth process pathways for the formation of the trimer on the surface for (a) Pt_3, (b) Pd_3, (c) Au_3 and (d) Ag_3. The growth process proceeds in two steps starting from three monomers on the surface, (i) $3M \rightarrow M_2 + M$, and (ii) $M_2 + M \rightarrow M_3$. The barriers for both the steps are higher in the case of Pt as compared to Pd, Au or Ag. Note that while the numbers in black are absolute values of the total energy of the system (with the energy of the initial state set equal to 0), the numbers in red are values of the barrier height for the forward reaction for that individual step. Values for Pd, Au and Ag are extracted from Refs. 26–28.*

growth of Pt clusters, we see that the rate limiting step is the monomer diffusion step, with a high barrier of 0.88 eV, leading to the formation of a dimer and a monomer on the surface.

The barriers for both the steps involved in the growth process of the trimer are higher for Pt than for Pd, Au or Ag. This suggests that sintering is kinetically more difficult to occur for Pt clusters than for other clusters. However, we also note that the energy gained by the system due to the formation of a trimer in this process is highest in the case of Pt. In other words, kinetics makes sintering least favorable for Pt, but thermodynamics makes sintering most favorable for Pt.

Growth of a tetramer on the defect-free MgO surface

In Fig. 3.17, we show the various possible pathways and the energetics involved in the growth of (a) Pt_4, (b) Pd_4, (c) Au_4 and (d) Ag_4 on the MgO(100) surface. We assume here also that the growth begins from four monomers adsorbed on the surface of MgO. The growth occurs in three steps and can occur via two possible pathways, viz., path (A): $4M \rightarrow M_2 + 2M \rightarrow M_3 + M \rightarrow M_4$ or path (B): $4M \rightarrow M_2 + 2M \rightarrow M_2 + M_2 \rightarrow M_4$. The difference in the two pathways is in the second intermediate state; in path (A), in this second intermediate state, the clusters on the surface prefer to be a trimer and

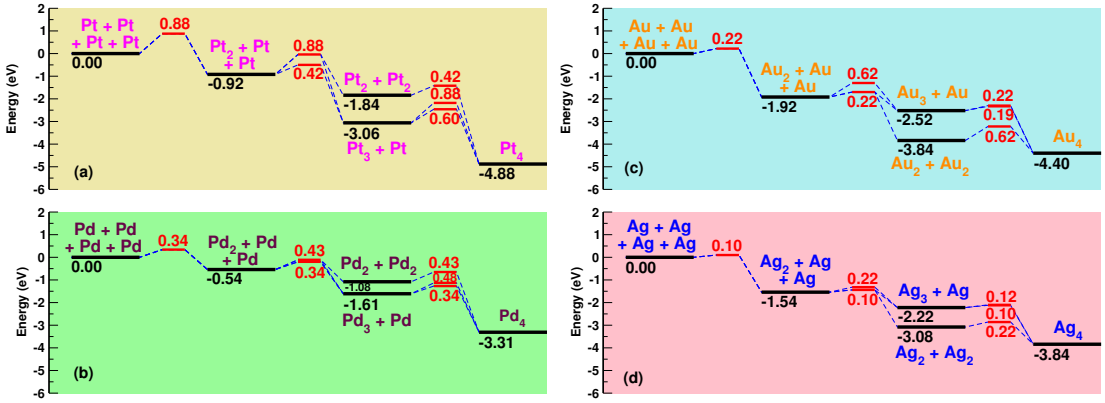

Figure 3.17: *Possible pathways for the growth of tetramers on the MgO(100) surface are shown here. (a)–(d) correspond to the growth of the Pt_4, Pd_4, Au_4 and Ag_4 cluster respectively. This is a three step process. For Pt_4 and Pd_4, we see that the energetically favored process is $4M \rightarrow M_2 + 2M \rightarrow M_3 + M \rightarrow M_4$, while for Au and Ag, we see that the energetically favored process is $4M \rightarrow M_2 + 2M \rightarrow M_2 + M_2 \rightarrow M_4$. Note that while the numbers in black are absolute values of the total energy of the system (with the energy of the initial state set equal to 0), the numbers in red are values of the barrier height for the forward reaction for that individual step. Values for Pd, Au and Ag are extracted from Refs. 26–28.*

a monomer, while in path (B), in this intermediate state, the clusters prefer to be two dimers. The configuration that can lower the energy of the system by a higher amount would be energetically preferred over the other. In the case of Pt and Pd, we can see that the clusters would energetically prefer path (A) for the growth of the tetramer, while Au and Ag prefer path (B). The energies that are in competition here are the sintering energies for the formation of the trimer and for the formation of the dimer. In the case of Pt and Pd, we see that the sintering energy for the formation of the trimer is much higher than the sintering energy for the formation of the dimer, while in the case of Au and Ag, the reverse is true.

For the growth of the Pt_4 cluster, we see that the rate limiting step is again the monomer diffusion. The growth proceeds via path (A). On looking carefully at the growth process diagram and noting the preferred minimum energy pathway, we can see that the barriers in the three steps in the process correspond to monomer diffusion, dimer diffusion and trimer diffusion respectively. This is because the dimers and trimers are more mobile on the surface than a monomer. In the first step, the monomer diffuses to form a dimer, in the second step, the dimer diffuses to combine with a monomer and forms a trimer and finally in the third step, the trimer diffuses to combine with a monomer and forms the

tetramer.

On comparing the growth process of Pt_4 with that of Pd_4, we can see a clear difference. In the minimum energy pathway for the growth of Pd_4 clusters, all the three barriers in the process correspond to the monomer diffusion. The cluster grows in size by the diffusion and addition of a monomer at every step in the growth process. From this observation, we can suggest that Pd clusters would prefer the single-step growth process.

Au and Ag tetramers seem to prefer path (B) for the growth, and the process of growth seem to be identical for these two elements. In the first step, a monomer diffuses to form a dimer on the surface. In the second step, another monomer diffuses to combine with yet another monomer to form a second dimer on the surface, and in the third step, the two dimers combine to form the tetramer with a barrier that corresponds to the dimer diffusion barrier. In the cases of Au and Ag, we can see that the clusters do not energetically prefer the single-step growth process.

From the thermodynamics, i.e., the net energy gain upon forming the tetramer, it should be most favorable to form the Pt tetramer, followed by Au_4, Ag_4 and Pd_4. However, if we were to look at the kinetics, i.e., look at the height of the barrier for the rate limiting step, then Pt_4 would be the slowest to form, followed by Au_4, Pd_4 and Ag_4; note that in coming to this conclusion we have ignored the prefactors involved. According to the Brønsted-Evans-Polanyi (BEP) relationship,[111,112] one would expect that a lower energy in the final state would correlate with a lower barrier. That is clearly not the case here, i.e., the BEP relationship does not hold. This is because the transition states do not resemble the final states.

Growth of clusters at an F-center site on the MgO surface

In Fig. 3.18, we show the pathways and energetics for the growth of a dimer [in (a) and (b)], a trimer [in (c) and (d)] and a tetramer [in (e) and (f)] at an F-center site on the MgO surface (M_2/F). We show our results for Pt [in (a), (c) and (e)], and compare with the diagrams generated for Pd [in (b), (d) and (f)] using the results from previous studies.[26,27] These diagrams were generated using the information from the sintering energy, trapping energy and the diffusion barriers of these clusters on the MgO surface. We assume that

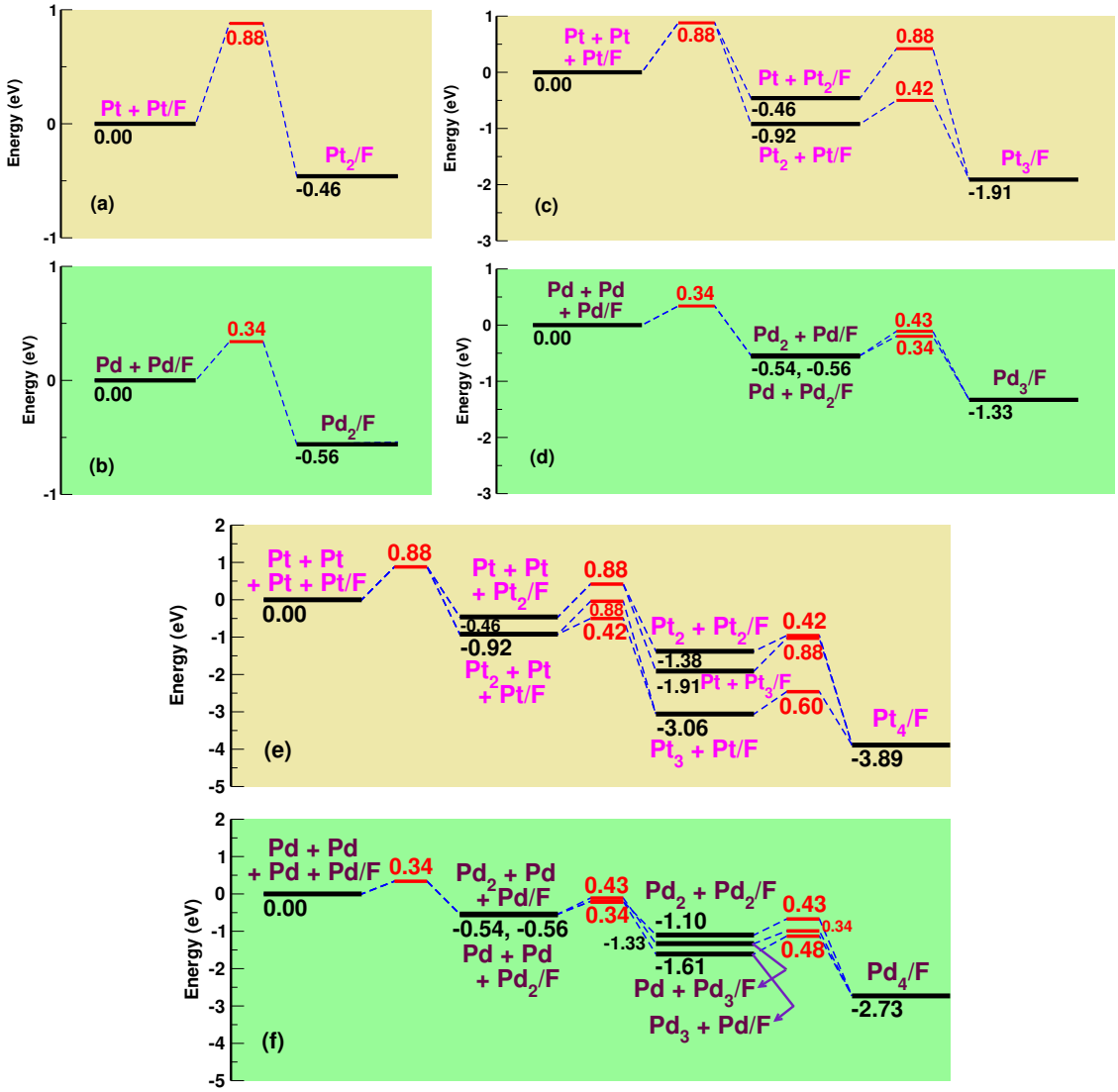

Figure 3.18: *The pathways for the growth for clusters at an F-center site on the MgO surface. The formation of (a) Pt_2/F, (b) Pd_2/F, (c) Pt_3/F, (d) Pd_3/F, (e) Pt_4/F and (f) Pd_4/F are shown here; all processes start from a monomer trapped at a F-center site and other monomers adsorbed on the defect free surface. Note that while the numbers in black are absolute values of the total energy of the system (with the energy of the initial state set equal to 0), the numbers in red are values of the barrier height for the forward reaction for that individual step. Values for Pd are extracted from Refs. 26,27.*

the growth begins with a monomer trapped at a F-center site and other monomers on the defect free surface.

We see the pathway for the growth of the dimer at the F-center in Figs. 3.18(a) and (b) for Pt_2/F and Pd_2/F respectively. We know from our calculations that the monomer binding energy at the F-center is really high for Pt (6.09 eV), we find that the binding of

a second monomer at the F-center is less favored by a lowering in energy of only 0.46 eV compared to the dimer formation energy on the defect-free surface which is 0.92 eV. It is interesting to note here that a previous study has reported contrasting results stating that the dimer formation at the defect site is not favorable, and has a trapping energy of -0.14 eV. This would mean that the two Pt atoms would rather be separated than form a bond when one of them is trapped in an O-vacancy.[96] We find, however, that the Pt dimer formation is possible but is energetically less favored than the formation of Pd_2/F. On comparing energetics for the growth of Pt_2 and Pd_2 at the F-center, we can see that the monomer diffusion barrier is higher for Pt than for Pd, and hence this first step may be less likely for Pt than for Pd.

The possible growth pathways for the growth of a trimer at the F-center are shown in Figs. 3.18(c) and (d) for Pt_3/F and Pd_3/F respectively. Two pathways possible here are path (A): 2M + M/F $\rightarrow$ M + M_2/F $\rightarrow$ M_3/F and path (B): 2M + M/F $\rightarrow$ M_2 + M/F $\rightarrow$ M_3/F. The minimum energy pathway for Pt clusters corresponds to path (B), the energy difference between the two paths is significant, with path (B) offering the lower energy pathway. For Pd clusters, however, the energy difference between the two pathways is negligible and both paths will compete. The reason for the Pt clusters preferring path (B) may be the especially high binding energy observed for the monomer at the F-center site, the Pt/F tends to remain as it is without adding more atoms to the F-center site. The rate limiting step in the growth of the Pt_3/F is the monomer diffusion step, and the barriers observed in both steps are higher for Pt than for Pd, suggesting that sintering should proceed more slowly for Pt than for Pd. For the growth of the Pt_3/F, the first step proceeds by monomer diffusion and the second step proceeds by dimer diffusion, whereas in the growth of the Pd_3/F, we see that both the steps in the process proceed by monomer diffusion.

The growth pathways for the growth of Pt_4/F and Pd_4/F are shown in Figs. 3.18(e) and (f) respectively. The diagrams generated are slightly more complicated than the earlier diagrams for the growth of the other clusters. Among the several pathways possible, we see that the minimum energy pathway for both Pt and Pd is 3M + M/F $\rightarrow$ M_2 + M +

$M/F \rightarrow M_3 + M/F \rightarrow M_4/F$.

For Pd, in the first intermediate state, the two possible situations $M_2 + M + M/F$ and $2M + M_2/F$ are almost degenerate, however, we believe that the cluster would prefer to be in the $M_2 + M + M/F$ state as this leads to the second intermediate state with the lowest energy and therefore stabilizes the system by a greater amount. In the minimum energy pathway for the growth of Pt_4/F, we see that the barriers in the three steps in the process correspond to that of monomer diffusion, dimer diffusion and trimer diffusion respectively. However, in the minimum energy pathway for the growth of Pd_4/F, we see that the barriers in the first two steps correspond to that of monomer diffusion and the barrier in the third step corresponds to that of trimer diffusion. The energy differences between the possible pathways are much higher for Pt than for Pd, which suggests that in the case of Pd, these paths may compete more easily.

For every step in the growth process, the barriers are higher for Pt than for Pd, this suggests that growth and sintering of Pt clusters should be slower than for Pd clusters. Pt clusters energetically prefer a multi-step growth process while in the case of Pd clusters, the pathways are very close in energy and hence both the multi-step growth process and the single-step growth process will compete.

On comparing the energy gained by the system due to the trapping of atoms at the F-center, we see that the formation of the dimer at the F-center is less favored for Pt than for Pd. However, the formation of the trimer and the tetramer at an F-center is more energetically favorable for Pt clusters than for Pd clusters. In both these cases, the system lowers its energy by a larger amount in the case of Pt clusters as compared to Pd clusters. This suggests that Pt atoms have a greater tendency than Pd to coalesce and form larger clusters when supported on the MgO surface.

3.4 Conclusions

We have studied the formation and diffusion of small Pt_n clusters, for $n = 1$–4, using DFT combined with the NEB method to calculate saddle point geometries and energies. We find that the surface O site is the most favorable site for the adsorption of Pt atoms, clusters of

other elements (studied by previous authors) also tend to favor adsorption geometries that allow binding to the O sites on the surface. We see a strong tendency of Pt clusters, starting from the dimer, not to wet the MgO surface but form upright adsorption geometries. This is similar to the adsorption geometries for Au and Ag obtained by previous authors, who have reported that Au and Ag clusters prefer not to wet the MgO surface.[28] Small Pd clusters (at least the dimer and trimer) on the other hand, are known to be stable in geometries where the cluster wets the MgO surface.[26,27]

We see that these small clusters of Pt diffuse on the surface of MgO in very interesting ways. We find a hopping mechanism for the monomers, a cartwheeling mechanism for the dimers, a skating mechanism for the trimer and a rolling mechanism for the tetramer. We have calculated the energetics for the diffusion pathways and determined the activation barriers using the NEB method. We find that the barriers involved in the diffusion of Pt clusters are higher than those of Pd, Au and Ag clusters, for all the sizes considered here, with the exception of the dimer.

A full study of the growth process would require that one also have access to the values of the Arrhenius prefactors for the diffusion processes of these clusters. However, already from the energetics of the barriers, we have attempted to gain an understanding about how the growth processes of Pt clusters may differ from that of Pd, Au and Ag clusters.

We have generated diagrams showing possible pathways for the growth of small M_n clusters on the MgO surface (M = Pt, Pd, Au and Ag) using our results for binding energies and diffusion barriers for Pt clusters, as well as the corresponding results (where available) of previous authors for clusters of Pd, Au and Ag.[26–28] We find that the rate limiting step in the growth of all Pt_n clusters considered here is the monomer diffusion, which has a high barrier of 0.88 eV. On comparing the minimum energy pathways and the barriers involved in every step in the growth process of clusters, we find that at every step the barrier is highest in the case of Pt than for Pd, Au or Ag. This suggests that kinetics will oppose the sintering of small Pt clusters, i.e., sintering should occur more slowly for Pt clusters on MgO, than for clusters of Pd, Au or Ag. At the same time, however, the energy lowering upon sintering is greatest for Pt, i.e., the thermodynamics

favors sintering of Pt clusters over that of the other elements (except for the two cases of dimer formation on the MgO surface, with or without an F-center present). Thus, in the limit of infinitely long timescales, Pt clusters are more likely to sinter than those of the other metals. This results in an interesting juxtaposition, with kinetics opposing, but thermodynamics favoring, the sintering of Pt clusters. Note that this also implies that the BEP relationship[111,112] does not hold for the processes studied in this chapter.

Considering the growth process of a M_n cluster on the defect-free surface, we find that Pt, Au and Ag clusters prefer the multi-step growth process, while Pd clusters prefer the single-step growth process. For the growth of a M_n cluster at a F-center site on the MgO surface, we find that Pt clusters prefer the multi-step growth process, while in the case of Pd clusters, the multi-step growth process and the single-step growth process compete, as the energy differences between the possible pathways are very small.

Finally, we note that in constructing the reaction pathways displayed in this chapter, we have made use of diffusion barriers that were calculated in the dilute limit, i.e., in the absence of other nearby clusters or defects on the surface. It remains to be seen whether this is a valid approximation, and whether the trends observed will change if diffusion barriers are calculated in more realistic scenarios.

Section B


SO, HOW'S THE DATA LOOKING?
UH...
GOOD.
HOW GOOD?
PRETTY GOOD.
IT'S WORTH ITS WEIGHT IN GOLD.
DATA DOESN'T WEIGH ANYTHING.
NO, BUT IT'S SHINY AND OVERPRICED.
JORGE CHAM © 2015
"PILED HIGHER AND DEEPER" BY JORGE CHAM
WWW.PHDCOMICS.COM

Chapter 4

Tuning the Morphology of Gold Clusters by Substrate Doping

4.1 Introduction

Bulk gold is famously inert. Its inert nature makes it a precious metal with popular use in jewellery and decorations. The factors responsible for making gold the noblest of all metals were laid out by Hammer and Nørskov, based on a study of the reactivity of extended transition metal surfaces like Ni, Cu, Pt and Au towards H_2 molecule adsorption: the factors being (i) the degree of filling of the antibonding states on adsorption, and (ii) the degree of the metal orbital overlap with the adsorbate.[39]

The surprising fact that, in marked contrast to extended Au systems, nano-sized Au can be a catalyst, was discovered in 1987 by Haruta *et al.*, who found that gold nanoparticles supported on semiconducting transition metal oxides could efficiently catalyze CO oxidation at low temperatures[14]. This drew a lot of attention towards these new and unrecognized properties of gold.

Soon there was a huge wave of research on Au nanoclusters, their catalytic activity and other potential applications. Au clusters were found to be oxidation resistant, making them effective oxidation catalysts,[113] they were found to have applications in detection technology for polynucleotides, replacing radioactive atoms and organic substituents,[114]

also ligand-stabilized Au nanoparticles were found to be of high interest for applications like nanoelectronics and biomedicine.[115] In addition to the oxidation of carbon monoxide, Au nanoparticles were found to also effectively catalyze several other reactions, e.g., the epoxidation of propene to propene oxide,[116] the water-gas shift reaction,[117] selective hydrogenation of unsaturated hydrocarbons,[118] and several liquid phase oxidation reactions relevant for the cosmetics and food industries.[119]

As the interest in Au nanoparticles for applications has grown, it has become important to more deeply understand the nature, stability and structure of these particles, as well as the role of the oxide substrate on which these clusters are commonly supported. The substrate helps to anchor the clusters, thereby prevent sintering; and in some cases, mediates a charge transfer between the substrate and the cluster, thereby changing the charge state of the cluster.[120] This has led to studies of how one can manipulate the clusters, the support, or their environment, so as to improve the desired properties in the cluster. For Au catalytic clusters, for example, this could be done by (i) changing the atomic structure, morphology or shape of the cluster,[7] (ii) changing the properties of the catalytic support like composition, structure or thickness,[8,11,31] or (iii) application of external electric fields.[36] It was found that changing any of these characteristics can alter the adsorption energy of the cluster on the support, the reactivity of chemical reactants towards the cluster, and also the reaction barriers involved in the catalytic reaction.

Given a size n of a cluster, there are several structural geometries possible, i.e., clusters may exist in several structural isomers. These isomers may be close in energy, but could, however, differ drastically in their mechanical, chemical, electronic and thermal properties. These differences may be particularly noticeable when the morphology of the cluster changes from a three-dimensional compact shape to a two-dimensional planar geometry. This is true not only when the clusters are in the gas phase but also when they are supported on an oxide substrate.

Another property that is very crucial in determining the activity or performance of a Au cluster catalyst is the charge state of the atoms in the cluster. For catalytic CO oxidation by Au clusters, it has been seen that while neutral clusters are only moderately

active, negatively charged clusters show excellent CO conversion yield and rates.[34] A combination of experimental and theoretical work has shown that Au clusters become negatively charged[9] (with the magnitude of the charge transfer dependent on the cluster geometry[121]), when placed on oxygen vacancies on an MgO substrate. Molecular oxygen that adsorbs on these negatively charged Au atoms gets activated to a superoxo or peroxo state, by the transfer of electrons from the Au to the O_2 $2\pi^*$ antibonding orbitals. The occupation in the antibonding orbitals makes the molecular bond weak and lowers the dissociation barrier for the O-O bond, thereby easing the pathway for CO oxidation.

An example of a cluster-support system where the interplay between cluster geometry, cluster-support interactions and charging effects has been extensively studied is the Au_{20} cluster on MgO(001).[10,11,31,35,36] The Au_{20} cluster has been found to be highly catalytically active owing to its extremely large HOMO-LUMO gap and high electron affinity.[33] It has a three-dimensional tetrahedral (T) structure in the gas phase [see Fig. 4.1(a)]. The cluster has been found to be extremely robust against distortions even when supported on pristine MgO, as well as defect-rich MgO with oxygen vacancies.[34] Another possible low-energy isomer for this cluster is the Au_{20} with a two-dimensional planar geometry (P) [see Fig. 4.1(b)]. Although it is known that the (T) cluster is more stable than the (P) cluster in the gas phase as well as when supported on MgO [see Figs. 4.1(c) and (d)], there is reason to believe that the (P) cluster, if it could be stabilized in some way, would be the better catalyst.[31]

Previous authors have shown that the planar arrangement can be stabilized in two ways. When Au_{20} clusters were supported on an ultra thin film of MgO (1–7 layers) on an underlying Mo(100) substrate, the two-dimensional (P) clusters were lowered in energy with respect to the otherwise stable (T) clusters with an energy difference of 3.3 eV, and the charge transfer to the (P) and (T) clusters was calculated to be 1.62 e and 1.06 e, respectively.[10] The increased contact area leading to larger accumulation of interfacial charge, and electrostatic interactions may be the source of the stabilization of the planar geometry. The second method proposed was to apply an external electric field of the order of 1 V/nm to a system of Au_{20} placed on MgO supported over Ag(100).[36] While these

methods of controlling the morphology of the cluster are of fundamental interest, they may not be very easy to implement in actual applications.

In this chapter, we present a third method which, we believe, is conceptually simple yet experimentally and technologically feasible, viz., doping the oxide substrate with electron donor impurity atoms. We first demonstrate that this method achieves the same goal of flipping the stability of the Au cluster towards favoring the planar arrangement of atoms, by considering a model system: Au_{20} supported on Al-doped MgO.[37] Soon after our work on this system was published, there was an experimental validation for our idea, where they showed that the morphology of Au clusters deposited on CaO flipped from three-dimensional to planar when the CaO was doped with the electron donor Mo.[38,122] In this chapter, we also present results of our calculations on Au_{20} supported on Mo-doped CaO, confirming the experimental finding. Finally, to confirm that this technique of substrate doping will be effective for Au clusters of many sizes, we also present results of calculations on an Au atom, Au dimer and Au trimer supported on undoped and Al-doped MgO, and show how the preferred adsorption geometries of these clusters on the substrate change on doping.

Some of the results presented in this chapter were published by us in Ref. 37.

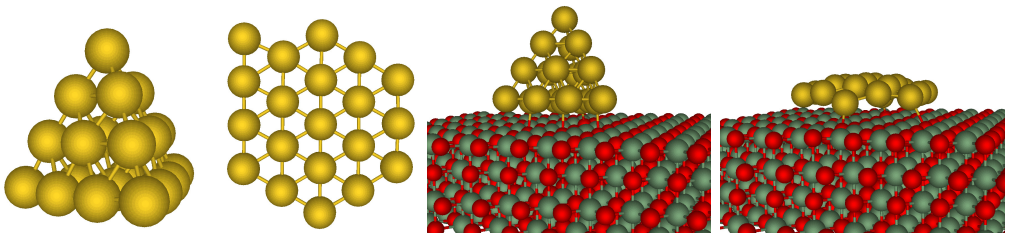

Figure 4.1: *The optimized geometries for (a) Au_{20}(T), (b) Au_{20}(P), both in the gas phase; (c) Au_{20}(T)/MgO and (d) Au_{20}(P)/MgO. The yellow, grey and red spheres represent Au, Mg and O atoms respectively. We confirm previously known results[10,31] and find that, in the gas phase the (T) cluster is more stable than the (P) cluster by 1.52 eV, and when supported on undoped MgO, the (T) cluster continues to be more stable than the (P) cluster with an energy difference of 0.60 eV.*

4.2 Au_{20} supported on undoped and Al-doped MgO

4.2.1 Methods

We have employed spin-polarized density functional theory (DFT), as implemented in the Quantum ESPRESSO package,[50] to study the model system of Au 20-atom clusters supported on undoped and doped MgO. The Kohn-Sham wavefunctions[20] were expanded in a plane-wave basis set with a plane-wave energy cut off of 30 Ry and a charge density cut off of 240 Ry. For the self consistent calculations, convergence was deemed to be achieved when the estimated energy error was less than 10^{-8} Ry. The exchange-correlation interactions were treated with the generalized gradient approximation (GGA) (Perdew-Wang 91).[49] The pseudopotentials used to approximate the interactions between the ionic cores and the valence electrons were ultrasoft (Vanderbilt) pseudopotentials.[63] Scalar relativistic pseudopotentials were used for Au and Mo. Convergence for calculations with the MgO (CaO) substrate was hastened by smearing the occupations using Marzari-Vanderbilt cold smearing[71] with a broadening width of 0.068 eV (0.136 eV).

All atomic coordinates were relaxed, using forces calculated by the Hellmann-Feynman theorem.[72] The convergence criterion for the ionic minimization was that all components of the forces on the atoms had to be less than 10^{-3} Ry/bohr and the energy difference between two consecutive ionic steps had to be less than 10^{-4} Ry.

MgO has a face centered cubic (FCC) crystal system. The MgO(001) surface was considered as the support for the gold cluster adsorption. This surface forms a square lattice with a two-atom basis. The properties of bulk MgO and aluminium-doped MgO were compared using a $3 \times 3 \times 3$ cell. The bulk doped MgO was created by replacing one of the 27 Mg atoms in this cell by Al, resulting in a dopant concentration of 3.7%. The calculations on the 20-atom clusters of gold were carried out with the Makov-Payne correction[123]. Calculations on gas phase (T) and (P) clusters were performed using a cubical box of side 16.9 Å and a cuboid of size $20.1 \times 20.1 \times 9.5$ Å respectively. The calculations for the Au_{20} cluster adsorbed on the MgO (doped and undoped) were carried out using a slab comprised of four substrate layers, with a 6×6 surface unit cell, so that we have 36 atoms of Mg and 36 atoms of O per layer. A vacuum of thickness $\sim$14 Å in

the [001] direction was used for these calculations. k-point sampling for the cells with the clusters was done only at the zone center, whereas the sampling for the clean surface of undoped MgO, with a 3×3 surface unit cell, was done using a $2 \times 2 \times 1$ Monkhorst-Pack mesh[67].

4.2.2 Results

4.2.2.1 Au_{20} clusters in gas phase and supported on pristine MgO

In order to validate our computational approach, we have first performed calculations on previously studied systems. Our results confirm that in the gas phase and on a four-layer thick MgO(001) substrate, the (T) morphology is favored over (P), by 1.53 eV and 0.60 eV respectively (see Fig. 4.1). When supported on MgO, we find that the Au(T) cluster acquires a negative charge of 0.60 e, while the Au(P) cluster acquires a negative charge of 0.91 e. These results are in good agreement with those of previous authors[31].

4.2.2.2 Effect of doping on the oxide substrate

Replacing a divalent Mg atom by a trivalent Al atom results in the delocalization of the extra electron of Al in the system, and causes the Fermi level of the system to shift to the conduction band for a sufficiently high doping concentration (see Fig. 4.2).

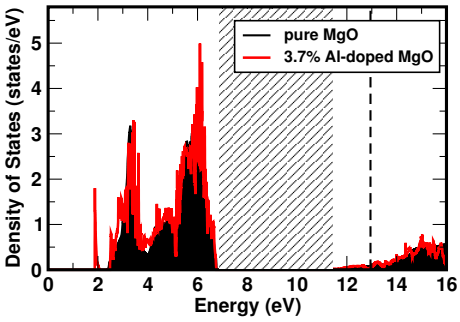

Figure 4.2: *Density of states of pristine MgO (in black) and 3.7% Al-doped MgO (in red). The black hatched area is the forbidden gap of the MgO insulator; this is underestimated with respect to experiments due to DFT errors. The dashed line is the position of the Fermi level of 3.7% Al-doped MgO, which is now in the conduction band; Al-doped MgO is no longer an insulator.*

Such a doping of MgO with an electron donor also lowers the work function of the system. For 2.78% Al-doped MgO(001), we calculate the work function to be 1.81 eV.

One may then speculate that the system would release its electrons more easily to Au clusters than pure MgO, and the clusters would gain a higher negative charge, possibly stabilizing the (P) cluster over the (T) cluster; below we demonstrate that this is indeed what happens.

4.2.2.3 Effect of substrate doping on the supported Au_{20} clusters

We now consider possible morphologies of an Au_{20} cluster placed on an MgO(001) substrate where some of the Mg atoms have been substituted with Al atoms. We consider two cases, Al replacing a Mg atom in (i) the second layer and (ii) the third layer from the surface. We have considered three doping concentrations in each of these cases, viz., 0.69%, 1.39% and 2.78%. We also consider two possible lateral positions of the Al atom in the 0.69% Al-doped MgO, one in which the single dopant Al atom is directly below the Au cluster, and another in which the Al atom is positioned away from the cluster.

Our results for the difference in energies between the (P) and (T) supported clusters, and the charge transferred from the substrate to the clusters, are summarized in Figs. 4.3(a) and (b) respectively.

From Fig. 4.3(a), we see that the stability of the planar cluster over the tetrahedral cluster increases linearly as a function of the doping concentration in the substrate. We find that this stability is independent of the dopant position: i.e., it does not depend on whether the dopant Al atom is in the second or the third layer from the surface, or whether the Al atom is directly below the cluster or away from it; the stability depends only on the dopant concentration. Most strikingly, we find that for all the doping concentrations and configurations considered by us, the planar arrangement (P) is significantly favored over the tetrahedral arrangement (T). The least concentration of Al required to flip the stability of the cluster from the tetrahedral geometry to the planar geometry is around 0.4%.

The adsorption energy (E_b^{Au}) of the cluster to the substrate is calculated as the energy required to separate the supported cluster into the bare substrate and the isolated cluster

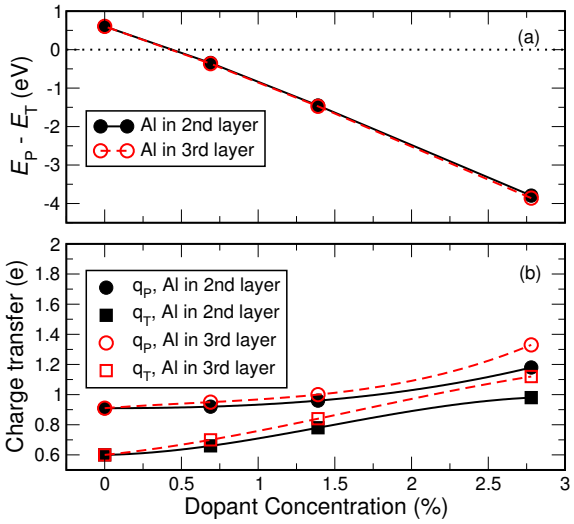

Figure 4.3: *Trends in energetics and charge transfer as a function of substrate doping: (a) As the Al-doping concentration in the MgO substrate is increased, we see that the planar structure (P) of Au_{20} becomes progressively more favored over the tetrahedral structure (T); E_P and E_T are the total energies of the supported clusters (P) and (T) respectively. (b) Charge transfer values q_P and q_T for (P) and (T) increase monotonically as the doping concentration is increased. Black/red symbols correspond to data where the dopant atoms are in the second/third layer from the surface. In all cases the Al atom is directly below the cluster. Reprinted with permission from Ref. 37. ©(2011) American Chemical Society.*

in the gas phase. It is computed as $E_b^{\mathrm{Au}}(\mathrm{P/T})$ = -{E[$\mathrm{Au_{20}}$(P/T) on Al-doped MgO] - E[$\mathrm{Au_{20}}$(P/T)] - E(Al-doped MgO)}, where E is the total energy (from DFT) of the corresponding system. Our results for these values are listed in Table 4.1. With increasing doping concentration in the MgO substrate, we observe an increase in E_b^{Au}. This is slightly reduced when the dopant atom is moved from the second to the third layer, or from below the cluster to away from the cluster.

In Fig. 4.4, we have plotted isosurfaces of the charge transfer that occurs when the (P) and (T) $\mathrm{Au_{20}}$ clusters are placed upon the substrate, for the particular case where the Al concentration is 2.78% (i.e., 4 of the 36 Mg atoms in the second layer of the substrate have been replaced by Al). Magenta and blue lobes represent charge accumulation and charge depletion, respectively. We draw particular attention to the layer of electronic charge that is accumulated at the interface, between the cluster and the substrate.

For the (T) case, we see that there is a depletion of electronic charge from the substrate and an accumulation of charge within the cluster, mainly at the three corner sites at the interface between the cluster and the substrate, while in the (P) case, there is a larger

Al position	Conc. (%)	E_b^{Au}(P) (eV)	E_b^{Au}(T) (eV)
II layer	2.78	12.17	6.92
	1.39	7.42	4.44
	0.69 (below)	5.12	3.26
	0.69 (away)	4.94	3.07
III layer	2.78	11.65	6.27
	1.39	7.22	4.23
	0.69 (below)	5.01	3.12
	0.69 (away)	4.92	3.06
pure MgO	0	2.85	1.94

Table 4.1: *Calculated values of adsorption energies, $E_b^{Au}(P)$ and $E_b^{Au}(T)$ of planar and tetrahedral Au_{20} clusters, respectively, for different positions and concentrations (Conc.) of dopant Al atoms in Al-doped MgO substrate. Reprinted with permission from Ref. 37. ©(2011) American Chemical Society.*

depletion of charge from the substrate, and a larger accumulation of charge both within the Au layer and in between the Au and the substrate. We also wish to point out that the sites of charge accumulation on the cluster are believed to be the active sites for oxidation reactions, where the oxygen molecules preferentially adsorb. Comparing the regions of charge accumulation on both the clusters, [the three vertices for (T) and the peripheral atoms for (P)], we can say that the (P) cluster may have more active sites than (T), and may therefore prove to be more catalytically active for oxidation reactions. We note that none of the features discussed in the above paragraph are very sensitive to the position of the Al atom(s).

The layer of electronic charge accumulated at the interface can also be seen in panels (c) and (f) of Fig. 4.4, where we show the planar integral of the charge transfer vs. z, the coordinate normal to the surface. The integral of the charge accumulated from the interface between the cluster and the substrate up to the vacuum gives the total charge acquired by the cluster from the substrate.

In Fig. 4.3(b), where we have plotted these charge transfer values, as a function of the dopant concentration, we see that the electron transfer from the substrate to the cluster increases monotonically as the doping concentration in the substrate increases. We also find that in all cases, the charge transferred to the planar cluster is higher than the charge transferred to the tetrahedral cluster.

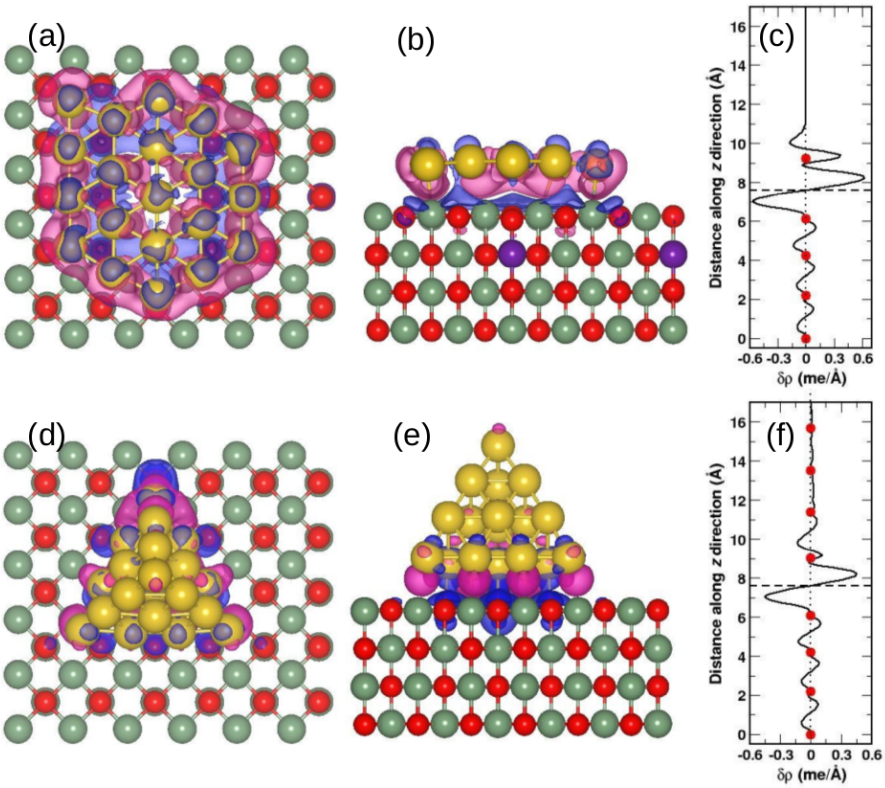

Figure 4.4: *The charge transfer isosurfaces for the (a) top view, (b) side view of Au_{20} (P), and (d) top view, (e) side view of Au_{20} (T), all deposited on 2.78% Al-doped MgO. The green, red, purple and yellow spheres represent Mg, O, Al and Au atoms respectively. The blue and magenta lobes show the regions of charge depletion and charge accumulation respectively. The isosurfaces shown correspond to 0.001 e/Å^3. The planar integral of the charge difference along the z direction for (c) Au_{20}(P)/Al-doped MgO and (f) Au_{20}(T)/Al-doped MgO are shown. The red dots in (c) and (f) show the average atomic positions along the z direction and are aligned to the atoms in the side view of the isosurface plots. Reprinted (adapted) with permission from Ref. 37. ©(2011) American Chemical Society.*

In summary, we have demonstrated theoretically that doping an MgO substrate with Al atoms stabilizes a planar Au_{20} isomer over the tetrahedral isomer. We have shown that the stabilization energy as well as the charge transferred from the substrate to the cluster does not depend on the dopant position, but depend monotonically on the dopant concentration. Substrate doping can be used to tune the morphology of supported Au clusters; in the next chapter, we investigate whether such substrate doping also affects the reactivity of these supported Au clusters.

4.3 Au_{20} supported on undoped and Mo-doped CaO

The method that we have suggested above, of substrate doping for controlling the morphology of Au clusters, was subsequently experimentally verified,[38,122] using Mo (Cr) as the electron donor, and CaO (MgO) as the oxide substrate.

The doped substrate was prepared by chemical vapor deposition by adding 2 atm% Mo to the Ca/O vapor and oxide films of 60 monolayer thickness were grown. It was prepared such that the topmost layers are free of Mo, to prevent Mo segregation to the surface. 0.7 ML Au was deposited on these films to form the metal particles on the surface; they form particles of approximate size 10 × 10 nm^2. In Figs. 4.5(a) and (b), we show the STM images of the Au particles on the undoped CaO surface and Mo-doped CaO surface, respectively. On pristine CaO surfaces, the authors find that the Au particles adopt pronounced three-dimensional shapes with a height to diameter ratio of 0.35±0.10 [see Fig. 4.5(a)]. On the doped substrate, however, the authors find that these particles grow only in two-dimensional arrangements with a height to diameter ratio of 0.07±0.02 [see Fig. 4.5(b)].[38] These experiments provide dramatic evidence that the method we proposed and verified theoretically, actually works in practice. We also note that the clusters formed in the experiment are significantly larger in size than the 20-atom Au clusters that we used for our calculations, thus suggesting that our ideas are not restricted to this cluster size or system alone.

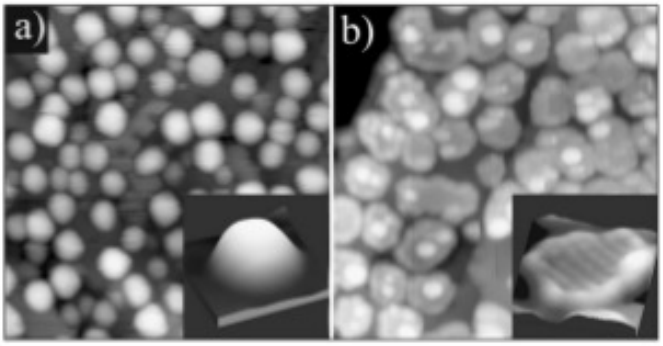

Figure 4.5: *STM images of Au clusters on (a) pristine and (b) Mo-doped CaO. The insets show close-ups of two characteristic particles of approximate size 10 × 10 nm^2. Note the three-dimensional cluster geometry for Au clusters on pristine CaO in (a), and the flat planar arrangement of atoms in the cluster when supported on Mo-doped CaO in (b). Reproduced with permission from Ref. 38.*

Motivated by these experiments, we have carried out calculations on the Au_{20} (P) and (T) clusters supported on undoped and Mo-doped CaO. These calculations help us to confirm the experimental results, and also to understand the difference between the two substrates, Al-doped MgO and Mo-doped CaO. The main difference is the dopant atom. Al prefers the fixed oxidation state of +3, while Mo is a transition metal that has variable oxidation states; in Mo-doped CaO, to maintain charge neutrality, the Mo atom takes the oxidation state +2, however, on placing Au particles on the substrate, the Mo atom can attain higher oxidation states like +4 and +6. This suggests that when Au particles are placed on Mo-doped CaO, they can gain more negative charge than when placed on Al-doped CaO; this is indeed what we find from our results below.

4.3.1 Methods

Similar to MgO, CaO also has a face centered cubic (FCC) crystal system. The CaO(001) surface was considered as the support for the gold cluster adsorption. The properties of bulk CaO and Mo-doped CaO were compared using a $3 \times 3 \times 3$ cell. The bulk doped CaO was created by replacing one of the 27 Ca atoms by Mo, resulting in a dopant concentration of 3.7%. The calculations for the Au_{20} cluster adsorbed on the CaO (doped and undoped) were carried out on a 6×6 surface unit cell of 4 layers, with 36 atoms of Ca and 36 atoms of O per layer. A vacuum of thickness $\sim$14 Å in the [001] direction was used for these calculations. k-point sampling for the cells with the clusters was done only at the zone center.

All the other calculation details are identical to those employed for Au_{20}/Al-doped MgO.

4.3.2 Results

4.3.2.1 Au_{20} supported on pristine CaO

When Au_{20} (T) and (P) clusters are supported on pristine CaO [see Figs. 4.7(a) and (b)], we find that the (T) cluster is more stable than the (P) cluster only by a small energy difference of 0.07 eV compared to when these clusters are supported on pristine MgO

(0.60 eV). We see a charge transfer of 0.87 e and 1.24 e from the CaO substrate to the (T) and (P) cluster respectively. The calculated values for the charge transfer from the CaO substrate are higher than the charge transfer values calculated for the Au(T) and Au(P) clusters deposited on pristine MgO (0.60 e and 0.91 e respectively). Recall that for Au clusters on MgO, as the doping was increased, the charge transferred to both the (T) and (P) clusters was increased, and the (T) cluster became progressively more destabilized with respect to the (P) cluster. Now, on CaO, we find that the charge transferred is greater than on MgO, this may be why the energy difference between the (T) and (P) isomers is much less than it was on MgO.

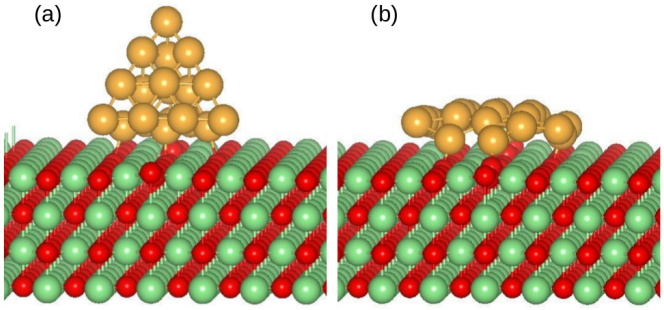

Figure 4.6: *The optimized geometries obtained for (a) Au(T)/CaO and (b) Au(P)/CaO. The light green, red and yellow spheres represent the Ca, O and Au atoms respectively. When placed on CaO, the (T) cluster is favored over the (P) cluster by 0.07 eV.*

4.3.2.2 Effect of Mo-doping on the CaO substrate

CaO is an insulator. The addition of Mo atoms in the system gives rise to defect states in the energy gap. The Fermi level of the doped system lies at one of these defect states, and the system is no longer an insulator. This suggests that when Au clusters are placed over the substrate, the substrate may more easily lend its electrons to the Au cluster making it negatively charged. Note that on adding Mo atoms to the CaO substrate, the system becomes magnetic.

4.3.2.3 Effect of substrate doping on supported Au_{20} clusters

We consider the same two possible morphologies of the Au_{20} cluster, (T) and (P) [that we had already considered in the case of the MgO substrate above], placed on CaO(001)

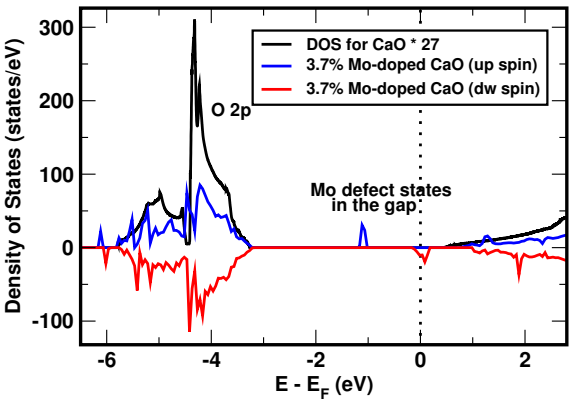

Figure 4.7: *The densities of states (DOS) of bulk CaO and 3.7% Mo-doped CaO. Since Mo-doped CaO is magnetic in nature, the DOS of the up-spin electrons (in blue) and down-spin electrons (in red) are shown separately. The dotted vertical line shows the position of the Fermi level of the Mo-doped CaO system. Note that the band gap of CaO is underestimated as is typical of a conventional DFT calculation.*

where some of the Ca atoms have been substituted with Mo atoms. Since, for MgO, we had already established that the dopant position does not matter significantly, here we restrict ourselves to examining a smaller number of configurations than we did for the case of the MgO substrate. Accordingly, we consider two doping concentrations: 0.69% and 2.78%; in all systems, Mo replaces the appropriate number of Ca atoms in the third layer from the surface. For 0.69% doping concentration, we consider the dopant atom to be directly below the Au_{20} cluster.

Already at 0.69%, we find that the (P) cluster is favored over the (T) cluster by the rather large amount of 2.32 eV. The charge transfer from the substrate to the (T) and (P) cluster is calculated to be 0.82 e and 1.22 e respectively. At 2.78% doping concentration however, we find that the (P) cluster is favored over the (T) cluster by 0.44 eV. On increasing the doping concentration from 0.69% to 2.78%, the electron transfer from the substrate to the Au(T) and Au(P) cluster increases to 1.19 e and 1.96 e, respectively. While the Au(T)/2.78% Mo-doped CaO system is found to be magnetic, Au(P)/2.78% Mo-doped CaO is found to be non-magnetic. This loss of magnetic moment may be the reason for the reduced energy difference between (T) and (P) when supported on 2.78% Mo-doped CaO.

The adsorption energy (E_b^{Au}) of the cluster on the substrate is computed as E_b^{Au}(P/T)

= E[Au_{20}(P/T) on Mo-doped CaO] - E[Au_{20}(P/T)] - E(Mo-doped CaO), where E is the total energy from DFT of the corresponding system. These values, along with the magnetic moments of the systems and the charge transferred from the substrate to the cluster, are listed in Table 4.2. With increasing concentration of the dopant atom in the CaO substrate, we observe an increase in the adsorption energy for both the (T) and (P) clusters. While (T) is favored on undoped CaO, (P) is favored on Mo-doped CaO. The addition of Mo atoms to CaO makes the system magnetic, Au_{20}(P/T)/0.69% Mo-doped CaO and Au(T)/2.78% Mo-doped CaO are also magnetic, while Au(P)/2.78% Mo-doped CaO is found to be non-magnetic. The charge transfer from the substrate to the cluster is slightly lowered on going from the pristine CaO substrate to the 0.69% Mo-doped CaO substrate, but on increasing the doping concentration further to 2.78%, the charge transfer to the cluster increases. The (P) cluster always gains more negative charge than the (T) cluster on the substrate.

Mo doping conc. (%)	E_b^{Au} (eV)		Mag. mom. (μ_B/Mo atom)		$q(Au_{20})$ (e)	
	Au(P)	Au(T)	Au(P)	Au(T)	Au(P)	Au(T)
2.78	8.83	6.87	0.00	3.00	1.96	1.19
0.69 (below)	7.67	3.81	1.19	2.32	1.22	0.82
0	3.58	2.13	0.00	0.00	1.24	0.87

Table 4.2: *Calculated values of adsorption energies, the magnetic moments of the system Au_{20}/Mo-doped CaO and the charge gained by the planar and tetrahedral Au_{20} clusters due to the electron transfer from the substrate to the cluster, for different concentrations of dopant Mo atoms in Mo-doped CaO substrate.*

In Fig. 4.8, we have plotted isosurfaces of the charge transfer that occurs when the (P) and (T) Au_{20} clusters are placed upon the CaO substrate, for the particular case where the Mo doping concentration is 0.69% (i.e., one of the Ca atoms in the third layer of the substrate has been replaced by Mo). We draw attention again to the layer of electronic charge that is accumulated at the interface between the cluster and the substrate. This can be clearly seen in the charge transfer plots as well as in the plots of the planar integral of the charge difference along the z direction in Figs. 4.8(c) and (f). These plots look very similar to the charge transfer plots obtained when Au_{20} clusters were placed on Al-doped MgO, except for one notable difference. We can clearly see a region of electron

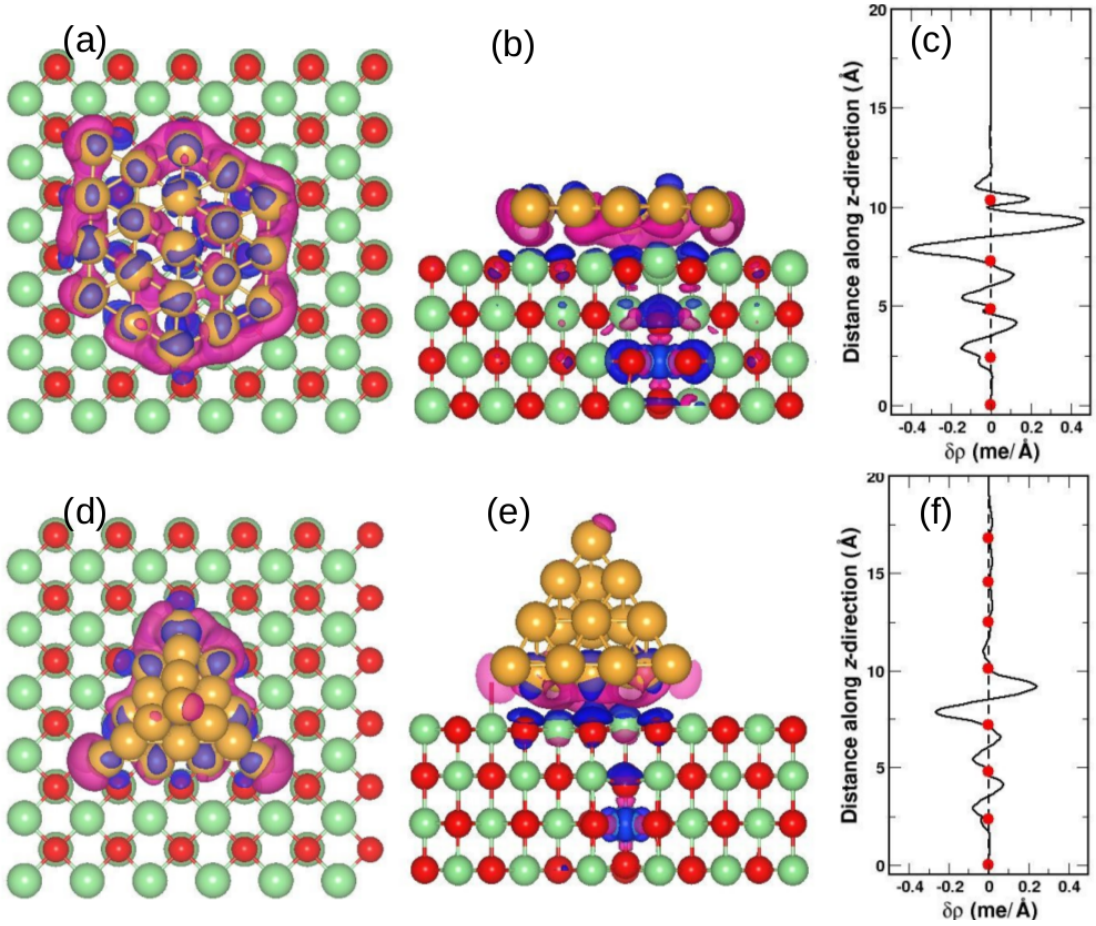

Figure 4.8: *The charge transfer isosurfaces for the (a) top view, (b) side view of $Au_{20}(P)$, and (d) top view, (e) side view of $Au_{20}(T)$ over 0.69% Mo-doped CaO. The light green, red and yellow spheres represent Ca, O and Au atoms respectively. The blue and pink isosurfaces show the regions of charge depletion and charge accumulation respectively. In (b) and (e), the Mo dopant atom (in the third layer from the surface) is not visible as it is covered by a blue lobe. The isosurfaces shown correspond to 0.001 e/Å^3. The planar integral of the charge difference along the z direction for (c) $Au_{20}(P)$/Mo-doped CaO and (f) $Au_{20}(T)$/Mo-doped CaO are shown. The red dots show the average atomic positions along the z direction.*

depletion in the third layer from the surface exactly at the position of the Mo atom. This suggests that the Mo atom loses electrons *after* the deposition of the Au clusters on the substrate. This is in accordance with statements by previous authors,[38,122] who attribute the performance of Mo-doped CaO towards stabilizing the planar cluster, to the ability of the Mo atoms to evolve from a +2 oxidation state in clean CaO to a +6 oxidation state on depositing Au clusters on the doped surface. This phenomenon has also been rationalized and interpreted in terms of redox chemistry.[124] This may not be the case when we use

dopants like Al (Cr) which can be stable only in the +3 (+2 and +3) oxidation state (states). It has been suggested that thes electrons (released by the Al or Cr dopant) could be sucked into cationic vacancies or defects in the oxide, and no charge transfer to Au clusters may actually take place. Therefore, the system of Mo-doped CaO may be the better candidate compared to Al(Cr)-doped oxides for stabilizing two-dimensional planar shapes of Au particles deposited on the substrate.[38,122]

We have calculated the values of charge transfer from the substrate to the cluster by integrating the plots in Figs. 4.8(c) and (f) from the interface between the cluster and the substrate to the vacuum; these values are tabulated in Table 4.2. In all cases considered, for Au(P)/Mo-doped CaO, we see a greater depletion of charge from the substrate and a larger accumulation of charge in the Au layer and at the interface, as compared to Au(T)/Mo-doped CaO.

As was the case in Al-doped MgO, here again we see that the regions of charge accumulation on the (T) cluster are the three vertices at the interface, with a slight accumulation of electrons at the apex atom, and the regions of charge accumulation on the (P) cluster are distributed along the peripheral atoms of the cluster.

4.4 Small Au clusters supported on undoped and Al-doped MgO

As a supplement to our detailed investigation above on Au_{20} clusters, in order to investigate whether and how the method of substrate doping affects the adsorption of small Au clusters on oxide substrates, we have done calculations on an Au atom, an Au dimer and an Au trimer adsorbed on the surface of undoped and Al-doped MgO. For these calculations, we choose one value of doping concentration, viz., 2.78%, where one of the Mg atoms in a four-layer slab with a 3×3 surface unit cell was replaced by an Al atom.

4.4.1 Methods

The calculations on the Au_n clusters in the gas phase were done in a cubical box of side 15 Å. The calculations for Au_n adsorbed on the MgO (doped and undoped) were carried out

on a 3×3 surface unit cell of four layers, with nine atoms of Mg and nine atoms of O per layer. A vacuum of thickness ∼14 Å in the [001] direction was used for these calculations. k-point sampling for the substrate cells with and without the clusters was done using a $2 \times 2 \times 1$ Monkhorst-Pack mesh[67].

All the other calculation details are identical to those employed for Au_{20}/Al-doped MgO.

4.4.2 Results

4.4.2.1 Au_n clusters in gas phase

The binding energy of an Au_n cluster, the energy for breaking the cluster into Au atoms, was calculated using the formula: $BE(Au_n) = -\frac{1}{n}[E(Au_n) - nE(Au)]$, where E is the total energy of the corresponding system.

For the Au_2 cluster, we calculate a binding energy of 1.36 eV/atom, with an optimized Au-Au bond distance of 2.50 Å [see Fig. 4.9(a)]. For the Au_3 cluster, we considered two possible geometries: a triangular geometry and a linear geometry [see Figs. 4.9(b) and (c)]. The binding energies obtained by us for the triangular and linear geometries are 1.366 eV/atom and 1.359 eV/atom respectively. The triangular geometry is favored over the linear geometry by 0.02 eV. We find that Au_3 forms an isosceles triangle with two of the sides having Au-Au distance 2.65 Å and the third side having Au-Au distance 2.64 Å. In the less stable linear geometry, the optimized Au-Au distances were found to be 2.56 Å. The geometries for Au_2 and Au_3 are in good agreement with previous DFT results,[125,126] however one study reports that the linear geometry for Au_3 is lower in energy by 0.04 eV compared to the triangular geometry.[126]

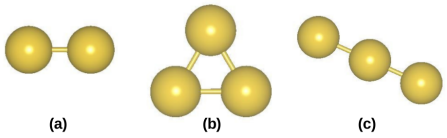

Figure 4.9: *The optimized geometries obtained for (a) Au_2, (b) triangular Au_3 and (c) linear Au_3. For the Au_3 cluster, the triangular geometry is found to be more stable than the linear geometry by 0.02 eV.*

4.4.2.2 Effect of substrate doping on supported Au_n clusters

Substrate doping is found to have a substantial effect on the preferred adsorption site and the adsorption geometries of small Au_n clusters. The adsorption energy of a cluster to the substrate is computed by the equation: $E_b^{Au_n}$ = -{E(Au_n on Al-doped MgO) - E(Au_n) - E(Al-doped MgO)}.

For a single Au atom deposited on pristine MgO, we find that the Au atom preferentially adsorbs atop a surface O atom [see Fig. 4.10(a)] with an adsorption energy of 0.96 eV. This is in fairly good agreement with previous results.[127] This adsorption geometry is lower in energy by 0.43 eV as compared to an adsorption geometry atop a surface Mg atom. The charge transfer from the substrate to the Au atom is 0.22 e. On doping the substrate with 2.78% Al atoms however, we find that the Au atom now prefers to bind to the surface Mg atom [see Fig. 4.10(b)], with an adsorption energy of 1.87 eV. When adsorbing an Au atom at the O site on Al-doped MgO, we see that the Au atom does not bind to O, it moves and binds to a surface Mg atom. The Au atom gains a negative charge of 0.35 e due to electron transfer from the substrate to the Au atom; due to this high negative charge, the Au atoms are attracted to the Mg^{2+} ions on the surface and bind to them more strongly than to the surface O ions.

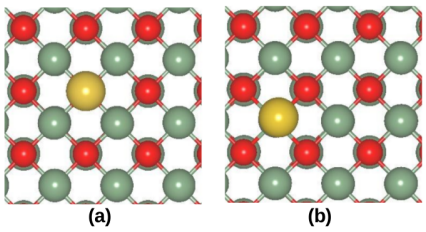

Figure 4.10: *Top views of the lowest energy adsorption geometries for (a) Au/MgO and (b) Au/2.78% Al-doped MgO. The grey, red and yellow spheres are Mg, O and Au atoms respectively. The dopant Al atom is in the third layer from the surface in (b) and cannot be seen in this figure. On MgO, Au prefers to bind to the surface O atom, whereas on Al-doped MgO, it prefers to bind to the surface Mg atom.*

The Au_2 cluster, when placed on undoped MgO, is found to bind to the surface in a geometry where the cluster is standing up vertically, bonding to one surface O atom [see Figs. 4.11(a) and (b)], with an adsorption energy of 1.56 eV and a charge transfer of 0.16 e. The geometry and adsorption energy are in fairly good agreement with previous

results.[127] We have also considered another geometry where the Au_2 cluster would be flat on the surface binding to two surface O atoms, but it is found to be unfavorable, the cluster breaks one of the Au-O bonds and relaxes to form the geometry in Fig. 4.11(a). When however the substrate is 2.78% Al-doped MgO, the scenario changes. In this case, the cluster prefers to bind to two surface Mg atoms, lying flat on the surface [see Fig. 4.11(c) and (d)], with an adsorption energy of 0.94 eV. The charge transfer in this case is 0.35 e; this increased charge transfer explains why the Au_2 cluster on the doped substrate now prefers to wet the surface. Here, the vertical standing geometry, atop a Mg atom is also possible, but this is higher in energy by 0.52 eV compared to the flat lying cluster.

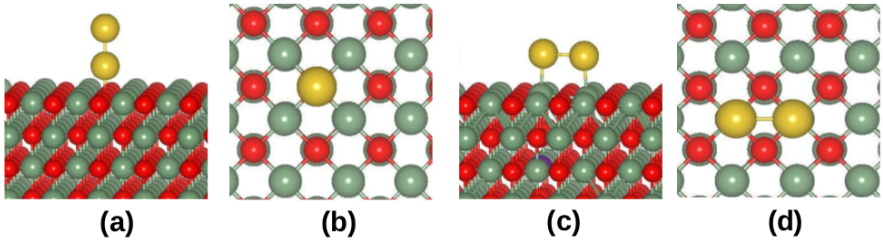

Figure 4.11: *(a) side view, (b) top view of the lowest energy adsorption geometry obtained for Au_2/MgO; and (c) side view, (d) top view of the lowest energy adsorption geometry for Au_2/2.78% Al-doped MgO. The grey, red, purple and yellow spheres represent Mg, O, Al and Au atoms respectively. The Au_2 cluster prefers to stand upright on undoped MgO while preferring to lie flat on the surface of Al-doped MgO.*

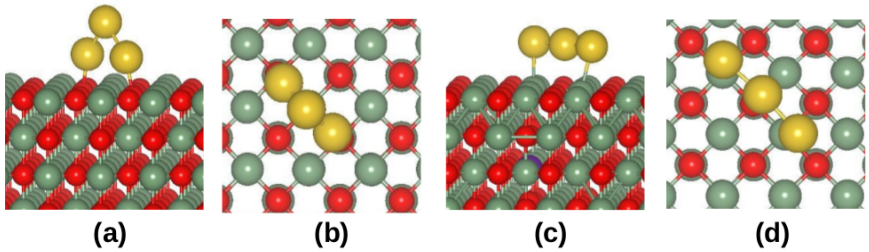

Figure 4.12: *(a) side view, (b) top view of the lowest energy adsorption geometry obtained for Au_3/MgO; and (c) side view, (d) top view of the lowest energy adsorption geometry for Au_3/2.78% Al-doped MgO. The grey, red, purple and yellow spheres represent Mg, O, Al and Au atoms respectively. The Au_3 cluster prefers a triangular geometry perpendicular to the surface on undoped MgO while on Al-doped MgO it prefers to lie flat forming a linear chain.*

In the case of Au_3 adsorbed on undoped MgO, we see that the preferred adsorption geometry is the one in which the Au atoms form an isosceles triangle, where only two of the Au atoms make bonds to the surface O atoms [see Figs. 4.12(a) and (b)]; this

	Charge gained by Au_n (e)	
	undoped MgO	2.78% Al-doped MgO
Au	0.22	0.35
Au_2	0.16	0.35
Au_3	0.29	0.39

Table 4.3: *The charge gained by the Au atom, Au dimer and Au trimer due to the electron transfer from the doped and undoped MgO to the supported Au_n cluster.*

adsorption geometry has an adsorption energy of 1.81 eV and the charge transferred from the substrate to Au_3 is calculated to be 0.29 e. The geometry and the binding energy of the Au_3 cluster on MgO are in good agreement with previous results.[28] We also considered another geometry where the Au_3 would be flat on the surface, binding to three surface O atoms, but on performing structural optimization, the cluster breaks one of the Au-O bonds and relaxes to the geometry in Figs. 4.12(a) and (b). Here again, on doping the substrate with Al atoms, we see that the Au_3 cluster prefers to lie flat on the surface [see Figs. 4.12(c) and (d)], due to an increased charge transfer of 0.39 e. The cluster forms a three-atom linear chain above a Mg-O-Mg chain on the surface; this has an adsorption energy of 2.74 eV.

The charge transferred from the substrate to the Au_n clusters is tabulated in Table. 4.3. For all three sizes considered, we find that the charge transfer from the substrate to the Au atom and Au_n increases when we go from undoped MgO to doped MgO.

In agreement with our results on Au_{20}/doped MgO, we find that substrate doping significantly affects the geometry of the Au_n cluster deposited on the substrate. We see that for Au_2 and Au_3, vertical upright geometries are preferred on undoped MgO, while the clusters wet the surface on Al-doped MgO; the increased charge transfer from the substrate to the Au_n cluster explains this change in geometry.

4.5 Conclusions

In summary, we have demonstrated a new, simple and working method to tune the morphology of supported gold clusters. We have theoretically shown that doping an oxide

substrate with electron donor impurity atoms causes an electron transfer from the substrate to the Au cluster, making it negatively charged. The large accumulation of charge at the interface between a planar cluster and the substrate, along with a strong electrostatic interaction, stabilize the planar arrangement of atoms over a three-dimensional arrangement.

We first predicted and demonstrated this method using the model system of Au_{20} supported on Al-doped MgO.[37] Soon after, experiments were performed that provided convincing evidence that our idea of tuning the morphology of Au clusters by doping the oxide substrate with an electron donor works; the authors performed experiments on Au clusters supported on Mo (Cr)-doped CaO (MgO).[38,122] We have also confirmed theoretically the finding in these experiments using the system Au_{20} supported on Mo-doped CaO. Subsequently other authors have followed our line of thought and made similar theoretical suggestions, e.g., depositing Au_{20} on N-doped graphene,[128] or on silicene supported on Ag(111),[129] has also been shown to stabilize the Au_{20} (P) cluster over the (T) cluster.

We also showed in this chapter that the method of substrate doping has a considerable effect on the adsorption sites and adsorption geometries of very small Au_n clusters, n = 1–3. While Au atoms bind to the surface O atoms on undoped MgO, we find that they prefer to bind to the surface Mg atoms on Al-doped MgO; the negatively charged Au atoms are attracted to the Mg^{2+} ion on the surface. The Au_2 and Au_3 clusters prefer upright geometries or geometries where not all Au atoms bind to the surface, when placed on pristine MgO. On doping the MgO with electron donors, however, we see that these clusters prefer to the wet the surface such that all Au atoms in the cluster lie on and bind to the surface.

In this chapter, we showed how substrate doping affects the morphology of supported Au clusters. While this approach was very successful, we must keep in mind that part of the motivation for doing this was to improve the catalytic activity of the clusters. Therefore, in the next chapter, we will investigate how substrate doping affects the reactivity of these supported Au clusters.

Chapter 5

Tuning the Reactivity of Gold Clusters by Substrate Doping

In the previous chapter we showed how introducing electron donor impurities in an oxide can serve as a simple and effective technique to control the morphology of Au clusters supported on the oxide substrate. This was done with the ultimate motivation of tuning the reactivity of Au clusters. In this chapter, we ask the truly interesting question of how this method affects the reactivity of the supported Au clusters. We do this by performing calculations on an Au_{20} cluster supported on MgO with and without Al-doping. To study the reactivity of these clusters we consider a simple model reaction, viz., dissociation of oxygen.

5.1 Introduction

Catalysts play a crucial role in chemical industries and industrial research. With a catalyst, reactions occur faster along an alternative reaction pathway with a lower activation barrier. The field of catalysis demands the constant development of new catalysts with better efficiency. An improved or new catalyst that can lower barriers further by even a few percent would have a significant impact on the reaction rates.

Gold in nanometer sizes is known to catalyze several reactions.[120] The first discovered and most studied reaction is the conversion of carbon monoxide to carbon dioxide.[121,130–135] This reaction is environmentally important because of its utility in devices like catalytic converters in automobiles and fuel cells. The heterogeneous catalysis of CO oxidation on Au is suggested to occur via two possible mechanisms, the Langmuir-Hinshelwood (L-H) mechanism or the Eley-Rideal (E-R) mechanism.[136–138] In the L-H mechanism, the O_2 and the CO molecules co-adsorb on the Au cluster, while in the E-R mechanism, which usually occurs in high pressure conditions, the CO remains in the gas phase while interacting with adsorbed O_2 molecules at the Au-support interfaces. In both mechanisms, the activation of the O_2 molecule is an important step in the oxidation reaction.

The catalytic role of Au has been extensively studied by a combination of experimental and theoretical work. Soon after the initial discovery by Haruta,[14] it was realized that the catalytic properties of Au could be improved or fine-tuned by controlling factors such as the size and shape of Au clusters, changing the composition of the support, as well as by doping either the clusters themselves or the support on which they are placed.[139,140] A number of studies have shown that negatively charging gold clusters has a significant effect on their reactivity towards O_2.[32,34,121,141–143] Earlier authors have demonstrated the possibility offered by substrate doping, by studying gold clusters on doped ceria substrates;[140] they found that the presence of the dopants affects the vacancy formation energy in the substrate, and improves the reactivity of the Au clusters. They also suggested that the vacancy formation energy in the substrate serves as a good reactivity descriptor for CO oxidation in the combined system.

The *d*-band model of catalysis[4] is a recent paradigm suggested by Hammer and Nørskov to explain trends in the reactivity of transition metal catalysts. It is extremely successful in describing the trends in the reactivity of metals with not only partially filled *d*-states, but also metals with filled (or nearly filled) *d*-states like Au. It has been used to explain why, in extended systems, gold is the noblest of all metals,[39] and also why gold becomes catalytically reactive in nanometer sizes.[30,144]

The main assumption underlying this model is that the adsorption energy of a molecule on a catalyst is largely dependent on the electronic structure of the catalyst itself. Hammer and Nørskov derived this model using the example of gaseous hydrogen adsorbing on different metal surfaces. They suggested that there are two primary contributions to the interaction between an adsorbate and a metal. The first of these is the interaction of the molecular states, let us say a bonding state ε_b and an antibonding state ε_a, with the metal *s*-band. This interaction, which is attractive in nature, leads to a broadening of the adsorbate levels and a downshift in their energy, to levels $\varepsilon_b\prime$ and $\varepsilon_a\prime$. In their model, this interaction is considered to be the same for all transition metals. The second contribution is from the interaction of the renormalized molecular levels $\varepsilon_b\prime$ and $\varepsilon_a\prime$ with the metal *d*-band which is narrow and is approximated to a single energy level called the *d*-band center ε_d. ε_d is obtained from the *d*-electron density of states $g_d(\varepsilon)$, as:

$$\varepsilon_d = \frac{\int_{-\infty}^{\infty} \varepsilon g_d(\varepsilon) \mathrm{d}\varepsilon}{\int_{-\infty}^{\infty} g_d(\varepsilon) \mathrm{d}\varepsilon}, \tag{5.1}$$

and is measured relative to the Fermi level. Here ε denotes energy. Hammer and Nørskov present the equation describing the interaction between the renormalized adsorbate levels and the metal *d*-band, leading to an equation for the energy of the transition state:[5]

$$\delta E_{ts} \sim -\frac{2V^2}{\varepsilon_a\prime - \varepsilon_d} - 2(1-f)\frac{2V^2}{\varepsilon_d - \varepsilon_b\prime} + \alpha V^2. \tag{5.2}$$

Here, f is the occupation of the metal *d*-band (normalized to one), V is the coupling matrix element between the molecular orbitals and the *d*-states of the metal, and α is the proportionality constant involved in the orthogonalization term. The first term on the right-hand-side describes the interaction between the molecular level $\varepsilon_a\prime$ and the metal ε_d; this interaction leads to an occupied bonding state and an empty antibonding state which makes the interaction attractive. The second term on the right-hand-side describes the interaction between the molecular level $\varepsilon_b\prime$ and the metal ε_d; this interaction leads to an occupied bonding state and a partially filled antibonding state, whose filling f is

approximated to the d-band filling of the metal. Since the interaction with the metal s-band is considered to be the same for all transition metals, $\varepsilon_a\prime$ and $\varepsilon_b\prime$ are constants for a given molecule and for all transition metals. This model suggests that the one variable, ε_d, can be used as a descriptor for the reactivity of a metal. A higher d-band center lowers the denominator in the first term on the right-hand-side making the first term more negative. A higher d-band center also corresponds to an increase in energy of the levels with respect to the Fermi level and a subsequent decrease in the filling f in the antibonding state created by the interaction between ε_d and $\varepsilon_b\prime$, which makes the adsorbate-metal system less destabilized. Both these effects translate to stronger binding between the adsorbate and the metal. In other words, the higher in energy ε_d is, the better the catalyst. Even though this model was suggested for the case of adsorption of hydrogen on metal surfaces, it has been successfully and widely used as a reasonable model to explain trends in the adsorption of oxygen and other molecules.[145]

In the d-band model, the s (and p) electrons are largely ignored, on the grounds that they behave the same way in all situations; their role is restricted to an "initial" step of renormalizing down molecular energy levels, all the "action" is in what the d electrons are doing. While these generally made assumptions are indeed valid for many systems, we will see below that they need to be set aside for certain systems like ours. While our arguments about the role of s and p electrons in lowering the reaction barriers apply to negatively charged Au clusters, we note that the behavior of s electrons has also been invoked to explain the enhanced reactivity of positively charged Au clusters in gas phase and on an undoped oxide substrate.[146]

In the last chapter, we looked into how the method of doping an oxide substrate with electron donors affects the morphology and the charge state of supported Au clusters. On progressively doping the substrate, the Au clusters became more negatively charged due to the transfer of electrons from the substrate to Au.[37] In this chapter, we demonstrate that this method also drastically improves the reactivity of the Au clusters towards O_2. As a proof of concept of lowering of reaction barriers by substrate doping, we present results on Au_{20} placed on a MgO substrate with Al dopant atoms. To study the reactivity of these

clusters, we consider oxygen dissociation as a simple model reaction, and find that such doping significantly reduces reaction barriers, by an amount proportional to the doping concentration. We find that this lowering of dissociation barriers cannot be explained by the behavior of the *d*-band center of Au atoms alone. Instead, we propose that the lowering of barriers is primarily due to the lowering of the energies of gold electrons in the *s*- and *p*-bands. We also suggest a suitable descriptor for the reactivity of Au clusters: the difference in energy between the Au *sp* and *d* states. Due to the general nature of our arguments, we suggest that the principles applied here should hold true for several other reactions where negatively charged gold clusters are involved.

5.2 Methods

We have employed spin-polarized density functional theory (DFT), as implemented in the quantum ESPRESSO package,[50] to study the adsorption and dissociation of O_2 on Au 20-atom clusters supported on the doped and undoped oxide substrate MgO. We have used a plane wave basis set, with cut-offs of 30 Ry and 240 Ry for wave functions and charge densities respectively. Exchange-correlation interactions were treated using the PW91 form of the Generalized Gradient Approximation.[49] Test calculations indicate that upon using PBE0 hybrid functionals, numerical results change, but qualitative conclusions are maintained. Ultrasoft pseudopotentials were used to treat the interactions between the ionic cores and the valence electrons. Convergence was hastened by smearing the occupations using Marzari-Vanderbilt cold smearing[71] with a broadening width of 0.068 eV. All atoms in the calculations were relaxed.

The calculations for O_2 adsorbed on the Au_{20} cluster supported on the MgO (doped and undoped) were carried out using a 6×6 surface unit cell of 4 layers. A vacuum of thickness $\sim$14 Å in the surface-normal direction was used for these calculations. k-point sampling for the cells with the clusters was done only at the zone center. The O_2 dissociation barriers on the Au clusters supported on MgO were computed using the technique of constrained minimization. The charge gained by an O_2 molecule upon adsorption was calculated by Bader analysis.

5.3 Results

5.3.1 Adsorption of Oxygen molecules on Au(P)/Al-doped MgO

To determine the active sites on the Au(P) cluster supported on the oxide, we study the adsorption of O_2 molecules at different sites on the Au(P) cluster deposited on 2.78% Al-doped MgO (see Fig. 5.1), all at the interface between the Au cluster and the substrate.[147] In these systems, the dopant atoms were placed in the third layer from the surface. We label the sites in Fig. 5.1(a)–(h) as P1–P8 respectively. These geometries are similar to the favored adsorption sites predicted for O_2 on Au clusters supported on oxide substrates.[132,147]

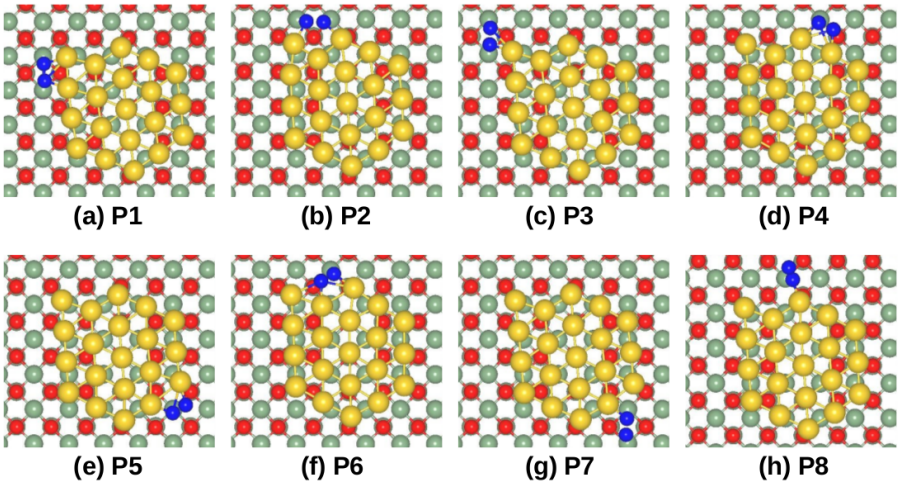

Figure 5.1: *Top views of different optimized adsorption geometries considered for O_2 on Au_{20}(P) supported over 2.78% Al-doped MgO. The grey and yellow spheres represent Mg and Au atoms respectively. O atoms in the substrate/adsorbed on the surface are red/blue. In the P1 geometry, O_2 has the highest adsorption energy, and in the P2 geometry, O_2 is most activated.*

We define the adsorption energy as $E_{\rm ads} = -\{E_{\rm tot}[({\rm Au_{20}} + {\rm O_2})/{\rm MgO}] - E_{\rm tot}({\rm Au_{20}/MgO}) - E_{\rm tot}({\rm O_2})\}$, where the terms on the right-hand-side are the total energies of respectively (i) the system consisting of O_2 adsorbed on the Au_{20} cluster on a MgO substrate, (ii) just the Au_{20} on MgO, and (iii) O_2 in the gas phase; all these are computed in relaxed geometries. The adsorption energies and the O-O bond distances in the activated O_2 molecules after adsorption at the sites P1 - P8 are listed in Table 5.1. As one can see, each site has a different adsorption energy, and may have different barriers for O_2 dissociation; it is known that in actual experimental situations, several sites on the Au cluster may be occupied,

and one will see a combined effect.[148]

Adsorption site	E_{ads} (eV)	d(O-O) Å
P1	0.95	1.50
P2	0.69	1.50
P3	0.94	1.43
P4	0.91	1.49
P5	0.86	1.48
P6	0.52	1.46
P7	0.51	1.40
P8	0.36	1.35

Table 5.1: *Calculated values of adsorption energies (E_{ads}) and activation of the O-O bond [d(O-O)] for the different sites considered for O_2 adsorption on Au_{20}(P) supported on 2.78% Al-doped MgO.*

At the site P1, the O atoms are bonded to two Au atoms and two surface Mg atoms; this scenario leads to a high binding energy and an elongation in the O-O bond length from the equilibrium gas phase O-O distance of 1.21 Å to 1.50 Å. One of the Au atoms that the molecule is bonded to, the corner atom that is outside the hexagon, is the Au atom with the highest *d*-band filling. At the site P2, the O atoms are again bonded to two Au atoms and two Mg atoms on the surface. Although the binding energy is not as high as in the P1 site, the O_2 molecule is highly activated, with an elongated O-O bond distance of 1.50 Å. At the site P3, the O_2 molecule is bonded to only one Au atom and two Mg atoms on the surface.

Next, we compute the dissociation barriers E_{diss} of the O_2 molecule adsorbed at the sites P1, P2 and P3. We do this using the approach of constrained minimization, with the O-O bond distance as the reaction coordinate. As an example, we show in Fig. 5.2, how the total energy of the system varies as a function of the O-O bond length at the P2 site. We compute the O_2 dissociation barriers for the three adsorption sites P1, P2 and P3 to be 0.53 eV, 0.29 eV and 1.71 eV respectively.

The effect of substrate doping on the adsorption of O_2 on the bare MgO substrate was also investigated (i.e., when no Au clusters are present). It is unfavorable for O_2 to bind on bare undoped MgO, but on bare 2.78% doped MgO [see Fig. 5.3(a)], we find that the adsorption energy increases to a high value of 3.30 eV, with a high dissociation barrier of 2.00 eV. In the presence of Au(P) clusters however, we find that the highest value of E_{ads}

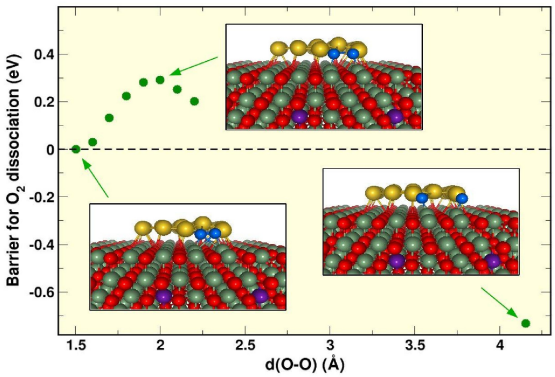

Figure 5.2: *Example of a computation of a dissociation barrier: results for total energy versus O-O bond length for adsorption geometry P2 on 2.78% Al-doped MgO. The insets depict the system geometry at various stages of the reaction. Grey, purple, and yellow spheres represent Mg, Al and Au atoms respectively. O atoms in the substrate/adsorbed on the surface are red/blue. Reprinted with permission from Ref. 149. ©(2015) AIP Publishing LLC.*

away from the cluster is 0.59 eV [see Fig. 5.3(b)]. This suggests that in the presence of Au clusters, the O_2 molecule would preferentially bind to the Au clusters and not to bare uncovered areas on the MgO surface.

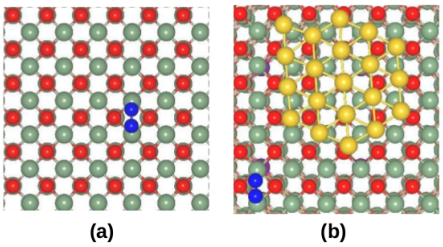

Figure 5.3: *Top views of the optimized geometries of (a) O_2 adsorbed on the substrate in the absence of Au clusters and (b) O_2 and $Au_{20}(P)$ co-adsorbed on the substrate. In both cases, the substrate is 2.78% Al-doped MgO. Grey and yellow spheres represent Mg and Au atoms respectively. O atoms in the substrate/adsorbed on the surface are red/blue.*

5.3.2 Adsorption of Oxygen molecules on Au(T)/Al-doped MgO

To study the adsorption of O_2 on the tetrahedral Au(T) cluster supported on 2.78% Al-doped MgO, we considered six different configurations shown in Fig. 5.4. The adsorption energies and the activation of the O_2 bond at these adsorption sites are listed in Table 5.2. We find that the most preferred site for the adsorption of O_2 is at the interface between the Au cluster and the oxide substrate. At the energetically most preferred site T1, the

O atoms in the molecule are bonded to two Au and two Mg atoms on the surface, and the O-O bond is elongated to a distance of 1.51 Å. At this site, we obtain a dissociation barrier for O_2 of 0.39 eV. However, note that at a doping concentration of 2.78%, the tetrahedral cluster is energetically less favorable, and only planar clusters will be present.

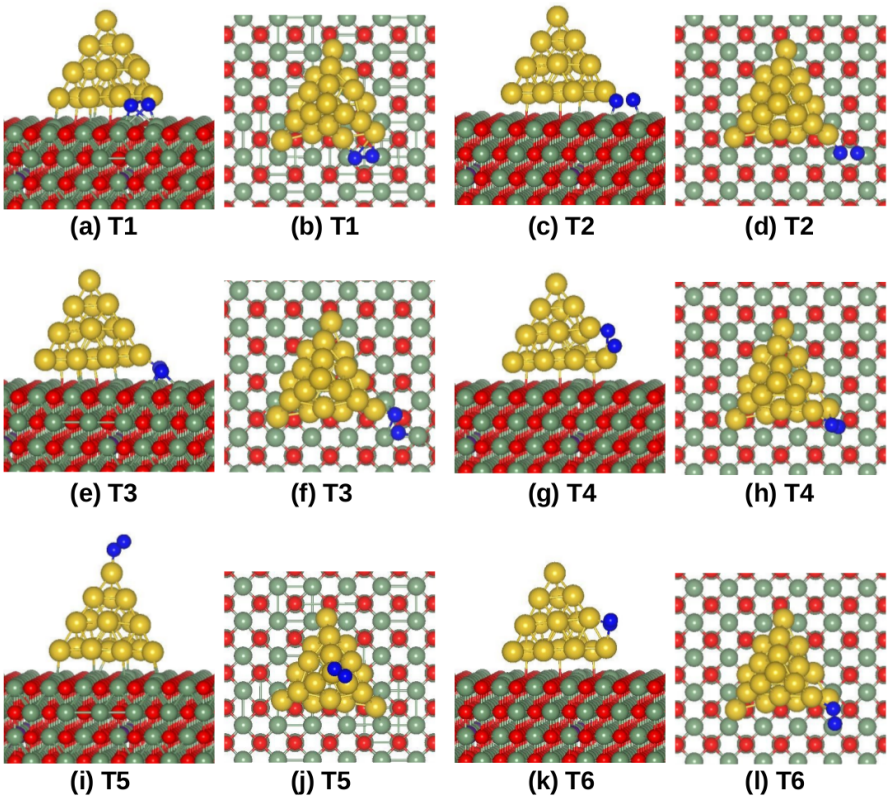

Figure 5.4: *Side and top views of the optimized adsorption geometries for O_2 adsorbed on $Au_{20}(T)$ supported on 2.78% Al-doped MgO. (a), (c), (e), (g), (i) and (k) are the side views; and (b), (d), (f), (h), (j) and (l) are the top views of the six adsorption geometries T1 - T6 respectively. Grey, purple and yellow spheres represent Mg, Al and Au atoms respectively. O atoms in the substrate/adsorbed on the surface are red/blue.*

5.3.3 Effect of Progressive Substrate Doping on Reaction Barriers

To examine the effects of progressive substrate doping on the reactivity of Au clusters, we have considered four dopant concentrations: 0%, 0.69%, 1.39% and 2.78%. The dopant atoms were placed in the third layer from the surface in all systems. We computed the dissociation barriers at the sites P1 and P2 at each doping concentration.

Adsorption site	E_{ads} (eV)	d(O-O) Å
T1	2.61	1.51
T2	2.38	1.48
T3	2.20	1.52
T4	0.98	1.43
T5	0.49	1.32
T6	0.22	1.34

Table 5.2: *Calculated values of adsorption energies (E_{ads}) and activation of the O-O bond [d(O-O)] for the different sites considered for O_2 adsorption on Au_{20}(T) supported on 2.78% Al-doped MgO.*

We find that substrate doping significantly lowers dissociation barriers for the P geometries. More interestingly, we find that it is also possible to tune E_{diss} by varying the doping concentration in the substrate. In Fig. 5.5(a), we see a dramatic decrease in the dissociation barriers as a function of doping concentation; as the doping concentration increases, the barrier for O_2 dissociation reduces monotonically. For the site P1, we see a lowering of the barrier from 1.24 eV to 0.53 eV on going from 0 to 2.78% doping concentration, which amounts to a reduction of 57%. For the P2 site, we see a lowering of the barrier from 0.83 eV to 0.29 eV on going from 0% to 2.78% doping concentration, which amounts to a reduction of 65%. Note however that on undoped MgO, it is the Au(T) cluster that is lower in energy than the Au(P) cluster; on undoped MgO for the T1 site on the Au(T) cluster we obtain E_{diss} of 0.68 eV. Upon doping, the Au(P) cluster becomes more stable than the Au(T) cluster. This suggests that the barrier for P2 at 2.78% doping concentration represents a huge reduction in barrier by 57% with respect to the barrier at T1 on undoped MgO. A reduction in E_{diss} by more than 50% corresponds to a speeding up of reaction rates by five orders of magnitude at room temperature (assuming that the pre-exponential factors remain the same).

To examine the effects of the position of the dopant atom on the barriers, we moved the dopant atom from the third layer to the second layer from the surface; we find that for the P1 site the dissociation barrier changes from 0.53 eV to 0.55 eV. This suggests that the position of the dopant atom has very little effect on the reactivity on these clusters, just as we found that the position of the dopant atom has very little effect on the energetics of the morphology change in the Au clusters in the previous chapter.[37]

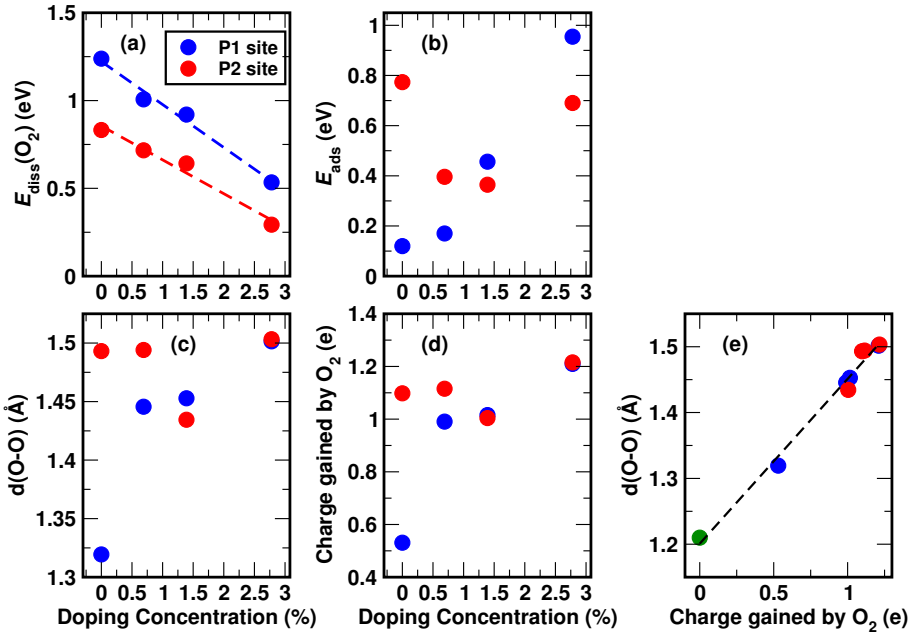

Figure 5.5: *(a) the barrier for O_2 dissociation E_{diss}, (b) the adsorption energy for O_2 E_{ads}, (c) the elongation of the O-O bond in the adsorbed O_2 molecule, (d) the charge transferred to the O_2 molecule from the substrate or cluster, all for the two adsorption sites P1 and P2 in the planar Au_{20} cluster as a function of substrate doping concentration. In (e), we show the correlation between the charge gained by the O_2 and the activation in the molecule. We see that all the points corresponding to the P1 and P2 sites at all doping concentrations and the point that corresponds to the equilibrium gas phase O_2 (in green) collapse onto one line.*

Upon substrate doping, we also observe a similar reduction of barriers for the Au(T) clusters; we find that the barrier for O_2 dissociation is lowered from 0.68 eV to 0.39 eV when the dopant concentration is 2.78%. From these results, we understand that the dramatic lowering of dissociation barriers is caused primarily by the increasing charge transfer from the substrate to the cluster due to the increasing doping concentration, rather than an effect of the change in the cluster morphology.

The results for the adsorption energy of O_2 at the two sites P1 and P2 are shown in Fig. 5.5(b). On the undoped MgO, for the Au(P) cluster, we see that the P2 is the most favorable adsorption geometry with $E_{\text{ads}} = 0.73$ eV, while the P1 has $E_{\text{ads}} = 0.12$ eV. However, at 2.78% doping concentration of Al, we see that P1 becomes the most stable geometry with $E_{\text{ads}} = 0.95$ eV, while the P2 geometry has $E_{\text{ads}} = 0.69$ eV.

We also computed the adsorption energy per oxygen atom after dissociation at the P1 and P2 sites both at a doping concentration of 2.78%, to be 0.76 eV and 0.71 eV

respectively. Previous authors have determined the intermediate range for the adsorption energy of atomic oxygen that would lead to optimum CO oxidation rates,[132] to be from 0.2 eV to 1 eV. Our calculated values are in the given range for the reaction to be favorable.

We now try to understand why substrate doping affects the reactivity of Au clusters. We first look into the trends in the activation of the O-O bond [see Fig. 5.5(c)] and the charge transfer to the O_2 molecule upon adsorption on the Au(P) cluster, at the P1 and P2 sites [see Fig. 5.5(d)]. As expected, when the O_2 molecule is adsorbed on the Au(P) cluster supported on MgO, the molecule gains charge; this leads to an increase in the interatomic bond length with respect to the equilibrium gas phase value of 1.21 Å. The excellent correlation between the charge gained by O_2 and the activation in the O-O bond is shown in Fig. 5.5(e). In addition to the points for the P1 and P2 sites for all doping concentrations, we have added as reference, a point representing the equilibrium gas phase condition, where the charge on the O_2 molecule is zero and the equilibrium O-O bond length is 1.21 Å. As the O_2 molecule gains electrons, the antibonding orbital in the molecule becomes occupied, leading to the weakening and elongation of the O-O bond.

The charge gained by the O_2 molecule clearly explains the elongation of the O-O bond. This is independent of the doping concentration or the site at which the O_2 is adsorbed. However, the trends in the charge transfer and the activation of O_2 at the P1 and P2 sites does not seem to correlate with the dissociation barriers obtained at these sites. The trends in the dissociation barrier obtained for P1 and P2 are the same, however, one sees a clear difference between the trends at P1 and P2 for the charge transfer to O_2 and the activation of O_2. At P1, as the doping concentration increases from 0 to 2.78%, the charge gained by O_2 increases monotonically from 0.53 e to 1.20 e, this leads to a significant increase in the O-O bond length from 1.32 Å to 1.50 Å. However, at the P2 site, the changes observed for the charge transfer and the activation of O_2 are much smaller and not even monotonic. This suggests that one needs to look further in order to explain satisfactorily the observed trends in the dissociation barriers as a function of substrate doping.

Next, we attempt to examine how the electronic structure of the Au cluster changes upon substrate doping. We first examine the filling in the *d*-states and *s*- and *p*-states of

the Au cluster as a function of substrate doping concentration. Unlike isolated atomic Au, the d-states of Au in the cluster are only partially filled. For the Au_{20} cluster supported on MgO, we compute the average filling in the d, s and p states in the Au(P) cluster to be 9.62 e, 0.60 e and 0.60 e respectively, and in the Au(T) cluster to be 9.63 e, 0.59 e and 0.67 e respectively. This is in agreement with previous results for electronic filling in d-, s- and p-states of small Au clusters.[150] The filling in the d-states and the s- and p-states in the Au(P) cluster as a function of doping concentration are shown in Figs. 5.6(a) and 5.6(b). Upon doping the oxide with electron donors, the additional electrons are transferred to the Au cluster. On going from undoped MgO to 2.78% Al-doped MgO, only 0.09 electrons go into the d states of Au(P), whereas 0.58 electrons go into the s- and p-states. This large intake of electrons may be explained by the high electronegativity of Au atoms.[151,152]

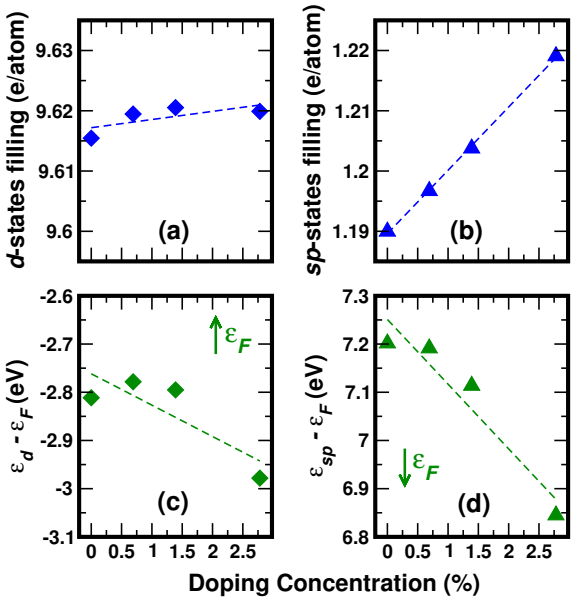

Figure 5.6: *(a) the filling in the Au d-states, (b) the filling in the Au sp-states, both averaged over all atoms in the cluster, (c) the position of the d-band center, ε_d, and (d) the center of the sp-bands, ε_{sp}, all as a function of doping concentration. The arrows in (c) and (d) show the direction of the Fermi energy. Reprinted (adapted) with permission from Ref. 149. ©(2015) AIP Publishing LLC.*

We compute the d-band center of the atoms in Au(P) cluster using Eq. (5.1), for each doping concentration considered. To characterize the shifts in energy of the sp-states, we look at a single energy ε_{sp}, defined as the energy where these states would achieve

half-filling:

$$\int_{-\infty}^{\varepsilon_{sp}} g_{sp}(\varepsilon)\mathrm{d}\varepsilon \equiv 4; \tag{5.3}$$

where $g_{sp}(\varepsilon)$ is the density of states of the s and p electrons. This definition for band center has an advantage over the definition in Eq. (5.1); it does not require the computation of eigenvalues of a huge number of empty states. For a rectangular band however, the two definitions would yield the same answer.

As a result of the electron transfer to the Au cluster, we see that the d-band center as well as the sp-band center of Au moves *down* in energy. This is shown in Figs. 5.6(c) and (d). The downward shift in ε_{sp} is greater than the downward shift in ε_d, primarily due to the higher intake of electrons in the sp states. The reason for the downshift in the electronic states of Au is shown in the cartoon model in Fig. 5.7. Most importantly, note that the the d-band center is moving opposite to the direction one would expect if the d-band model could explain the enhanced reactivity of Au clusters. We find that substrate doping has a considerable effect on the filling and the energy of the sp-states of Au; one might then tend to believe that the assumption that the sp-states behave in the same way in all situations, may no longer hold.

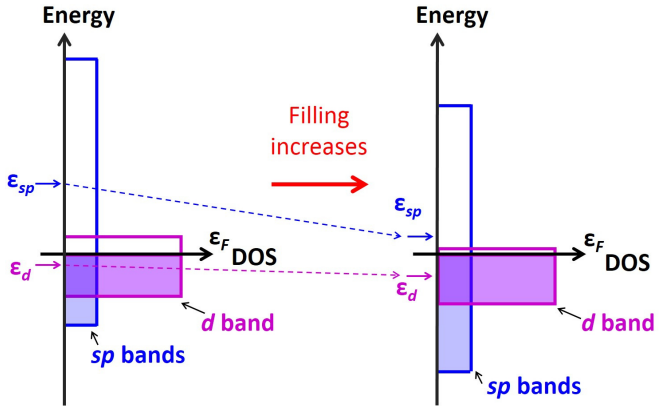

Figure 5.7: *Cartoon model showing the densities of states (DOS) of the sp- and d-bands, and the downshift in energies of both upon an increase in filling. The downward shift is more for the sp-bands than the d-band because of both the larger injection of charge and the shape of the DOS. ε_{sp}, ε_d, and ε_F are the sp-band center, d-band center and Fermi energy respectively. Note that this figure is schematic only, and in reality the Au d DOS is far from rectangular, with a peak well below ε_F, and a tail extending to higher energies. Reprinted with permission from Ref. 149.*

We go back now to the equation for the energy of the transition state for the dissociation process, Eq. (5.2). Since the *d*-states in the Au cluster are almost full ($f \sim 1$), we can neglect the second term on the right-hand-side reducing the equation to:[5]

$$\delta E_{ts} \sim -\frac{2V^2}{\varepsilon_a\prime - \varepsilon_d} + \alpha V^2 \tag{5.4}$$

In the original *d*-band model, $\varepsilon_a\prime$ remains the same in all situations. However in our case, we believe that it changes with doping concentration. Since the quantity $\varepsilon_a\prime$ is the energy of the molecular level after interaction with the Au *sp*-states alone, we cannot separately obtain this energy from our DFT calculations. However, if we go back to the first step of the model and examine the interaction between the adsorbate level ε_a and the metal *sp*-states, one could obtain an indication of how the level $\varepsilon_a\prime$ shifts with doping. The interaction between a molecular adsorbate level and a metal *sp*-band can be understood by considering the interaction between a discrete energy level and a continuum of energy states as explained by Newns and Anderson. P. W. Anderson in 1961 described the effect of the presence of a magnetic impurity in alloys,[153] and in 1969, D. M. Newns proposed a model equivalent to Anderson's description, to explain the chemisorption of a H atom on transition metal surfaces.[154]

Consider the molecular level ε_a, and a metal with unperturbed eigen states $|k>$ describing an infinitely wide metal *sp*-band, with eigen values ε_k. If the matrix elements of the interaction are given by V_{ak}, the Green's function of the molecule $G_{aa}(\varepsilon)$ is given by[154]

$$G_{aa}(\varepsilon) = \left[\varepsilon - \varepsilon_a - \sum_k \frac{|V_{ak}|^2}{\varepsilon - \varepsilon_k + is}\right]^{-1}, s = 0^+ \tag{5.5}$$

$$= \left[\varepsilon - \varepsilon_a - \Lambda(\varepsilon) + i\Gamma(\varepsilon)\right]^{-1}, \tag{5.6}$$

$$\tag{5.7}$$

where $\Lambda(\varepsilon)$ is the energy shift and $\Gamma(\varepsilon)$ is the half width of the broadened and renormalized

adsorbate level.

$$\Gamma(\varepsilon) = -\mathrm{Im}\sum_k \left[\frac{|V_{ak}|^2}{\varepsilon - \varepsilon_k + is}\right] \tag{5.8}$$

$$= \pi \sum_k |V_{ak}|^2 \delta(\varepsilon - \varepsilon_k). \tag{5.9}$$

$$\tag{5.10}$$

Assuming V_{ak} to be a constant V_{sp}, for all states in the *sp*-band, and considering the *sp*-band to be a flat band with density of states, ρ_{sp},

$$\Gamma(\varepsilon) = \pi |V_{sp}|^2 \rho_{sp}, \tag{5.11}$$

$$\text{and } \Lambda(\varepsilon) = \frac{P}{\pi}\int_{-\infty}^{\infty} \frac{\Gamma(\varepsilon')d\varepsilon'}{\varepsilon - \varepsilon'}. \tag{5.12}$$

where P denotes the Cauchy principal value.

If the *sp*-band was infinitely wide, ρ_{sp}, and therefore Γ, would be a constant for all values of ε, and the shift $\Lambda(\varepsilon)$ would vanish.

Here, the *sp*-band has a finite band width, let us say with states extending between the energies ε^{sp}_{min} and ε^{sp}_{max}, then

$$\rho_{sp} = \begin{cases} \text{constant}, & \text{if } \varepsilon^{sp}_{min} < \varepsilon < \varepsilon^{sp}_{max} \\ 0, & \text{otherwise} \end{cases} \tag{5.13}$$

$$\text{Similarly } \Gamma(\varepsilon) = \begin{cases} \pi |V_{sp}|^2 \rho_{sp} & \text{if } \varepsilon^{sp}_{min} < \varepsilon < \varepsilon^{sp}_{max} \\ 0, & \text{otherwise} \end{cases} \tag{5.14}$$

The limits of the integral for $\Lambda(\varepsilon)$ now change, leading to:

$$\Lambda(\varepsilon) = \frac{1}{\pi}\int_{\varepsilon^{sp}_{min}}^{\varepsilon^{sp}_{max}} \frac{\pi |V_{sp}|^2 \rho_{sp} d\varepsilon'}{\varepsilon - \varepsilon'}, \tag{5.15}$$

$$= \frac{|V_{sp}|^2}{W_{sp}} \ln\left(\left|\frac{\varepsilon - \varepsilon^{sp}_{min}}{\varepsilon^{sp}_{max} - \varepsilon}\right|\right), \tag{5.16}$$

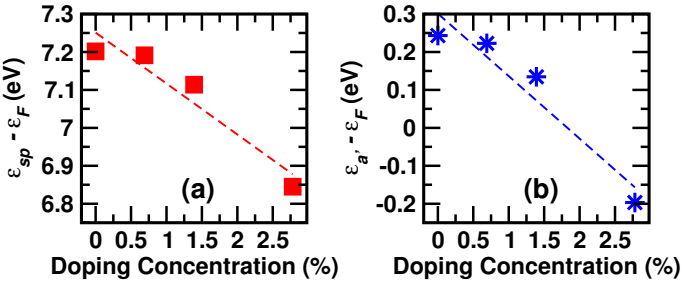

Figure 5.8: *(a) The center of the sp-states, ε_{sp} (plotted again for easy comparison), and (b) the renormalized adsorbate level, $\varepsilon_{a\prime}$, both as a function of the doping concentration in the substrate. All energies are referenced to the Fermi level. In (b) we used $V_{sp}^2 = 3.4\ eV^2$. Reprinted with permission from the Supplementary material of Ref. 149. ©(2015) AIP Publishing LLC.*

where W_{sp} is the bandwidth of the metal *sp*-band.

The energy of the renormalised and downshifted energy, $\varepsilon_{a\prime}$ will be given by:

$$\varepsilon_{a\prime} = \varepsilon_a + \frac{V_{sp}^2}{W_{sp}} \ln\left(\left|\frac{\varepsilon_a - \varepsilon_{min}^{sp}}{\varepsilon_{max}^{sp} - \varepsilon_a}\right|\right), \tag{5.17}$$

$$\approx \varepsilon_a - (\varepsilon_{sp} - \varepsilon_a)\frac{4V_{sp}^2}{W_{sp}^2}, \tag{5.18}$$

$$\approx \varepsilon_a - (\varepsilon_{sp} - \varepsilon_a)\frac{V_{sp}^2}{(\varepsilon_{sp} - \varepsilon_{min}^{sp})^2} \tag{5.19}$$

The value for the antibonding orbital ε_a, or the LUMO of the oxygen molecule was calculated to be -4.71 eV with respect to vacuum, in fairly good agreement with previous DFT results.[155] Using the value of ε_a of O_2, our calculated results for ε_{sp} and ε_{min}^{sp} for the different doping concentrations and Eq. (5.19), we have estimated how $\varepsilon_{a\prime}$ changes as a function of doping concentration in the substrate (see Fig. 5.8).

Upon comparing the shift in the *sp*-band center and the renormalized molecular level, we see that we can approximate $\varepsilon_{a\prime} = \varepsilon_{sp} - \delta$, where δ is a constant shift in energy. We can therefore now extend the *d*-band model to incorporate the changes in the behavior of *sp* electrons upon substrate doping, by writing:

$$\delta E_{ts} \sim -\frac{2V^2}{\varepsilon_{sp} - \varepsilon_d - \delta} + \alpha V^2. \tag{5.20}$$

This suggests that the quantity $\Delta\varepsilon \equiv \varepsilon_{sp} - \varepsilon_d$ could be a good descriptor of the reactivity of gold clusters. The smaller the value of $\Delta\varepsilon$, the better will be the catalyst.

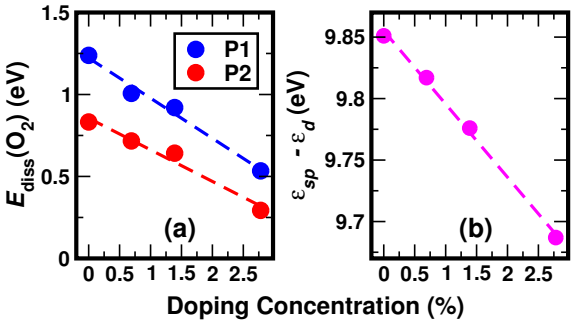

Figure 5.9: *(a) the barrier for O_2 dissociation for the P1 and P2 geometries of the Au(P) cluster (repeated), and (b) $\varepsilon_{sp} - \varepsilon_d$, both as a function of doping concentration. We believe that the result in (b) is the key to understanding the monotonic lowering of barriers on the Au clusters caused due to substrate doping. Reprinted (adapted) with permission from Ref. 149. ©(2015) AIP Publishing LLC.*

The *d*-band model focuses on making $\varepsilon_a\prime - \varepsilon_d$ or $\Delta\varepsilon$ small by pushing up ε_d for increasing the catalytic activity of metals. In our case however, we have made $\Delta\varepsilon$ small by pulling down ε_{sp}. $\varepsilon_{sp} - \varepsilon_d$, like the *d*-band center, has the advantage that it can be easily computed and is independent of the adsorbate molecule, i.e., it is a property of the catalyst alone. It also has the additional advantage that it is independent of any choice of reference energy. In Fig. 5.9, we have plotted again the dissociation barriers for P1 and P2 sites, and the difference in the energies of the *sp*- and *d*-states, both as a function of the substrate doping concentration. One sees that indeed, $\varepsilon_{sp} - \varepsilon_d$ decreases monotonically upon doping the substrate, which is primarily due to the downshift in energies of the *s* and *p* electrons. This is responsible for the progressive lowering of the denominator in the first term on the right-hand-side of Eq. (5.20) leading to lower transition state energies and lower dissociation barriers.

5.4 Conclusions

We have demonstrated that the method of substrate doping can be used not only to control the morphology of gold clusters, but also to radically enhance the reactivity of supported Au clusters towards O_2 dissociation. We observe a monotonic decrease in the barriers at two sites on the Au(P) cluster as the substrate is progressively doped. Upon doping to a level of 2.78%, the reduction in barriers is more than 50% with respect to the barrier on Au

clusters on undoped MgO. The general nature of these arguments suggests that this should hold true also for other oxidation reactions where the dissociation of O_2 is important. The importance of nanoparticle-support interactions in determining the catalytic activity of clusters is underlined in this work.

We find that the enhancement in the reactivity of the Au cluster cannot be explained satisfactorily solely by charge transfer or by the activation of the adsorbed O_2 molecule. The *d*-band model in its original and simple form also does not explain the observed trend in reactivity, although it has been cited as the source of the enhanced catalytic activity of small gold clusters.[30] However, on including the effect of the changes in the *s*- and *p*-states of Au, we find that we can explain the reduction in barriers. We believe that similar arguments involving the *s*- and *p*-states of Au should hold also for other sizes of gold clusters, on other oxide substrates, other dopant atoms, and also for other methods that could transfer electrons to the cluster. We have also proposed an appropriate descriptor of the reactivity of gold nanoparticles: $\varepsilon_{sp} - \varepsilon_d$, the difference in energies of the *sp* and *d* states.

In this chapter, we have shown that the assumption that *sp*-states play little or no role in determining the reactivity of transition metals, does not hold true in the case of Au clusters supported on doped oxide substrates. In the next chapter we investigate if the *s* and *p* electrons of Au are affected or if they play any role in three scenarios that have shown to improve the reactivity of Au: (a) reducing the Au coordination on going from bulk extended systems to nano systems (b) going from high coordination to low coordination sites on the same Au cluster and (c) negatively charging Au clusters.

Chapter 6

Role of s- and p-electrons in Au Reactivity

In the previous chapter, we demonstrated how substrate doping improves the reactivity of the supported Au_{20} cluster towards O_2 dissociation. The *d*-band model in its original form assumes that the *sp*-states are static and play no role in explaining the trends in the reactivity of transition metals or noble metals. However, it has been demonstrated that there are situations in which the *d*-band model fails.[146,156,157] Indeed, we too have shown in the previous chapter that the *d*-band model breaks down, and that the assumption that the *sp*-bands are static is not true in the case of Au clusters supported on doped substrates. Accordingly, we proposed a new descriptor for the reactivity of Au, viz., $\varepsilon_{sp} - \varepsilon_d$. In this chapter, we investigate whether the assumption that the *sp*-states are static is true when we: (a) change the Au coordination number by reducing the dimensionality, (b) change the coordination number by going from a face site to an edge site and to an apex site of an Au_{20} tetrahedral (T) cluster in the gas phase and (c) negatively charge Au clusters.

6.1 Introduction

Bulk gold is known to be chemically inert, it is a precious metal used for coinage, jewelery and other arts. It resists corrosion and remains passive towards the most highly reactive gases.

In an effort to understand why Au is the most noble of all metals, Hammer and Nørskov[39] examined a simple surface reaction, the adsorption of hydrogen gas on the gold surface and compared it to similar reactions on the surfaces of copper, nickel and platinum. The metal-adsorbate interaction can be conveniently understood in two steps. In the first step the H $1s$ state interacts with the metal $4s$ (Cu and Ni) or $6s$ (Au and Pt) band to form a deep lying filled bonding state and an empty antibonding state. This interaction is therefore attractive in nature, and this attraction is assumed to be about the same for all four metals. In the second step, this bonding state interacts with the metal d-band. In this suggested model, which is called the d-band model, it was found that all the important 'action' happens in this step. In this step, the renormalized molecular level interacts with the d-band forming a further lowered bonding state and an antibonding state just above the d-band. The degree of filling of this antibonding state is one of the factors that decides the strength of the metal-adsorbate interaction. For metals like Cu and Au, which have a filled d-band, this antibonding state is filled, and hence the interaction with the metal d-band is repulsive in nature. For metals like Ni and Pt however, the d-band is not entirely filled, and these antibonding states are empty, which gives rise to an extra attractive interaction in addition to the attractive interaction with the metal s-band.[39] This explains why Ni and Pt are more reactive than Cu and Au.

The binding of hydrogen to Cu is marginally stable, however the situation is completely unstable for Au. To understand why Au is more noble than Cu, the authors compare the absolute magnitude of the coupling matrix element V_d and the overlap S_d for the interaction between the renormalized molecular level and the metal d-band.[39] The orthogonalization energy for this interaction is proportional to V_d^2, which is considerably larger for $5d$ metals than $3d$ metals because of the extended $5d$-states. The magnitude of V_d, and therefore the orthogonalization energy, increases as we go down in a group of the periodic table; this renders Au less reactive than Cu. Hence, the d-band model successfully explains why Au is the most noble of all metals.[39]

Due to the noble nature of Au, it was long considered that its chemistry was not particularly exciting, and it was overlooked as a potential catalyst. However, it was

discovered in the 1980s by Haruta *et al*,[14] that finely divided nanoparticles of Au when supported on oxides have a high activity towards CO oxidation at low temperatures. This led to several important studies which suggest that perhaps Au is one of the most interesting metals in the periodic table with respect to its potential to act as a catalyst. In addition to being a low temperature catalyst for CO oxidation, Au is predicted to be the best catalyst for ethyne hydrochlorination[158,159] and is also found to be a good catalyst for the oxidation of alcohols with a high selectivity.[160]

The reason for this unusually high activity in nanosized Au has been attributed to several effects. The chemical activity of Au is found to change significantly with the particle size.[121] It is known that the fraction of low-coordinated Au atoms scales approximately with the catalytic activity; this suggests that atoms on the corners and the edges of Au nanoparticles are the active sites.[161] Au nanoparticles supported on reducible oxides like TiO_2, Fe_2O_3 and NiO have been reported to show an exceptionally high activity towards CO oxidation; it was proposed that the support supplies oxygen to form active gold sites.[162] The presence of the support is also known to bring about active sites at the gold-support interface that have been shown to have high activity in CO oxidation.[8] Another explanation is the charge transfer between the support and the Au particles; F-center defects are known to make the supported Au particles negatively charged and increase their reactivity.[9] Au particles supported on ultra thin films of MgO placed on a metal slab[10,11,31,35,36] and our results on Au clusters supported on doped oxide substrates[37,149] (in the last chapter) also show the strong effect that the substrate has on the morphology and the reactivity of the supported Au particles. Other effects like strain in the Au particles due to the lattice mismatch of the lattices in Au and the substrate,[163] and a metal to non-metal transition in small Au particles have also been suggested as playing an important role in the catalytic properties of Au nanoparticles.[164]

A comparative study of all these effects was carried out, which reported that the size of the nanoparticle has considerably more influence on the catalytic activity of gold than the effects due to the support.[30] This suggests that the dominant effect in the exceptional catalytic activity of Au nanoparticles must be a property that is directly related to the size

of the gold particle. The authors also report that the chemical reactivity of gold towards CO and O_2 binding is strongly dependent on the coordination number of the gold atoms and explain this observation using the *d*-band model.[30] The Au atoms on the Au(111) surface have *d*-states that are so low in energy that they are unable to interact with the oxygen $2p$ states. However, on going to Au atoms at steps or kinks and corners in Au nanoparticles, the coordination number of the Au atoms is reduced significantly, and the *d*-states move closer to the Fermi energy. This leads to a stronger interaction with the oxygen valence states.[30]

Note that in these seminal works, the authors have explained the inactivity or nobleness of bulk Au[39] and the exceptional activity of nano Au,[30] both in terms of the *d*-band model. This model looks at the position of the *d*-states (approximated to a single energy level, the *d*-band center ε_d) with respect to the Fermi level. The higher in energy the *d*-band center is, the better is the reactivity of the catalyst. It assumes that the *sp*-states are static and have the same effect for all transition metals or noble metals, and in all cases. In the previous chapter, we showed that the *d*-band model in its original form cannot explain the observed increase in the reactivity of the Au cluster towards O_2 dissociation due to substrate doping. We showed that in addition to the *d*-states of Au, the *s*- and *p*-states of Au are also significantly affected by substrate doping; we find that the *sp*-states actually shift more than the *d*-states of Au. Hence, our results show that the *s*- and *p*-states are not just passive spectators but play an important role in explaining the observed increase in reactivity.

Reducing the coordination number of Au atoms[30] and negatively charging Au clusters[143] are two ways that have been shown to improve the reactivity of Au clusters. In this chapter, we investigate whether the *s*- and *p*-states of Au are truly static or whether they are significantly affected when the coordination number of Au atoms and the charge state of an Au cluster are altered. To study the effect of reducing the coordination number, we have looked at two scenarios: (a) reducing the dimensionality of Au by considering realistic and hypothetical extended systems in three, two, one and zero dimensions, i.e., going from face-centered-cubic (FCC) bulk gold to nanoclusters, and (b) going from a face

site to an edge site and to an apex site on the Au_{20} tetrahedral (T) cluster. To study the effect of negatively charging Au clusters, we have studied three different clusters, Au_3, Au_8 and Au_{20} (T), with charges +2, +1, 0, -1 and -2.

A small part of the results presented in this chapter were published in Ref. 165.

6.2 Methods

We have performed spin-polarized density functional theory calculations as implemented in the Quantum ESPRESSO package.[50] The Kohn-Sham wave functions were expanded using a plane wave basis set, with an energy cutoff of 30 Ry. An energy cutoff of 240 Ry was used for charge densities. Ultrasoft pseudopotentials were used to describe the interaction between the ions and the valence electrons for all elements.[63] The exchange-correlation potential was treated within the Generalized Gradient Approximation (GGA).[47] Marzari-Vanderbilt cold smearing of width 0.005 Ry was used.[71] A Monkhorst-Pack k-point mesh[67] was used for calculations on extended systems and surfaces, with eight divisions in repeating directions and one division in artificially repeating directions. For calculations on clusters, the k-space sampling was done only at the Brillouin zone center Γ. The surface calculations for Au(100), Au(110) and Au(111) were done using a slab with six atomic layers and a 1×1 surface cell, with a vacuum of ∼15 Å in the surface normal direction to prevent spurious interactions between periodic images. In the case of two-dimensional systems and nanoparticles, a vaccum distance of ∼10 Å was considered in all artificially repeating directions.

For the extended systems, the lattice constants were optimized, and for the clusters, the structures were optimized using Hellmann-Feynman forces[72] and the BFGS algorithm.[98–101] The initial geometries for Au_6 and Au_8 were taken from Refs. 166, 167 and 168 and were then further optimized.

For each of the gold systems, we have calculated a parameter, the effective coordination number (ECN)[169] which is defined as:

$$n_e^i = \frac{12 \sum_j \rho_j^{at}(R_{ij})}{[12\rho^{at}(R_{bulk}^{1NN}) + 6\rho^{at}(R_{bulk}^{2NN}) + 24\rho^{at}(R_{bulk}^{3NN}) + ...]}, \tag{6.1}$$

where n_e^i is the ECN of the i^{th} atom, j runs over all neighbors of the atom i (in practice, this is truncated after some distance), $\rho_j^{at}(r)$ is the electronic charge density of the j^{th} atom, R_{ij} is the distance of the i^{th} atom from the j^{th} atom. R_{bulk}^{1NN}, R_{bulk}^{2NN}, R_{bulk}^{3NN}, ..., are respectively the first nearest neighbor distance, second neighbor distance, third neighbor distance, and so on in the bulk FCC system. The value for ECN is converged with respect to the number of coordination spheres around an atom. For systems with more than one inequivalent atom, the average value of the ECN for atoms i in the system was noted. The advantage of the ECN over the usual definition of coordination number (where one just counts the number of nearest-neighbor atoms) is that it accounts not just for how many neighbors an atom has, but how far away they are; in earlier work, we have found that it is more appropriate a descriptor to see how quantities such as adsorption energies and activation barriers scale when coordination number is changed and/or strain is applied.[170,171] The ECN is a measure of the ambient electron density (due to its neighbors) that an atom i sits in; in this sense, it can be said to be in the spirit of semi-empirical models of interatomic interactions such as the embedded atom model,[172,173] the glue model,[174] or effective medium theory.[175]

The electronic filling and the bandwidths of the Au *d*- and *sp*-states were calculated from projected density of states calculations. The *d* bandwidth, W_d, was calculated using the equation: $W_d = E_{max}^d - E_{min}^d$, where E_{max}^d and E_{min}^d are the energy maximum and energy minimum, respectively, of the *d*-band density of states, using a threshold value. The *d*-band center, ε_d,[4] was calculated from the Au *d*-electron density of states, $g_d(\varepsilon)$, using the equation:

$$\varepsilon_d = \frac{\int_{-\infty}^{\infty} \varepsilon g_d(\varepsilon) \mathrm{d}\varepsilon}{\int_{-\infty}^{\infty} g_d(\varepsilon) \mathrm{d}\varepsilon}. \tag{6.2}$$

We have characterized the shifts in the energy of the *sp* states using a single energy level ε_{sp},[149] defined as the energy where these states achieve half-filling:

$$\int_{-\infty}^{\varepsilon_{sp}} g_{sp}(\varepsilon) \mathrm{d}\varepsilon \equiv 4; \tag{6.3}$$

where $g_{sp}(\varepsilon)$ is the density of states of the *s* and *p* electrons. The *sp* bandwidth W_{sp} was

calculated using the equation: $W_{sp} = 2(\varepsilon_{sp} - E^{sp}_{min})$, where E^{sp}_{min} is the energy minima of the Au *sp*-band states, again using a threshold value.

6.3 Results

Below, we investigate the electronic properties of the *d*-states and the *sp*-states of Au and how they are affected on (a) changing the coordination number of Au atoms by reducing dimensionality, (b) changing the coordination number by going from a face site to an edge site to an apex site of an Au_{20} (T) cluster and (c) changing the charge state of Au clusters.

6.3.1 Changing Au Coordination by Reducing Dimensionality

To study the effect of reducing coordination number on the electronic properties of Au, we have considered a number of real and hypothetical systems of Au (see Fig. 6.1). We have considered four three-dimensional (3D) periodic systems: Au in a face centered cubic (FCC) lattice, body centered cubic (BCC) lattice, simple cubic (SC) lattice and diamond (D) lattice [see Figs. 6.1(a)–(d)]; three two-dimensional (2D) sheets: Au in a triangular sheet (TS), square sheet (Sq) and honeycomb (HC) sheet [see Figs. 6.1(e)–(g)]; and a one-dimensional (1D) linear (L) chain [see Fig. 6.1(h)]. We have also considered three surfaces of FCC Au, viz., Au(111), Au(100) and Au(110) [see Figs. 6.1(i)–(k)], and six nanoclusters in the gas phase, viz., Au_{20}(P), Au_{20}(T), Au_8, Au_6, Au_3 and Au_2 [see Figs. 6.1(l)–(q)]. Note that Au_{20}(P) and Au_{20}(T) are respectively the low energy planar and tetrahedral isomers of the 20-atom Au cluster in the gas phase; these structures have already been discussed in the previous two chapters.

The coordination number of an atom is generally defined as the number of nearest neighbors. It is found that the interatomic bond distances usually decrease when the dimensionality of the system (and therefore the coordination number) is reduced. [176,177] In Fig. 6.2, we show how the nearest neighbor distances in the extended systems considered change as a function of the coordination number of Au in the system. We obtain the highest nearest neighbor distance, 2.93 Å for the FCC system, and the lowest nearest neighbor distance, 2.52 Å for the one-dimensional linear chain. This finding is in agreement with

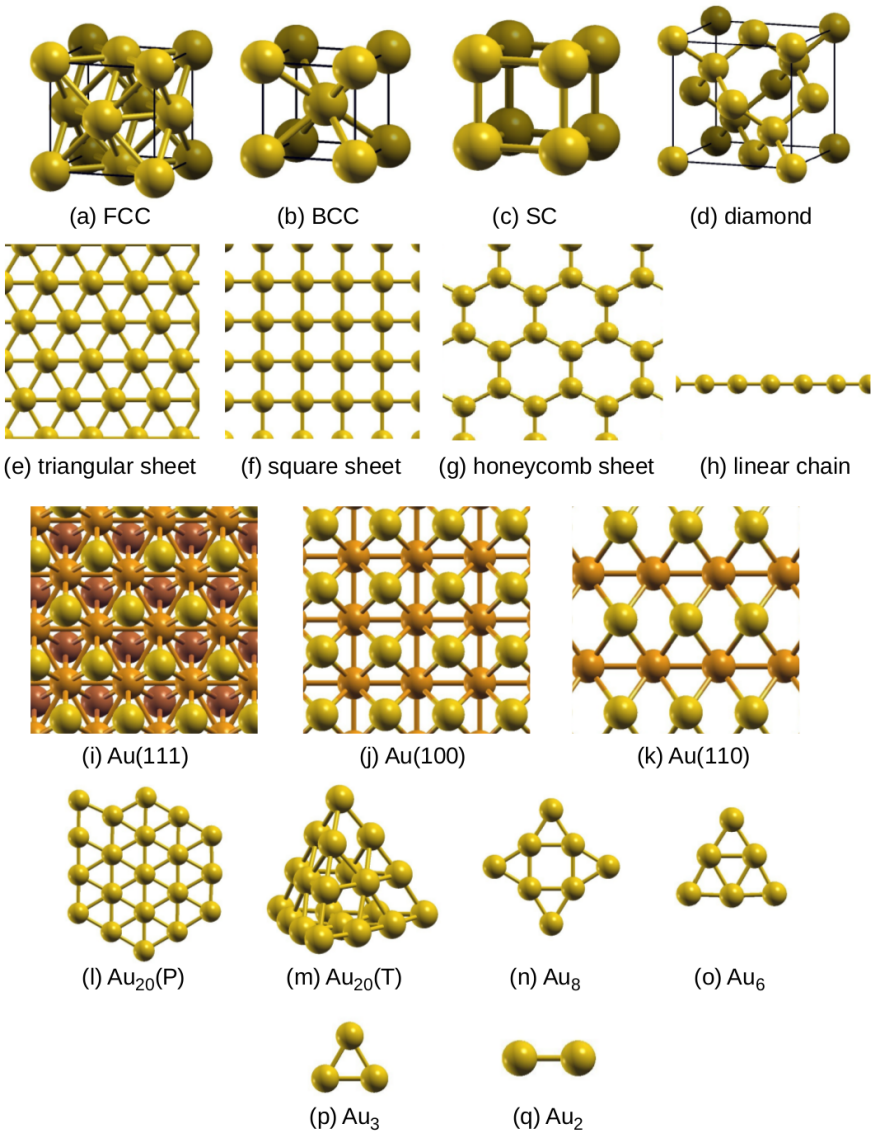

Figure 6.1: *Structures of all the real and hypothetical Au systems considered in Section 6.3.1. (a)–(h) are extended systems: (a)–(d) 3D extended systems (conventional cubic unit cells of the periodic lattices are shown), (e)–(g) 2D sheets and (h) 1D linear chain. (i)–(k) are the Au(111), Au(100) and Au(110) surfaces respectively; the atoms in the first, second and third layer from the surface are colored yellow, orange and brown respectively. (l)–(q) are the gas phase Au clusters: (l) $Au_{20}(P)$, (m) $Au_{20}(T)$, (n) Au_8, (o) Au_6, (p) Au_3 and (q) Au_2.*

previous results.[165,178]

In order to take into account not only the number of nearest neighbors but also the Au-Au bond distances, we characterize each system by a parameter called the 'effective coordination number' (ECN) defined by Eq. (6.1). To calculate this quantity, we have considered not only the first coordination sphere (the first nearest neighbors), but also the

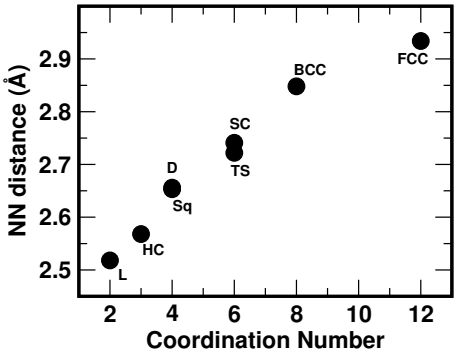

Figure 6.2: *The nearest neighbor distances obtained from our calculations for Au in different extended periodic lattices are plotted as a function of the nominal coordination number (number of nearest neighbors). As coordination number decreases, Au-Au bond distances also decreases. See the text for the meanings of the abbreviations used next to the symbols.*

second, third, fourth coordination sphere and so on, until a converged value for the ECN was obtained. The values for the nominal coordination number and the ECN for each system are listed in Table. 6.1.

When considering the ECN of extended systems, we can see that the ECN decreases when we go from three-dimensional structures to two-dimensional and to one-dimensional structures. It is interesting to note that Au in the BCC lattice has a slightly higher ECN than Au in the FCC lattice, even though the nominal coordination number is smaller in the BCC structure. This is due to the difference in the bond distances between an atom and its neighbors in the two systems. The smaller the bond distance, the higher is the charge density felt by an atom due to the presence of its neighbors, and hence the higher is the effective coordination number. When we consider the Au surfaces, we see that the ECN decreases for an Au atom on the surface in the order Au(111) > Au(100) > Au(110). For the nanoclusters, the ECN of an Au atom in an Au_n cluster decreases as particle size, n, decreases.

In Fig. 6.3, we show our results for how the electronic properties of Au change as a function of the effective coordination number of Au. Let us first look at Figs. 6.3(a) and (b), where we show how the bandwidths of the *d*-states and the *sp*-states are affected by reducing the dimensionality of the Au system. We see that as the ECN decreases, or as the dimensionality of the system reduces, the bandwidths of both the *d*-states and the *sp*-states decrease. This is as expected; as the effective coordination number of Au atoms decreases,

System	Coordination Number	Effective Coordination Number
FCC	12	12
BCC	8	12.20
SC	6	10.59
Triangular sheet	6	8.71
Diamond	4	7.80
Square sheet	4	7.38
Honeycomb sheet	3	6.40
Linear chain	2	4.51
Au(111)	9	8.57
Au(100)	8	8.31
Au(110)	7	7.17
Au_{20}(P)	-	6.05
Au_{20}(T)	-	5.78
Au_8	-	5.12
Au_6	-	4.87
Au_3	-	3.30
Au_2	-	2.59

Table 6.1: *The nominal coordination number (CN) and the average effective coordination number (ECN) of Au atoms in all the real and hypothetical systems studied. The structures of all systems are shown in Fig. 6.1*

the hybridization between the electronic states on neighboring atoms decreases, leading to more localized states with smaller bandwidths. Note that the *sp*-bandwidth reduces by a higher amount compared to the *d*-bandwidth; the *sp*-bandwidth decreases by 20.7 eV, whereas the *d*-bandwidth decreases only by 7.2 eV, when the effective coordination number reduces from 12 to 2.59.

In Figs. 6.3(c) and (d), we show the filling in the Au *d*- and *sp*-states respectively. As ECN decreases, the *d*-band filling increases, while the filling in the *sp*-band decreases. Note that it is only in an isolated atom of Au that the electronic configuration is $5d^{10}\ 6s^1$; in nanoclusters, surfaces and extended systems of Au however, the *d*-states are only partially filled. We find that in addition to the *d*- and *s*-states, the *p*-states are also partially filled in agreement with previous experimental findings for Au nanoclusters.[150] As we go from an isolated atom to bulk systems, the electrons in the *d*-states move to the *s*- and *p*-states in the system.

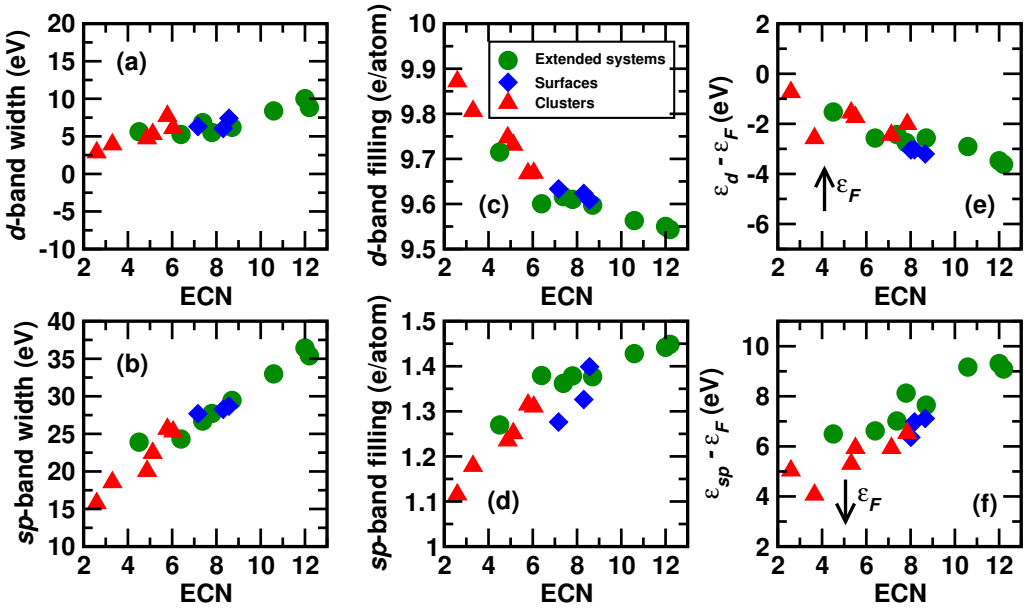

Figure 6.3: *Changes in the electronic structure of Au atoms when the coordination is reduced: (a) d-bandwidth, (b) sp-bandwidth, (c) d-band filling, (d) sp-band filling, (e) d-band center, ε_d, and (f) sp-band center ε_{sp} all as a function of the effective coordination number of Au atoms in the system. The points corresponding to the extended systems, surfaces and nanoclusters are shown in green circles, blue diamonds and red triangles respectively. The positions of ε_d and ε_{sp} plotted are with respect to the Fermi level of the systems.*

Next, we look into the shifts in the *d*- and *sp*-states as the effective coordination number of Au is reduced. The position of the *d*-band center, ε_d, and *sp*-band center, ε_{sp}, are defined by Eqs. (6.2) and (6.3) respectively. In agreement with previous results, we find that the *d*-band center moves up in energy closer to the Fermi level as we go from bulk systems to nanoclusters.[30] This has been cited as the reason for the origin of the catalytic activity in nano Au. As ε_d moves up in energy, the states become more accessible to interact with reactant molecules like O_2, and the reactivity of Au increases.[30] On looking at the shift in the *sp*-states of Au, we find that at the same time, the *sp*-band center shifts downward in energy, coming closer to the Fermi level, as the ECN of the system decreases. We see that ε_d shifts upward by ∼2.9 eV, whereas ε_{sp} shifts downward by ∼5.2 eV. This is very interesting since we find that the *sp*-states that were considered static, actually shift by a larger amount as compared to the *d*-states of Au on reducing coordination number.

The *d*-states move up in energy, while the *sp*-states move down in energy as ECN is reduced; this difference in behavior is explained by the cartoon model in Fig. 6.4. It

explains how a band shifts in energy on reducing the coordination number depending on whether the band is (a) more than half-filled or (b) less than half-filled. In Au, the *d*-states are more than half-filled and correspond to the panel (a) in Fig. 6.4, while the *sp*-states are less than half-filled and correspond to the panel (b) in Fig. 6.4. In both panels (a) and (b), the bandwidth decreases; this is brought about by the decrease in ECN. To keep the filling constant, the bands shift such that: (a) the band center of the more than half-filled band moves up in energy, whereas (b) the band center of the less than half-filled band moves down in energy. This explains why the *d*- and *sp*-states shift in opposite directions on reducing coordination.

Note that for the above arguments to hold, it is necessary to have partially filled bands; if in our systems the *d*-states of Au were completely occupied (as they are in the Au atom), then the *d*-band center would *not* go up on reducing coordination; the reason this argument works is that some *d* electrons in all the systems considered by us are transferred to *s* and *p* states [see Figs. 6.3 (c) and (d)].

Note moreover that this model explains the shift in the energy states due to a reduction in the bandwidth (brought about by decreasing ECN) assuming that the filling in the states is constant. However, from Figs. 6.3(c) and (d), we see that the filling in the *d*- and *sp*-states varies as a function of ECN. The reducing bandwidth and the change in filling have opposite effects on the band centers. In the case of the *d*-states, when the bandwidth decreases keeping filling constant, the band center of the more than half-filled band is expected to go up in energy, whereas when filling increases keeping the bandwidth constant, the band center is expected to move down in energy. (A cartoon model of how an increase in the filling in the states affects band centers is shown in Fig. 5.7.) In the case of the *sp*-states, when the bandwidth decreases keeping filling constant, the band center of the less than half-filled band is expected to move down in energy, whereas when the filling decreases keeping the bandwidth constant, the band center is expected to move up in energy. The filling in both states changes by only 0.3 e over the range of ECN studied by us, while the bandwidths of the *d*- and *sp*-states reduce by 2.9 eV and 5.2 eV respectively. This suggests that the shifts in band centers may be mainly governed by the reduction in

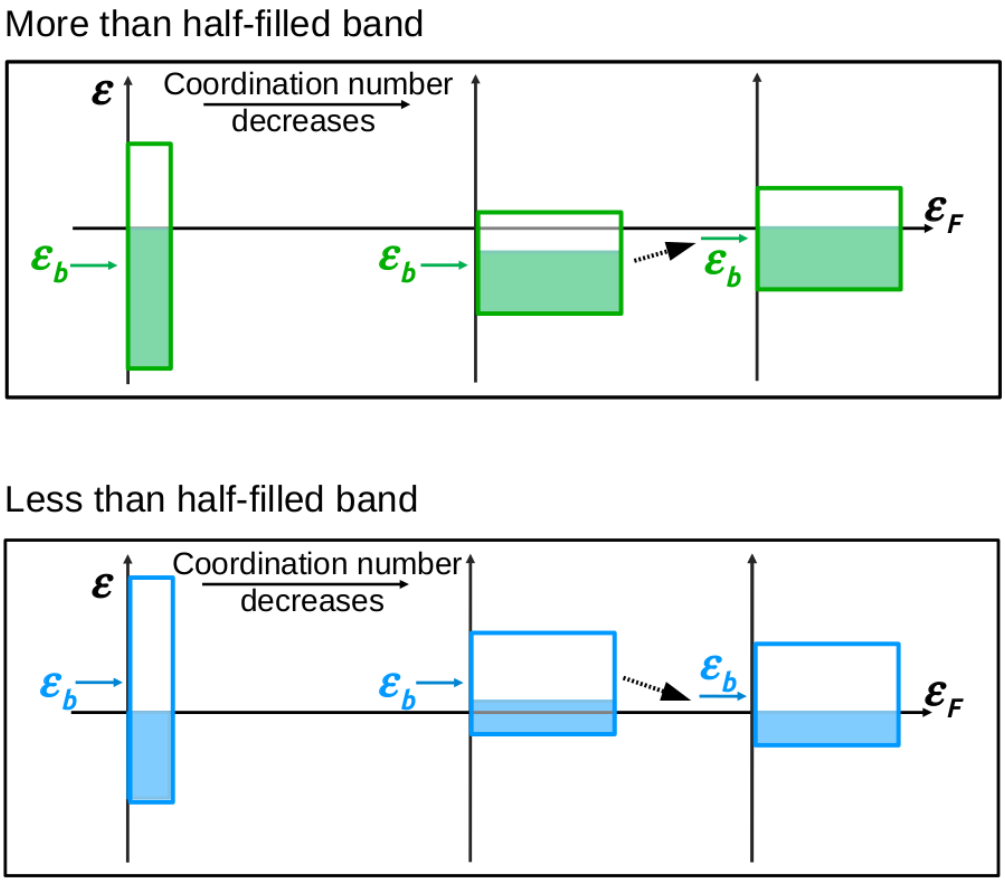

Figure 6.4: *Cartoon model showing the densities of states (DOS) of two bands with (a) more than half-filling and (b) less than half-filling. For both cases bandwidth decreases with the decrease in the coordination number and to keep filling constant, (a) the band with more than half-filling moves up in energy, while (b) the band with less than half-filling moves down in energy. Panel (a) is relevant to Au d-states and panel (b) is relevant to Au sp-states.*

the bandwidth, and hence we see the observed results.

In the d-band model proposed by Hammer and Nørskov,[5] the equation for the energy of the transition state after the interaction of the molecule with the metal s- and d-bands is given by:

$$\delta E_{ts} \sim -\frac{2V^2}{\varepsilon_a\prime - \varepsilon_d} - 2(1-f)\frac{2V^2}{\varepsilon_d - \varepsilon_b\prime} + \alpha V^2. \tag{6.4}$$

Here, $\varepsilon_a\prime$ and $\varepsilon_b\prime$ are the energies of the molecular levels after interaction with the metal s-band, f is the occupation of the metal d-band (normalized to one), V is the coupling matrix element between the molecular levels and the d-band of the metal and α is the proportionality constant in the orthogonalization term. (This equation is explained in

detail in the previous chapter.) Since in Au, the *d*-band is almost completely filled ($f \sim 1$), this equation reduces to:

$$\delta E_{ts} \sim -\frac{2V^2}{\varepsilon_a\prime - \varepsilon_d} + \alpha V^2. \tag{6.5}$$

In the *d*-band model, since the interaction with the *s*-band is considered to be the same for all metals, $\varepsilon_a\prime$ is a constant. So the only way to reduce the transition state energy (to make the first term on the right-hand-side more negative) is by pushing up ε_d. As ε_d moves up in energy, the transition state energy decreases, and the reactivity of the metal increases.

From our results however, we find that the *sp*-states are not static and they shift in energy by a larger extent than the *d*-states. In the previous chapter, we showed how one can approximate $\varepsilon_a\prime = \varepsilon_{sp} - \delta$, where δ is a constant shift in energy. To incorporate the changes in the behavior of the *sp*-electrons, we extend the *d*-band model to:

$$\delta E_{ts} \sim -\frac{2V^2}{\varepsilon_{sp} - \varepsilon_d - \delta} + \alpha V^2. \tag{6.6}$$

We suggested in the previous chapter that $\Delta E \equiv \varepsilon_{sp} - \varepsilon_d$ could be a descriptor for the reactivity of Au clusters. The lower the value of ΔE, better is the reactivity. In the *d*-band model, the focus is on pushing up ε_d for increasing the reactivity of the metal. On reducing the dimensionality of Au, or on reducing ECN, we see two effects: ε_d moves up in energy and ε_{sp} moves down in energy. Both effects act to lower ΔE and increase the reactivity of Au. In Fig. 6.5, we show how $\varepsilon_{sp} - \varepsilon_d$ varies as a function of ECN. As ECN decreases, $\varepsilon_{sp} - \varepsilon_d$ decreases.

We show that in addition to the *d*-states of Au, the *sp*-states are also affected when we go from bulk systems to nano Au. We find that the *sp*-states shift by a greater extent than the *d*-states as ECN is reduced. The *d*-band model or the position of ε_d successfully explains the increase in reactivity when we go from bulk systems to nano Au. We find that our descriptor, $\varepsilon_{sp} - \varepsilon_d$, also explains the observed trend in reactivity; further work is needed in order to identify situations where one or the other descriptor works better.

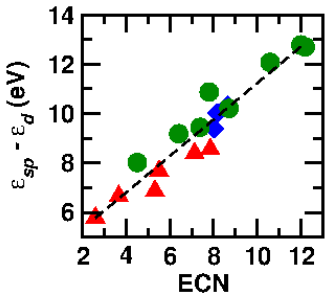

Figure 6.5: *$\varepsilon_{sp} - \varepsilon_d$, the difference in energies of the sp- and d-states of Au as a function of effective coordination number (ECN). As ECN decreases, $\varepsilon_{sp} - \varepsilon_d$ also decreases.*

(We note that in the case of substrate doping studied in the previous chapter, ε_d was not a successful descriptor of barrier lowering upon doping, whereas $\varepsilon_{sp} - \varepsilon_d$ seemed to be rather promising.)

6.3.2 Changing Au Coordination by going from a Face site to an Edge site to an Apex site on an Au cluster

Au_{20} is a highly stable nanocluster of Au[33] and is found to be highly catalytically active towards CO oxidation. It has been the subject of investigation for several previous studies.[10,11,31,34,36,121,179] It is known to have a highly robust tetrahedral structure with all its atoms on the surface.[33] There are three inequivalent Au sites in this cluster: a face site, an edge site and an apex site; they are shown by the brown, orange and yellow spheres respectively in Fig. 6.6. The nominal coordination numbers of Au atoms in the face, edge and apex sites are 9, 6 and 3 respectively; their effective coordination numbers are 9.38, 7.63 and 4.67 respectively. In this section, we study how the electronic properties of Au atoms change on going from the face site to the edge site and to the apex site in this cluster.

In Fig. 6.7, we show our results for how the properties like bandwidths, filling and band centers change on going from the face site to the edge site and to the apex site. In Figs. 6.7(a) and (b), we show how the bandwidths of the *d*-states and *sp*-states respectively change as a function of ECN. On reducing ECN, or on going from the face site to the apex site, we see that the bandwidth of the *d*-states reduces slightly, the bandwidth of the *sp*-states however reduces by a large amount. The reduction in the bandwidth is expected,

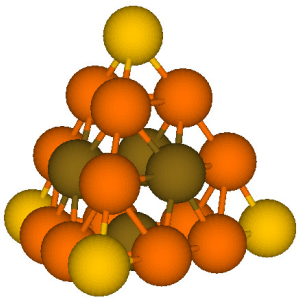

Figure 6.6: *The optimized geometry obtained for the Au_{20} tetrahedral cluster in the gas phase. It is a highly symmetric cluster, and has three inequivalent Au sites: it has four Au atoms in the face site, 12 Au atoms in the edge site and four Au atoms in the apex site. The atoms in the face, edge and apex sites are represented by the brown, orange and yellow spheres respectively.*

since it is known that bandwidth reduces on reducing coordination number.

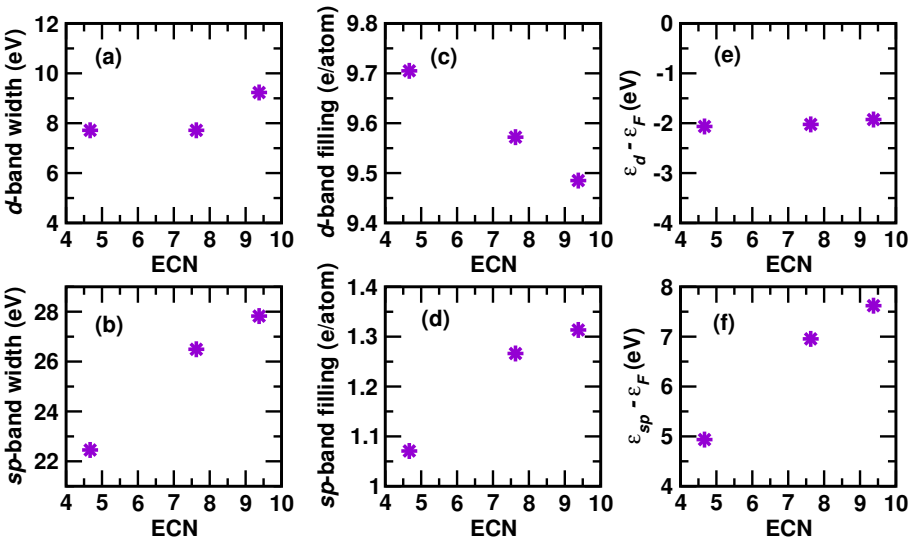

Figure 6.7: *Changes in the electronic structure when the effective coordination number (ECN) of Au atoms in the $Au_{20}(T)$ cluster is reduced: (a) d-bandwidth, (b) sp-bandwidth, (c) d-band filling, (d) sp-band filling, (e) d-band center, ε_d, and (f) sp-band center ε_{sp}, all as a function of the ECN. On moving from the face site to the edge site to the apex site, we are reducing ECN. Note that ε_d and ε_{sp} are referenced to the Fermi level.*

On examining the filling in the *d*- and *sp*-states [see Figs. 6.7(c) and (d)], we find that as ECN reduces, *d*-band filling increases while *sp*-band filling decreases. This is in agreement with what we found on reducing the dimensionality of Au, on going from bulk and extended systems to nanoclusters.

Next, we look at how the band centers shift as we go from a face site to an edge site and to an apex site on the Au(T) cluster. In Fig. 6.7(e), we see that the *d*-band center shifts

slightly in energy, but in a direction opposite to what is expected. As ECN decreases, the *d*-band center moves down in energy. In Fig. 6.7(f) however, we find that the *sp*-band center shifts downward by a large amount, closer to the Fermi energy.

It is known that the active sites for a reaction tend to be the corner sites or low coordination sites on a cluster. For Au_{20}(T), previous authors have reported that the most active site is the apex site.[10,31,34,180] We would like to confirm this, and we study the adsorption of an O_2 molecule at the face site, edge site and apex site on the Au_{20}(T) cluster. We define the adsorption energy of O_2, $E_b^{O_2} = -\{E[O_2/Au(T)] - E[Au(T)] - E(O_2)\}$, and show our results in Fig. 6.8(a). We find, in agreement with earlier studies, that the apex site shows the highest reactivity towards O_2 adsorption, followed by the edge site. The adsorption of O_2 at the face site is unfavorable, this is also in agreement with earlier studies.[34] We find a good correlation between the ECN of the Au atom on which the O_2 is adsorbed and $E_b^{O_2}$.

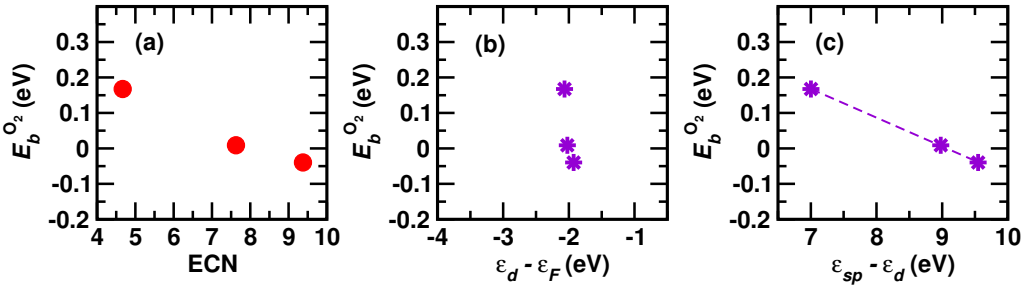

Figure 6.8: *Looking for descriptors for binding on Au_{20}(T): (a)$E_b^{O_2}$, the adsorption energy of O_2 at different sites on the Au(T) cluster. Highest binding is observed at the apex site. (b) $E_b^{O_2}$ is plotted against the d-band center, ε_d, of the Au atom to which the O_2 is binding; ε_d moves down in energy as we move from the face site to the apex site on the cluster which is opposite to what is expected if the d-band model were to explain these results. (c) $E_b^{O_2}$ is plotted against the descriptor $\varepsilon_{sp} - \varepsilon_d$ of the Au atom to which the O_2 is binding; $E_b^{O_2}$ increases as $\varepsilon_{sp} - \varepsilon_d$ moves down in energy, as expected.*

In Fig. 6.8(b), we examine how the *d*-band center of the Au atom to which O_2 is binding correlates with the adsorption energy of O_2, $E_b^{O_2}$. We find that the *d*-band center shifts in a direction opposite to what is expected if the *d*-band model were to explain these results. The *d*-band model suggests that the higher the *d*-band center, better will be the reactivity; however we see that ε_d moves down in energy while observing an increase in $E_b^{O_2}$.

In Fig. 6.8(c), we show how $\varepsilon_{sp} - \varepsilon_d$ of the Au atom to which O_2 is binding, correlates with $E_b^{O_2}$. On going from the face site to the edge site and to the apex site, we see that $\varepsilon_{sp} - \varepsilon_d$ comes down in energy; $E_b^{O_2}$ increases as $\varepsilon_{sp} - \varepsilon_d$ decreases. This means that $\varepsilon_{sp} - \varepsilon_d$ explains the observed trend in reactivity.

To summarize the findings in this section: on changing the coordination of Au by going from a face site to an edge site and to an apex site, we find that the *sp*-states of Au are significantly affected, in addition to the *d*-states of Au. The *sp*-electrons shift by a higher extent on reducing ECN, as compared to *d*-electrons. We find that the reactivity towards O_2 increases in the order face site > edge site > apex site. We find that ε_d moves in a direction opposite to what is expected; the *d*-band model fails to explain the observed trend in reactivity. However, the descriptor $\varepsilon_{sp} - \varepsilon_d$ is able to explain this trend successfully.

6.3.3 Changing the Charge state of Au clusters

The decrease in coordination number is known to be the most important factor in improving the reactivity of Au in nanosystems. Another effect that has been shown to improve the reactivity of Au clusters towards O_2 is negatively charging Au clusters.[30,32,34,142,143] To study the effect of the charge state on the electronic properties of an Au cluster, we have considered three Au clusters viz., Au_{20}(T), Au_8 and Au_3, each with charges +2, +1, 0, -1 and -2.

We have not (yet) performed calculations to study the trend in the reactivity of these clusters towards O_2 as a function of the charge state. In this chapter, we only discuss how the electronic properties vary as a function of the charge state of the cluster.

We show our results for the *d*-bandwidth and *sp*-bandwidth in Figs. 6.9(a) and (b) respectively for the three clusters: Au_{20}(T), Au_8 and Au_3 as a function of the charge state of the cluster. We find that the *d*-bandwidth of the clusters changes almost negligibly on positively or negatively charging the clusters. The *sp*-bandwidth of the clusters however decreases monotonically for each cluster as the charge state of the cluster changes from +2 to +1 to 0 to -1 to -2. The *sp*-bandwidths of Au_{20}(T), Au_8 and Au_3 reduces by 3.5

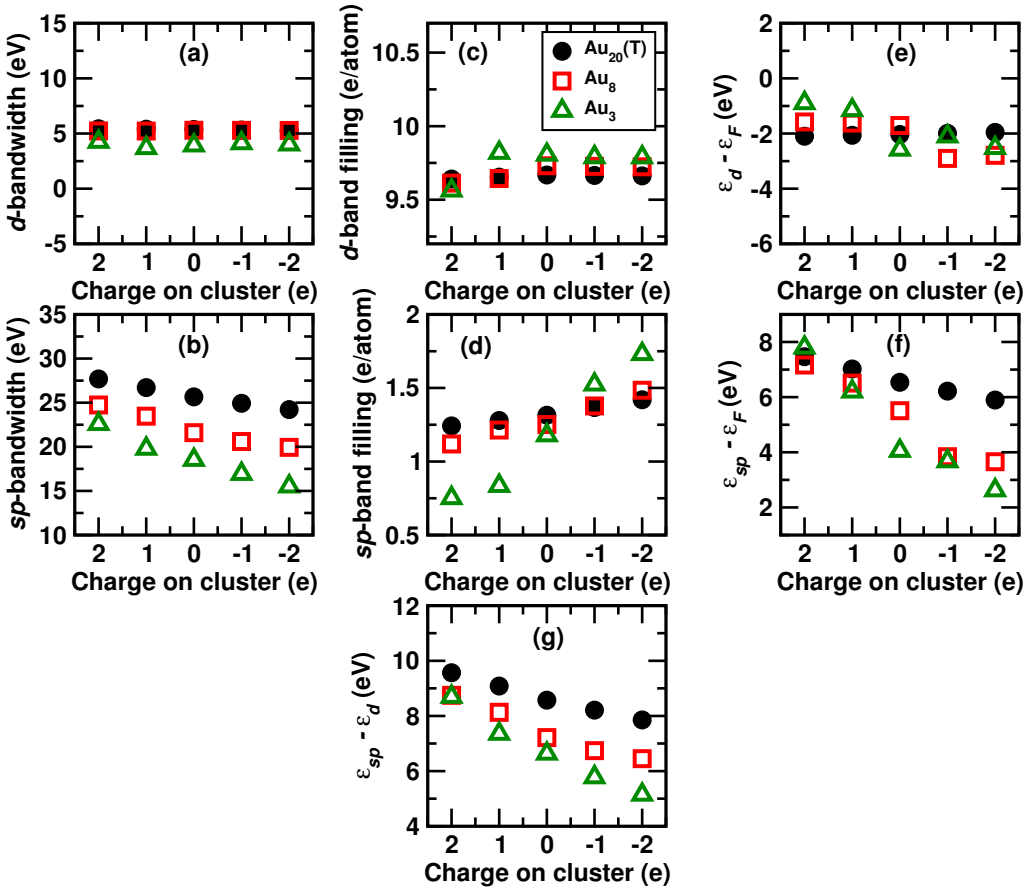

Figure 6.9: *Changes in the electronic structure of $Au_{20}(T)$, Au_8 and Au_3 clusters upon charging: (a) d-bandwidth, (b) sp-bandwidth, (c) d-band filling, (d) sp-band filling, (e) d-band center, ε_d, (f) sp-band center, ε_{sp} and (g) $\varepsilon_{sp} - \varepsilon_d$, all averaged over the atoms in the cluster plotted as a function of the charge state of the cluster. The black filled circles, red hollow squares and green hollow triangles represent $Au_{20}(T)$, Au_8 and Au_3 respectively.*

eV, 4.8 eV and 7.1 eV respectively as the charge state changes from +2 to -2; the smaller the cluster, the larger is the effect on the *sp* bandwidth of the change in the charge state.

In Figs. 6.9(c) and (d), we show our results for the *d*-band filling and *sp*-band filling respectively. We find that on changing the charge state of the Au_{20}(T), Au_8 and Au_3 clusters from +2 to -2, the *d*-band filling varies very little, however the *sp*-band filling increases by a large amount. The effect of the change in the charge state of a cluster decreases as the size of the cluster increases, this is because the charge on the cluster is uniformly distributed over all the atoms in the cluster.

In Figs. 6.9(e) and (f), we show our results for the *d*-band center and *sp*-band center positions as a function of the charge state of the cluster. For the Au_{20}(T) cluster, on

changing the charge state from +2 to -2, we see that the *d*-band center shifts monotonically up in energy by 0.1 eV, for the Au_8 and Au_3 clusters however, we see that the *d*-band center position shifts non-monotonically. For Au_8, we see that ε_d shifts down in energy on going from +2 to +1 to 0 and to -1 and slightly shifts up in energy when the charge state is -2. In the case of Au_3, we see that both positively charged and negatively charged clusters have a higher ε_d compared to the neutral cluster. For both Au_8 and Au_3, we find that ε_d is higher for the positively charged clusters than for the negatively charged clusters. This is opposite to what we would expect; the *d*-band model cannot explain why negatively charged clusters have better reactivity towards O_2 than positively charged clusters. The *sp*-band centers of all the three clusters considered move down in energy as the charge state changes from +2 to -2. In Fig. 6.9(g), we show how $\varepsilon_{sp} - \varepsilon_d$ varies due to the change in the charge state of the cluster. For all three clusters, we see that on changing the charge state of the cluster from +2 to -2, $\varepsilon_{sp} - \varepsilon_d$ decreases monotonically. Negatively charged Au clusters have a lower value of $\varepsilon_{sp} - \varepsilon_d$ than neutral or positively charged clusters. If indeed $\varepsilon_{sp} - \varepsilon_d$ is a satisfactory descriptor for the reactivity of charged Au clusters, this suggests that negatively charged Au clusters will have a higher reactivity towards O_2 adsorption compared to neutral or positively charged clusters. However, further calculations on adsorption energies and barriers, and possibly other sizes of clusters, are needed before we can say this conclusively.

6.4 Conclusions

In this chapter, we have looked at how the *s* and *p* electrons of Au behave on reducing the coordination number of Au and on changing the charge state of an Au cluster. We have studied two situations where the coordination number of Au is reduced: (a) when we go from extended systems to nano systems and (b) when we go from a face site to an edge site and to an apex site on the same nanocluster.

We find that the *s* and *p* electrons of Au are significantly affected by the reduction in coordination as well as the change in charge state; this manifests as larger changes in the bandwidths and energies of the *sp*-electrons than the *d*-electrons of Au. On going from

bulk extended systems to surfaces to nanoclusters, we see that the bandwidths of the both the *d*- and *sp*-states reduce significantly, and this results in an upward shift in energy of the *d*-band center while the *sp*-band center shifts downward in energy. The *d*-band model has been used to explain the tremendous increase in the activity of Au on going from bulk to nano systems; the new descriptor suggested by us, $\varepsilon_{sp} - \varepsilon_d$, is also able to successfully explain this trend.

On going from the face site to the edge site and to the apex site on an Au_{20}(T) cluster, we find that on reducing the coordination number of Au, the *d*-bandwidth and *d*-band center of Au are not significantly affected. The *d*-bandwidth reduces by 1.52 eV, and the *d*-band center moves down in energy (opposite to what we expect) by 0.14 eV. The *sp*-bandwidth however, reduces significantly (by 5.37 eV) and the *sp*-band center shifts down in energy by 2.68 eV (i.e., in the expected direction). We study the adsorption of O_2 at the three sites, and find that the adsorption energy is highest at the apex site followed by the edge site and the face site. We find that the O_2 adsorption energy, $E_b^{O_2}$, correlates very well with the effective coordination number of these atoms; the lower is the ECN, the higher is $E_b^{O_2}$. The *d*-band center shifts downward in energy on going from the face site to the edge site and to the apex site on the cluster, hence the *d*-band model fails to explain the observed trend in reactivity. We, however, find that the new descriptor, $\varepsilon_{sp} - \varepsilon_d$, correlates very well with the calculated value of $E_b^{O_2}$; the lower the value of $\varepsilon_{sp} - \varepsilon_d$, the higher is the adsorption energy; we obtain a linear relationship between the two.

On changing the charge state of Au clusters, we find that the *d*-bandwidth of Au changes negligibly, however the *sp*-bandwidth of Au decreases monotonically for a cluster as the charge state changes from +2 to +1 to 0 to -1 to -2. The *d*-band filling is affected very little, and the removal or addition of electrons due to positively or negatively charging these clusters occurs mainly in the Au *sp*-states. The *d*-band center of Au_{20}(T) increases monotonically on negatively charging the cluster, but only by a very small amount of 0.1 eV. The *d*-band centers of Au_8 and Au_3 show a non-monotonic behavior as a function of charge, but show that positively charged clusters have higher ε_d than negatively charged clusters. This again is opposite to what is expected if the *d*-band model would explain

why negatively charged clusters have better reactivity towards O_2 than positively charged clusters. The *sp*-band centers, ε_{sp}, move down in energy monotonically for all clusters as we go from positively charged clusters to neutral and negatively charged clusters; and shift by a larger amount than ε_d. We also find that $\varepsilon_{sp} - \varepsilon_d$ reduces significantly on going from positively charged clusters to neutral to negatively charged clusters. If indeed $\varepsilon_{sp} - \varepsilon_d$ is a satisfactory descriptor for the reactivity of charged Au clusters, this suggests that negatively charged Au clusters will have a higher reactivity towards O_2 adsorption compared to neutral or positively charged clusters. However, further calculations on adsorption energies and barriers, and possibly other sizes of clusters, are needed before we can say this conclusively.

Our results suggest that the *s* and *p* electrons, in addition to the *d* electrons, may play a vital role in explaining the improved reactivity of Au on going from bulk to nano systems, the high reactivity at low coordinated sites on an Au cluster, and also the improved reactivity observed in negatively charged Au clusters compared to neutral and positively charged Au clusters. We consider the work presented in this chapter to be in the light of an intriguing preliminary study that suggests the conclusions drawn in the previous chapter about the importance of *s* and *p* electrons in Au nanocatalysis may be extended to a wider domain; a larger number of calculations is needed before a full picture can emerge.

Section C

Chapter 7

Size-dependent Oxidation and Reduction of Gas phase Cu clusters

In this chapter, we investigate the oxidation and reduction of gas phase Cu clusters. We examine the size-dependence of these phenomena by studying three different sizes of Cu clusters in the gas phase: $n = 4$, 12 and 20, in oxidizing and reducing environments.

7.1 Introduction

Oxidation is a process in which different substances react with oxygen. Photosynthesis in plants, respiration and the internal metabolism in humans, and combustion of fuels to generate energy are only a few examples of processes where oxidation is of paramount significance. However, the oxidation process may not always be beneficial, for example, the rusting of iron can lead to structural damage, and oxidation of a metal catalyst can lead to the loss of its catalytic activity. Metals in nanosizes are now widely being recognized as good catalysts for several reactions; the reduction in the size not only increases the exposed surface area per unit cost of the metal, but also significantly improves the catalytic activity of the metal.

In the nano-regime, size is central in determining the physical, chemical and electronic properties of a particle. The size of a particle also affects its tendency to oxidize, and particles with different sizes may be in different oxidation states in a given reaction condition. Therefore, when dealing with metal nanoparticles, it is crucial to know what size of the catalyst is best for a given chemical reaction. For a chemical reaction with a specified set of environmental conditions, a metal nanoparticle may be catalytically most active when it has a particular size and a particular oxidation state. A change in the oxidation state of the metal may lead to a degradation in its catalytic activity. So, given a set of experimental conditions, one needs to know what is the stable oxidation state of a given size of a metal nanoparticle. There are several chemical reactions where these questions have strong implications; as two examples we mention the commercially important Fischer-Tropsch synthesis of hydrocarbons using Co, Fe, or Ru as the catalyst, and the proton exchange membrane fuel cells using Pt nanoparticles as the catalyst. In both these cases, the catalyst is catalytically active in its elemental, unoxidized form, and its performance is severely degraded by the oxidation of the metal catalyst.[181]

In this chapter, we investigate size effects on the oxidation/reduction of copper nanoparticles in the gas phase. Cu is known to be a catalyst for several important reactions like the synthesis of methanol from aldehyde,[18] the oxidative steam reforming of methanol to produce hydrogen,[19,182] and soot removal in diesel exhausts.[183] In certain reactions, it is preferable for the catalyst to be in the elemental state,[184] while for others it is preferable for the catalyst to have a certain degree of oxidation. For the steam reforming reaction, it has been observed that a CuO catalyst has the highest activity,[40,185] and for methanol oxidation to aldehyde, the catalyst becomes active only in the presence of a certain amount of oxygen.[186] For all such reactions, it is hence necessary to have knowledge about the oxidation state that copper nanoparticles of a given size would acquire under a given set of environmental conditions.

Previous studies that deal with size effects in the oxidation of metal nanoparticles have been very few in number, and all for other metals. It was found in an earlier experimental study on iron–iron oxide core-shell nanoparticles that the oxide content increased as the

size of the particle was reduced. Fe atoms in smaller particles were found to be in relatively higher oxidation states: smaller particles were richer in maghemite (γ-Fe_2O_3) as compared to magnetite (Fe_3O_4).[187] A theoretical study on Co nanoparticles using empirical model potentials was able to conclude that particles with diameter less than 4.4 nm would not be stable in their elemental state in realistic conditions that exist for Fischer-Tropsch synthesis.[188] This was validated by an experimental finding that only Co clusters with a diameter of more than 6 nm are stable against oxidation in such conditions.[189]

From a first-principles study using DFT combined with *ab initio* atomistic thermodynamics (AIATD) on the oxidation of gas phase Ag clusters,[190] it was reported that very small Ag clusters are *more* resistant to oxidation than bulk Ag or Ag surfaces; the thermal stability of the oxide was found to decrease with cluster size. This result is opposite to what one would expect considering that Ag is easily susceptible to oxidation,[191,192] and the fact that all the other metals reported above show an increased reactivity towards oxygen as size decreases. For the oxidation of small Mg clusters in the gas phase, using a combination of DFT and AIATD, it was found that non-stoichiometric ($Mg_MO_{x>M}$) clusters are favored over stoichiometric (Mg_xO_x) clusters at smaller sizes.[193] To the best of our knowledge, these techniques have not been used previously to study the oxidation of Cu nanoparticles. However, they have been applied to study the bulk $Cu_2O \rightarrow CuO$ transition,[194] the phase diagram of bulk Cu and its oxides,[195] the oxidation of Cu surfaces,[196–198] and the reduction of copper oxide surfaces.[199]

In this chapter, we study three sizes of Cu_n clusters with $n = 4$, 12 and 20, in their elemental phase and also in different oxide phases. To study the processes of both oxidation and reduction, we consider the clusters in two environments: (a) oxidizing environment in the presence of O_2, and (b) in the presence of H_2 and H_2O; this can be either an oxidizing or reducing environment, depending on the relative partial pressures of H_2 and H_2O.

7.2 Methods

The general strategy followed in this study was to first generate starting geometries for the clusters using semi-empirical classical potentials and simulated annealing as implemented

in the LAMMPS code[85]; these structures were then refined using *ab initio* density functional theory (DFT) calculations. The *ab initio* atomistic thermodynamics method was then used to determine the relative stability of the different oxide phases, under varying temperatures and partial pressures of oxygen, water and hydrogen.

7.2.1 Step 1: Initial Guesses for Cluster Geometries using Classical Potentials

The initial guesses for the geometries of the elemental clusters Cu_n, and oxidized clusters Cu_nO_x, were obtained by molecular dynamics (MD) simulations treating the interatomic interactions with the charge optimized many-body (COMB) potential[82]. For these calculations, all clusters were placed in a cubical box of side 30 Å. Low energy geometries were then obtained using simulated annealing: the clusters were first heated to high temperatures (1000 K for Cu_4 and Cu_{12} clusters and 1500 K for Cu_{20} clusters) and then cooled at four different rates to obtain four different low energy structures, for each size of cluster and each value of x considered.

7.2.2 Step 2: Refinement of Geometries using Density Functional Theory

Density functional theory calculations were then performed on the elemental and oxide clusters, using the final structures obtained using classical potentials + simulated annealing as the initial geometries, and then further optimizing these geometries so as to obtain stable geometries; the lowest in energy of these was then considered to be the ground state structure which was used further in Step 3. Note that the lowest energy geometry obtained from the classical potentials need not necessarily lead to the lowest energy structure as given by DFT, this is the reason why we retain several of the geometries obtained in Step 1 for each n and each x; this phenomenon occurs because of errors in the classical potentials.

The reason for following such a two-step procedure is that it not only allows us to span a space of several possible geometries, but is believed to increase the likelihood of finding the global minimum structure, which is of course a hard problem to solve.

The *ab initio* spin polarized DFT calculations were performed using the VASP package,[54–57] with the Perdew-Burke-Ernzerhof (PBE) approximation for the exchange correlation functional[47] and Projector Augmented Wave (PAW) potentials[65,200]. The wavefunctions were expanded using a plane wave basis set, with an energy cut-off of 400 eV. The Brillouin zone was sampled only at the zone center Γ. In the DFT calculations too, the clusters were placed in a cubical box of side 30 Å.

7.2.3 Step 3: AIATD to study Oxidation and Reduction

The *ab initio* atomistic thermodynamics (AIATD) method[24,25] was utilized to study the relative stability of the elemental and oxide phases of Cu clusters in two kinds of equilibrium conditions:

(i) in the presence of O_2:

$$2\mathrm{Cu}_n + x\mathrm{O}_2 \rightleftharpoons 2\mathrm{Cu}_n\mathrm{O}_x, \tag{7.1}$$

(ii) in the presence of H_2 and H_2O:

$$\mathrm{Cu}_n\mathrm{O}_x + x\mathrm{H}_2 \rightleftharpoons \mathrm{Cu}_n + x\mathrm{H}_2\mathrm{O}. \tag{7.2}$$

The Gibbs free energy of oxide formation, at a temperature T, and a partial pressure of oxygen p_{O_2}, of $\mathrm{Cu}_n\mathrm{O}_x$ clusters in the presence of oxygen, is given by:

$$\Delta G(T, \Delta\mu_{\mathrm{O}}) \approx E^{DFT}_{\mathrm{Cu}_n\mathrm{O}_x} - E^{DFT}_{\mathrm{Cu}_n} - x\left[\frac{1}{2}E^{DFT}_{\mathrm{O}_2} + \frac{1}{2}E^{ZPE}_{\mathrm{O}_2} + \Delta\mu_{\mathrm{O}}(T, p_{\mathrm{O}_2})\right]; \tag{7.3}$$

where $\Delta\mu_O(T, p_{\mathrm{O}_2})$ is defined by:

$$\Delta\mu_{\mathrm{O}}(T, p_{\mathrm{O}_2}) = \mu_O(T, p_{\mathrm{O}_2}) - \frac{1}{2}E^{DFT}_{\mathrm{O}_2} - \frac{1}{2}E^{ZPE}_{\mathrm{O}_2}. \tag{7.4}$$

Here, $E^{DFT}_{\mathrm{Cu}_n\mathrm{O}_x}$ and $E^{DFT}_{\mathrm{Cu}_n}$ are the total energies from DFT of the oxide cluster and the elemental cluster respectively. Note that $\mu_{\mathrm{O}} = (1/2)\mu_{\mathrm{O}_2}$, where μ_{O} and μ_{O_2} are the chemical potentials of oxygen atoms and oxygen molecules respectively. $E^{DFT}_{\mathrm{O}_2}$ is the total

energy (as obtained from DFT) of an isolated O_2 molecule in the gas phase, and $E_{O_2}^{ZPE}$ is its zero point energy, which is evaluated by making use of vibrational frequencies obtained using density functional perturbation theory.[201,202]

The temperature and pressure dependence of $\Delta\mu_O$ is given by:

$$\Delta\mu_O(T, p_{O_2}) = \mu_O(T, p^0) - \mu_O(T^0, p^0) + \frac{1}{2}k_B T \ln(p_{O_2}/p^0); \tag{7.5}$$

where T^0 and p^0 are the reference temperature and pressure respectively, and k_B is Boltzmann's constant. The values of $\mu_{O_2}(T, p^0)$ are obtained from the JANAF thermochemical tables.[203]

Substituting Eq. (7.5) in Eq. (7.3), we get:

$$\begin{aligned}\Delta G(T, p_{O_2}) \approx\ & E_{Cu_nO_n}^{DFT} - E_{Cu_n}^{DFT} \\ & - x\left(\frac{1}{2}E_{O_2}^{DFT} + \frac{1}{2}E_{O_2}^{ZPE} + \mu_O(T, p^0) - \mu_O(T^0, p^0) + \frac{1}{2}k_B T \ln(p_{O_2}/p^0)\right).\end{aligned} \tag{7.6}$$

In Eq. (7.2), the forward reaction represents the reduction of copper oxide clusters to form elemental Cu clusters and H_2O. The Gibbs free energy for the reduction reaction is given by:

$$\begin{aligned}\Delta G(T, \Delta\mu_{H_2}, \Delta\mu_{H_2O}) \approx\ & E_{Cu_n}^{DFT} + x\left[E_{H_2O}^{DFT} + E_{H_2O}^{ZPE} + \Delta\mu_{H_2O}(T, p_{H_2O})\right] \\ & - E_{Cu_nO_x}^{DFT} - x\left[E_{H_2}^{DFT} + E_{H_2}^{ZPE} + \Delta\mu_{H_2}(T, p_{H_2})\right];\end{aligned} \tag{7.7}$$

where $\Delta\mu_X$ is defined by:

$$\Delta\mu_X(T, p_X) = \mu_X(T, p_X) - E_X^{DFT} - E_X^{ZPE}; \tag{7.8}$$

here $\mu_X(T, p_X)$, E_X^{DFT}, and E_X^{ZPE} are respectively the chemical potential at temperature T and partial pressure p_X, the total energy, and the zero point energy, of the chemical species X.

The temperature and pressure dependence of $\Delta\mu_X$ is given by:

$$\Delta\mu_X(T, p_X) = \mu_X(T, p^0) - \mu_X(T^0, p^0) + k_\mathrm{B}T\ln(p_X/p^0). \tag{7.9}$$

The values of $\mu_X(T, p^0)$ are obtained from the JANAF thermochemical tables.[203]

Substituting Eq. (7.9) for $X = H_2O$ and $X = H_2$ in Eq. (7.7), we get:

$$\begin{aligned}\Delta G(T, p_{H_2}, p_{H2O}) \approx\ & E^{DFT}_{Cu_n} + x\left(E^{DFT}_{H_2O} + E^{ZPE}_{H_2O} + \mu_{H_2O}(T, p^0) - \mu_{H_2O}(T^0, p^0)\right) \\ & - E^{DFT}_{Cu_nO_x} - x\left(E^{DFT}_{H_2} + E^{ZPE}_{H_2} + \mu_{H_2}(T, p^0) - \mu_{H_2}(T^0, p^0)\right) \\ & - xk_\mathrm{B}T\ln(p_{H_2}/p_{H_2O}).\end{aligned} \tag{7.10}$$

We assume that for reactions in both the O_2 environment and the $H_2 + H_2O$ environment, the vibrational contributions will largely cancel out between Cu_n and Cu_nO_x.

7.3 Results

7.3.1 Step 1: Initial Guesses for Cluster Geometries using Classical Potentials

In Fig. 7.1, we show three low energy geometries each for $n = 4$, 12 and 20, obtained from simulated annealing using the COMB potentials. The geometries in Figs. 7.1(a), (d) and (g) are the lowest energy structures obtained for Cu_4, Cu_{12} and Cu_{20}, respectively. The relative total energy of each cluster with respect to the lowest energy structure for that n is noted below each structure.

From these classical simulations, we find that a tetrahedral geometry for Cu_4 has the lowest energy. However, it is known from previous DFT calculations (which are expected to be more accurate than these classical calculations) that a Cu_4 cluster in the gas phase prefers a rhombus geometry as shown in Fig. 7.1(b).[204,205] Further below, we will see that we too find in Step 2, where we perform DFT calculations, that the lowest energy geometry is a rhombus rather than a tetrahedron. This serves as an example of why it is good to retain several of the low energy geometries obtained in Step 1, when proceeding

to Step 2.

The lowest energy structure obtained from these classical simulations for Cu_{12} is an icosahedron. This is in agreement with previous DFT results.[206] However in this previous DFT study, the authors have considered only structures with high symmetries viz., icosahedral symmetry (I_h) and octahedral symmetry (O_h). Further below in Step 2, from our DFT calculations we find a structure that is lower in energy by 1.5 eV compared to the icosahedral structure.

For the Cu_{20} cluster, the classical simulations fail to reproduce previous DFT results, which suggests a compact structure with C_s symmetry for Cu_{20}.[179] In Step 2, from our DFT calculations we obtain a structure with C_s symmetry which is the lowest energy structure and is only slightly distorted from the structure given by previous authors.[179]

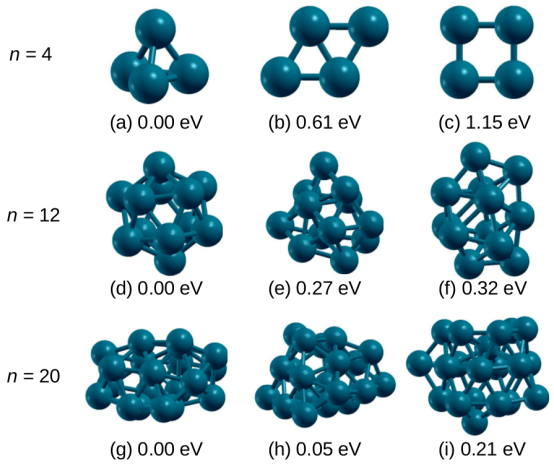

Figure 7.1: *Low energy geometries obtained from classical potentials for elemental (a), (b), (c) Cu_4, (d), (e), (f) Cu_{12}, and (g), (h) and (i) Cu_{20} clusters. For $n = 4$, the structures were obtained by relaxation using the BFGS algorithm, while all the other structures were generated using simulated annealing. The geometries in (a), (d) and (g) are the lowest energy structures obtained for Cu_4, Cu_{12} and Cu_{20} respectively. The relative energy of a cluster with respect to the lowest energy structure for that n is noted below each cluster.*

To study Cu_4O_x clusters, we have considered values of $x = 1 - 8$, similarly to study $Cu_{12}O_x$ and $Cu_{20}O_x$ clusters, we have considered values of $x = 1 - 12$, and $x = 1 - 20$, respectively. Two low energy structures generated for each Cu_4O_x, $Cu_{12}O_x$ and $Cu_{20}O_x$ are shown in Figs. 7.2, 7.3 and 7.4 respectively. The binding energy of oxygen for Cu_nO_x was computed using the equation: $E_b^O = -\frac{1}{x}\{E_{Cu_nO_x} - E_{Cu_n} - \frac{x}{2}E_{O_2}\}$, where $E_{Cu_nO_x}$, E_{Cu_n} and E_{O_2} are the total energies of the oxide cluster, elemental cluster and an O_2

molecule in the gas phase, respectively, obtained from our classical MD simulations. The values of E_b^{O} calculated are noted below each cluster in Figs. 7.2 – 7.4. We see that in most cases, the geometries of the oxide clusters look very different from those of the corresponding elemental clusters.

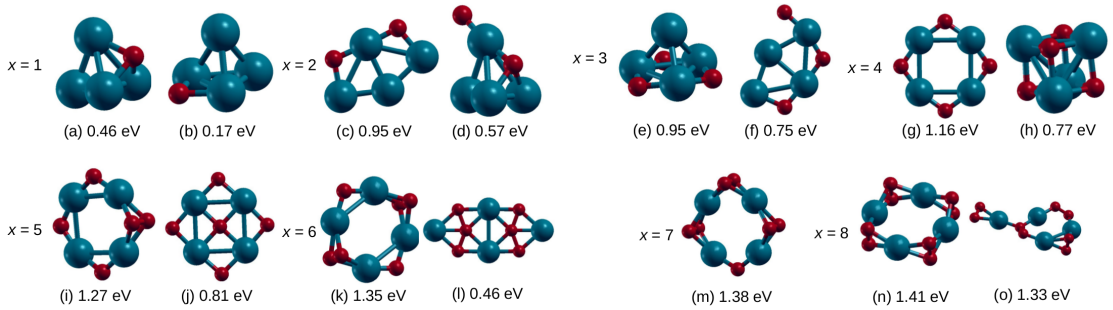

Figure 7.2: *Structures for Cu_4O_x, $x = 1 - 8$, generated using classical potentials: (a), (b) $x = 1$, (c), (d) $x = 2$, (e), (f) $x = 3$, (g), (h) $x = 4$, (i), (j) $x = 5$, (k), (l) $x = 6$, (m) $x = 7$, (n) and (o) $x = 8$. E_b^O, the binding energy of oxygen, calculated for each cluster, is noted below its figure. The blue and red spheres represent Cu and O atoms respectively.*

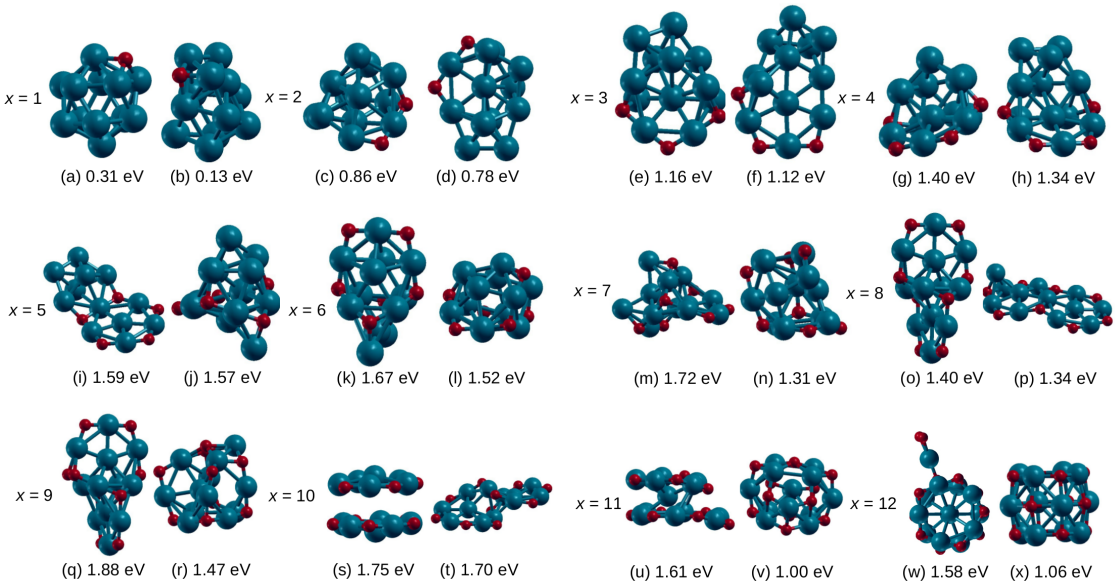

Figure 7.3: *Structures for $Cu_{12}O_x$, $x = 1 - 12$, generated using classical potentials: (a), (b) $x = 1$, (c), (d) $x = 2$, (e), (f) $x = 3$, (g), (h) $x = 4$, (i), (j) $x = 5$, (k), (l) $x = 6$, (m), (n) $x = 7$, (o), (p) $x = 8$, (q), (r) $x = 9$, (s), (t) $x = 10$, (u), (v) $x = 11$, (w) and (x) $x = 12$. E_b^O, the binding energy for oxygen, calculated for each cluster, is noted below its figure. The blue and red spheres represent Cu and O atoms respectively.*

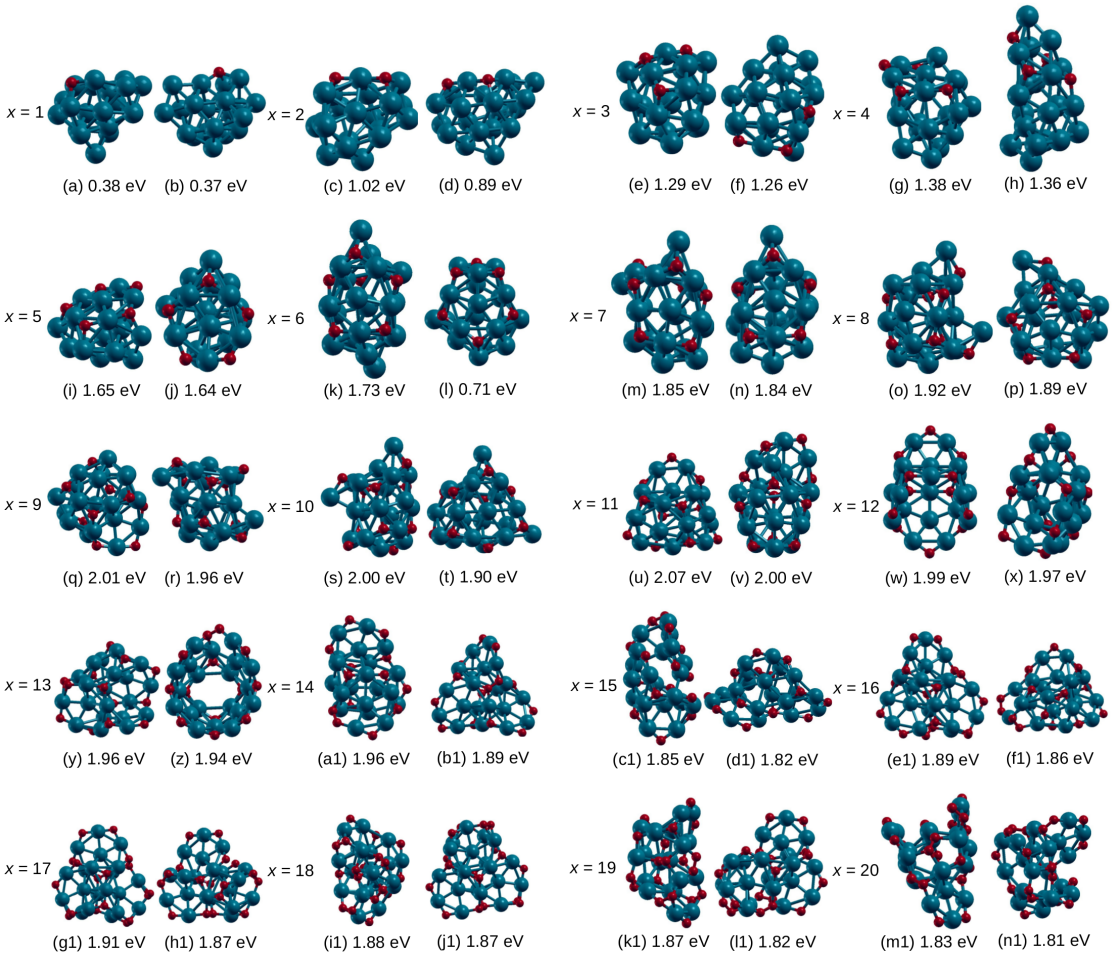

Figure 7.4: *Structures for $Cu_{20}O_x$, $x = 1 - 12$, generated using classical potentials: (a), (b) $x = 1$, (c), (d) $x = 2$, (e), (f) $x = 3$, (g), (h) $x = 4$, (i), (j) $x = 5$, (k), (l) $x = 6$, (m), (n) $x = 7$, (o), (p) $x = 8$, (q), (r) $x = 9$, (s), (t) $x = 10$, (u), (v) $x = 11$, (w), (x) $x = 12$, (y), (z) $x = 13$, (a1), (b1) $x = 14$, (c1), (d1) $x = 15$, (e1), (f1) $x = 16$, (g1), (h1) $x = 17$, (i1), (j1) $x = 18$, (k1), (l1) $x = 19$, (m1) and (n1) $x = 20$. E_b^O, the binding energy for oxygen, calculated for each cluster, is noted below its figure. The blue and red spheres represent Cu and O atoms respectively.*

In this way a very large number of candidate clusters and structures was generated. In order to eliminate some of these, so that we would be left with a smaller number of clusters that could be handled by DFT calculations, the pool of candidates was reduced by performing atomistic thermodynamics on all the structures obtained using classical potentials. For each value of x retained, a few low energy structures were chosen to be further refined using DFT.

7.3.2 Step 2: Refinement of Geometries using Density Functional Theory

For DFT calculations we studied clusters with $x = 0 - 8$ for Cu_4O_x, clusters with $x =$ 0, 1, 2, 3, 4, 6, 8, 9 and 12 for $Cu_{12}O_x$, and clusters with $x = 0$, 1, 2, 10, 12, 15 and 20 for $Cu_{20}O_x$. The lowest energy geometries obtained from DFT for Cu_4O_x, $Cu_{12}O_x$ and $Cu_{20}O_x$ are shown in Fig. 7.5.

The lowest energy geometry obtained for Cu_4 is a rhombus, and this is in agreement with previous DFT results.[204,207] Also the structures for Cu_4O,[204,205] Cu_4O_4,[208] and Cu_4O_5[205] are in good agreement with previous DFT results. It is interesting to note that in all the Cu_4O_x structures, the four Cu atoms more or less maintain the rhombus-like arrangement that is seen in the elemental Cu_4 cluster.

For Cu_{12}, previous DFT results suggest that the lowest energy structure is an icosahedron, however we note that the authors of this previous study have only considered geometries with high symmetry, viz., icosahedral symmetry (I_h) and octahedral symmetry (O_h).[206] We find from our DFT calculations a structure for Cu_{12} that has lower symmetry and is lower in energy by 1.5 eV compared to the icosahedral structure [see Fig. 7.5(j)]. We find that the geometry of elemental Cu_{12} changes considerably upon addition of oxygen atoms to the cluster.

For Cu_{20}, we obtain a compact structure with C_s symmetry as the lowest energy structure. This geometry is only slightly distorted from the structure reported earlier for Cu_{20} clusters in the gas phase.[179] For all other clusters shown in Fig. 7.5, to the best of our knowledge, there are no previous results for the ground state geometries.

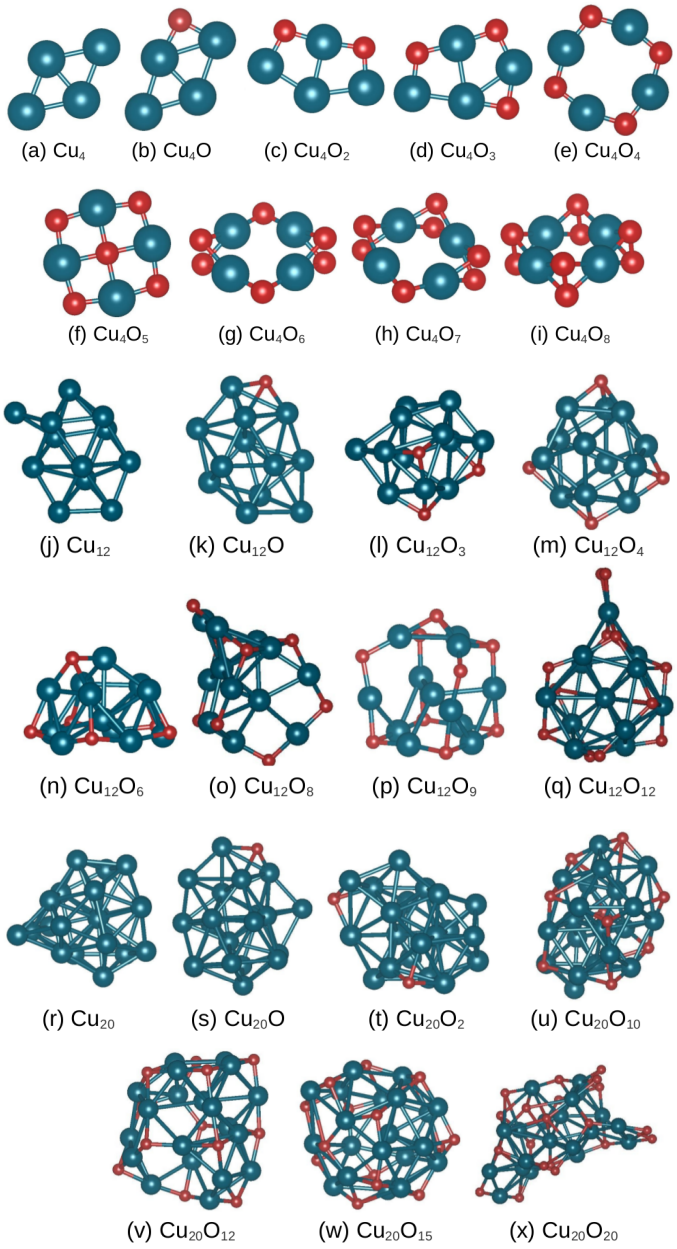

Figure 7.5: *The lowest energy geometries obtained from DFT for (a) – (i) Cu_4O_x, (j) – (q) $Cu_{12}O_x$ and (r) – (x) $Cu_{20}O_x$. The first and second rows: Cu_4O_x, with x = 0 – 8; the third and fourth rows: $Cu_{12}O_x$, with x = 0, 1, 3, 4, 6, 8, 9 and 12; the fifth and sixth rows: $Cu_{20}O_x$, with x = 0, 1, 2, 10, 12, 15, 20. The blue and red spheres represent the Cu and O atoms respectively.*

7.3.3 Step 3: AIATD to study Oxidation and Reduction

Next, we study the processes of oxidation and reduction for the clusters and bulk forms of Cu and its oxides. In the bulk, the stable phases are known to be Cu, Cu_2O and CuO.

7.3.3.1 Computing the Gibbs Free Energy

We consider the reactions in Eqs.(7.1) and (7.2) which correspond to the oxidation and reduction of the Cu species. The Gibbs free energies for the two reactions at a temperature T are given by Eqs. (7.3) and (7.7).

Cu clusters in O_2 environment

In Figs. 7.6(a) – (d), we show the plots of ΔG vs. $\Delta\mu_O$ for the bulk, and for the Cu_nO_x clusters shown in Fig. 7.5 for $n = 4$, 12 and 20. At any value of $\Delta\mu_O$, the stable structure is given by the system with the lowest ΔG. For the bulk, in Fig. 7.6(a), we see, as expected, the three stable phases, viz., Cu, Cu_2O and CuO. On comparing with the clusters in Figs. 7.6(b) – (d), we first note that we do not see the same corresponding phases for the clusters as we see in the bulk. Even when comparing among the different sizes of clusters considered, we do not see the same phases for all the clusters.

For $n = 4$, we obtain only two stable phases in the phase diagram, viz., Cu_4 and Cu_4O_4. For $n = 12$ and 20, we find that Cu_n, $Cu_nO_{n/2}$ and $Cu_nO_{3n/4}$ are stable phases, along with an additional intermediate phase for Cu_{20}, viz., $Cu_{20}O_{12}$. We do not see a Cu_nO_n phase for the clusters with $n = 12$ and 20.

We find that for $n = 4$, the cluster oxidizes to a phase with a higher oxygen to metal ratio as compared to clusters with $n = 12$ or 20: the Cu atoms in Cu_4O_4 are in the +2 oxidation state, while in the highest oxidation level possible for $n = 12$ and 20, that is in $Cu_{12}O_9$ and $Cu_{20}O_{15}$ respectively, the Cu atoms have only a +1.5 oxidation state. This suggests that the tendency to oxidize is higher for smaller clusters. This is in agreement with previous results on other metals that smaller clusters oxidize to a higher extent and more easily than larger clusters.[187]

Note the black dashed lines separating the Cu_n and $Cu_nO_{n/2}$ phases for the bulk and for the clusters with $n = 12$ and 20 in Figs. 7.6(a), (c) and (d) respectively. As the size reduces from the bulk to $n = 20$ to $n = 12$, we see that this line moves monotonically to the left. This suggests that as the size reduces, Cu_n can be more easily oxidized to $Cu_nO_{n/2}$. For $n = 4$, we do not see this transition as the Cu_4O_2 phase is absent here. This may be due to the extra stability of the Cu_4O_4 cluster, which is brought about by

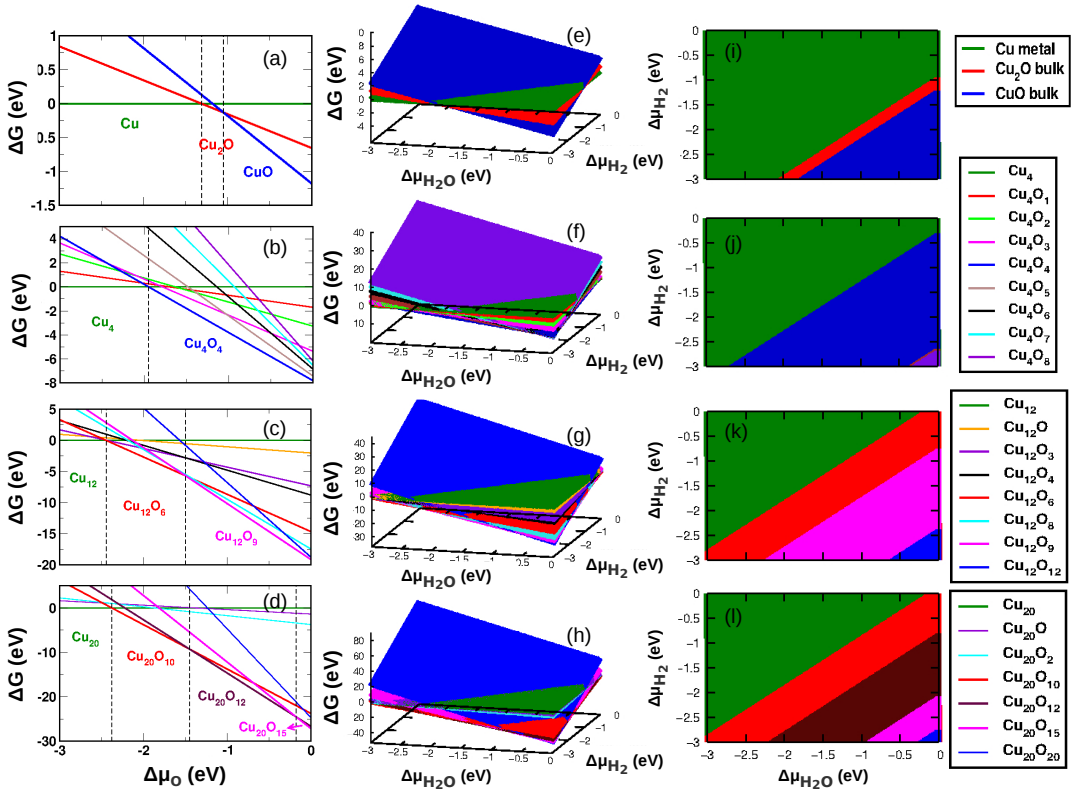

Figure 7.6: *Obtaining phase diagrams by looking for the phase with lowest Gibbs free energy, by applying atomistic thermodynamics to DFT results. The first row of figures [(a), (e), (i)] corresponds to the bulk, the second row [(b), (f), (j)] to n = 4, the third row [(c), (g), (k)] to n = 12, and the fourth row [(d), (h), (l)] to n = 20. Panels (a), (b), (c), and (d) are relevant to the oxidation process of Eq. (7.1) and show plots of ΔG, the change in Gibbs free energy, as a function of $\Delta\mu_O$, the change in the chemical potential of oxygen. Each colored line corresponds to a different structural phase (see legend on the extreme right), and the vertical dashed lines indicate phase transitions. All the remaining panels are relevant to clusters in a H_2 + H_2O environment, see Eq. (7.2). In panels (e), (f), (g) and (h), we plot ΔG as a function of $\Delta\mu_{H_2}$ as well as $\Delta\mu_{H_2O}$, the chemical potentials of hydrogen and water respectively. The panels (i), (j), (k) and (l) show the most stable phase for each ($\Delta\mu_{H_2}$, $\Delta\mu_{H_2O}$); i.e., they are projections of the results in the second column onto the ($\Delta\mu_{H_2}$, $\Delta\mu_{H_2O}$) plane.*

an electronic shell closing with 68 electrons.[209]

The binding energy of oxygen in these stable phases was calculated using the equation: $E_b^{\mathrm{O}} = -\frac{1}{x}\{E^{DFT}_{\mathrm{Cu}_n\mathrm{O}_x} - E^{DFT}_{\mathrm{Cu}_n} - \frac{x}{2}E^{DFT}_{\mathrm{O}_2}\}$. The results for E_b^{O} are listed in Table. 7.1. We see that for a given value of x, E_b^{O} decreases monotonically as n increases and is higher for clusters than for the bulk. For a given n, as the oxidation state of Cu reduces to +1 from higher oxidation states, we that E_b^{O} increases: this may be due to the progressive approach toward achieving a filled $3d$-orbital. We note that for both bulk CuO and bulk Cu_2O, our values for E_b^{O} are in good agreement with previous GGA results;[194,210] however,

they are underestimated with respect to experiments. The reason for this was suggested to be GGA errors in computing the binding energy of O_2 as well as the formation energy of O^{2-} from O_2.[194]

	E_b^O (eV/O atom)			
	$n = 4$	$n = 12$	$n = 20$	Bulk
$Cu_nO_{n/2}$	-	2.38	2.32	1.25
$Cu_nO_{3n/5}$	-	-	2.17	-
$Cu_nO_{3n/4}$	-	2.07	1.76	-
Cu_nO_n	1.89	1.51	1.30	1.12
Cu_nO_{2n}	0.71	-	-	-

Table 7.1: *Binding energy per O atom computed for Cu clusters and Cu bulk phases.*

In Table. 7.2, we list the relative thermal stability of all clusters in the O_2 environment. It is defined as the temperature at which oxygen would desorb completely to result in the elemental Cu_n cluster. This temperature T_d is obtained by putting $\Delta G(T_d, \Delta\mu_O) = 0$ in the ΔG vs. $\Delta\mu_O$ plots in Figs. 7.6(a)–(d), with $p(O_2) = 1$ atm. From the results, we can see that the thermal stability of the clusters increases as size decreases, and is higher for the clusters than it is for the bulk. This is in contrast with previous results for small gas phase Ag clusters; the clusters were found to be less thermally stable than the corresponding bulk or surface.[190] For a given size of the cluster, we find that the thermal stability of the cluster decreases as the oxygen content in the cluster increases.

	Thermal desorption temperature, T_d (K)			
	$n = 4$	$n = 12$	$n = 20$	Bulk
$Cu_nO_{n/2}$	-	2005	1960	1163
$Cu_nO_{3n/5}$	-	-	1848	-
$Cu_nO_{3n/4}$	-	1777	1547	-
Cu_nO_n	1647	-	-	1062

Table 7.2: *The relative thermal stability of Cu_nO_x clusters in the oxidizing environment, i.e., the temperature at which all the oxygen atoms in the cluster would desorb to result in the elemental Cu_n cluster.*

Cu clusters in H_2 + H_2O environment

Note that in the reaction in an O_2 environment described above, in addition to Cu_n and Cu_nO_x, there is only one more species, viz., O_2. Hence, above we had plotted how ΔG varies as a function of the single parameter $\Delta\mu_O$. In a H_2 + H_2O environment however, there are two additional species, viz., H_2 and H_2O. Here, we therefore calculate how ΔG varies as a function of two variables $\Delta\mu_{H_2}$ and $\Delta\mu_{H_2O}$. In Figs. 7.6(e) – (h), we show the three-dimensional plots of ΔG as a function of $\Delta\mu_{H_2}$ and $\Delta\mu_{H_2O}$ for the bulk, and for the Cu_nO_x clusters shown in Fig. 7.5 for n = 4, 12 and 20. Here again, at any given $(\Delta\mu_{H_2}, \Delta\mu_{H_2O})$, the stable structure corresponds to that with the lowest Gibbs free energy. These lowest lying configurations are determined and then plotted in Figs. 7.6(i) – (l).

From these figures we see that the bulk exhibits the same stable phases in presence of H_2 + H_2O as it does in the presence of O_2. For the clusters however, we see that an additional phase appears in the phase diagram at high $\Delta\mu_{H_2O}$ and low $\Delta\mu_{H_2}$. For n = 4, we see a small domain of stability for Cu_4O_8 [shown in violet in Fig. 7.6(j)], also for n = 12 and 20, we see an additional phase that corresponds to Cu_nO_n [shown in blue in Figs. 7.6(k) and (l)]. This suggests that the clusters oxidize to a higher extent in H_2O-rich conditions than in O_2-rich conditions.

We see that the domain of stability for the Cu_nO_n phase reduces as n increases [see phases marked by blue color in Figs. 7.6(j) – (l)]. This suggests that the Cu_nO_n phase becomes more stable as the size of the cluster reduces, which is again in agreement with expectations that the tendency to oxidize increases as the size of the cluster decreases.

We observe the intermediate phase $Cu_nO_{3n/4}$ for n = 12 and n = 20 clusters as we did in the O_2 environment. Here again we see that the domain of stability of this phase reduces as size increases from n = 12 to n = 20 [see phases marked by magenta color in Figs. 7.6(k) and (l)].

The domain of stability for the $Cu_nO_{n/2}$ phase for n = 12 and n = 20 is almost the same, and is much larger for the clusters than in the bulk [see phases marked by red color in Figs. 7.6(j), (k) and (l)]. For n = 20, we see an additional intermediate phase, viz., $Cu_{20}O_{12}$ shown by the region marked by maroon color in Fig. 7.6(l).

7.3.3.2 Pressure-Temperature Phase Diagrams

Cu clusters in O_2 environment

Next, we generate pressure-temperature phase diagrams using the data contained in Figs. 7.6(a) – (d), and we present these in Fig. 7.7. These phase diagrams are relevant to the oxidation reaction in Eq. (7.1). Here the stable phases in an O_2 environment are plotted as a function of T and $p(O_2)$.

Note that though we have extended the temperature axis in Fig. 7.7 to 3000 K, it is known that the bulk phases of Cu, Cu_2O and CuO melt at 1358 K, 1505 K and 1599 K, respectively.

From Figs. 7.7(a) – (d), we can see that the oxidation state of Cu increases as $p(O_2)$ increases and/or T decreases. For the bulk, we find that the transition temperatures are shifted with respect to experiment; these errors may be due to the errors in the binding energy from using GGA as well as self interaction errors.[194,195] As we saw in the Gibbs free energy diagrams, for $n = 4$ in Fig. 7.7(b), we observe a phase transition (oxidation) from Cu_4 (0 oxidation state) to Cu_4O_4 (2+ oxidation state); for $n = 12$ in Fig. 7.7(c), we see three phases, Cu_{12} (0 oxidation state) $\rightarrow$ $Cu_{12}O_6$ (1+ oxidation state) $\rightarrow$ $Cu_{12}O_9$ (1.5+ oxidation state); and for $n = 20$ in Fig. 7.7(d), we see Cu_{20} (0 oxidation state) $\rightarrow$ $Cu_{20}O_{10}$ (1+ oxidation state) $\rightarrow$ $Cu_{20}O_{12}$ (1.2+ oxidation state) $\rightarrow$ $Cu_{20}O_{15}$ (1.5+ oxidation state).

We see that the region of stability for the $Cu_nO_{n/2}$ phase is relatively much smaller for the bulk than it is for the clusters with $n = 12$ and 20, while this phase is absent in the case of the $n = 4$ cluster.

The $n = 12$ and 20 clusters do not form the Cu_nO_n phase, but rather form intermediate phases like $Cu_nO_{3n/4}$ (for $n = 12$ and 20) and $Cu_nO_{3n/5}$ (for $n = 20$). We see the formation of Cu_nO_n only in the case of $n = 4$, suggesting that smaller clusters are able to oxidize to a higher extent than clusters with $n = 12$ and 20.

Next, the transition temperatures at $p(O_2) = 10^{-12}$ atm, shown by the black dashed lines in Fig. 7.7, are extracted and noted in Fig. 7.8, for the bulk and for clusters with n = 4, 12 and 20. This value of $p(O_2)$ is an example of an ultra high vacuum condition.

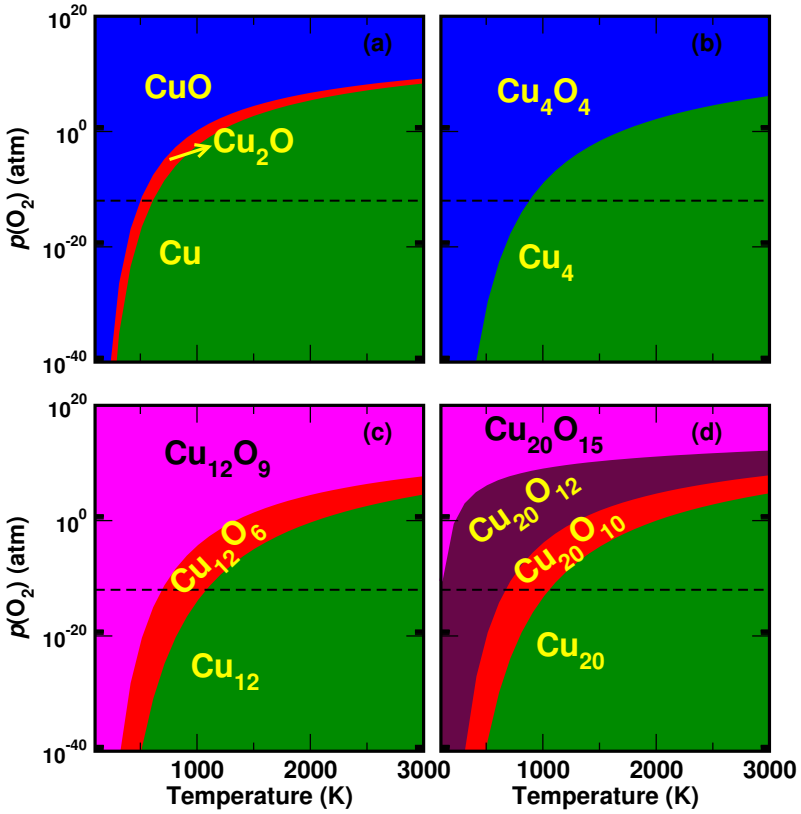

Figure 7.7: *Phase stability under oxidizing conditions. We show temperature – partial pressure of O_2 phase diagrams for (a) bulk, (b) $n = 4$, (c) $n = 12$, and (d) $n = 20$. Oxidation takes place as $p(O_2)$ increases and/or T decreases. The dashed line corresponds to $p(O_2) = 10^{-12}$ atm.*

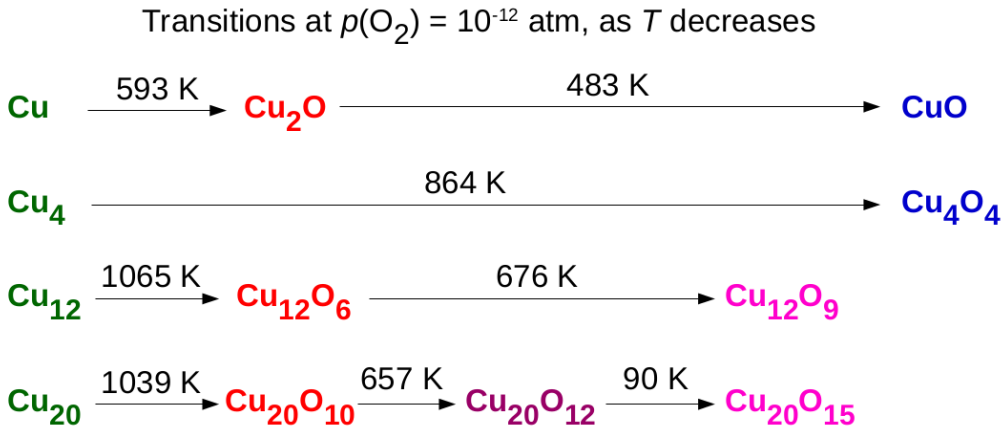

Figure 7.8: *The transition temperatures for the transitions observed in the oxidizing environment at $p(O_2) = 10^{-12}$ atm, for the bulk, and for clusters with $n = 4$, 12 and 20. Note that oxidation takes place as temperature T decreases.*

For the transition between $Cu_nO_{n/2}$ and Cu_n, as the size reduces from the bulk to clusters with $n = 20$ to $n = 12$, the transition temperature increases monotonically; note

that the low-temperature phase is the oxide, and thus the tendency to oxidize increases as the size decreases. This trend is confirmed by examining Fig 7.8, where we have summarized our results for the transition temperatures for the bulk and clusters at $p(O_2) = 10^{-12}$ atm.

Considering the stable phase of these systems at $p(O_2) = 10^{-12}$ atm and at room temperature, we find that the bulk and $n = 4$ cluster are in the Cu_nO_n phase, while the $n = 12$ cluster is in the $Cu_nO_{3n/4}$ phase and the $n = 20$ cluster is in the $Cu_nO_{3n/5}$ phase. This is very interesting, as we see that the clusters oxidize to different levels depending on their size; the smaller the cluster, the higher is the extent of oxidation. These results are again in agreement with our expectation that the reactivity towards oxidation increases as size decreases.

Cu clusters in H_2 + H_2O environment

Similarly, we obtain temperature-dependent phase diagrams that describe the behavior in the H_2 + H_2O environment, using data from Figs. 7.6(e) – (l); we show these phase diagrams in Fig. 7.9. In this case, as we have two additional species H_2 and H_2O, apart from the oxide and the elemental cluster, we generate two-dimensional plots with T in the abscissa and $p(H_2)/p(H_2O)$, the ratio of the partial pressure of hydrogen to the partial pressure of water, in the ordinate.

In these figures, we see a marked difference in the behaviour of clusters with $n = 12$ and 20, compared to the bulk and clusters with $n = 4$. In Figs. 7.9(a) and (b), we see that for both transitions observed, the phase boundaries are convex upward, and for a fixed value of $p(H_2)/p(H_2O)$, the reduction occurs as temperature T decreases. However, for the clusters with $n = 12$ and 20, we see that the phase boundaries for the transitions from Cu_nO_n up to $Cu_nO_{n/2}$ remain convex upward, whereas the boundary separating $Cu_nO_{n/2}$ and Cu_n is now concave upward. For the former reactions, for a fixed value of $p(H_2)/p(H_2O)$, reduction occurs as T decreases, but for the latter, the reduction occurs as T increases. We note that these two kinds of transitions occur for different ranges of $p(H_2)/p(H_2O)$, i.e., there is no value of $p(H_2)/p(H_2O)$ at which both kinds of transitions can occur.

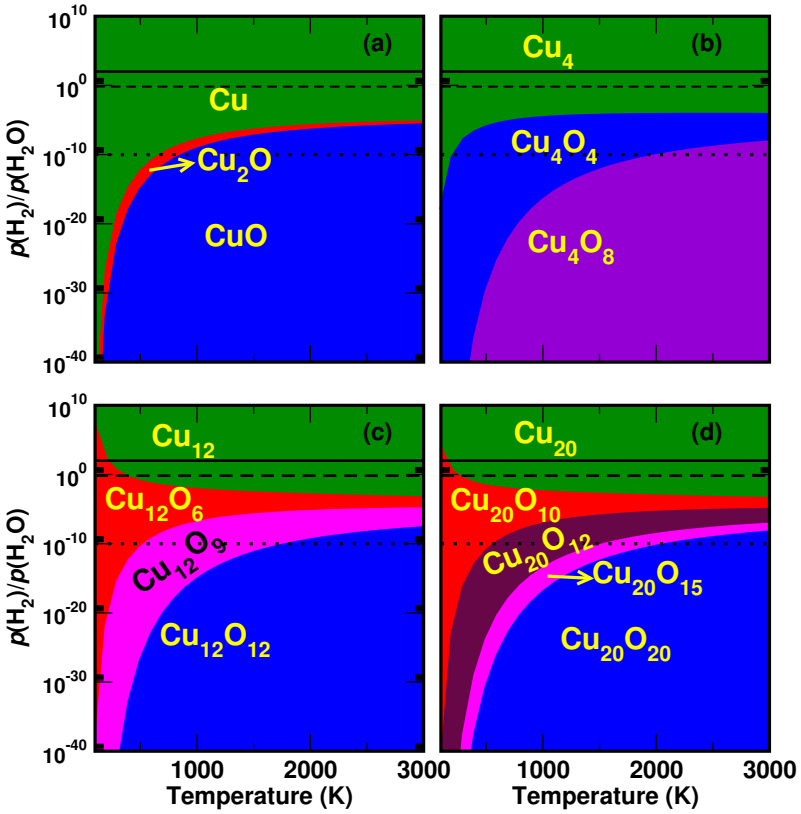

Figure 7.9: *Phase stability in the presence of H_2 + H_2O. In (a) – (d), we show phase diagrams as a function of temperature T and $p(H_2)/p(H_2O)$, the ratio of partial pressures of hydrogen to water, for (a) bulk, (b) $n = 4$, (c) $n = 12$, and (d) $n = 20$. The black solid, dashed and dotted lines correspond to $p(H_2)/p(H_2O) = 100$, 0.67 and 10^{-10} respectively.*

In Fig. 7.9, we have marked three values of $p(\mathrm{H_2})/p(\mathrm{H_2O}) = 100$, 0.67 and 10^{-10} with black solid, dashed and dotted lines respectively. The first value is an example of hydrogen-rich conditions, the second value is a condition typical of chemical reactions like the water-gas shift reaction, and the third value is an example of water-rich conditions.

At $p(\mathrm{H_2})/p(\mathrm{H_2O}) = 100$ and 0.67, note that the bulk and $n = 4$ clusters are already in their elemental reduced state at all temperatures, and we see phase transitions occuring only in the $n = 12$ and $n = 20$ clusters. The phase boundaries that are intersected by the lines $p(\mathrm{H_2})/p(\mathrm{H_2O}) = 100$ and $p(\mathrm{H_2})/p(\mathrm{H_2O}) = 0.67$ are concave upward in Fig. 7.9 which means that reduction occurs as T increases. The transition temperatures at these values of $p(\mathrm{H_2})/p(\mathrm{H_2O})$ are extracted and plotted in Fig. 7.10. At both these values of $p(\mathrm{H_2})/p(\mathrm{H_2O})$, we find that the transition temperature increases as n decreases from 20 to 12, which means that $n = 12$ clusters are more resistant to reduction (i.e., more prone

to oxidation) than $n = 20$ clusters. Note that for $n = 4$, we see no transition and the elemental cluster is stable at all temperatures.

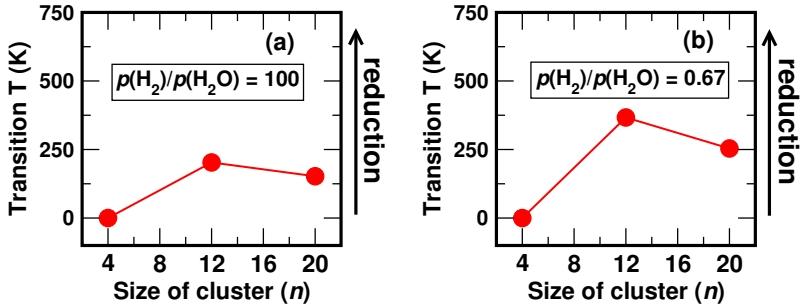

Figure 7.10: *The transition temperatures at two values of $p(H_2)/p(H_2O)$: (a) 100 and (b) 0.67 are plotted as a function of n, the number of Cu atoms in the cluster. Reduction occurs as temperature increases. The bulk and $n = 4$ clusters are already in their elemental state at $T = 0$, while for the $n = 12$ and $n = 20$ clusters we observe the transition from $Cu_nO_{n/2} \rightarrow Cu_n$. $n = 12$ clusters reduce at a higher temperature as compared to $n = 20$ clusters.*

In Fig. 7.10(b), $p(H_2)/p(H_2O) = 0.67$; this is a condition that is in the range relevant for several chemical reactions. In these conditions, if the reaction requires the catalyst to be in the elemental state, note that the Cu_4 elemental cluster is stable and hence would be catalytically active at all temperatures. However, for $n = 12$ and 20, the temperature for the reaction would need to be higher than 367 K and 254 K respectively, in order for the catalyst to be in its elemental state and catalytically active for the reaction. At a temperature of around 500 K, which is typical for the low temperature water gas shift reaction, all the three sizes of clusters considered here would be in their elemental reduced state.

Now let us consider the transitions in water-rich conditions such as when $p(H_2)/p(H_2O) = 10^{-10}$. From the phase diagrams in Fig. 7.9, we see that the phase boundaries that are intersected by the line $p(H_2)/p(H_2O) = 10^{-10}$ are convex upward. The reduction process takes place as temperature decreases. The transition temperatures for all transitions observed at this value of $p(H_2)/p(H_2O)$ are noted in Fig. 7.11.

In Fig. 7.11, let us first consider the reduction of the Cu_nO_n phase; we can see that the transition temperature for the reduction of Cu_nO_n clusters decreases monotonically as n decreases from 20 to 12 to 4. The smaller the size, the more resistant the cluster is to reduction. On comparing with the bulk transition temperature, we find that the $n = 12$

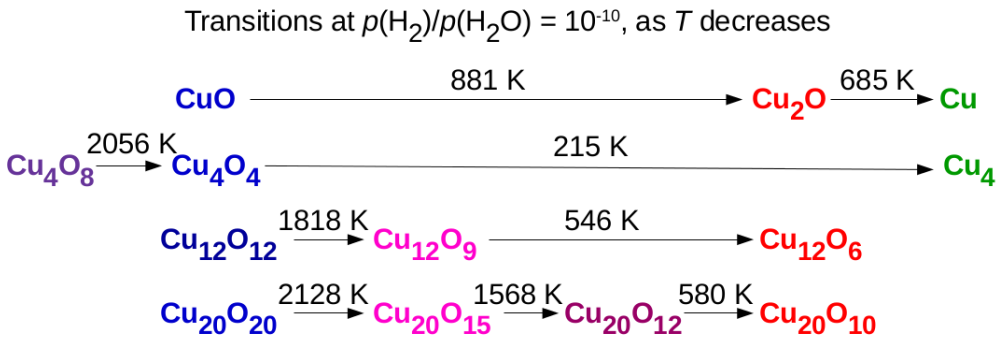

Figure 7.11: *The transition temperatures for the transitions observed in water-rich conditions when $p(H_2)/p(H_2O) = 10^{-10}$, for the bulk and for clusters with $n = 4$, 12 and 20. Note that reduction occurs as temperature decreases.*

and 20 clusters are more easily reducible than the bulk, whereas $n = 4$ clusters are more resistant to reduction than the bulk.

Considering the reduction of the $Cu_nO_{3n/4}$ phase for $n = 12$ and 20 clusters, we see a similar trend: the transition temperature is lower for $n = 12$ than it is for $n = 20$ clusters.

7.4 Conclusions

In this chapter, we have obtained phase diagrams for small clusters of copper and copper oxides, using *ab initio* atomistic thermodynamics in an O_2 environment and a H_2 + H_2O environment. For the bulk, it is known that the stable phases are Cu, Cu_2O and CuO; in general, the corresponding phases Cu_n, $Cu_nO_{n/2}$ and Cu_nO_n are also observed in the phase diagrams for the clusters, though the Cu_4O_2 phase is absent for $n = 4$. However, additional stoichiometries appear in the phase diagrams for the clusters: a high-oxygen-content phase Cu_4O_8 for $n = 4$ in water-rich conditions, and intermediate stoichiometries, viz., $Cu_{12}O_9$, $Cu_{20}O_{12}$ and $Cu_{20}O_{15}$ for $n = 12$ and $n = 20$.*

In an O_2 environment, for the transition between $Cu_nO_{n/2}$ and Cu_n, which is observed only for the $n = 12$ and 20 clusters, we see that as the size of the cluster decreases, the oxide phase is stable up to a higher temperature, and these transition temperatures are higher for the clusters than for the bulk.

For $n = 4$ in an O_2 environment, we see that there is a direct transition from Cu_4O_4

*Note: One may choose to term these 'intermediate' stoichiometries to be instead 'non-stoichiometric'.

to Cu_4, with no other intervening phase; this occurs at a temperature higher than the transition temperature between CuO and Cu_2O in the bulk. This means that the Cu_nO_n phase is comparatively more stable in the cluster with $n = 4$ than in the bulk. For $n =$ 12 and 20, the Cu_nO_n phase is not stable in the presence of oxygen.

When we consider an example of an ultra-high vacuum (UHV) experimental condition, such as room temperature and $p(O_2) = 10^{-12}$ atm, we find that the three sizes of clusters exhibit different levels of oxidation; for $n = 4$, 12 and 20, the stable phases are Cu_nO_n, $Cu_nO_{3n/4}$ and $Cu_nO_{3n/5}$ respectively. This is very interesting and important as it clearly shows how size affects the stable oxidation state of a cluster in a given environmental condition. These results are in agreement with the understanding that the tendency to oxidize increases as the size of the cluster decreases.

The size-dependent trends obtained in the H_2-rich environment are consistent with those obtained in the O_2 environment, i.e., the smaller the cluster, the more resistant it is to reduction. Under typical reaction conditions [for example when $p(H_2)/p(H_2O) = 0.67$], our results suggest that clusters with $n = 4$ will always be in the reduced elemental state at all temperatures, whereas for $n = 12$ and 20, clusters will be in the reduced state only when T is greater than 367 K and 254 K respectively. At a temperature of around 500 K, which is typical of conditions where reactions such as the low temperature water-gas shift reactions are carried out, all the clusters considered here will be in their reduced elemental state.

In this chapter, we have considered clusters in the gas phase. However, in any actual application, the clusters will be placed on a solid substrate, which may affect their structural and oxidative properties significantly. In the next chapter, we will repeat calculations similar to those carried out above; however, we will place the Cu clusters on an alumina support, and see whether and how the presence of the support affects our results.

Chapter 8

Size-dependent Oxidation and Reduction of Supported Cu clusters

In the previous chapter, we studied the processes of oxidation and reduction of gas phase Cu clusters, and examined the size-dependence of these phenomena. In this chapter, we study the same processes, on a system that may be more relevant for applications, viz., Cu clusters supported on hydroxylated amorphous alumina. Here again, we investigate how the size of a cluster affects its tendency to oxidize or reduce. We study three sizes of Cu clusters: $n = 4$, 12 and 20. In addition, we also compare our computational results with experimental results for XANES spectra of Cu clusters in oxidizing and reducing environments.

8.1 Introduction

In the previous chapter we discussed oxidation, which is one of the most important types of chemical reactions, and that plays a vital role in most areas of human life and endeavor. We mentioned how oxidation sometimes leads to the loss of the catalytic activity in catalysts.[181]

The importance of studying oxidation/reduction processes in clusters was discussed in detail. It is important to know the oxidation state that a given size of the cluster would achieve in a given set of environmental conditions, as this (together with information about reaction barriers and selectivity) allows us to determine the optimal cluster size that one should use as a catalyst in a given set of experimental conditions. For most applications where clusters are used, and especially for heterogeneous catalysis, they are generally placed on an oxide support. The support is known to influence the electronic structure, the morphology as well as the catalytic properties of these supported clusters. The changes in the catalytic properties of a cluster brought about by the presence of the support are mainly due to (a) changes in the charge state of the cluster due to electron transfer between the cluster and the support, (b) effects related to possible changes in the shape of the clusters when deposited on the support and also (c) the appearance of catalytically active sites at the cluster-support interface.[211]

In order to attempt to answer the question of what phase clusters of a particular size would be in, for a given reaction with a given set of experimental conditions, we first studied (in the previous chapter) three different sizes of gas phase Cu clusters and Cu_nO_x clusters, in two different types of chemical environments, and we extracted size dependent trends in their oxidation and reduction. In this chapter, we consider these Cu clusters deposited on a support, viz., hydroxylated amorphous alumina, and try to answer the same questions raised in the previous chapter. We generate phase diagrams for these clusters in an O_2 environment as well as in a H_2 + H_2O environment, and extract transition temperatures to understand the size-dependence of the oxidation and reduction processes in these supported clusters.

In addition, in this chapter we also compare our theoretical results on Cu_nO_x/Al_2O_3, with experimental X-ray absorption near edge structure (XANES) spectra obtained for the same systems in O_2-rich and H_2-rich conditions.*

XANES is a type of absorption spectroscopy that measures features in the X-ray absorption spectra that provide information regarding the environmental chemistry and

*All experimental data discussed in this chapter were provided by the group of Prof. Stefan Vajda from Argonne National Laboratory.

the oxidation state of an atom. The position of the absorption edge in these spectra is known to be primarily influenced by the oxidation state of the atom and undergoes a systematic shift towards higher energy as the oxidation state of the atom increases.[212] For example, in a study of the XANES spectra of the sulfur K-edge in different compounds like heavy petroleum, coal and soil, one sees that as the oxidation state of S changes from S^{2-} to S^{6+}, the XANES K-edge increases in energy monotonically with a large energy shift of $\sim$11 eV.[213] Also for metals, there exists a number of studies that show a correlation between the position of the XANES K-edge peak and the oxidation state of the metal in a compound.[214,215] The XANES spectra of new compounds or alloys are usually interpreted in terms of XANES spectra of the same atom in some of its known standard compounds, and the oxidation state of an atom in a new compound usually is deduced from its XANES K-edge position.

The XANES spectra of small clusters are however tricky and less straightforward to interpret. The spectra of small clusters are also often compared to spectra of known standard compounds; however this may prove to be a little difficult, since the edges in the XANES spectra of clusters are usually not as sharply pronounced as the XANES spectra of bulk compounds; this may be because all atoms in a cluster may not have the same oxidation state and also because clusters occupy different adsorption sites on the surface and hence have different environmental chemistry. Also it is possible that an atom in a cluster may have an intermediate oxidation state that is not observed in standard bulk compounds.

In this study, we propose to interpret the XANES spectra of small clusters of Cu_n and Cu_nO_x supported on hydroxylated amorphous alumina, in terms of a simple quantity that can be calculated easily. viz., the "Bader charge". This quantity helps us to compare our theoretical results with the experimental XANES results. The phase transitions predicted theoretically in these cluster systems, in a given environment, as a function of temperature, are also tested against the XANES spectra measured experimentally in the same environment as a function of temperature. We will see below that this approach produces convincingly good agreement between theory and experiment. We are not aware of any

previous work that has followed a similar approach, i.e., that has attempted to correlate theoretically calculated Bader charges with experimentally measured XANES spectra, in an attempt to study temperature-dependent phase transitions.

8.2 Computational Methods

8.2.1 Step 1: Optimizing Substrate Geometry

The initial geometry for hydroxylated amorphous alumina was generated by molecular dynamics using the LAMMPS code.[85] The interatomic interactions were treated with potentials of the Buckingham type derived by Matsui,[80] and a simulated annealing procedure as suggested by Adiga *et al* was followed:[81] to create the hydroxylated amorphous alumina slab, we started with a crystalline bulk alumina structure, using a 4 × 4 periodic unit cell with four layers (with box dimensions 19.04 Å × 16.49 Å× 8.17 Å). To achieve the desired H concentration in the system, a specific number of Al atoms at random positions was replaced with H atoms, and for every Al atom removed, an O atom was also removed to maintain charge neutrality. The bulk system thus created was heated to 4000 K, equilibrated for 5 ns and quenched over 0.1 ps. Free surfaces were then created in the system by introducing a vacuum distance of 50 Å along the z direction. This surface slab was annealed by increasing the temperature to 1500 K over 1.5 ns, equilibrating for 5 ns and subsequently quenching to 0 K over 0.1 ps. Geometric relaxation was then performed at 0 K; the pair correlation functions [$g(r)$] for the structure thus obtained confirmed that the structure was amorphous in nature. In agreement with previous results,[81] we find that the hydrogen atoms tend to segregate to the surface of the slab so as to form hydroxyl groups. This final structure was then input as the starting geometry to a DFT calculation, which was used to further optimize the structure of the amorphous hydroxylated alumina slab.

8.2.2 Step 2: Optimizing Geometries of Alumina supported clusters

The optimized geometries for the gas phase elemental Cu_n clusters and oxide Cu_nO_x clusters obtained in the previous chapter were used to generate initial geometries for

supported Cu_n/Al_2O_3 and Cu_nO_x/Al_2O_3.

The optimized Cu_n cluster was placed at several (at least five) non-equivalent adsorption sites on the substrate to generate initial geometries for Cu_n/Al_2O_3. The initial geometries for Cu_nO_x/Al_2O_3 were generated in two ways: (1) by depositing the optimized gas phase Cu_nO_x cluster at different sites on the substrate and (2) by adding x O atoms to the already optimized structure of Cu_n/Al_2O_3. These structures were optimized using spin polarized DFT as implemented in the VASP code,[54–57] with a generalized gradient approximation for the exchange correlation functional[47] and Projector Augmented Wave (PAW) potentials.[65,200] The wavefunctions were expanded using a plane wave basis set, with an energy cut-off of 400 eV. The Brillouin zone was sampled only at the zone center Γ. For the calculations on supported clusters, the substrate consisted of a slab of hydroxylated amorphous alumina of thickness 8.17 Å and surface cell area = 19.04 Å × 16.49 Å. A vaccum separation ≥ 13 Å was introduced perpendicular to the substrate.

We note that (apart from the presence of, and treatment of, the substrate) all calculation methods used in this chapter are identical to those used in the previous chapter.

8.2.3 Step 3: AIATD to study Oxidation and Reduction

The *ab initio* atomistic thermodynamics (AIATD) method[24,25] was utilized to study the relative stability of the oxide phases of supported Cu clusters in two kinds of equilibrium conditions: (i) in the presence of O_2:

$$Cu_n/Al_2O_3 + \tfrac{x}{2}O_2 \rightleftharpoons Cu_nO_x/Al_2O_3, \tag{8.1}$$

(ii) in the presence of H_2 and H_2O:

$$Cu_nO_x/Al_2O_3 + xH_2 \rightleftharpoons Cu_n/Al_2O_3 + xH_2O. \tag{8.2}$$

The Gibbs free energy of oxide formation, at a temperature T, and a partial pressure of oxygen p_{O_2}, of alumina supported Cu_nO_x clusters in the presence of oxygen, is given by:

$$\Delta G(T, \Delta\mu_{\mathrm{O}}) \approx E^{DFT}_{\mathrm{Cu}_n\mathrm{O}_x/\mathrm{Al_2O_3}} - E^{DFT}_{\mathrm{Cu}_n/\mathrm{Al_2O_3}} - x\left[\frac{1}{2}E^{DFT}_{\mathrm{O_2}} + \frac{1}{2}E^{ZPE}_{\mathrm{O_2}} + \Delta\mu_{\mathrm{O}}(T, p_{\mathrm{O_2}})\right]; \tag{8.3}$$

where $\Delta\mu_O(T, p_{\mathrm{O_2}})$ is defined as:

$$\Delta\mu_{\mathrm{O}}(T, p_{\mathrm{O_2}}) = \mu_O(T, p_{\mathrm{O_2}}) - \frac{1}{2}E^{DFT}_{\mathrm{O_2}} - \frac{1}{2}E^{ZPE}_{\mathrm{O_2}}. \tag{8.4}$$

Here, $E^{DFT}_{\mathrm{Cu}_n\mathrm{O}_x/\mathrm{Al_2O_3}}$ and $E^{DFT}_{\mathrm{Cu}_n/\mathrm{Al_2O_3}}$ are the total energies from DFT of the oxide cluster and the elemental cluster respectively, supported on hydroxylated amorphous alumina. Note that $\mu_{\mathrm{O}} = (1/2)\mu_{\mathrm{O_2}}$, where μ_{O} and $\mu_{\mathrm{O_2}}$ are the chemical potentials of oxygen atoms and oxygen molecules, respectively. $E^{DFT}_{\mathrm{O_2}}$ is the total energy (as obtained from DFT) of an isolated $\mathrm{O_2}$ molecule in the gas phase, and $E^{ZPE}_{\mathrm{O_2}}$ is its zero point energy, which is evaluated by making use of vibrational frequencies obtained using density functional perturbation theory.[201,202]

The temperature and pressure dependence of $\Delta\mu_{\mathrm{O}}$ is given by:

$$\Delta\mu_O(T, p_{\mathrm{O_2}}) = \mu_O(T, p^0) - \mu_O(T^0, p^0) + \frac{1}{2}k_{\mathrm{B}}T\ln(p_{\mathrm{O_2}}/p^0); \tag{8.5}$$

where T^0 and p^0 are the reference temperature and pressure respectively, and k_{B} is Boltzmann's constant. The values of $\mu_{\mathrm{O_2}}(T, p^0)$ are obtained from the JANAF thermochemical tables.[203]

Substituting Eq. (8.5) in Eq. (8.3), we get:

$$\begin{aligned}\Delta G(T, p_{\mathrm{O_2}}) \approx\ & E^{DFT}_{\mathrm{Cu}_n\mathrm{O}_x/\mathrm{Al_2O_3}} - E^{DFT}_{\mathrm{Cu}_n/\mathrm{Al_2O_3}} \\ & - x\left[\frac{1}{2}E^{DFT}_{\mathrm{O_2}} + \frac{1}{2}E^{ZPE}_{\mathrm{O_2}} + \mu_{\mathrm{O}}(T, p^0) - \mu_{\mathrm{O}}(T^0, p^0) + \frac{1}{2}k_{\mathrm{B}}T\ln(p_{\mathrm{O_2}}/p^0)\right].\end{aligned} \tag{8.6}$$

In Eq. (8.2), the forward reaction represents the reduction of copper oxide clusters to form elemental Cu clusters and $\mathrm{H_2O}$. The Gibbs free energy for the reduction reaction is

given by:

$$\begin{aligned}\Delta G(T, \Delta\mu_{\mathrm{H_2}}, \Delta\mu_{\mathrm{H_2O}}) \approx\ & E^{DFT}_{\mathrm{Cu}_n/\mathrm{Al_2O_3}} + x\left[E^{DFT}_{\mathrm{H_2O}} + E^{ZPE}_{\mathrm{H_2O}} + \Delta\mu_{\mathrm{H_2O}}(T, p_{\mathrm{H_2O}})\right] \\ & - E^{DFT}_{\mathrm{Cu}_n\mathrm{O}_x/\mathrm{Al_2O_3}} - x\left[E^{DFT}_{\mathrm{H_2}} + E^{ZPE}_{\mathrm{H_2}} + \Delta\mu_{\mathrm{H_2}}(T, p_{\mathrm{H_2}})\right];\end{aligned} \tag{8.7}$$

where $\Delta\mu_X$ is defined by:

$$\Delta\mu_X(T, p_X) = \mu_X(T, p_X) - E^{DFT}_X - E^{ZPE}_X; \tag{8.8}$$

here $\mu_X(T, p_X)$, E^{DFT}_X, and E^{ZPE}_X are respectively the chemical potential at temperature T and partial pressure p_X, the total energy, and the zero point energy, of the chemical species X.

The temperature and pressure dependence of $\Delta\mu_X$ is given by:

$$\Delta\mu_X(T, p_X) = \mu_X(T, p^0) - \mu_X(T^0, p^0) + k_{\mathrm{B}}T\ln(p_X/p^0); \tag{8.9}$$

where T^0 and p^0 are the reference temperature and pressure respectively, and k_{B} is Boltzmann's constant. The values of $\mu_X(T, p^0)$ are obtained from the JANAF thermochemical tables.[203]

Substituting Eq. (8.9) for $X = \mathrm{H_2O}$ and $X = \mathrm{H_2}$ in Eq. (8.7), we get:

$$\begin{aligned}\Delta G(T, p_{\mathrm{H_2}}, p_{\mathrm{H2O}}) \approx\ & E^{DFT}_{\mathrm{Cu}_n/\mathrm{Al_2O_3}} + x\left(E^{DFT}_{\mathrm{H_2O}} + E^{ZPE}_{\mathrm{H_2O}} + \mu_{\mathrm{H_2O}}(T, p^0) - \mu_{\mathrm{H_2O}}(T^0, p^0)\right) \\ & - E^{DFT}_{\mathrm{Cu}_n\mathrm{O}_x/\mathrm{Al_2O_3}} - x\left(E^{DFT}_{\mathrm{H_2}} + E^{ZPE}_{\mathrm{H_2}} + \mu_{\mathrm{H_2}}(T, p^0) - \mu_{\mathrm{H_2}}(T^0, p^0)\right) \\ & - xk_{\mathrm{B}}T\ln(p_{\mathrm{H_2}}/p_{\mathrm{H_2O}}).\end{aligned} \tag{8.10}$$

We assume that, for the reactions in both the $\mathrm{O_2}$ environment and the $\mathrm{H_2}$ + $\mathrm{H_2O}$ environment, the vibrational contributions largely cancel out between $\mathrm{Cu}_n/\mathrm{Al_2O_3}$ and $\mathrm{Cu}_n\mathrm{O}_x/\mathrm{Al_2O_3}$.

8.3 Results

We have studied three different sizes of Cu_n clusters: $n = 4$, 12 and 20; and different oxide clusters Cu_nO_x for each value of n. For Cu_4O_x clusters, we studied clusters with $x = 1$, 2, 4, and 8, for $Cu_{12}O_x$ clusters, $x = 1$, 2, 3, 6, 9, and 12, and for $Cu_{20}O_x$ clusters, we considered $x = 1$, 2, 10, 12, 15, and 20. All elemental clusters and oxide clusters were supported on hydroxylated amorphous alumina, whose structure was obtained following the procedure described in Section 8.2.1 above.

We have divided our results into five sections. The first section describes our computational results for hydroxylated amorphous alumina, from which we extract information about structural features of the substrate. In the following two sections, we discuss separately our computational and experimental results on alumina supported Cu_nO_x clusters in the presence of O_2 and in the presence of H_2 + H_2O.

We then analyze the bulk Cu standards that are usually used to interpret the XANES spectra of Cu clusters, and we propose that the simple quantity "Bader charge" that is calculated from theory can be used as a measure to interpret the experimental XANES results. Finally in the last section we compare our theoretical predictions for the stable phases as a function of temperature, as well as for the size-dependent transition temperatures, with the corresponding experimental results.

8.3.1 Hydroxylated Amorphous Alumina

We have generated an amorphous alumina slab with 5.26 % of hydrogen in the system, following the procedure described in Section 8.2.1 above. We observe that the hydrogen atoms tend to segregate to the surface of the slab as expected,[81] so as to form hydroxyl groups, as can be seen in Fig. 8.1(a), where we have depicted the relaxed structure obtained by us for the bare alumina slab, on which we will subsequently deposit Cu clusters. In Fig. 8.1(b), we have plotted pair correlation functions [$g(r)$] for the alumina slab; from these, it is clearly evident that the structure is amorphous in nature.

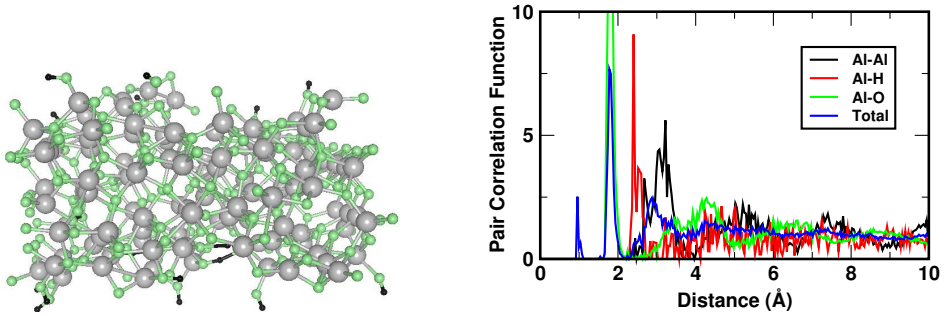

Figure 8.1: *(a) The hydroxylated amorphous alumina slab generated by our MD simulations and used as the substrate for cluster deposition. The Al, O and H atoms are represented by grey, light green and black spheres respectively. (b) The pair correlation functions of different pairs of atoms and the total pair correlation function of all pairs of atoms in the constructed amorphous Al_2O_3 slab are shown.*

8.3.2 Clusters supported on Hydroxylated Amorphous Alumina: Computational Results

In Fig. 8.2, we show our lowest energy geometries for each Cu_nO_x. For Cu_4O_x clusters, we studied clusters with $x = 0$, 2, 4, and 8, for $Cu_{12}O_x$ clusters, $x = 0$, 1, 2, 3, 6, 9, and 12, and for $Cu_{20}O_x$ clusters, we considered $x = 0$, 1, 2, 10, 12, 15, and 20. Comparison with results for gas phase clusters obtained in the previous chapter shows that the optimal geometry changes significantly upon deposition on the alumina substrate, and also upon oxidation. Note also the presence of hydrogen atoms (small black spheres) in the substrate that are found to preferentially diffuse toward the surfaces of the slab.

Next, we consider the reactions in Eqs. (8.1) and (8.2). In the forward direction, Eq. (8.1) describes the oxidation of the cluster in the presence of O_2 and Eq. (8.2) describes the reduction of the cluster in the presence of H_2 and H_2O. We use the AIATD method to obtain the Gibbs free energy of oxidation/reduction at a temperature T, which is given by Eqs. (8.3) and (8.7).

8.3.2.1 Supported Cu clusters in the presence of O_2

Figs. 8.3(a)–(d) show plots of ΔG vs. $\Delta\mu_O$ for the bulk, as well as for all the Cu_nO_x structures depicted in Fig. 8.2, for $n = 4$, 12 and 20. The stable structure at any given $\Delta\mu_O$ is the system with the lowest ΔG. For $n = 4$ and $n = 20$, we obtain only three stable

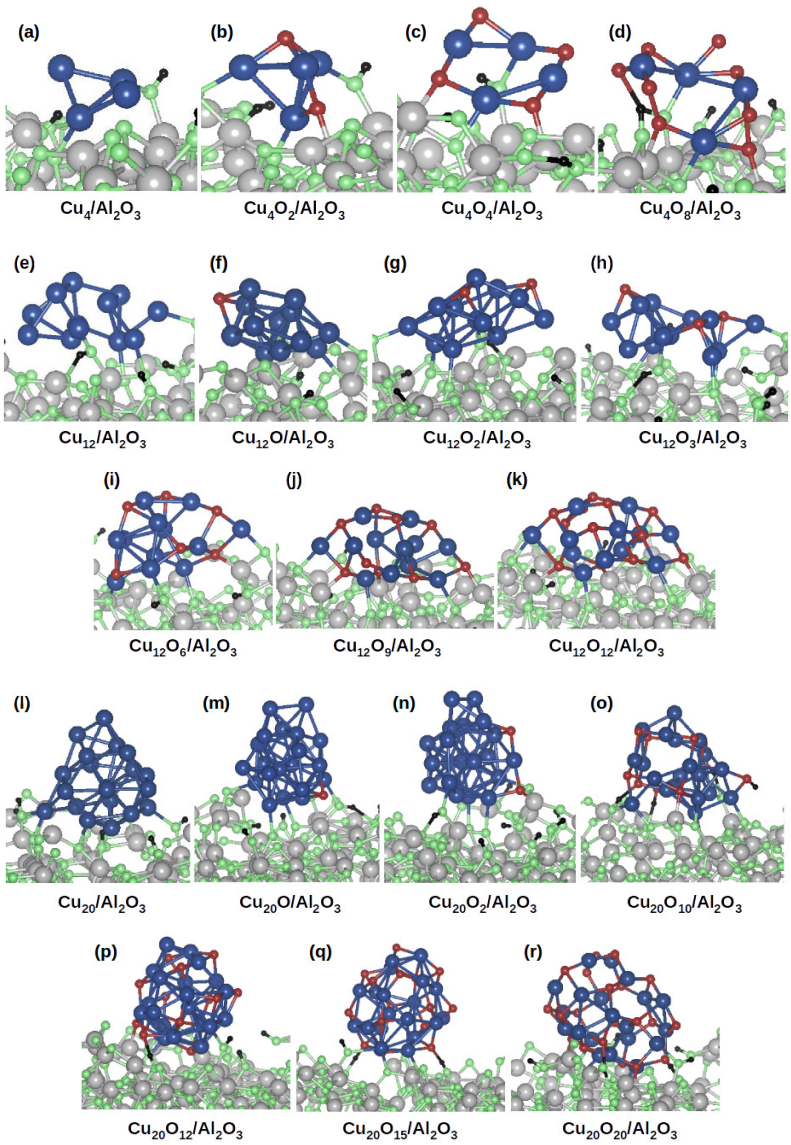

Figure 8.2: *The lowest energy structures obtained for all the elemental and oxide clusters (on the hydroxylated amorphous alumina support), as obtained from our DFT calculations. The first row: Cu_4O_x clusters, with x = 0, 2, 4, 8; the second and third rows: $Cu_{12}O_x$ clusters, with x = 0, 1, 2, 3, 6, 9, 12; and fourth and fifth rows: $Cu_{20}O_x$ clusters, with x = 0, 1, 2, 10, 12, 15, 20. The grey, black and light green spheres represent Al, H and O atoms respectively in the support, and the blue and red spheres represent the Cu and O atoms respectively in the cluster.*

phases in the phase diagram, viz., Cu_n, $Cu_nO_{n/2}$ and Cu_nO_n. Interestingly, these phases have the same stoichiometry as the phases observed in the bulk: Cu, Cu_2O and CuO [see Fig. 8.3(a)]. However, for $n = 12$, we also obtain an additional intermediate phase, viz., $Cu_{12}O_9$. It is interesting to note that this corresponds to the metastable Cu_4O_3 (paramelaconite) phase of the bulk.[195]

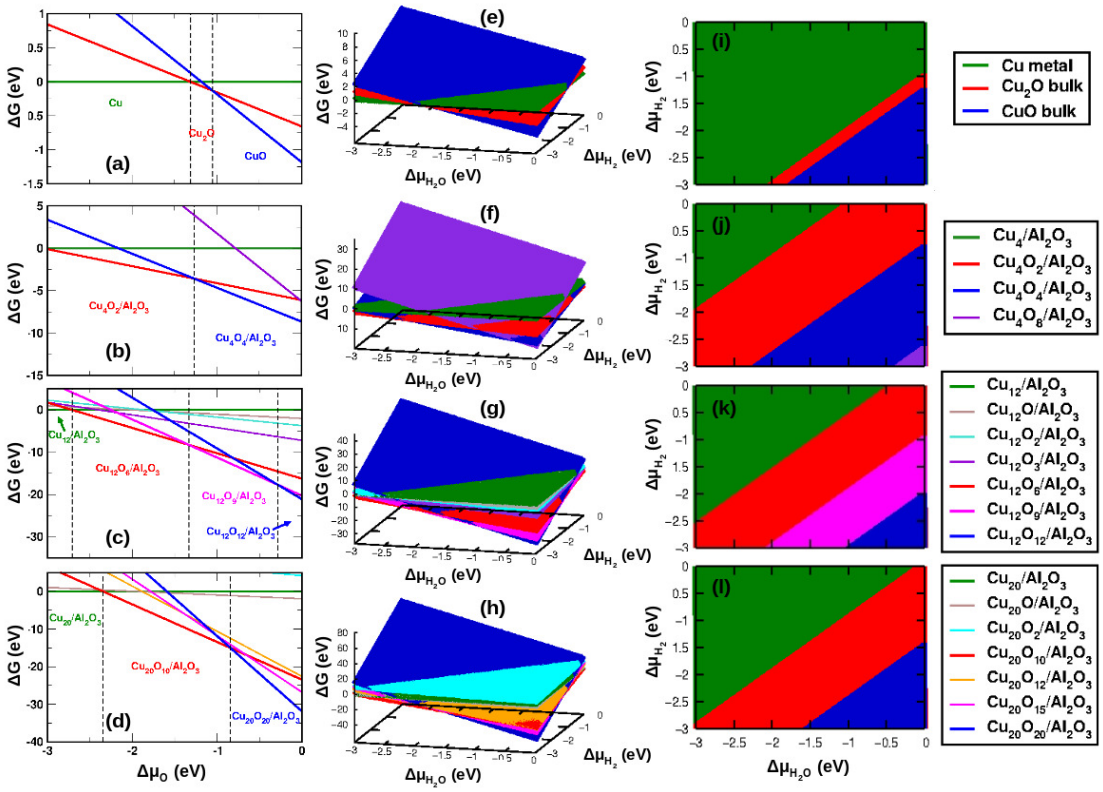

Figure 8.3: *Obtaining phase diagrams by looking for the phase with lowest Gibbs free energy, using atomistic thermodynamics. The first row of figures [(a), (e), (i)] corresponds to the bulk, the second row [(b), (f), (j)] to $n = 4$, the third row [(c), (g), (k)] to $n = 12$, and the fourth row [(d), (h), (l)] to $n = 20$. Panels (a), (b), (c), and (d) are relevant to the oxidation process of Eq. (8.1) and show plots of ΔG, the change in Gibbs free energy, as a function of $\Delta\mu_O$, the change in the chemical potential of oxygen. Each colored line corresponds to a different structural phase (see legend on the extreme right), and the vertical dashed lines indicate phase transitions. All the remaining panels are relevant to the reduction process of Eq. (8.2). In panels (e), (f), (g) and (h), we plot ΔG as a function of $\Delta\mu_{H_2}$ as well as $\Delta\mu_{H_2O}$, the chemical potentials of hydrogen and water respectively. The panels (i), (j), (k) and (l) show the most stable phase for each ($\Delta\mu_{H_2}$, $\Delta\mu_{H_2O}$).*

It is also interesting to compare the stable phases observed in O_2 environment for the gas phase Cu clusters (from the previous chapter) to those now obtained for the supported Cu clusters. In the gas phase, for $n = 4$ we see only two stable phases, viz., Cu_4 and Cu_4O_4. However, when these clusters are supported on amorphous alumina, we also see the intermediate Cu_4O_2 phase in addition to Cu_4 and Cu_4O_4. For $n = 12$, in the gas phase we find Cu_{12}, $Cu_{12}O_6$ and $Cu_{12}O_9$. The phase with the higher oxidation state $Cu_{12}O_{12}$ does not seem to be stable in the gas phase in contrast to what we find when these clusters are supported on amorphous alumina. Also for $n = 20$, we see that

the phase with the highest oxidation state $Cu_{20}O_{20}$ is not stable in the gas phase while it is found to be stable when supported on amorphous alumina. From these results, we can conclude that the support strongly influences the phase diagram of clusters: we see that, in the presence of O_2, the clusters placed on the alumina support are able to reach higher oxidation states more easily as compared to when the clusters are in the gas phase. (However, in the gas phase we see two additional intermediate phases for $n = 20$, viz., $Cu_{20}O_{12}$ and $Cu_{20}O_{15}$, which are not observed after the deposition on the support.)

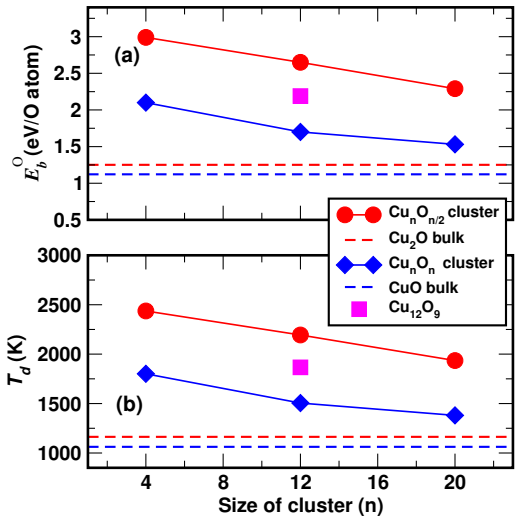

Figure 8.4: *Size-dependent energetics. (a) E_b^O, binding energy per O atom vs. n, the number of Cu atoms in the cluster, and (b) the thermal desorption temperature T_d vs. n. See the text for the definition of these quantities. The dashed blue and red lines correspond to the values for bulk CuO and Cu_2O respectively. Note that the thermal stability increases with decreasing size, and the oxide clusters are more thermally stable than the corresponding bulk oxides.*

In Fig. 8.4(a) we show how E_b^{O}, the binding energy of oxygen to the cluster, varies with n, for the stable phases. This is obtained by computing $E_b^{\mathrm{O}} = -(1/x)[E^{DFT}_{\mathrm{Cu}_n\mathrm{O}_x/\mathrm{Al_2O_3}} - E^{DFT}_{\mathrm{Cu}_n/\mathrm{Al_2O_3}} - (x/2)E^{DFT}_{\mathrm{O_2}}]$. We see that E_b^{O} decreases monotonically as n increases, and is higher for the nanoparticles than for the bulk, for both +1 and +2 oxidation states. Moreover, for a given n, as the oxidation state of Cu decreases from +2 to +1, E_b^{O} increases, due to the progressive approach toward achieving a filled $3d$-orbital. As already noted in the previous chapter, for both bulk CuO and bulk Cu_2O, our values for the binding energy (formation enthalpy) are in good agreement with previous GGA calculations,[194,210] but

Average Charge on Cu atoms	$n = 4$	$n = 12$	$n = 20$	Bulk
Cu_n	-0.06	-0.01	0.00	0.00
$Cu_nO_{n/2}$	0.54	0.55	0.54	0.57
$Cu_nO_{3n/4}$	-	0.79	-	-
Cu_nO_n	0.93	1.00	0.94	1.06

Table 8.1: *Average charge on Cu atoms as obtained from Bader analysis*

are underestimated with respect to experiments; this has been attributed to GGA errors in computing the binding energy of the O_2 molecule as well as the formation energy of O^{2-} from O_2.[194]

In Fig. 8.4(b) we show the relative thermal stability of $Cu_nO_{n/2}$ (red symbols) and Cu_nO_n (blue symbols), i.e., the temperature at which oxygen would desorb completely to result in the elemental Cu_n cluster. This temperature (T_d) is obtained by putting $\Delta G(T_d, \Delta\mu_O) = 0$ in Figs. 8.3(a)–(d), with $p(O_2) = 1$ atm. On comparing with the corresponding results for the bulk (dashed lines), we see that the thermal stability of the clusters increases as size decreases. This is in marked contrast to previous results for small gas phase Ag clusters, which were reported to be less thermally stable than the corresponding bulk or surface.[190]

In order to validate the comparison between the clusters and the bulk, as well as a subsequent comparison with XANES data, we compute the average charge on Cu atoms using Bader analysis.[108,109] These values are presented in Table 8.1; it is interesting to note that the average Bader charge (and therefore oxidation state) of the Cu atoms in a supported Cu_nO_x cluster is the same as that of the corresponding bulk phase, even though there is a spread in the values of the Bader charges on the different Cu atoms in a cluster [see Fig. 8.14(d)–(f) further below], and despite the fact that some of the Cu atoms are, in addition, also bonded to O atoms in the substrate. We note that the charges obtained from the Bader analysis are considerably smaller than the expected nominal charges (by a factor of ~ 2); our values are in good agreement with those reported by previous authors for the Bader charges on Cu atoms in bulk Cu_2O and CuO.[199,216] A similar observation about lower Bader charges than nominal charges has also been made earlier by several authors, e.g., for Pt atoms[217] and Ag atoms[218] in their respective bulk oxides.

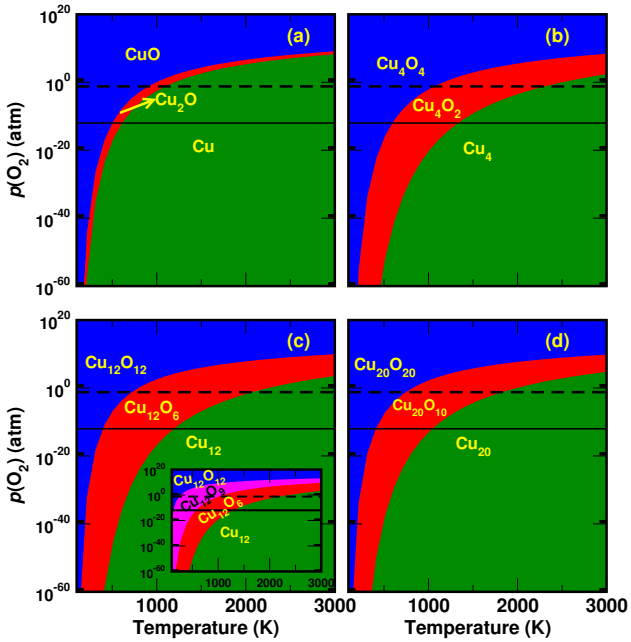

Figure 8.5: *Theoretical results for phase stability under oxidizing conditions. We show pressure-temperature phase diagrams for (a) bulk, (b) $n = 4$, (c) $n = 12$, and (d) $n = 20$. $p(O_2)$ is the partial pressure of oxygen. The black dashed and solid lines correspond to $p(O_2) = 0.06$ atm and 10^{-12} atm respectively. In all panels, green, red and blue phases correspond to Cu_n, $Cu_n O_{n/2}$ and $Cu_n O_n$ phases respectively. The inset in (c) shows the intermediate phase $Cu_{12}O_9$ in magenta.*

The data contained in Figs. 8.3(a)–(d) are used to generate the phase diagrams relevant to Eq. (8.1). These are presented in Fig. 8.5, where we have plotted the stable phases as a function of temperature T, and $p(O_2)$, the partial pressure of O_2. As we have already remarked in the previous chapter, in agreement with previous authors, we find that for the bulk, the transition temperatures are shifted with respect to experiment; we believe these errors arise from an error in the binding energy due to the use of the GGA (as already discussed above) as well as self interaction errors.[194,195] From Figs. 8.5(a)–(d), we see that, as expected, the oxidation state of Cu increases as $p(O_2)$ increases and/or T decreases. The domain of stability of $Cu_nO_{n/2}$ is much larger for the nanoparticles than for the bulk; note however that for $n = 12$, there are actually two intermediate transitions because of the presence of the $Cu_{12}O_9$ phase [see inset to Fig. 8.5(c)]. Also note that though we have extended the temperature axis in Fig. 8.5 to 3000 K, it is known that the bulk phases of Cu, Cu_2O and CuO melt at 1358 K, 1505 K and 1599 K, respectively.

In order to examine size-dependent trends in oxidation, we extract data from the phase

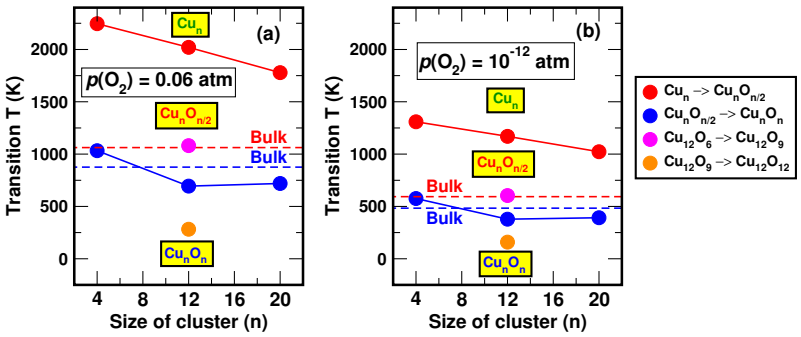

Figure 8.6: *In (a) and (b), we show our results for the transition temperatures at two values of $p(O_2)$, viz., 0.06 atm and 10^{-12} atm respectively, both as a function of n, the number of Cu atoms in the cluster. The red lines and symbols indicate the $Cu_n \rightarrow Cu_nO_{n/2}$ transition, while blue lines and symbols indicate the $Cu_nO_{n/2} \rightarrow Cu_nO_n$ transition. The magenta and orange symbols indicate the intermediate $Cu_{12}O_6 \rightarrow Cu_{12}O_9$ and $Cu_{12}O_9 \rightarrow Cu_{12}O_{12}$ transitions respectively.*

diagrams of Figs. 8.5(a)–(d) at two values of $p(O_2)$, viz., 0.06 atm and 10^{-12} atm, see the black dashed and solid lines respectively. The former value corresponds to that used in the experiments that we will compare to further below, while the latter is an example of ultra high vacuum (UHV) conditions. In this way, we obtain the phase transition temperatures plotted in Figs. 8.6(a) and (b). For the transition $Cu_n \rightarrow Cu_nO_{n/2}$ (shown in red), we see that the transition temperature increases as cluster size decreases and is higher for the clusters than for the bulk (red dashed line). This is in agreement with our expectation that the reactivity toward oxidation increases as size decreases. However, for the transition $Cu_nO_{n/2} \rightarrow Cu_nO_n$ (shown in blue), we do not see the same trend. We see that Cu_4O_2 oxidizes more easily than the bulk, whereas $Cu_{12}O_6$ and $Cu_{20}O_{10}$ oxidize at almost the same temperature and are more resistant to oxidation than the bulk (blue dashed line). The transition temperatures for the two intermediate transitions in the case of Cu_{12} are also included in Figs. 8.6(a) and (b). From Fig. 8.6(a), one can see that in O_2 rich conditions like $p(O_2) = 0.06$ atm and at room temperature, all clusters will be in their fully oxidized state.

To understand the difference between the results obtained for the bulk, the supported clusters and the gas phase clusters, we plot the stable phases observed at $p(O_2) = 10^{-12}$ atm as a function of temperature in the three cases in Fig. 8.7.

Note that in these figures the green phase denotes the elemental Cu_n phase and the blue phase denotes the Cu_nO_n phase which is the one with the highest oxygen content to

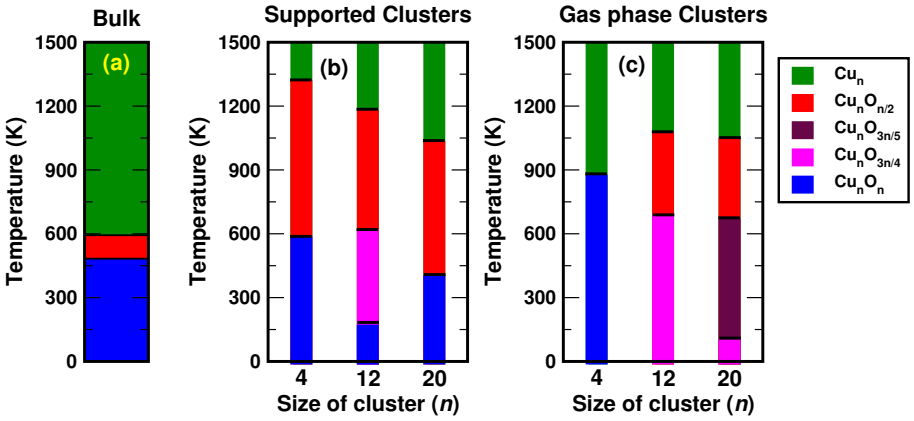

Figure 8.7: *The stable phases observed at $p(O_2) = 10^{-12}$ atm as a function of temperature for (a) the bulk, (b) the hydroxylated alumina-supported clusters and (c) the gas phase clusters.*

appear in the phase diagram; oxidation occurs when we move from the green phase to the blue phase as temperature decreases. When considering the oxidation of the green phase to the first oxide phase, for $n = 4$ and 12 clusters, we see that the presence of the support increases the tendency to oxidize, whereas for $n = 20$ clusters, we see that the presence of the support decreases the tendency to oxidize. Both the supported clusters and the gas phase clusters have a higher tendency to oxidize than the bulk, which is as expected.

On comparing the extent of oxidation in the supported and gas phase clusters, we see that the presence of the support allows the clusters with $n = 12$ and 20 to oxidize 'completely' to form the Cu_nO_n phase (shown in blue) which is not observed in the gas phase. However, note that the tendency for the $n = 12$ and 20 supported clusters to be in the Cu_nO_n phase is lower than the tendency for the bulk to be in the CuO phase. For $n = 4$ clusters, we see that the gas phase clusters have a higher tendency to oxidize to the Cu_nO_n phase than the supported $n = 4$ clusters. Both the supported and gas phase $n = 4$ clusters have a higher tendency to oxidize to the Cu_nO_n phase than the bulk.

(In the paragraphs above, we note that when we refer to 'a higher tendency to oxidize' we mean that the oxide phase is stable up to a higher temperature.)

8.3.2.2 Supported Cu clusters in the presence of H_2 and H_2O

In Eq. (8.2), in addition to Cu_n/Al_2O_3 and Cu_nO_x/Al_2O_3, there are two additional species, viz., H_2 and H_2O. As noted in the previous chapter, this environment can promote either

oxidation or reduction, depending on the relative partial pressures of H_2 and H_2O.

We now calculate how ΔG depends on the two variables $\Delta\mu_{H_2O}$ and $\Delta\mu_{H_2}$. Figs. 8.3(e)-(h) show three-dimensional plots of ΔG as a function of $\Delta\mu_{H_2O}$ and $\Delta\mu_{H_2}$ for the bulk, as well as for all the Cu_nO_x/Al_2O_3 structures depicted in Fig. 8.2, for $n = 4$, 12 and 20. The lowest lying configuration at each value of ($\Delta\mu_{H_2O}$, $\Delta\mu_{H_2}$) is then determined, so as to obtain the phase diagrams plotted in Figs. 8.3(i)-(l). From these figures we see that for the bulk, as well as for the clusters, we now obtain the same stable phases, as we did when studying the systems in the presence of O_2 (compare the first and third columns in Fig. 8.3). However, one additional phase does appear in the phase diagram for $n = 4$: we see a small domain of stability for Cu_4O_8 at high $\Delta\mu_{H_2O}$ and low $\Delta\mu_{H_2}$ (indicated in violet).

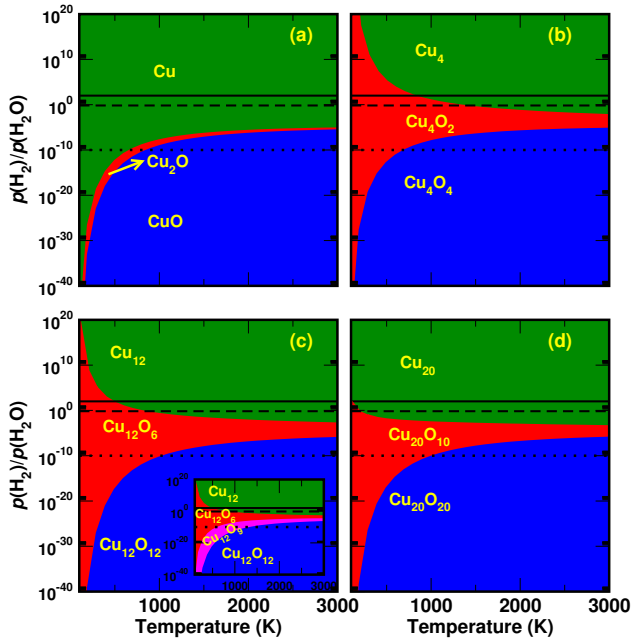

Figure 8.8: *Theoretical results for phase stability under reducing conditions. In (a)–(d), we show the phase diagrams as a function of temperature, T, and the ratio of hydrogen to water, $p(H_2)/p(H_2O)$, for (a) bulk, (b) $n = 4$, (c) $n = 12$, and (d) $n = 20$. $p(H_2)$, and $p(H_2O)$ are the partial pressures of hydrogen and water respectively. The black solid, dashed and dotted lines correspond to $p(H_2)/p(H_2O) = 100$, 0.67 and 10^{-10} respectively. In all panels, the green, red and blue phases correspond to the Cu_n, $Cu_nO_{n/2}$ and Cu_nO_n phases respectively. The inset in (c) shows the intermediate phase $Cu_{12}O_9$ in magenta.*

As we did before in the case of an O_2 environment, we now obtain temperature-dependent phase diagrams in the presence of H_2 and H_2O; these plots are shown in

Figs. 8.8(a)–(d). In order to obtain two-dimensional plots that are easily interpreted, we choose $p(H_2)/p(H_2O)$ as the ordinate for these plots. A striking feature is that the behavior is quite different now for the supported clusters compared to the bulk. For the bulk, we see from Fig. 8.8(a) that the phase boundaries separating CuO from Cu_2O, and Cu_2O from Cu, are convex upward. This means that for both transitions, if $p(H_2)/p(H_2O)$ is held fixed, reduction occurs as the temperature T is decreased. However, for the clusters, while the phase boundary separating Cu_nO_n and $Cu_nO_{n/2}$ remains convex upward, the boundary separating $Cu_nO_{n/2}$ and Cu_n is now concave upward. [Compare and contrast with Fig. 7.9.] As a result, for the former transition, reduction occurs when T is decreased, but for the latter, it occurs when T is increased. We note, however, that the two transitions occur for different ranges of $p(H_2)/p(H_2O)$, i.e., there is no value of $p(H_2)/p(H_2O)$ at which both transitions can occur. The transitions with phase boundaries curved concave upwards occur at high values of $p(H_2)/p(H_2O)$ or in H_2-rich conditions, while the transitions with phase boundaries curved convex upwards occur at low values of $p(H_2)/p(H_2O)$ or in H_2O-rich conditions. We shall consider the transitions in both these situations separately to extract size-dependent trends.

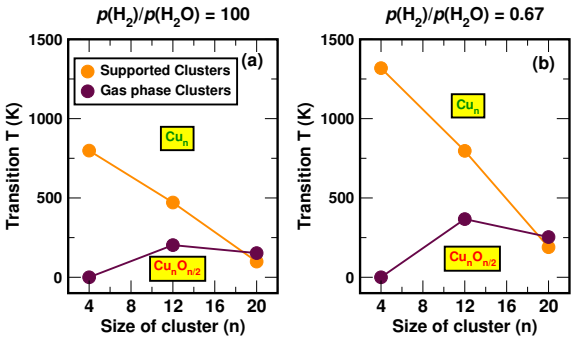

Figure 8.9: *In (a) and (b), we show our results for the transition temperatures at two values of $p(H_2)/p(H_2O)$, viz., 100 atm and 0.67 respectively, both as a function of n, the number of Cu atoms in the cluster. The orange lines and symbols indicate the $Cu_n \rightarrow Cu_nO_{n/2}$ transition in the supported clusters, while the maroon lines and symbols indicate the same transition in the gas phase clusters.*

Let us first consider the case where the phase boundaries are shaped concave upwards. We extract transition temperatures for the supported clusters, as we did for the gas phase clusters in the previous chapter, for two values of $p(H_2)/p(H_2O)$, viz., 100 and 0.67. These values are marked in Figs. 8.8(a)–(d) by black solid and dashed lines respectively. The

former value is an example of hydrogen-rich conditions and the latter is a condition typical of those in which the low-temperature water-gas shift reaction is carried out. We see that these lines in Fig. 8.8(a) intersect no phase boundaries in the case of the bulk; the bulk metallic Cu phase is the stable phase in these conditions at all temperatures. For the three supported clusters however, we see that these lines cut phase boundaries that are curved concave upwards and separate the red and green regions in the plot. As temperature increases, we move from the red region to the green region, this denotes the reduction from the $Cu_nO_{n/2}$ phase to the Cu_n phase.

The transition temperatures at the two values of $p(H_2)/p(H_2O) = 100$ and 0.67, for the supported clusters (in orange) and the gas phase clusters (in maroon) are shown in Figs. 8.9(a) and (b) as a function of n, the size of the cluster. The trends as a function of size are the same in the two graphs, we see that the transition temperatures are lower when $p(H_2)/p(H_2O) = 100$ as compared to the transition temperatures when $p(H_2)/p(H_2O) = 0.67$. This just means that as the ratio of $p(H_2)/p(H_2O)$ increases, the H_2 content in the system increases, and the less resistant the clusters become to reduction.

For the supported clusters, we see a clear size-dependent trend. We see that the smaller the cluster, the higher is the transition temperature, i.e., the smaller the cluster the more resistant it is to reduction (in agreement with our results for oxidation); the cluster with $n = 20$ will be reduced to elemental Cu already at a very low temperature. On comparing the transition temperatures for the supported clusters and the gas phase clusters, we find the following: in terms of resistance to reduction, we see that for $n = 4$ and 12 clusters, the presence of the support makes the clusters more resistant to reduction, whereas for $n = 20$ the presence of the support makes the cluster less resistant to reduction. In terms of tendency to oxidize, we see that for $n = 4$ and 12 clusters, the presence of the support increases the tendency to oxidize whereas for $n = 20$ the presence of the support decreases the tendency to oxidize.

There is important data that we can extract from these graphs. For example, in Fig. 8.9(b) where we show transition temperatures at $p(H_2)/p(H_2O) = 0.67$ in the supported clusters, we see that at a temperature of around 500 K, only the supported Cu_{20}

cluster will be in its elemental state, whereas the supported $n = 4$ and 12 clusters are in still their oxidized state. The value of $p(H_2)/p(H_2O)$ chosen is an example of an experimental condition in which several reactions like the low-temperature water-gas shift reaction proceed; if the Cu catalyst is required to be in its elemental state, one would therefore need to use clusters of size larger than $n = 20$.

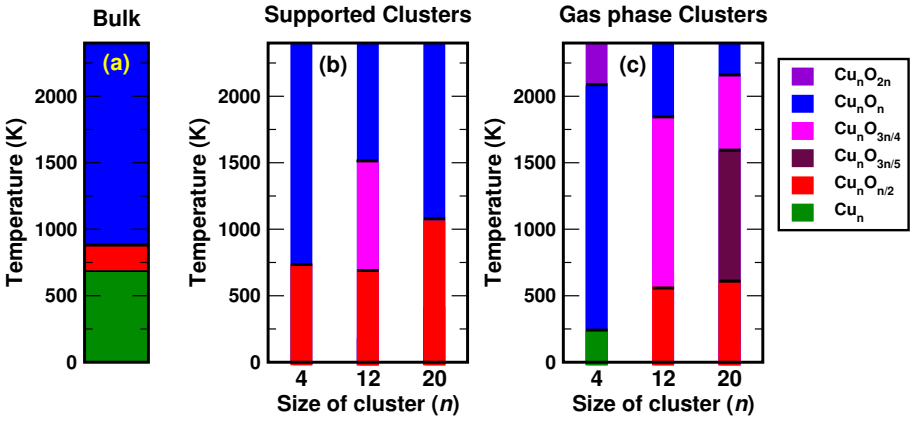

Figure 8.10: *The stable phases observed for (a) the bulk, (b) the supported clusters and (c) the gas phase clusters at in an environmental condition of $p(H_2)/p(H_2O) = 10^{-10}$ as a function of temperature. The green, red and blue phases represent the stoichiometric phases Cu_n, $Cu_nO_{n/2}$ and Cu_nO_n respectively; oxidation occurs as temperature increases.*

Now we shall consider the transitions where the phase boundaries are shaped convex upwards, for example at $p(H_2)/p(H_2O) = 10^{-10}$, which is shown by the black dotted line in Figs. 8.8(a)–(d). This is a water-rich condition, where oxidation occurs as temperature increases. In Figs. 8.10(a)–(c), we show the stable phases and the transitions observed at $p(H_2)/p(H_2O) = 10^{-10}$ for the bulk, the supported clusters and the gas phase clusters. Let us consider the oxidation of the clusters and the bulk to the Cu_nO_n phase shown by blue in these figures. We see that the $n = 4$ supported and gas phase clusters oxidize more easily (i.e., the Cu_nO_n phase becomes stable at lower temperatures) than the bulk. However for $n = 12$ and 20, we see that the supported clusters as well as the gas phase clusters oxidize to the Cu_nO_n phase at much higher temperatures than the bulk. On comparing the transition temperatures for the oxidation to the Cu_nO_n phase for the supported and the gas phase clusters, we see that the presence of the support decreases the tendency to oxidize in the case of $n = 4$, whereas for $n = 12$ and 20, the presence of the support increases the tendency to oxidize.

8.3.3 Clusters supported on Hydroxylated Amorphous Alumina: Experimental Results

8.3.3.1 Supported clusters in O_2-rich conditions

The XANES data for the clusters and for the Cu compounds used as standards are shown in Fig. 8.11. The supported clusters are kept in an environment with $p(O_2) = 0.06$ atm and heated up to a high temperature $T = 898$ K. The XANES measurements are taken before the introduction of O_2 in He environment and then after the introduction of O_2 as the system is heated from 298 K to 898 K for every 75 K increase in T. A final XANES measurement is also taken after the system is cooled down back to room temperature. Note that the x-ray edge is not as sharp for clusters as for bulk XANES standards, this may be due to the fact that in small clusters all the atoms in a given cluster may not experience the same environment and also due to the several different adsorption sites that the cluster has occupied on the amorphous surface. By looking at the spectra and comparing them with the standards, one can roughly say that the experiments support the existence of Cu_nO_n at 298 K, for all three sizes of clusters studied, even before the introduction of oxygen (see Fig. 8.11). In general, for most of the XANES spectra recorded in the various environments, we do not with such a rough visual examination, see any significant change in the spectra as T is increased; however, we will see further below that the data does, in fact, in many cases contain information about rather sharp temperature-dependent phase transitions.

8.3.3.2 Supported clusters in H_2-rich conditions

XANES spectra obtained for the clusters with $n = 4$, 12 and 20 in a H_2 environment are shown in Fig. 8.12 along with the XANES spectra for some of the bulk Cu compounds that are used as standards. As was done in the case of an O_2-rich environment, here again the XANES measurements are made before the introduction of H_2 in He environment, and after the introduction of H_2, as the system is heated from 298 K to 898 K, for every 75 K increase in T. A final XANES measurement is also taken after the system is cooled down back to room temperature.

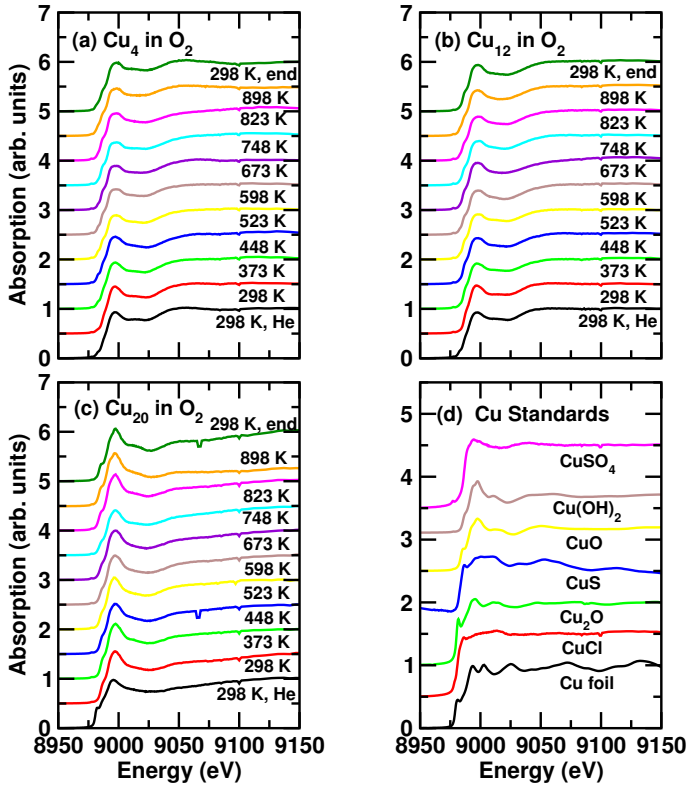

Figure 8.11: *Experimental results for the oxidation of Cu clusters on amorphous alumina in the presence of O_2. XANES spectra for supported (a) Cu_4, (b) Cu_{12} and (c) Cu_{20} clusters in O_2 for different T. By comparing with the XANES standards in (d), we see that there is experimental evidence for the presence of Cu^{1+} and Cu^{2+} oxidation states.*

By a rough visual inspection of the spectra and comparison with the standards, one can see indications of changes in the spectra of the clusters as temperature increases. The spectrum at 298 K looks similar to the spectra of Cu in compounds with +2 and +1 oxidation states and as temperature increases, it begins to look more like the spectrum of bulk Cu foil. Further below, we will analyze and quantify these changes more precisely.

8.3.4 Bulk Cu Standards: A novel way to Correlate *Ab initio* data with Experimental X-ray edges

One would like to find a simple way to correlate results from our *ab initio* results on phase transitions in the Cu clusters, with the experimental XANES data. We note that actually simulating XANES spectra theoretically is rather cumbersome, and also often involves making use of several free parameters. However, we believe that the 'Bader charge' [108,109]

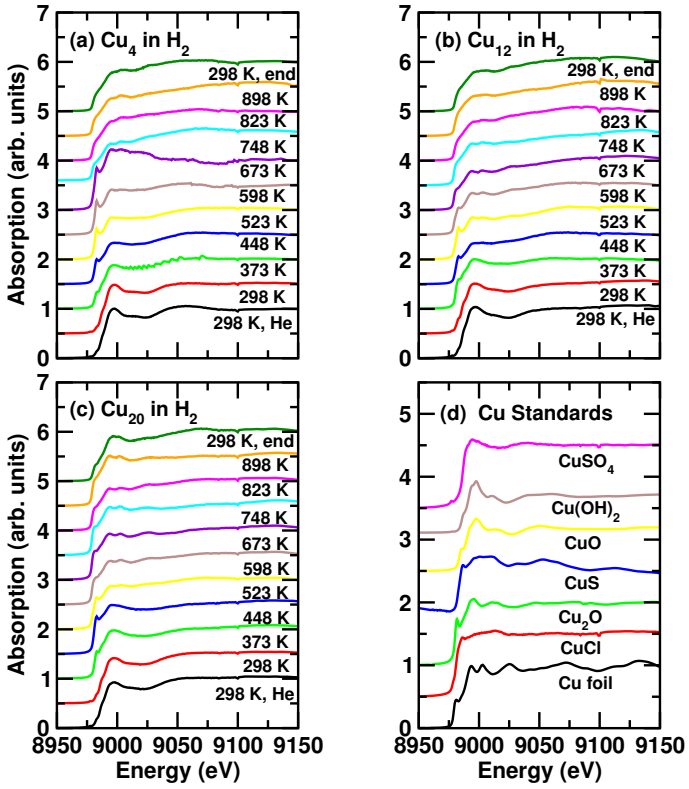

Figure 8.12: *Experimental results for the reduction of Cu clusters on amorphous alumina in the presence of H_2. XANES spectra for supported (a) Cu_4, (b) Cu_{12} and (c) Cu_{20} clusters in H_2 for different T. By comparing with the XANES standards in (d) we see that there is experimental evidence for the reduction process in presence of H_2: $Cu^{2+} \rightarrow Cu^{1+} \rightarrow Cu^0$.*

on the Cu atoms, offers a simple yet precise way of making such a correlation. To check the feasibility of such an approach, in this section we first consider the extended Cu compounds, whose XANES spectra serve as standards to which the spectra of clusters are compared to.

Accordingly, we have performed DFT calculations to obtain the optimized bulk structures and charge densities for Cu, CuCl, Cu_2O, CuS, CuO, $Cu(OH)_2$ and $CuSO_4$. Of these, Cu metal has the Cu atoms in the zero charge state; for CuCl and Cu_2O, the nominal charge on the Cu atoms is +1, and for all the remaining systems, it is +2. However, when we compute the Bader charge $\rho_B(\mathrm{Cu})$ on the Cu atoms by partitioning the charge density as prescribed by Bader,[108,109] we find that in all the cases except for the trivial case of elemental Cu, the computed charge on the Cu atoms is considerably less than the expected nominal charge $\rho_N(\mathrm{Cu})$; this is because the chemical bonds in these systems are

not purely ionic in nature.[219]

In Fig. 8.13(a) we have plotted the ratio of the nominal charge to the Bader charge as a function of the electronegativity χ of the atom or group that the Cu atoms are bonded to. Note that for the anionic elements, the Pauling electronegativity is used, while the values of χ for the OH and SO_4 groups have been taken from Ref. 220. From this figure, we see that we obtain a very clear linear relationship between the Bader charge and the electronegativity of the anion. This is indicative of the fact that the Bader charge is found to be less than the nominal charge has a real chemical origin, and the Bader charge represents accurately the chemical environment of the Cu atoms in the compound; since such a chemical environment is also what the position of the XANES K-edge is sensitive to,[212,213] it appears natural to try to correlate these two quantities, which we will do further below.

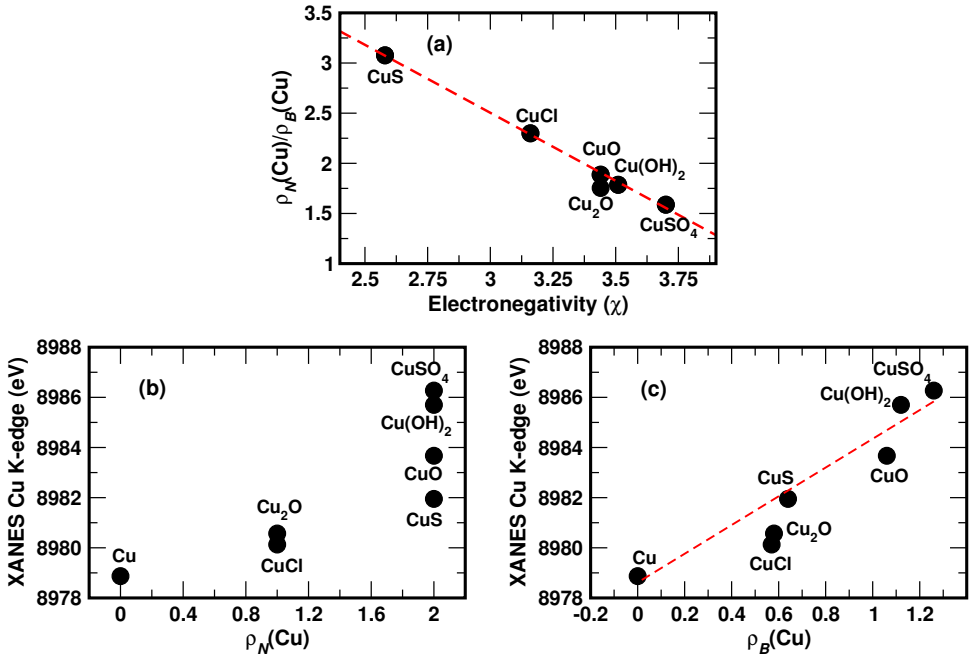

Figure 8.13: *Bader charges on Cu atoms are determined by the electronegativity of the anion and correlate well with the position of the Cu K-edge in XANES spectra. In panel (a), the ordinate is the ratio of $\rho_N(Cu)$, the nominal oxidation state of Cu as expected from the valency, to $\rho_B(Cu)$, the charge on the Cu atoms as computed by Bader analysis. The abscissa is the electronegativity χ of the anionic atom or group that Cu atoms are bonded to. Note the linear relationship. In panel (b) the ordinate is the XANES Cu K-edge position, and the abscissa is $\rho_N(Cu)$; we do not see a linear relationship here. In panel (c), the ordinate is the position of the XANES Cu K-edge and the abscissa is $\rho_B(Cu)$.*

In Fig. 8.13(b), we have plotted the position of the Cu K-edge as determined by the position of the first peak in the first derivative of the XANES spectrum in a given compound, against the nominal oxidation state of Cu, ρ_N(Cu), in the corresponding compound; such plots have frequently been drawn by previous authors.[212,213] Note that there is a clear increase in the energy position as the oxidation state increases, but we do not see a linear correlation between the two quantities. However, when we attempt to instead use the Bader charges to correlate with the XANES edge positions from experiments, which we show in Fig. 8.13(c), to a good approximation, we find a linear relationship between ρ_B(Cu) in a given compound and the XANES Cu K-edge position of the corresponding compound. We will therefore use the Bader charges from theory to correlate with the XANES edges from experiment, using both as simultaneous probes of oxidation states. We are not aware of any previous work where the authors have attempted to make use of such a correlation. We shall now use this new information to compare our theoretical results with the experimental XANES results for Cu_nO_x/Al_2O_3 in both O_2 and H_2 + H_2O environments.

8.3.5 Theoretical Predictions vs. Experimental Observations

8.3.5.1 Supported clusters in O_2-rich environment

Our theoretical results for the supported clusters in an O_2-rich environment [$p(O_2) = 0.06$ atm], suggest that at room temperature all sizes of clusters considered are in their oxidized state and as temperature increases one would observe the first reduction from $Cu_nO_n \rightarrow Cu_nO_{n/2}$, and at very high temperatures the further reaction from $Cu_nO_{n/2} \rightarrow Cu_n$. To compare our theoretical results with the XANES results, we first plot the Bader charge averaged over all the Cu atoms in the stable phase of the cluster at a given T vs. T for n = 4, 12 and 20 respectively, in panels Figs. 8.14(a)–(c) and we plot the individual Bader charges on each Cu atom in the stable phase of the cluster at a given T, vs. T, again for n = 4, 12 and 20 respectively, in panels Figs. 8.14(d)–(f). The theoretical Bader charge results are shown by the solid blue, red, green and magenta lines in all panels. The Bader charges of the Cu atoms in $CuSO_4$ and metallic Cu are also shown on the left hand side

of all panels as black bars for reference. Although the average value of the Bader charge of Cu atoms in the clusters matches well with the bulk phase with the same stoichiometry (see Table 8.1), we see that there is a spread in the individual Bader charges of the Cu atoms in the cluster. This is because each Cu atom in the cluster experiences a different bonding environment and hence has a different value of the Bader charge.

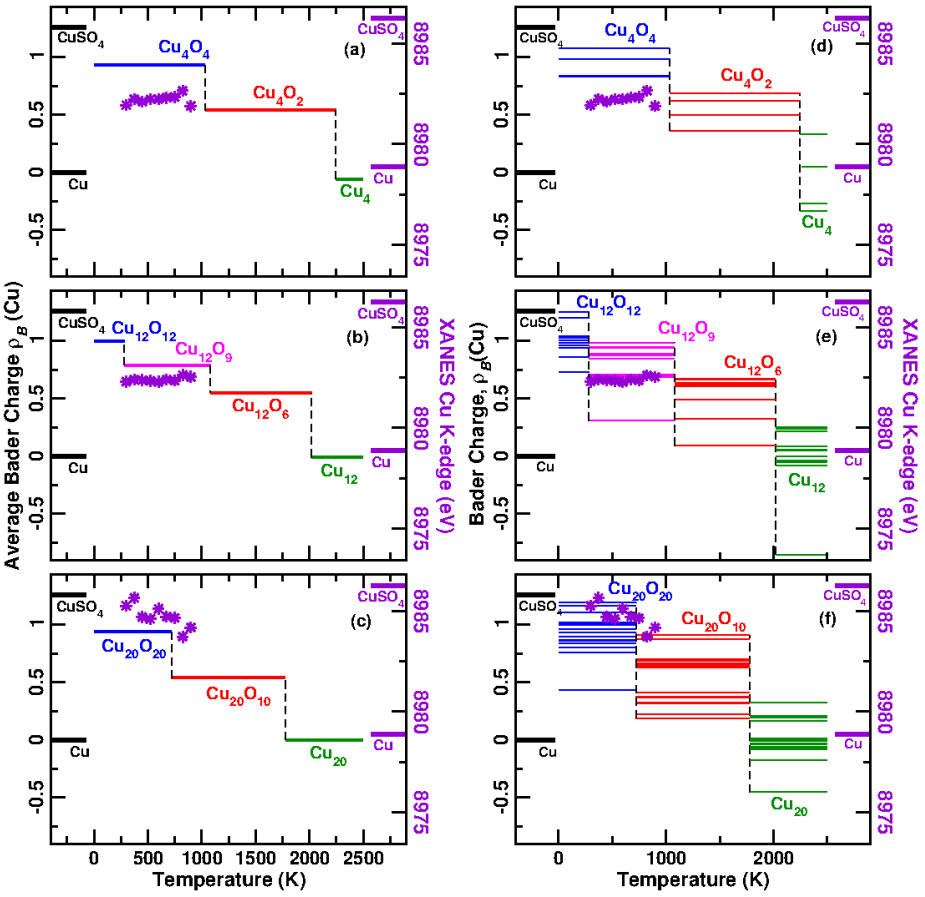

Figure 8.14: *Comparison of our theoretical results of Bader charge for the stable structure at a given T vs. the temperature T and our experimental results of XANES Cu K-edge positions for the cluster at a given T vs. T. In panels (a)–(c), the Bader charge is averaged over all the Cu atoms in the cluster, for $n = 4$, 12 and 20 respectively. In contrast in panels (d)–(f), the individual Bader charges for all the Cu atoms in the cluster are depicted, again for $n = 4$, 12 and 20 respectively. In order to facilitate comparison with XANES spectra results, we have plotted the XANES Cu K-edge positions for the cluster $n = 4$ in (a) and (d), for cluster $n = 12$ in (b) and (e) and for cluster $n = 20$ in (c) and (f), all as a function of T. The two ordinates are aligned according to the equation of the line obtained from Fig. 8.13(c). The black bars on the left hand side and the violet bars on the right hand side of each graph show the Bader charges and XANES Cu K-edge positions respectively of the Cu atoms in $CuSO_4$ and metallic Cu. The color convention for the solid lines is the same as in Fig. 8.3.*

For our experimental results, we extract the position of the Cu K-edge as determined

by the position of the first maximum in the first derivative of the XANES spectra for the clusters with $n = 4$, 12 and 20 shown in Fig. 8.11, and plot them in Fig. 8.14 as a function of T. The XANES Cu K-edge positions for the clusters at different T are shown by the violet stars in Fig. 8.14. As reference, we also show the XANES edge positions for Cu in $CuSO_4$ and metallic Cu foil as violet bars on the right hand side of each panel. The scale for the Bader charges shown on the left ordinate and the scale for the XANES edge positions shown on the right ordinate are aligned according to the equation of the line in Fig. 8.13(c).

We see that our results for the Bader charge of Cu atoms in the clusters and the XANES Cu K-edge positions for the clusters match very well. The discrepancy seen in the y-coordinates in panels Figs. 8.14(a)–(c), is presumably explained by the spread in the Bader charges of the individual Cu atoms in the cluster as seen in Figs. 8.14(d)–(f). In addition, in the experiments, all the clusters may not be in the ground state geometry, one may have a distribution of various low-energy isomers, as well as various adsorption sites on the amorphous hydroxylated alumina substrate.

The temperature range used in our experiments is unfortunately just short of capturing the phase transition to the $Cu_nO_{n/2}$ phase. Even so, for $n = 4$, we begin to see a dip in the XANES edge energy at around $T = 898$ K, and for $n = 20$, we see a clear lowering in the position of the K-edge energy of the Cu atoms in the cluster at $T = 823$ K. It is interesting to note that the experimental data now show a clear evidence of a phase transition as the temperature is varied; these were not apparent when merely performing a visual inspection of the spectra in Figs. 8.11(a)–(c).The decrease in energy of the XANES Cu K-edge suggests the reduction of the Cu atoms in the clusters, as is predicted theoretically. Also the temperatures at which the decrease in the XANES Cu K-edge positions is observed are in good agreement with the theoretically predicted transition temperatures.

8.3.5.2 Supported clusters in H_2-rich environment

Similar to the procedure followed in the case of Cu clusters in an O_2 environment, we now compare our results for the theoretically predicted phase transitions as a function of T and

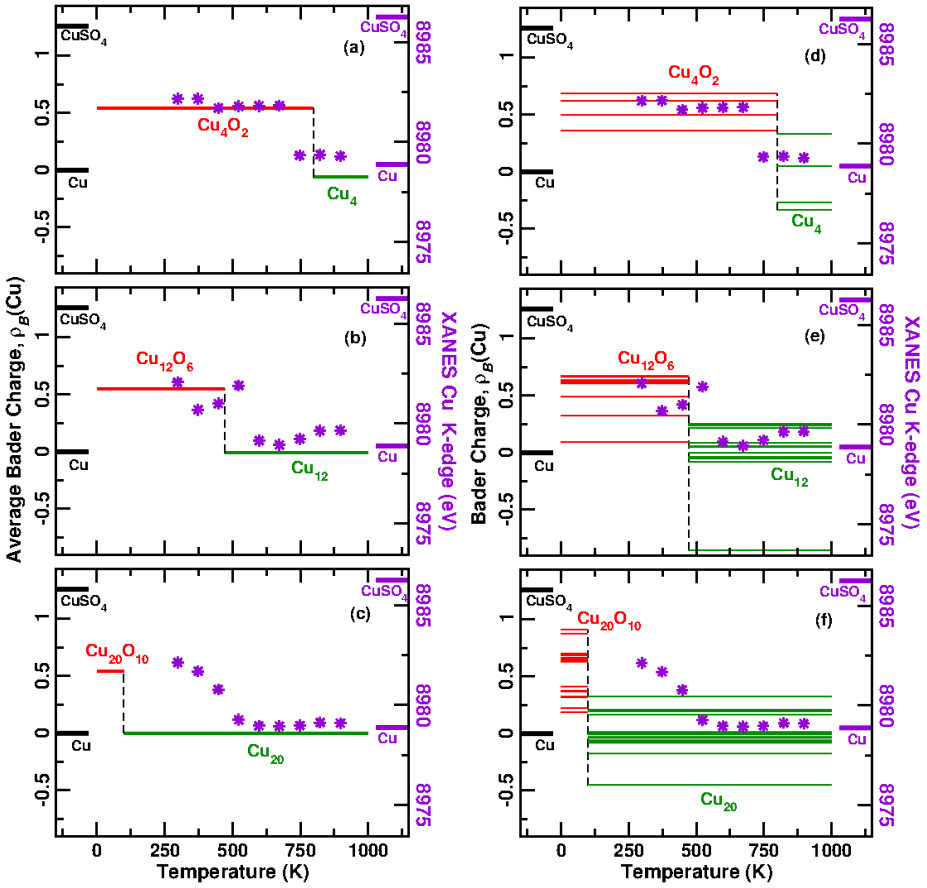

Figure 8.15: *Comparison of our theoretical results of Bader charge for the stable structure at a given T vs. the temperature T and our experimental results of XANES Cu K-edge positions for the cluster at a given T vs. T. In panels (a)–(c), the Bader charge is averaged over all the Cu atoms in the cluster, for $n = 4$, 12 and 20 respectively. In contrast in panels (d)–(f), the individual Bader charges for all the Cu atoms in the cluster are depicted, again for $n = 4$, 12 and 20 respectively. In order to facilitate comparison with XANES spectra results, we have plotted the XANES Cu K-edge positions for the cluster $n = 4$ in (a) and (d), for cluster $n = 12$ in (b) and (e) and for cluster $n = 20$ in (c) and (f), all as a function of T. The two ordinates are aligned according to the equation of the line obtained from Fig. 8.13(b). The black bars on the left hand side and the violet bars on the right hand side of each graph show the Bader charges and XANES Cu K-edge positions respectively of the Cu atoms in $CuSO_4$ and metallic Cu. The color convention for the solid lines is the same as in Fig. 8.3.*

our experimental results for the XANES Cu K-edge positions as a function of T in H_2-rich conditions. To do this, we make use of our theoretical results at $p(H_2)/p(H_2O) = 100$, which is our estimate of the conditions prevailing in the experiment. In Figs. 8.15(a)–(c) we show the average Bader charge of the Cu atoms in the stable phase of the cluster at a given temperature for $n = 4$, 12 and 20 clusters respectively and in Figs. 8.15(d)–(f) we show the individual Bader charges of the Cu atoms in the stable phase of the cluster

at a given temperature again for $n = 4$, 12 and 20 clusters, respectively, all as a function of T. The Bader charges are shown by the red and green solid lines in all panels. Here again, we see that the Bader charges in Figs. 8.15(d)–(f) show that every Cu atom in the cluster is different from the others. One striking result from these plots is that as the size of the cluster decreases, the transition temperature for the reduction from $Cu_nO_{n/2}$ $\rightarrow$ Cu_n (given by the T at which the red line ends and the green line begins) increases monotonically. This tells us that the temperature required to completely reduce a cluster to its elemental phase is very sensitive to the size of the cluster. Thus, when using size-selected Cu clusters as catalysts in experiments, one needs to go to higher temperatures as the size of the cluster decreases, if one wants to ensure that the cluster is in its elemental state.

The positions of the XANES Cu K-edge determined from the spectra in Fig. 8.12 for $n = 4$, 12 and 20 clusters are also plotted as a function of temperature in Fig. 8.15. Figs. 8.15(a) and (d) correspond to $n = 4$, Figs. 8.15(b) and (e) correspond to $n = 12$, and Figs. 8.15(c) and (f) correspond to $n = 20$. The K-edge energies are shown in violet stars and are positioned according to the scale on the right ordinate in these graphs. The Cu K-edge positions of Cu atoms in $CuSO_4$ and metallic Cu foil are also shown in violet bars as reference. The two ordinates in these graphs are aligned by the equation of the line in Fig. 8.13(c) as was done in Fig. 8.14. Doing this enables us to easily compare between our theoretical and experimental results.

We note that the analysis of the experimental data in this reducing environment now shows a clear evidence of phase transitions as the temperature is increased. Further, we note that these phase transitions display a clear size-dependent trend. The experimental XANES results also suggest the same size dependent trend predicted by theory, for the reduction temperature; as the size of the cluster reduces we see that the reduction temperature increases monotonically. We find that even the temperature-dependence of the Bader charge and the XANES edge position match very well.

Our results in Fig. 8.15 suggest an excellent agreement between our theoretically predicted and experimentally observed results. The violet stars (experimental results) almost

perfectly overlay the solid red and green lines (theoretical results) in each panel. The discrepancy between the XANES positions and the Bader charges in the case of $n = 20$ clusters at low T, we believe is due to kinetic effects that are involved in the removal of all the O atoms from $Cu_{20}O_{10}$ to form Cu_{20}; such kinetic effects are expected to be more marked as the size of the cluster increases.

8.4 Conclusions

We have obtained phase diagrams for small clusters of copper and copper oxides supported on hydroxylated amorphous alumina, using density functional theory combined with *ab initio* atomistic thermodynamics.

Interestingly, all the stable phases that appear in the phase diagrams for the supported clusters have the same stoichiometry as that of the stable (and metastable) phases observed in the bulk. In addition, a Bader charge analysis confirms that on average, the charge on the Cu atoms (and therefore the oxidation state and ionicity of the Cu-O bonds) is essentially the same for the clusters as in the corresponding bulk phase. The thermal stability of copper oxide clusters (i.e., the temperature at which oxygen would desorb entirely from the clusters) increases as the size of the cluster decreases. This is in contrast to an earlier reported result for silver oxide clusters.[190]

We also find that the presence of the support changes the phase diagram of the cluster significantly. For $n = 4$, the presence of the support stabilizes a stoichiometry not observed in the gas phase, viz., Cu_4O_2. Also for $n = 12$ and 20, the presence of the support stabilizes the Cu_nO_n phase that is not observed in the gas phase in the presence of O_2. For $n = 20$, two intermediate phases $Cu_{20}O_{12}$ and $Cu_{20}O_{15}$ that appear in the gas phase are no longer stable after deposition on the support.

We obtain clear size-dependent trends in both oxidizing and reducing environments for the supported clusters. We find that in an oxidizing environment in the presence of O_2, the transition temperature for $Cu_n \rightarrow Cu_nO_{n/2}$, increases as the size of the cluster decreases, and is larger for the clusters than for the bulk. However, for the transition $Cu_nO_{n/2} \rightarrow Cu_nO_n$, such a monotonic trend is not observed, instead we find that while

Cu_4O_2 oxidizes at a lower temperature than the bulk, $Cu_{12}O_6$ and $Cu_{20}O_{10}$ oxidize at almost the same temperature and are more resistant to oxidation than the bulk.

The size-dependent trends obtained in the presence of H_2 and H_2O are consistent with those obtained in the presence of O_2, i.e., the smaller the cluster, the more resistant it is to reduction. As the transition temperature is found to be very sensitive to the size of the cluster, in experiments where size-selected Cu clusters are used as catalysts, one needs to be sure that the temperature for reducing the Cu cluster to its elemental phase is sufficiently high enough. The smaller the cluster, the higher is the temperature required to completely reduce the Cu cluster to its elemental form.

In both the oxidizing environment in the presence of O_2 and in the reducing environment in H_2-rich conditions, we find that the presence of the support increases the tendency of the cluster to oxidize for $n = 4$ and 12 clusters, while it decreases the tendency to oxidize for $n = 20$ clusters.

Under conditions typical of those in which the low temperature water-gas shift reaction is carried out, our results suggest that a supported cluster with 20 Cu atoms will be in the reduced (elemental) state; however, this is not true of the smaller supported clusters studied here.

By performing DFT calculations on several three-dimensional Cu compounds, we have confirmed that the Bader charge on the metal (Cu) atom is sensitive to the electronegativity of the atom or functional group that it is bonded to. We show that this quantity provides a simple yet quantitative measure that makes it possible to correlate theoretical and experimental results on nanosystems to XANES standards based on extended bulk systems.

At an experimental condition of $p(O_2) = 0.06$ atm and at room temperature, all three sizes of cluster studied are oxidized. As temperature increases, theory suggests the reduction of these clusters takes place. The experimental XANES Cu K-edge positions match very well with those theoretically predicted by the Bader charges of the Cu atoms in the clusters at any given T. As the temperature is increased, the experiments also observe the beginning of reduction in these clusters at temperatures that are in good agreement

with the temperatures predicted for these transitions by our calculations.

In the H_2-rich environment, theory suggests that reduction occurs from the $Cu_nO_{n/2}$ phase to the Cu_n phase as temperature is increased. The experimental findings are in excellent agreement with these predictions. The temperature-dependent behavior of the Bader charges of Cu atoms in the clusters are well matched by the temperature-dependent behavior of the XANES Cu K-edge positions obtained for the Cu atoms in the clusters.

We believe this method of using Bader charge as a theoretical measure to interpret XANES spectra is very useful. It can be applied to other systems and also one can also use this as a means to study the changes in the oxidation state of a catalyst during any reaction and compare with the XANES measurements obtained.

Chapter 9

Summary and Outlook

In this chapter, we summarize the important results obtained in this thesis, and give a brief outlook for possible future lines of research.

We have investigated three major themes in this thesis, all pertaining to improving the performance of nanoclusters placed on an oxide support.

9.1 Diffusion and Sintering of Nanoclusters on a Support

In Chapter 3 of this thesis, we studied processes such as the diffusion and sintering of small Pt clusters on the MgO(100) surface. We found that, starting from the dimer, these clusters prefer to assume adsorption geometries that are upright on the surface, or geometries in which the cluster does not wet the surface. We also found that these clusters tend to bind more strongly at the F-center sites on the surface than on the defect-free surface. This suggests that F-center sites will act as pinning sites for the adsorption and growth of Pt clusters on the MgO surface. On comparing our results for the adsorption energies of the Pt clusters on the defect-free surface with corresponding results for other metal clusters like Pd,[27] Ag and Au[28] clusters, we found that of the four elements, it is the Pt clusters that bind most strongly to the MgO substrate.

We found that the diffusion barriers obtained for the Pt clusters are higher than those obtained for Pd, Ag and Au. However, we also found that the energy gained by the system upon sintering is higher in the case of Pt clusters as compared to Pd, Au or Ag

clusters. This suggests that thermodynamically, sintering of Pt clusters is greatly favored. The high barriers on the other hand suggest that the equilibrium condition in the case of Pt clusters will be achieved more slowly as compared to other metal clusters, i.e., while thermodynamics strongly favors the sintering of Pt clusters, kinetics hinders the sintering. Thus, at short time scales after cluster deposition, one should not observe sintering for these small Pt clusters; however, at long time scales one should observe it.

One assumption that was made in this chapter was that the diffusion barriers are the same in the dilute limit and close to another cluster or to a F-center. In future work, it would be desirable to check the validity of these assumptions. Moreover, one possibility would be to feed our results for the barriers for various elementary processes into a kinetic Monte Carlo simulation, so that one could actually try to study the growth and sintering process as a function of time and temperature.

9.2 Controlling the Morphology, Charge State and Reactivity of Nanoclusters

In Chapter 4, we proposed a simple and technically feasible method to tune the morphology and the charge state of a supported Au cluster. We demonstrated that the method of doping an oxide substrate with electron donor atoms can stabilize a two-dimensional planar geometry, in which the cluster wets the surface, over a three-dimensional geometry. The system we studied was a 20-atom Au cluster, which is known to have a stable tetrahedral geometry (T) in the gas phase as well as when supported on oxide substrates like MgO and CaO. Upon doping the substrate, we found that the supported Au clusters preferred a two-dimensional planar geometry (P), where all the Au atoms in the cluster bind to the surface. We showed that the extra electron from the electron donor impurity Al atom is transferred to the Au_{20} cluster. This makes the cluster negatively charged and the (P) cluster is stabilized over the (T) cluster, possibly due to electrostatic reasons.

We found that the stability of the (P) cluster with respect to the (T) cluster was dependent on the doping concentration in a linear fashion, and the minimum doping concentration required to flip the geometry from (T) to (P) was found to be 0.4 %. We

tried different concentrations and different positions for the dopant atoms, and in all cases we found that the stability of the (P) over the (T) depended only on the doping concentration and not the dopant position.

We calculated the charge transfer from the substrate to the Au cluster, and we found that in all cases, the (P) cluster was more negatively charged than the (T) cluster. Also, we found that as we increased the doping concentration, the charge transferred to the cluster increased monotonically.

This idea of tuning cluster morphology by substrate doping has subsequently been experimentally verified for the growth of Au clusters on Mo-doped CaO,[38] where the authors found that the Au clusters prefer a 3D growth on pristine CaO, while forming planar one-atomic-layer-thick clusters on Mo-doped CaO. Motivated by these experiments, we then carried out calculations on Au_{20} clusters supported on CaO. We found, in confirmation with the experiments, that the Au_{20} clusters prefer the 3D (T) geometry on pristine CaO but prefer to wet the surface to form the (P) cluster on Mo-doped CaO. Finally in this chapter, we also investigated the effect of substrate doping on small Au_n clusters; n = 1–3. We found that while on pristine MgO, the small clusters prefer to bind to the surface O atoms, on doping the substrate with Al atoms, the small clusters prefer to bind to the surface Mg atoms instead. In the case of the dimer and trimer, we saw that substrate doping makes the cluster wet the surface.

In Chapter 5, we showed that substrate doping not only affects the morphology of the supported Au clusters, but also, more interestingly, increases the reactivity of these clusters.[149] We have computed the reactivity of these supported Au clusters by considering the simple model reaction of the dissociation of an O_2 molecule adsorbed on the Au cluster. On comparing the barrier for O_2 dissociation on a Au_{20}(T) cluster on undoped MgO and on a Au_{20}(P) cluster on 2.78% Al-doped MgO, we saw a very significant reduction in the O_2 dissociation barrier. The barrier was more than halved, which corresponds to an increase in the reaction rates at room temperature of five orders of magnitude (if prefactors remain unaltered). We also found that the barriers for O_2 dissociation decreased monotonically as we increased the doping concentration in the substrate.

When trying to explain this observed increase in the reactivity, we found that the *d*-band model[4,5] fails to explain our observations. This model assumes that the *sp*-states are static and that all the action is solely in the *d*-states of a catalyst. However, on examining our results, we found that in addition to the *d*-states, the *s*- and *p*-states of Au are greatly affected by the substrate doping. We proposed a quantity that is the energy difference between the *sp*-states and the *d*-states, $\varepsilon_{sp} - \varepsilon_d$, to act as a novel descriptor for the reactivity of Au clusters deposited on a doped substrate. We found that $\varepsilon_{sp} - \varepsilon_d$ comes down in energy as doping concentration increases, and we believe that this parameter can explain the increased reactivity of Au clusters when deposited on a doped substrate.

In Chapter 6, we investigated the role of *s* and *p* electrons in Au reactivity. We tested the assumption that 'the *sp*-states are static' in three different scenarios: (a) on changing the coordination of Au atoms by reducing dimensionality (going from extended systems to surfaces to nanoclusters), (b) on going from a face site to an edge site to an apex site on a Au_{20}(T) cluster and (c) on negatively charging Au clusters. In all situations considered we found that the *sp*-states shift significantly and interestingly, shift more than the *d*-states.

We also found that the *d*-band model fails to explain the increase in the reactivity towards O_2 adsorption on going from a face site to an edge site to an apex site on the Au_{20}(T) cluster, and also on negatively charging Au clusters. The descriptor $\varepsilon_{sp} - \varepsilon_d$ however, is able to successfully explain the observed order of reactivity. From these results, we concluded that the *s*- and *p*-states play a vital role in the reactivity of Au nanoclusters, and further new catalysts can be screened using our new descriptor $\varepsilon_{sp} - \varepsilon_d$.

For future work, it would be of great interest to extend our investigations to the entire reaction of the catalytic oxidation of CO to CO_2, rather than merely the component step of O_2 dissociation. This reaction is of great industrial and environmental importance, and it would be good to know how the barriers for this reaction are altered on doping the substrate on which gold nanocatalysts are deposited.

It would also be of interest to examine other elements, to check whether the *d*-band model is valid for them, and in cases where it breaks down, to see whether our proposed descriptor $\varepsilon_{sp} - \varepsilon_d$ works better than ε_d alone, or whether it has to be modified further.

9.3 Controlling the Oxidation State of Atoms in a Nanocluster

In Chapter 7, where we studied three different sizes of gas phase Cu_nO_x clusters ($n = 4$, 12 and 20), we found that the phase diagrams obtained for the clusters are very different from the phase diagram of bulk Cu and its oxides, in both oxidizing and reducing environments. In the bulk, we know that the stable phases are Cu, Cu_2O and CuO. For $n = 4$, we do not see the $Cu_nO_{n/2}$ phase (which corresponds to the Cu_2O phase in the bulk), but at very high partial pressures of water, we see the presence of a high-oxygen-content stoichiometric phase Cu_4O_8. In addition to the phases seen in the bulk, viz., Cu_n, $Cu_nO_{n/2}$ and Cu_nO_n, we see intermediate phases $Cu_nO_{3n/4}$ for $n = 12$ and 20, and $Cu_nO_{3n/5}$ for $n = 20$.

In Chapter 8, we studied these Cu_nO_x clusters supported on hydroxylated amorphous alumina. We saw that the geometries of the Cu_nO_x clusters change significantly when deposited on the support as compared to the geometries in the gas phase. On analyzing the phase diagrams of these supported clusters in the oxidizing environment in the presence of O_2 and in the reducing environment in the presence of H_2 and H_2O, we saw a clear size-dependent trend, viz., the smaller the cluster, the more easily it is oxidized; alternatively, the smaller the cluster, the more resistant it is to reduction. We also compared our theoretical results with experimental results on the same system in O_2-rich and H_2-rich environments. We proposed that the Bader charge offers a simple and quantitative measure to compare theory and XANES experiments on nanoclusters based on the XANES spectra of known compounds. We found an excellent agreement between our theoretical predictions and experimental observations for the size-dependent phase transitions of supported Cu clusters. The agreement was very good for small clusters, it was less good for the largest size of cluster, presumably due to kinetic effects, which are expected to be more prevalent for the larger sizes.

Using the phase diagrams generated for both gas phase and supported clusters, one can now suggest the best size of a nanocatalyst that one can use for a given set of reaction conditions based on whether the catalyst is required to be in its elemental state or oxidized state.

One assumption made in these studies was that the vibrational entropy cancelled out between the elemental clusters and the oxide clusters; in future work, we plan to test the validity of this assumption, at least for a few test sizes. We also plan to repeat similar calculations for other elements and other substrates – it will be of great interest to see whether any universal trends emerge.

Bibliography

[1] W. Thiel *Angew. Chem. Int. Ed.*, vol. 53, p. 8605, 2014.

[2] P. Hohenberg and W. Kohn *Phys. Rev.*, vol. 136, p. B864, 1964.

[3] A. Warshel and M. Levitt *J. Mol. Bio.*, vol. 103, p. 227, 1976.

[4] B. Hammer and J. Nørskov in *Impact of Surface Science on Catalysis* (B. C. Gates and H. Knozinger, eds.), vol. 45 of *Advances in Catalysis*, p. 71, Academic Press, 2000.

[5] B. Hammer and J. Nørskov *Surf. Sci.*, vol. 343, no. 3, p. 211, 1995.

[6] J. R. C. H. C. J. K. Nørskov, T. Bligaard *Nature Chem.*, vol. 1, p. 37, 2009.

[7] M. S. Chen and D. W. Goodman *Catal. Today*, vol. 111, p. 22, 2006.

[8] L. M. Molina and B. Hammer *Phys. Rev. Lett.*, vol. 90, p. 206102, 2003.

[9] Z. Yan, S. Chinta, A. A. Mohamed, J. P. Fackler, and D. W. Goodman *J. Am. Chem. Soc.*, vol. 127, p. 1604, 2005.

[10] C. Harding, V. Habibpour, S. Kunz, A. N.-S. Farnbacher, U. Heiz, B. Yoon, and U. Landman *J. Am. Chem. Soc.*, vol. 131, p. 538, 2009.

[11] D. Ricci, A. Bongiorno, G. Pacchioni, and U. Landman *Phys. Rev. Lett.*, vol. 97, p. 036106, 2006.

[12] R. H. Petrucci, W. S. Harwood, G. E. Herring, and J. Madura, *General Chemistry: Principles and Modern Application*. Prentice Hall, 2007.

[13] S. Vajda, M. J. Pellin, J. P. Greeley, C. L. Marshall, L. A. Curtiss, G. A. Ballentine, J. W. Elam, S. Catillon-Mucherie, P. C. Redfern, F. Mehmood, and P. Zapol *Nature Mat.*, vol. 8, p. 213, 2009.

[14] M. Haruta, T. Kobayashi, H. Sano, and N. Yamada *Chem. Lett.*, vol. 16, no. 2, p. 405, 1987.

[15] M. C. Holz, K. Tölle, and M. Muhler *Catal. Sci. Technol.*, vol. 4, p. 3495, 2014.

[16] L. D. Burke and P. F. Nugent *Gold Bull.*, vol. 31, p. 39, 1998.

[17] C. T. Campbell and K. A. Daube *J. Catal.*, vol. 104, p. 109, 1987.

[18] G. J. J. Bartley and R. Burch *App. Catal.*, vol. 43, no. 1, p. 141, 1988.

[19] S. Rabe and F. Vogel *App. Catal. B: Envt.*, vol. 84, no. 34, p. 827, 2008.

[20] W. Kohn and L. J. Sham *Phys. Rev.*, vol. 140, p. A1133, 1965.

[21] G. Henkelman and H. Jónsson *J. Chem. Phys.*, vol. 113, p. 9978, 2000.

[22] D. Sheppard, R. Terrell, and G. Henkelman *J. Chem. Phys.*, vol. 128, p. 134106, 2008.

[23] S. Kirkpatrick, C. D. G. Jr., and M. P. Vecchi *Science*, vol. 220, no. 4598, p. 671, 1983.

[24] K. Reuter and M. Scheffler *Phys. Rev. B*, vol. 65, p. 035406, 2001.

[25] K. Reuter and M. Scheffler *Phys. Rev. B*, vol. 68, p. 045407, 2003.

[26] L. Xu, G. Henkelman, C. T. Campbell, and H. Jónsson *Phys. Rev. Lett.*, vol. 95, 2005.

[27] L. Xu, G. Henkelman, C. T. Campbell, and H. Jónsson *Surf. Sci.*, vol. 600, 2006.

[28] G. Barcaro and A. Fortunelli *New J. Phys.*, vol. 9, p. 22, 2007.

[29] B. Yoon, P. Koskinen, B. Huber, O. Kostko, B. von Issendorff, H. Häkkinen, M. Moseler, and U. Landman *Chem. Phys. Chem.*, vol. 8, p. 157, 2007.

[30] N. Lopez, T. Janssens, B. Clausen, Y. Xu, M. Mavrikakis, T. Bligaard, and J. Nørskov *J. Catal.*, vol. 223, no. 1, p. 232, 2004.

[31] C. Zhang, B. Yoon, and U. Landman *J. Am. Chem. Soc.*, vol. 129, p. 2228, 2007.

[32] B. Yoon, H. Häkkinen, and U. Landman *J. Phys. Chem. A*, vol. 107, no. 20, p. 4066, 2003.

[33] J. Li, X. Li, H.-J. Zhai, and L.-S. Wang *Science*, vol. 299, no. 5608, p. 864, 2003.

[34] L. Molina and B. Hammer *J. Catal.*, vol. 233, no. 2, p. 399, 2005.

[35] M. Sterrer, T. Risse, M. Heyde, H.-P. Rust, and H.-J. Freund *Phys. Rev. Lett.*, vol. 98, p. 206103, 2007.

[36] B. Yoon and U. Landman *Phys. Rev. Lett.*, vol. 100, p. 056102, 2008.

[37] N. Mammen, S. Narasimhan, and S. de Gironcoli *J. Am. Chem. Soc.*, vol. 133, no. 9, p. 2801, 2011.

[38] X. Shao, S. Prada, L. Giordano, G. Pacchioni, N. Nilius, and H.-J. Freund *Angew. Chem. Int. Ed.*, vol. 50, no. 48, p. 11525, 2011.

[39] B. Hammer and J. K. Nørskov *Nature*, vol. 376, p. 238, 1995.

[40] C. Jiang, D. Trimm, M. Wainwright, and N. Cant *App. Catal. A: General*, vol. 93, no. 2, p. 245, 1993.

[41] R. M. Martin, *Electronic Structure Basic Theory and Practical Methods*. Cambridge University Press, 2004.

[42] M. Born and J. R. Oppenheimer *Ann. Physik*, vol. 84, p. 457, 1927.

[43] P. Ghosh, *Theoretical Investigations of Properties of Low Dimensional Systems and Nanomaterials*. PhD thesis, Jawaharlal Nehru Centre for Advanced Scientific Research, Bangalore, India, 2007.

[44] K. Ulman, *First Principles Investigations of Nanomaterials for Electronic, Spintronic and Gas Storage Applications*. PhD thesis, Jawaharlal Nehru Centre for Advanced Scientific Research, Bangalore, India, 2015.

[45] D. D. Johnson *Phys. Rev. B*, vol. 38, p. 12807, 1988.

[46] D. Vanderilt and S. G. Louie *Phys. Rev. B*, vol. 30, p. 6118, 1984.

[47] J. P. Perdew, K. Burke, and M. Ernzerhof *Phys. Rev. Lett.*, vol. 77, p. 3865, 1996.

[48] J. P. Perdew, K. Burke, and M. Ernzerhof *Phys. Rev. Lett. (E)*, vol. 78, p. 1396, 1997.

[49] J. P. Perdew and Y. Wang *Phys. Rev. B*, vol. 46, p. 12947, 1992.

[50] P. Giannozzi, S. Baroni, N. Bonini, M. Calandra, R. Car, C. Cavazzoni, D. Ceresoli, G. Chiarotti, M. Cococcioni, I.Dabo, A. D. Corso, S. de Gironcoli, S. Fabris, G. Fratesi, R. Gebauer, U. Gerstmann, C. Gougoussis, A. Kokalj, M. Lazzeri, L. Martin-Samos, N. Marzari, F. Mauri, R. Mazzarello, S. Paolini, A. Pasquarello, L. Paulatto, C. Sbraccia, S. Scandolo, G. Sclauzero, A. P. Seitsonen, A. Smogunov, P. Umari, and R. M. Wentzcovitch *J. Phys. Condens. Matter*, vol. 21, p. 395502, 2009.

[51] X. Gonze, J.-M. Beuken, R. Caracas, F. Detraux, M. Fuchs, G.-M. Rignanese, L. Sindic, M. Verstraete, G. Zerah, F. Jollet, M. Torrent, A. Roy, M. Mikami, P. Ghosez, J.-Y. Raty, and D. C. Allan *Computational Materials Science*, vol. 25, p. 478, 2002.

[52] O. K. Anderson *et al.*, *Electronic Structure and Physical Properties of Solids. The Uses of the LMTO Method*. Springer, 2000.

[53] J. M. Soler, E. Artacho, J. D. Gale, A. García, P. O. J. Junquera, and D. Sánchez-Portal *J. Phys.: Condens. Matter*, vol. 14, p. 2745, 2002.

[54] G. Kresse and J. Hafner *Phys. Rev. B*, vol. 47, p. 558, 1993.

[55] G. Kresse and J. Hafner *Phys. Rev. B*, vol. 49, p. 14251, 1994.

[56] G. Kresse and J. Furthmüller *Comput. Mat. Sci.*, vol. 6, no. 1, p. 15, 1996.

[57] G. Kresse and J. Furthmüller *Phys. Rev. B*, vol. 54, p. 11169, 1996.

[58] C. Kittel, *Introduction to Solid State Physics*. Wiley - India, 2007.

[59] J. C. Phillips and L. Kleinman *Phys. Rev.*, vol. 116, p. 287, 1959.

[60] W. E. Pickett *Computer Physics Reports*, vol. 9, p. 115, 1989.

[61] S. Narasimhan, "Atoms and pseudopotentials." `http://www.iiserpune.ac.in/~smr2626/hands_on/week1/july1/pseudopotentials.pdf`, 2014. [Online; accessed 4-February-2015].

[62] D. R. Hamann, M. Schlüter, and C. Chiang *Phys. Rev. Lett.*, vol. 43, p. 1494, 1979.

[63] D. Vanderbilt *Phys. Rev. B*, vol. 41, p. 7892, 1990.

[64] P. E. Blöchl *Phys. Rev. B*, vol. 50, p. 17953, 1994.

[65] G. Kresse and J. Joubert *Phys. Rev. B*, vol. 59, p. 1758, 1999.

[66] O. K. Andersen *Phys. Rev. B*, vol. 12, p. 3060, 1975.

[67] H. J. Monkhorst and J. D. Pack *Phys. Rev. B*, vol. 13, p. 5188, 1976.

[68] S. Narasimhan, ""k-points" or brillouin zone sums in electronic structure calculations." `http://www.iiserpune.ac.in/~smr2626/hands_on/week1/july1/bzsums_mastani.pdf`, 2014. [Online; accessed 4-February-2015].

[69] C. L. Fu and K. M. Ho *Phys. Rev. B*, vol. 28, p. 5480, 1983.

[70] M. Methfessel and A. T. Paxton *Phys. Rev. B*, vol. 40, p. 3616, 1989.

[71] N. Marzari, D. Vanderbilt, A. D. Vita, and M. C. Payne *Phys. Rev. Lett.*, vol. 82, p. 3296, 1999.

[72] R. P. Feynman *Phys. Rev.*, vol. 56, p. 340, 1939.

[73] D. P. Bertsekas, *Constrained Optimization and Lagrange Multiplier Methods*. Athena Scientific, 1982.

[74] J.-P. Ryckaert, G. Ciccotti, and H. J. C. Berendsen *J. Comp. Phys.*, vol. 23, pp. 327 – 341, 1977.

[75] J. Li, *Handbook of Materials Modeling*. Springer, 2005.

[76] D. Frenkel and B. Smit, *Understanding Molecular Simulation - From Algorithms to Applications*. Academic Press, 1996.

[77] J. E. Lennard-Jones *Proc. R. Soc. London Ser. A*, vol. 106, p. 463, 1924.

[78] F. London *Z. Phys. Chem.*, vol. B11, p. 222, 1930.

[79] R. A. Buckingham *Proceedings of the Royal Society of London*, vol. 168, p. 264, 1938.

[80] M. Matsui *Miner. Mag.*, vol. 58A, p. 571, 1994.

[81] S. P. Adiga, P. Zapol, and L. A. Curtiss *J. Phys. Chem. C*, vol. 111, no. 20, p. 7422, 2007.

[82] T.-R. Shan, B. D. Devine, T. W. Kemper, S. B. Sinnott, and S. R. Phillpot *Phys. Rev. B*, vol. 81, p. 125328, 2010.

[83] T. Liang, T.-R. Shan, Y.-T. Cheng, B. D. Devine, M. Noordhoek, Y. Li, Z. Lu, S. R. Phillpot, and S. B. Sinnott *Mat. Sci. Eng*, vol. 74, p. 255, 2013.

[84] H. J. C. Berendsen, J. P. M. Postma, W. F. van Gunsteren, A. DiNola, and J. R. Haak *J. of Chem. Phys.*, vol. 8, p. 3684, 1984.

[85] S. Plimpton *J. Comp. Phys.*, vol. 117, no. 1, p. 1, 1995.

[86] A. Kokalj *Comp. Mater. Sci.*, vol. 28, p. 155, 2003.

[87] K. Momma and F. Izumi *J. Appl. Crystallogr.*, vol. 44, p. 1272, 2011.

[88] J. Shi, S. Gider, K. Babcock, and D. D. Awschalom *Science*, vol. 271, no. 5251, p. 937, 1996.

[89] T.-H. Lee and R. M. Dickson *Proc. Natl. Acad. Sci.*, vol. 100, no. 6, p. 3043, 2003.

[90] S. Abbet, K. Judai, L. Klinger, and U. Heiz *Pure Appl. Chem.*, vol. 74, p. 1527, 2002.

[91] C. T. Campbell, S. C. Parker, and D. E. Starr *Science*, vol. 298, no. 5594, p. 811, 2002.

[92] C. R. Henry *Surf. Sci. Rep.*, vol. 31, 1998.

[93] L. Xu, C. T. Campbell, H. Jónsson, and G. Henkelman *Surf. Sci.*, vol. 601, 2007.

[94] G. Haas, A. Menck, H. Brune, J. V. Barth, J. A. Venables, and K. Kern *Phys. Rev. B*, vol. 61, p. 11105, Apr 2000.

[95] M.-C. Wu, C. M. Truong, and D. W. Goodman *Phys. Rev. B*, vol. 46, p. 12688, Nov 1992.

[96] A. Bogicevic and D. Jennison *Surf. Sci.*, vol. 515, no. 23, p. L481, 2002.

[97] L. Giordano, C. Di Valentin, J. Goniakowski, and G. Pacchioni *Phys. Rev. Lett.*, vol. 92, p. 096105, Mar 2004.

[98] C. G. Broyden *J. Institute of Mathematics and Its Applications*, vol. 6, p. 76, 1970.

[99] R. Fletcher *Comp. J.*, vol. 13, p. 317, 1970.

[100] D. Goldfarb *Math. Comput.*, vol. 24, p. 23, 1970.

[101] D. F. Shanno *Math. Comput.*, vol. 24, p. 647, 1970.

[102] P. C. Jennings and R. L. Johnston *Comp. Theor. Chem.*, vol. 1021, p. 91, 2013.

[103] P. Błoński and J. Hafner *J. Chem. Phys.*, vol. 134, p. 154705, 2011.

[104] L. Xiao and L. Wang *J. Phys. Chem. B*, vol. 111, p. 1657, 2007.

[105] D. Dai and K. Balasubramanian *J. Chem. Phys.*, vol. 103, p. 648, 1995.

[106] J. Kua and W. A. G. III *J. Phys. Chem. B*, vol. 102, p. 9481, 1998.

[107] A. Nie, J. Wu, C. Zhou, S. Yao, C. Luo, R. C. Forrey, and H. Cheng *Intl. J. Q. Chem.*, vol. 107, p. 219, 2007.

[108] R. F. W. Bader, *Atoms in Molecules - A quantum theory.* New York: Oxford University Press, 1990.

[109] W. Tang, E. Sanville, and G. Henkelman *J. Phys.: Condens. Matter*, vol. 21, p. 084204, 2009.

[110] H. Grönbeck and P. Broqvist *J. Chem. Phys.*, vol. 119, p. 3896, 2003.

[111] J. N. Brønsted *Chem. Rev.*, vol. 5, p. 231, 1928.

[112] M. G. Evans and N. P. Polanyi *Trans. Faraday Soc.*, vol. 34, p. 11, 1938.

[113] H.-G. Boyen, G. Kästle, F. Weigl, B. Koslowski, C. Dietrich, P. Ziemann, J. P. Spatz, S. Riethmüller, C. Hartmann, M. Möller, G. Schmid, M. G. Garnier, and P. Oelhafen *Science*, vol. 297, no. 5586, p. 1533, 2002.

[114] R. Elghanian, J. J. Storhoff, R. C. Mucic, R. L. Letsinger, and C. A. Mirkin *Science*, vol. 277, no. 5329, p. 1078, 1997.

[115] M. Homberger and U. Simon *Phil. Trans. R. Soc. A*, vol. 368, no. 1915, p. 1405, 2010.

[116] T. Hayashi, K. Tanaka, and M. Haruta *J. Catal.*, vol. 178, p. 566, 1998.

[117] Q. Fu, H. Saltsburg, and M. Flytzani-Stephanopoulos *Science*, vol. 301, no. 5635, p. 935, 2003.

[118] J. Jia, K. Haraki, J. N. Kondo, K. Domen, and K. Tamaru *J. Phys. Chem. B*, vol. 104, no. 47, p. 11153, 2000.

[119] C. Bianchi, F. Porta, L. Prati, and M. Rossi *Topics in Catal.*, vol. 13, no. 3, p. 231, 2000.

[120] M. Haruta *Catal. Today*, vol. 36, p. 153, 1997.

[121] A. Sanchez, S. Abbet, U. Heiz, W.-D. Schneider, H. Häkkinen, R. N. Barnett, and U. Landman *J. Phys. Chem. A*, vol. 103, p. 9573, 1999.

[122] F. Stavale, X. Shao, N. Nilius, H.-J. Freund, S. Prada, L. Giordano, and G. Pacchioni *J. Am. Chem. Soc.*, vol. 134, no. 28, p. 11380, 2012.

[123] G. Makov and M. C. Payne *Phys. Rev. B.*, vol. 51, no. 7, 1995.

[124] J. Andersin, J. Nevalaita, K. Honkala, and H. Häkkinen *Angew. Chem. Int. Ed.*, vol. 52, no. 5, p. 1424, 2013.

[125] H. Häkkinen and U. Landman *Phys. Rev. B*, vol. 63, no. 4, p. 2287, 2000.

[126] J. Wang, G. Wang, and J. Zhao *Phys. Rev. B*, vol. 66, p. 035418, 2002.

[127] A. D. Vitto, G. Pacchioni, F. Delbecq, and P. Sautet *J. Phys. Chem. B*, vol. 109, p. 8040, 2005.

[128] S. S. Yamijala, A. Bandyopadhyay, and S. K. Pati *J. Phys. Chem. C*, vol. 118, no. 31, p. 17890, 2014.

[129] K. Mondal, C. Kamal, A. Banerjee, A. Chakrabarti, and T. K. Ghanty *J. Phys. Chem. C*, vol. 119, no. 6, p. 3192, 2015.

[130] G. C. Bond and D. T. Thompson *Gold Bulletin*, vol. 33, no. 2, p. 41, 2000.

[131] T. Bernhardt, U. Heiz, and U. Landman in *Nanocatalysis* (U. Heiz and U. Landman, eds.), Nanoscience and Technology, p. 1, Springer Berlin Heidelberg, 2007.

[132] H. Falsig, B. Hvolbæk, I. Kristensen, T. Jiang, T. Bligaard, C. Christensen, and J. Nørskov *Angew. Chem. Int. Ed.*, vol. 47, no. 26, p. 4835, 2008.

[133] N. Nikbin, N. Austin, D. G. Vlachos, M. Stamatakis, and G. Mpourmpakis *Catal. Sci. Technol.*, vol. 5, p. 134, 2015.

[134] M. Stamatakis, M. A. Christiansen, D. G. Vlachos, and G. Mpourmpakis *Nano Lett.*, vol. 12, no. 7, p. 3621, 2012.

[135] P. Ghosh, M. Farnesi Camellone, and S. Fabris *J. Phys. Chem. Lett.*, vol. 4, no. 14, p. 2256, 2013.

[136] A. Bongiorno and U. Landman *Phys. Rev. Lett.*, vol. 95, p. 106102, 2005.

[137] C. Zhang, P. Hu, and A. Alavi *J. Am. Chem. Soc.*, vol. 121, p. 7931, 1999.

[138] R. J. Baxter and P. Hu *J. Chem. Phys.*, vol. 116, no. 11, p. 4739, 2002.

[139] P. Schwerdtfeger *Angew. Chem. Int. Ed.*, vol. 42, no. 17, p. 1892, 2003.

[140] H. Y. Kim and G. Henkelman *J. Phys. Chem. Lett.*, vol. 3, no. 16, p. 2194, 2012.

[141] Q. Sun, P. Jena, Y. D. Kim, M. Fischer, and G. Gantefor *J. Chem. Phys.*, vol. 120, no. 14, p. 6510, 2004.

[142] B. Yoon, H. Häkkinen, U. Landman, A. S. Wörz, J.-M. Antonietti, S. Abbet, K. Judai, and U. Heiz *Science*, vol. 307, no. 5708, p. 403, 2005.

[143] A. Roldan, J. M. Ricart, F. Illas, and G. Pacchioni *Phys. Chem. Chem. Phys.*, vol. 12, p. 10723, 2010.

[144] M.-S. Miao, J. A. Kurzman, N. Mammen, S. Narasimhan, and R. Seshadri *Inorg. Chem.*, vol. 51, no. 14, p. 7569, 2012.

[145] V. Stamenkovic, B. S. Mun, K. J. J. Mayrhofer, P. N. Ross, N. M. Markovic, J. Rossmeisl, J. Greeley, and J. K. Nørskov *Angew Chem. Int. Ed.*, vol. 45, p. 2897, 2006.

[146] D. J. Mowbray, A. Migani, G. Walther, D. M. Cardamone, and A. Rubio *J. Phys. Chem. Lett.*, vol. 4, no. 17, p. 3006, 2013.

[147] L. M. Molina and B. Hammer *Phys. Rev. B*, vol. 69, p. 155424, 2004.

[148] P. Frondelius, H. Häkkinen, and K. Honkala *Angew. Chem. Int. Ed.*, vol. 49, no. 43, p. 7913, 2010.

[149] N. Mammen, S. de Gironcoli, and S. Narasimhan *J. Chem. Phys.*, vol. 143, no. 14, p. 144307, 2015.

[150] J. A. van Bokhoven and J. T. Miller *J. Phys. Chem. C*, vol. 111, no. 26, p. 9245, 2007.

[151] P. Schwerdtfeger *Chem. Phys. Lett.*, vol. 183, no. 5, p. 457, 1991.

[152] P. Schwerdtfeger *Heteroatom Chem.*, vol. 13, no. 6, p. 578, 2002.

[153] P. W. Anderson *Phys. Rev.*, vol. 124, p. 41, 1961.

[154] D. M. Newns *Phys. Rev.*, vol. 178, p. 1123, 1969.

[155] H. R. Liu, H. Xiang, and X. G. Gong *J. Chem. Phys.*, vol. 135, p. 214702, 2011.

[156] M. T. Gorzkowski and A. Lewera *J. Phys. Chem. C*, vol. 119, no. 32, p. 18389, 2015.

[157] H. Xin and S. Linic *J. Chem. Phys.*, vol. 132, p. 221101, 2010.

[158] G. J. Hutchings *J. Catal*, vol. 96, p. 292, 1985.

[159] G. J. Hutchings *Catal. Today*, vol. 100, p. 55, 2005.

[160] L. Prati and M. Rossi *J. Catal*, vol. 176, p. 552, 1998.

[161] B. Hvolbæk, T. V. W. Janssens, B. S. Clausen, H. Falsig, C. H. Christensen, and J. K. Nørskov *Nano Today*, vol. 2, no. 4, p. 14, 2007.

[162] M. M. Schubert, S. Hackenberg, A. C. van Veen, M. Muhler, V. Plzak, and R. J. Behm *J. Catal*, vol. 113, p. 197, 2001.

[163] M. Mavrikakis, P. Stoltze, and J. K. Nørskov *Catal. Lett.*, vol. 64, p. 101, 2000.

[164] M. Valden, X. Lai, and D. W. Goodman *Science*, vol. 281, p. 1647, 1998.

[165] M.-S. Miao, J. A. Kurzman, N. Mammen, S. Narasimhan, and R. Seshadri *Inorg. Chem.*, vol. 51, p. 7569, 2012.

[166] H. Häkkinen, B. Yoon, U. Landman, X. Li, H.-J. Zhai, and L.-S. Wang *J. Phys. Chem. A*, vol. 107, p. 6168, 2003.

[167] H. S. De, S. Krishnamurty, and S. Pal *J. Phys. Chem. C*, vol. 114, p. 6690, 2010.

[168] Y.-K. Han *J. Chem. Phys.*, vol. 124, p. 024316, 2006.

[169] R. Pushpa, P. Ghosh, S. Narasimhan, and S. de Gironcoli *Phys. Rev. B*, vol. 79, p. 165406, 2009.

[170] P. Ghosh, R. Pushpa, S. de Gironcoli, and S. Narasimhan *Phys. Rev. B*, vol. 80, p. 233406, 2009.

[171] R. Pushpa, P. Ghosh, S. Narasimhan, and S. de Gironcoli *Phys. Rev. B*, vol. 79, p. 165406, 2009.

[172] M. S. Daw and M. I. Baskes *Phys. Rev. Lett*, vol. 50, p. 1285, 1983.

[173] M. S. Daw *Phys. Rev. B*, vol. 39, p. 7441, 1989.

[174] F. Ercolessi, E. Tosatti, and M. Parrinello *Phys. Rev. Lett.*, vol. 57, p. 719, 1986.

[175] K. W. Jacobsen, J. K. Nørskov, and M. J. Puska *Phys. Rev. B*, vol. 35, p. 7423, 1987.

[176] J. Miller, A. Kropf, Y. Zha, J. Regalbuto, L. Delannoy, C. Louis, E. Bus, and J. A. van Bokhoven *J. Catal.*, vol. 240, no. 2, p. 222, 2006.

[177] W. Qi, B. Huang, and M. Wang *J. Comp. Theor. Nanoscience*, vol. 6, p. 635, 2009.

[178] J. Paul and S. Narasimhan *Bull. Mater. Sci.*, vol. 31, no. 3, p. 569, 2008.

[179] J. Wang, G. Wang, and J. Zhao *Chem. Phys. Lett.*, vol. 380, no. 56, p. 716, 2003.

[180] H. S. De, S. Krishnamurty, and S. Pal *J. Phys. Chem. C*, vol. 113, p. 7101, 2009.

[181] Y. Shao, G. Yin, and Y. Gao *J. Power Sources*, vol. 171, no. 2, p. 558, 2007.

[182] M. Turco, G. Bagnasco, C. Cammarano, P. Senese, U. Costantino, and M. Sisani *App. Catal. B: Envt.*, vol. 77, no. 1 2, p. 46, 2007.

[183] F. López-Suárez, A. Bueno-López, and M. Illán-Gómez *App. Catal. B: Envt.*, vol. 84, no. 34, p. 651, 2008.

[184] C.-S. Chen, W.-H. Cheng, and S.-S. Lin *Catal. Lett.*, vol. 68, no. 1-2, p. 45, 2000.

[185] J. Amphlett, K. Creber, J. Davis, R. Mann, B. Peppley, and D. Stokes *Int. J. Hydrogen Energy*, vol. 19, no. 2, p. 131, 1994.

[186] H. Bluhm, M. Hävecker, A. Knop-Gericke, E. Kleimenov, R. Schlögl, D. Teschner, V. I. Bukhtiyarov, D. F. Ogletree, and M. Salmeron *J. Phys. Chem. B*, vol. 108, no. 38, p. 14340, 2004.

[187] L. Signorini, L. Pasquini, L. Savini, R. Carboni, F. Boscherini, E. Bonetti, A. Giglia, M. Pedio, N. Mahne, and S. Nannarone *Phys. Rev. B*, vol. 68, p. 195423, 2003.

[188] E. van Steen, M. Claeys, M. E. Dry, J. van de Loosdrecht, E. L. Viljoen, and J. L. Visagie *J. Phys. Chem. B*, vol. 109, no. 8, p. 3575, 2005. PMID: 16851395.

[189] A. Saib, A. Borgna, J. van de Loosdrecht, P. van Berge, and J. Niemantsverdriet *App. Catal. A: General*, vol. 312, p. 12, 2006.

[190] S. Klacar, A. Hellman, I. Panas, and H. Grönbeck *J. Phys. Chem. C*, vol. 114, no. 29, p. 12610, 2010.

[191] A. Desireddy, B. E. Conn, J. Guo, B. Yoon, R. N. Barnett, B. M. Monahan, K. Kirschbaum, W. P. Griffith, R. L. Whetten, U. Landman, and T. P. Bigioni *Nature*, vol. 501, no. 7467, p. 399, 2013.

[192] Y. L. Mikhlin, E. A. Vishnyakova, A. S. Romanchenko, S. V. Saikova, M. N. Likhatski, Y. V. Larichev, F. V. Tuzikov, V. I. Zaikovskii, and S. M. Zharkov *App. Surf. Sci.*, vol. 297, p. 75, 2014.

[193] S. Bhattacharya, S. V. Levchenko, L. M. Ghiringhelli, and M. Scheffler *Phys. Rev. Lett.*, vol. 111, p. 135501, 2013.

[194] L. Wang, T. Maxisch, and G. Ceder *Phys. Rev. B*, vol. 73, p. 195107, 2006.

[195] M. Heinemann, B. Eifert, and C. Heiliger *Phys. Rev. B*, vol. 87, p. 115111, 2013.

[196] A. Soon, M. Todorova, B. Delley, and C. Stampfl *Phys. Rev. B*, vol. 73, p. 165424, 2006.

[197] X. Duan, O. Warschkow, A. Soon, B. Delley, and C. Stampfl *Phys. Rev. B*, vol. 81, p. 075430, 2010.

[198] C. Gattinoni and A. Michaelides *Surf. Sci. Rep.*, vol. 70, p. 424, 2015.

[199] Y. Maimaiti, M. Nolan, and S. D. Elliott *Phys. Chem. Chem. Phys.*, vol. 16, p. 3036, 2014.

[200] P. E. Blöchl *Phys. Rev. B*, vol. 50, p. 17953, 1994.

[201] S. Baroni, P. Giannozzi, and A. Testa *Phys. Rev. Lett.*, vol. 58, p. 1861, 1987.

[202] S. Baroni, S. de Gironcoli, A. Dal Corso, and P. Giannozzi *Rev. Mod. Phys.*, vol. 73, p. 515, 2001.

[203] D. R. Stull and H. Prophet, *NIST-JANAF Thermochemical Tables, 2nd Edition.* Washington D. C.: U.S. National Bureau of Standards, 1971.

[204] C. Liu, H. He, P. Zapol, and C. Larry A *Phys. Chem. Chem. Phys.*, vol. 16, p. 26584, 2014.

[205] F. Yang, Q. Sun, L. L. Ma, Y. Jia, S. J. Luo, J. M. Liu, W. T. Geng, J. Y. Chen, S. Li, and Y. Yu *J. Phys. Chem. A*, vol. 114, no. 32, p. 8417, 2010.

[206] Q. Sun, X. G. Gong, Q. Q. Zheng, D. Y. Sun, and G. H. Wang *Phys. Rev. B*, vol. 54, no. 15, p. 10896, 1996.

[207] I. Efremenko and M. Sheintuch *Chem. Phys. Lett.*, vol. 401, no. 13, p. 232, 2005.

[208] R. D. Parra and H. H. Farrell *J. Phys. Chem. C*, vol. 113, no. 12, p. 4786, 2009.

[209] W. A. de Heer *Rev. Mod. Phys.*, vol. 65, p. 611, 1993.

[210] S. Lany *Phys. Rev. B*, vol. 78, p. 245207, 2008.

[211] A. Stakheev and L. Kustov *App. Catal. A: General*, vol. 188, no. 12, p. 3, 1999.

[212] A. Gaur, B. D. Shrivastava, and H. L. Nigam *Proc. Indian Natn. Sci. Acad.*, vol. 79, no. 4, p. 921, 2013.

[213] G. N. George and M. L. Gorbaty *J. Am. Chem. Soc.*, vol. 111, no. 9, p. 3182, 1989.

[214] J. Wong, F. W. Lytle, R. P. Messmer, and D. H. Maylotte *Phys. Rev. B*, vol. 30, p. 5596, 1984.

[215] T. Resslera, J. Wienolda, R. E. Jentofta, and T. Neisius *J. Catal.*, vol. 210, p. 67, 2002.

[216] Z. Lu, Z. Yang, B. He, C. Castleton, and K. Hermansson *Chem. Phys. Lett.*, vol. 510, no. 13, p. 60, 2011.

[217] N. Seriani, Z. Jin, W. Pompe, and L. C. Ciacchi *Phys. Rev. B*, vol. 76, p. 155421, 2007.

[218] J. P. Allen, D. O. Scanlon, and G. W. Watson *Phys. Rev. B*, vol. 81, p. 161103, 2010.

[219] J. C. Phillips *Rev. Mod. Phys.*, vol. 42, p. 317, 1970.

[220] S. S. Batsanov and A. S. Batsanov, *Introduction to Structural Chemistry.* Springer, 2012.